



Fluorescent Silver Nanoclusters

Hector Henry Oyem

A thesis submitted in partial fulfilment of the requirements for
the award of

Doctor of Philosophy

School of Natural and Environmental Sciences

(Chemistry)

Newcastle University, Newcastle upon Tyne,
United Kingdom.

Supervisors:

Dr. B. R. Horrocks and Prof. Andrew Houlton

July 2018

ABSTRACT

Fluorescent metal nanoclusters (**Ag₂**, **Ag₃**, **Ag₄**, and **Cu₇**) were synthesized by reacting aqueous silver nitrate (AgNO₃) or copper nitrate (Cu(NO₃)₂) solution with equivalent portions of aqueous sodium borohydride (NaBH₄) solution in emulsion system at room temperature. Sodium bis-(2-ethyl hexyl) sulfosuccinate (AOT) was used to stabilize the microemulsion and 2, 2, 4-trimethyl pentane (isooctane) was the bulk (oil) phase. By confining the metal ions and reducing agents to the droplets of microemulsions, the number of atoms available to form metal clusters after reduction is controlled. This thesis is concerned with the synthesis of small, fluorescent metal clusters. Ordinarily, reduction of solutions metal salts in the presence of capping ligands leads to the formation of nanoparticles of diameter in the range of 10 – 100 nm. Such particles are already metallic, have no bandgap, and do not fluoresce, but exhibit plasmon resonances.

Dynamic light scattering (DLS) measurements of all emulsions indicated a predominant droplet diameter of 100 nm and a smaller diameter peak in the distribution corresponding to reverse micelles at 5 nm. Rayleigh scattering measurements were fitted to theory with the droplet diameter (50 nm) as the sole free parameter. Two reaction concentrations consisting of 90 μ M and 1 mM, with an average of 4 and 40 metal ions per droplet were investigated in detail. As well as chemical reduction, photochemical reduction of Ag (I) emulsions by UV light ($\lambda = 254$ nm) was also studied.

UV-Vis absorption spectra did not show plasmon resonance peaks in any of the microemulsion samples. In addition, all emulsion-synthesized NCs were fluorescent with an average emission intensity counts per second (cps) in the order of 3.0×10^5 cps. Generally, two emission bands were obtained at approximately $\lambda = 300$ nm and $\lambda = 430$ nm corresponding to optical gaps of 4.13 and 2.88 eV for Ag NCs. A third band at $\lambda = 610$ nm may be related to aggregation was also observed. Two emission bands were also observed for the Cu NCs at $\lambda = 350$ nm and $\lambda = 401$ nm corresponding to gaps of 3.54 and 3.09 eV. Confocal microscope images confirmed the luminescence of these MNCs, and together with the transmission electron microscopy (TEM), as well as, atomic force microscopy (AFM) demonstrated that small, roughly spherical NCs were synthesized. TEM and AFM results were in agreement for the NaBH₄ and photoreduced Ag NCs with estimated diameters of 1.4 – 2.4 nm. The estimated diameter of the Cu NCs was ~1.0 – 2.4 nm. Electrospray ionisation mass spectrometry (ESI-MS) results provided more the

molecular formulae of: $[\text{Ag}_2(\text{H}_2\text{O})\text{H}]^-$; $[\text{Ag}_4\text{B}_3\text{O}_5\text{BH}_3 \cdot 2\text{H}_2\text{O}]^-$; $[\text{Ag}_3(\text{H}_2\text{O})_n(\text{OH})]^-$ and $[\text{Ag}_4(\text{H}_2\text{O})_6(\text{OH})]^-$ (photoreduced samples), and $[\text{Cu}_7\text{B}_3\text{O}_5 \cdot \text{BH}_3 \cdot 2\text{H}_2\text{O}]^-$.

Alternatively, fluorescent metal NCs were prepared by reducing metal ions bound to polyvalent single-stranded deoxyribonucleic acids (ssDNAs) ligands. The concept requires that the ligand binds both the metal ions and elemental metal atoms. Three single-stranded DNAs of length 22, 29, and 34-bases which had been previously reported to facilitate the synthesis fluorescent Ag NC were chosen for investigation: (1) **5'-TGACTAAAAACCCTTAATCCCC-3'** (2) **5'-AGTCACCCCAACCTGCCCTACCACGGACT-3'** (3) **5'-GCAGGTTGGGGTGACTAAAAACCCTTAATCCCC-3'**.

Reduction of ssDNA-bound of Ag (I) ions disfavours aggregation in bulk solution and favours instead, the formation of small, fluorescent clusters. Two prominent emission bands were obtained with ssDNA1 in microemulsion, however one broad, but weak emission at 350 nm, in associated with a complex band comprising of four peaks with a maximum at 401 nm were observed for both the ssDNA2 and 3. However, emission spectra of the three ssDNA-Ag samples in 99 % deuterium oxide (D_2O) solution was different from those of the emulsion samples, with a common band at 388 nm, followed by a very broad one at 590 and 630 nm for the DNA2 and 3 respectively. Apart from the 388 nm emission, which was generally ascribed to the ssDNA molecules, no other band was seen in the spectrum of the ssDNA1-Ag sample in D_2O .

The results of this study demonstrate that stable NCs of specific cluster sizes could be made by adapting the reaction conditions to confine the metal ions to small reaction volumes in microemulsions or on single-stranded DNA molecules.

DEDICATION

To the Holy Spirit.

ACKNOWLEDGEMENT

I am immensely grateful to my beloved wife: Dr. Mrs I. M. Oyem, and our three sons for their sacrifice these years of my studying away from home.

I have been blessed with two supervisors: Dr. B. R. Horrocks and Professor A. Houlton, under whose professional guidance I have steadily grown this past four years; I owe a world of gratitude to you and will always remember you very dearly.

Special thanks to the then Head of School of Chemistry, Emeritus Professor Mike Green, and the then Secretary, Miss Isobel Lamb. Sincere thanks are due to my incumbent Head of School, Professor Andrew Benniston; Ms Jane McCartney, Claire Nicoll, Joanne Lackey, Kate Kirkpatrick, Kate Gorman, and Abby Danecki, all (except for Kate Kirkpatrick and Abby Danecki) former staff at the School Office.

I am grateful to my colleagues at Chemical Nanoscience Laboratory, Mansur Ibrahim Yahaya, Andres Aldana, Micheal Bracchi, Lamia, Al-Mohamad (PhD), Shams Ali, Atsinafe Barnabas Oshido, Steve Nomor (PhD), Patrick Higgs, Liam Mistry, Luke Saunders, Milene Dalmina, Colette Whitfield (PhD), Samantha Lunn, Rachel Little, and to Tom Bamford, Glenn Lamming, and especially to Thompson Izuagie (PhD), not forgetting Daniel Lebbie, Kate Phipps, Thaer Al-Rammahi (PhD) and Einas Abood.

I am particularly grateful to Dr. Osama for his assistance with the AFM instrument and data analysis. Thanks are due to Dr. Eimer Tuite for the initial training on the UV-Vis and fluorescence instruments. I am also grateful to Dr. Corinne Wills and Emeritus Professor Williams MacFardene for assisting with the NMR analyses. I am grateful to Mr Dave Dunbar for training me on the Walters ESI-MS and the FTIR instruments. Similarly, I acknowledge Dr Kathryn Whyte, Tracey Davey, and Ross Laws, all of the Medical School for their assistance with the TEM measurements. Finally, I also acknowledge, the team at NEXUS for the XPS analyses of my samples. Many thanks to Helen Mann, Drs Rachel Dack, and Jerry Hagon. I also thank Gary Day for his assistance.

I want to very warmly appreciate my friends at the Cathedral: Michael, John and Veronica, Marie, Angela, Andrew and Jerry; thanks for being my UK family and for supporting me all these years. And to Mr and Dr. Mrs Essiet

Thanks are due to Dr. Rajesh Sardar and his research group, especially Meghan Teunis Mcleod (PhD), Takshila Liyanage, Yang Yang, and Ashur, Sydney Schafer, Anthony, Manpreet Kaur, in the Department of Chemistry, Indiana University, Purdue University Indianapolis, U.S.A. Not forgetting the Dean of Science, Professor S. J. Rhodes, and also Dr. Mrs S. Sardar. As well as the Parish Priest of St John the Evangelist Catholic Church, Rev, Fr. Rick Nagel, Indianapolis, Indiana, U.S.A.

Many thanks to Jamila Oppong, Nuha Halawani, Hadiza Aminu Isah, Hind Alshaikh, and Abdullah all of the Johnston Laboratory, Bedson Building.

I am very grateful to His Royal Highness, the Obi of Owa, Dr. Emmanuel Efeizomor II for his assistance and advice during my preparation to travel out to the United Kingdom for my PhD.

I will never forget the enormous contribution I received especially from Dr. and Dr. Mrs F. O. Onwuka and their very good family friend, Mr J. Oriarewo. Likewise too, gratitude goes to Dr. (Barr.) Julius Ehikwe, Mr Davidson Dibie, and Dr. Mrs F. Omumu for your wonderful assistance. Worthy of mention also is Mr Edwin Udeh and family, as well as Sir Ken Ochei. Appreciations are due to Mrs T. Udemba and Ogor Njideka for your wonderful support and for looking after my family. Special mention to a dear friend, Mr Justin Okwuofu and wife, as well as Mrs T. Ugbechie. Thanks are due to Mr & Mrs Chukudi Ikukaiwe, and Mr Eric Ikaria and children. Special thanks to Alex and Osato of EduAbroad; and Pastor & Mrs Jacott Asabor.

To Rev. Sr Stella Maris Onwuka, and Mrs Funmilola Justina Ayodeji for always checking on me and encouraging me on. Not forgetting Mrs Christiana N. Ogwudiegwu for her kindness and prayers. And to Dr. Amii Isaac Usese of the University of Lagos, Nigeria.

Special thanks to Professors C. M. A. Ademoroti (Emeritus), M. A. Osuide, and C. E. Ochonogor, formerly of the University of Benin, Benin City; Ambrose Alli University, Ekpoma, both in Edo State Nigeria, and the University of South Africa (UNISA), respectively.

To my siblings: Mrs Tonia Jibunor, Engr. Andrew Oyem, Mike Oyem, Mrs Elizabeth Emefiene, Patrick Oyem, and Augustine Oyem. To my dear parents: Chief and Mrs Paul Oyem, and my mother-in-law, Lady (Mrs) C. D. Egwu, and to my uncle Mr Sunday Obah for your invaluable prayers, encouragement and support.

Gratitude is due to the Management and Governing Council of the College of Education, Agbor, Delta State, Nigeria, especially the Provost, Dr. J. O. Ukadike. I am also grateful to the former Provost, Dr. D. O. Okobia, and the then Registrar, Barrister Oscar Osagiede, for approving my study leave. Appreciations also to former Provosts Dr. Mrs J. E. Konyeme and Dr. E. U. Tibi and wife, Dr. Mrs P. Tibi.

Many thanks to the Government of Delta State, Nigeria for paying my salary while on study leave.

Immense gratitude to the Tertiary Education Trust Fund (TETFund) of the Federal Government of Nigeria through the Ministry of Education for the sponsorship.

Many thanks to the Erasmus mobility scheme for the scholarship to the Indiana University-Purdue University Indianapolis (IUPUI), Indiana, U.S.A.

Finally, I am grateful to the government of the United Kingdom and the City of Newcastle upon Tyne, for making this possible and for being my home in the last four years, and particularly to Newcastle University for this important milestone.

Table of Contents

Abstract.....i
Dedication.....v
Acknowledgement.....vi
Table of Contents.....ix
List of Figures.....xvii
List of Table.....xxvi

1 CHAPTER ONE 1
1.1 Aim of this Work 1
1.2 Nanoparticles4
1.2.1 Classification4
1.3 Quantum-size effect.....6
1.4 Wave Function.....7
1.4.1 Bandgaps9
1.5 Fermi Level.....9
1.6 Fluorescence 10
1.7 Electromagnetic radiation and spectrum..... 12
1.7.1 Electromagnetic Spectrum..... 13
1.8 Emulsion 15
1.9 Role of Emulsifiers 17
1.10 Microemulsion 18
1.10.1 Thermodynamic stability..... 19
1.11 Micelles..... 20
1.12 Deoxyribonucleic acids, DNA 22
1.12.1 Structure and nomenclature of DNA 22
1.12.2 Forms of DNA 27
1.12.3 Denaturation and renaturation 28
1.13 Reference 29
2 CHAPTER TWO.....39
2.1 EXPERIMENTAL..... 39
2.2 Introduction.....39

2.3	Materials.....	39
2.4	Instrumentations	40
2.4.1	Ultraviolet-Visible Spectrophotometer (UV-Vis spectrophotometer):.....	40
2.4.2	Fluorescence Spectrophotometer:	40
2.4.3	Confocal microscopy:	41
2.4.4	Dynamic Light Scattering (DLS):.....	41
2.4.5	Atomic Force Microscopy (AFM):	41
2.4.6	Transmission Electron Microscopy (TEM):	41
2.4.7	Electrospray Ionisation Mass Spectrometry (ESI-MS):.....	41
2.4.8	X-ray Photoelectron Spectroscopy (XPS):	42
2.4.9	Infrared Spectroscopy:	42
2.4.10	Nuclear magnetic resonance (NMR):	42
2.4.11	Rayonet Photochemical Reactors:	42
2.4.12	EmStat ³ Electrochemical Interface:	43
2.4.13	Electrophoresis:.....	43
2.5	Synthesis of silver (I) complex with ssDNA1 (22-mer) and reduction with sodium borohydride.	43
2.5.1	Absorbance and fluorescence determinations.....	43
2.6	Synthesis of silver (I) complex with ssDNA2 (29-mer) and reduction with sodium borohydride.	43
2.6.1	Absorbance and fluorescence measurements.....	44
2.7	Synthesis of silver (I) complex with ssDNA3 (34-mer) and reduction with sodium borohydride.	44
2.7.1	Absorbance and fluorescence measurements.....	44
2.8	Synthesis of silver nanoclusters in microemulsion	44
2.8.1	Absorbance and fluorescence determinations for 90 μ M and 1 mM silver nanoclusters in microemulsion	45
2.8.2	Dynamic light scattering (DLS) measurement of 90 μ M and 1 mM silver nanoclusters in microemulsion	45
2.8.3	Fourier Transform Infra-red (FTIR) analysis of 90 μ M and 1 mM Ag NCs in microemulsion	45
2.8.4	Atomic force microscope imaging of 90 μ M and 1 mM silver nanoclusters in microemulsion	45
2.8.5	Fluorescence microscope imaging of 90 μ M and 1 mM Ag NCs samples.....	45

2.8.6	Transmission Electrons Microscopy (TEM) of 90 μM and 1 mM Ag NCs samples	46
2.8.7	Separation of aqueous from the organic phase liquid in the emulsion system using a restek chromatography cartridge	46
2.8.8	Electrospray ionization mass spectrometry (ESI-MS) analysis of 90 μM and 1 mM Ag NCs samples	46
2.8.9	X-ray photoelectron microscopy (XPS) of 90 μM and 1 mM samples	47
2.8.10	Boron NMR analysis of 1 mM Ag NCs prepared by microemulsion	47
2.9	Syntheses of aqueous solutions of silver nanoparticles (no microemulsion)	47
2.9.1	Absorbance and fluorescence of 90 μM and 1 mM aqueous solutions (control) (No microemulsion)	47
2.9.2	Dynamic light scattering (DLS) measurement of 90 μM and 1 mM aqueous solutions (control) samples	48
2.9.3	Infra-red analyses of 90 μM and 1 mM aqueous solutions (control) samples	48
2.10	90 and 900 μL water in oil microemulsions (in 5 and 18 mL oil, no analytes) – (control samples)	48
2.10.1	Absorbance and fluorescence of 90 and 900 μL water in oil microemulsions (control) samples	48
2.11	Syntheses of 90, 150, 250, 500, 750, and 1000 μM Ag NCs in 5 mL microemulsion (at fixed ω values)	48
2.11.1	Absorbance and fluorescence determinations for 90, 150, 250, 500, 750, and 1000 μM Ag NCs in 5 mL microemulsion	49
2.11.2	Dynamic light scattering (DLS) measurement of 90, 150, 250, 500, 750, and 1000 μM Ag NCs in 5 mL microemulsion	49
2.11.3	Fourier Transform Infra-red analyses of 90, 150, 250, 500, 750, and 1000 μM Ag NCs in 5 mL microemulsion	49
2.12	Syntheses of 90, 150, 250, 500, 750, and 1000 μM Ag NCs in microemulsion (at varied ω values)	49
2.12.1	Absorbance and fluorescence determinations.	50
2.12.2	Dynamic light scattering (DLS) measurement.	50
2.13	Photochemical syntheses of 90 μM and 1 mM Ag NCs by reduction of Ag^+ ions in microemulsion	50
2.13.1	Absorbance and fluorescence measurements of 90 μM and 1 mM Ag NCs samples	50

2.13.2	Dynamic light scattering measurements of $90\ \mu\text{M}$ and $1\ \text{mM}$ Ag NCs samples	51
2.13.3	Electrospray ionisation mass spectrometry (ESI-MS) $90\ \mu\text{M}$ and $1\ \text{mM}$ Ag NCs samples	51
2.13.4	Transmission electron microscopy (TEM) of the photoreduced samples.....	51
2.13.5	Photoluminescence imaging of photoreducedmicroemulsion samples	51
2.14	Synthesis of aqueous solutions of $90\ \mu\text{M}$ and $1\ \text{mM}$ Ag NPs (without microemulsion) by photochemical reduction	51
2.14.1	Absorbance and fluorescence measurements of aqueous (control) photoreduced samples	51
2.14.2	DLS measurement of particles sizes	52
2.14.3	Electrochemical Cyclic voltammetry (CV) measurement	52
2.15	Kinetic study of the rate of formation of Ag NCs in microemulsion.....	52
2.16	Electrospray mass spectrometry analysis of Ag^+ ions in microemulsion without photoreduction (control).....	52
2.17	Syntheses of $90\ \mu\text{M}$ and $1\ \text{mM}$ Ag NCs on ssDNA1 (1:4) in microemulsion	53
2.17.1	UV-Vis and fluorescence measurements	53
2.17.2	Dynamic light scattering measurements	53
2.17.3	Fluorescence microscope imaging	53
2.17.4	Transmission electron microscope imaging.....	54
2.17.5	Electrospray ionization mass spectrometry measurement	54
2.18	Syntheses of $90\ \mu\text{M}$ and $1\ \text{mM}$ Ag NPs on ssDNA1 (1:4) in aqueous solution (control).....	54
2.18.1	UV-Vis and fluorescence measurements	54
2.18.2	Dynamic light scattering measurements	54
2.18.3	Fluorescence microscope imaging	55
2.18.4	Transmission electron microscope imaging.....	55
2.18.5	Electrospray ionization mass spectrometry measurement	55
2.19	Syntheses of $90\ \mu\text{M}$ and $1\ \text{mM}$ Ag NCs on ssDNA2 (1:5) in microemulsion	55
2.19.1	UV-Vis and fluorescence measurements	55
2.19.2	Dynamic light scattering measurements	56
2.19.3	Fluorescence microscope imaging	56
2.19.4	Transmission electron microscope imaging.....	56
2.19.5	Electrospray ionization mass spectrometry measurement	56
2.20	Syntheses of $90\ \mu\text{M}$ and Ag NPs on ssDNA2 in aqueous solution (control).....	56

2.20.1	UV-Vis and fluorescence measurements.....	56
2.20.2	Dynamic light scattering measurements.....	57
2.20.3	Fluorescence microscope imaging	57
2.20.4	Transmission electron microscope imaging	57
2.20.5	Electrospray ionisation mass spectrometry measurement.....	57
2.21	Syntheses of 90 μ M and 1 mM Ag NCs on ssDNA3 (1:6) in microemulsion.....	57
2.21.1	UV-Vis and fluorescence measurements.....	57
2.22	Syntheses of aqueous Ag NPs on ssDNA3 (control) sample solutions.....	58
2.23	Gel electrophoresis experiment of the microemulsion synthesized Ag NCs on ssDNAs	59
2.24	Synthesis of ssDNA1 in deuterated water for ^1H , ^{13}C , ^{31}P NMR, COSY, HSQC, and HMBC analyses	59
2.25	Synthesis of Ag^+ /ssDNA2 in deuterated water for ^1H , ^{31}P , and ^{13}C NMR analyses .	60
2.26	Synthesis of Ag NCs/ssDNA3 by reduction with NaBH_4 in deuterated water for ^1H , ^{31}P , and ^{13}C NMR analyses.....	61
2.27	Syntheses of Ag NPs on adenosine, cytidine, guanosine, and thymidine 5'-monophosphate disodium salts in D_2O	61
2.28	Syntheses of Cu NCs in microemulsion	62
2.28.1	UV-Vis and fluorescence measurements.....	62
2.28.2	Dynamic light scattering measurements.....	63
2.28.3	Fluorescence microscope imaging	63
2.28.4	Transmission electron microscope imaging	63
2.28.5	Fourier transform infrared (FTIR) measurement.....	63
2.28.6	Electrospray ionization mass spectroscopy measurement.....	63
2.29	Syntheses of 90 μ M and 1 mM aqueous solutions of Cu NPs (control)	63
2.29.1	Absorbance and fluorescence measurements of the 90 μ M and 1 mM Cu NPs control samples.....	63
2.29.2	Dynamic light scattering (DLS) measurement of 90 μ M and 1 mM Cu NPs aqueous solutions (control) samples	64
2.29.3	Infra-red analyses of 90 μ M and 1 mM Cu NPs aqueous solutions (control) samples	64
2.30	Principles of instrumental methods of analyses.....	64
2.30.1	Fluorescence spectroscopy	64
2.30.2	Dynamic light scattering.....	65

2.30.3	Electrospray ionisation mass spectrometry.....	68
2.31	Reference.....	70
3	CHAPTER THREE.....	71
3.1	RESULTS AND DISCUSSION I.....	71
3.2	Synthesis and Characterization of silver nanoclusters (Ag NCs) in Microemulsion	71
3.3	Introduction.....	71
3.4	Aims.....	72
3.5	Microemulsion reaction scheme for Ag NCs.....	72
3.6	Ultraviolet-visible spectroscopy.....	73
3.7	Fluorescence.....	76
3.8	Dynamic light scattering studies.....	81
3.9	Fluorescence microscopy.....	84
3.10	Transmission electron microscopy (TEM).....	85
3.11	Atomic force microscopy (AFM).....	86
3.12	Electrospray ionization mass spectrometry.....	87
3.13	Calibration curve for concentration vs number of silver atoms.....	88
3.14	¹¹ Boron NMR.....	92
3.15	X-ray photoelectron spectroscopy (XPS).....	93
3.16	Conclusion.....	94
3.17	Reference.....	95
4	CHAPTER FOUR.....	103
4.1	RESULTS AND DISCUSSION II.....	103
4.2	Synthesis and Characterization of Silver Nanoclusters in Microemulsion by Photochemical Reduction.....	103
4.3	Introduction.....	103
4.4	Aims.....	104
4.5	Reaction scheme.....	104
4.6	Fluorescence.....	107
4.7	Fluorescence kinetic study.....	111
4.8	Dynamic light scattering (DLS).....	114
4.9	Transmission electron microscopy.....	118
4.10	Cyclic Voltammetry.....	119
4.11	Electrospray ionization mass spectrometry.....	120
4.12	Conclusion.....	122

4.13	Reference	123
5	CHAPTER FIVE.....	125
5.1	RESULTS AND DISCUSSION III.....	125
5.2	Synthesis and Characterisation of Cu ₇ NCs in Microemulsion	125
5.3	Introduction.....	125
5.4	Aims.....	126
5.5	Method	126
5.6	Absorbance	128
5.7	Fluorescence	129
5.8	Dynamic light scattering	131
5.9	Transmission electron microscopy (TEM)	133
5.10	Atomic force microscopy (AFM)	134
5.11	Electrospray ionisation mass spectroscopy.....	136
5.12	X-ray photoelectron spectroscopy	137
5.13	Fourier transform infrared spectroscopy.....	139
5.14	Conclusion	140
5.15	Reference	141
6	CHAPTER SIX	145
6.1	RESULTS AND DISCUSSION IV	145
6.2	Syntheses and Characterisation of Ag NCs Templated on ssDNA in Microemulsion 145	
6.3	Introduction.....	145
6.4	Aims.....	147
6.5	Reaction Scheme.....	147
6.6	Absorbance	148
6.7	Fluorescence	151
6.8	Dynamic light scattering	163
6.9	Transmission electron microscopy	166
6.10	Electrophoresis.....	170
6.11	Electrospray ionization mass spectroscopy	171
6.12	Nuclear magnetic resonance spectroscopy	177
6.12.1	¹ H NMR study of Ag-DNA1	180
6.12.2	¹ H NMR of Ag: DNA2.....	184
6.12.3	¹ H NMR of Ag: DNA3.....	187

6.13	³¹ P NMR study of DNA1, 2, and 3 in D ₂ O solution	190
6.14	¹ H NMR of DNA Mononucleotides	192
6.14.1	Adenosine ¹ H NMR	193
6.14.2	Cytidine ¹ H NMR.....	194
6.14.3	Guanosine ¹ H NMR	195
6.14.4	Thymidine ¹ H NMR.....	196
6.15	³¹ P NMR of DNA Mononucleotides	197
6.16	Fluorescence analyses of the ssDNA1, 2, and 3 D ₂ O samples.....	200
6.17	Conclusion.....	204
6.18	Reference.....	206
7	CHAPTER SEVEN	211
7.1	CONCLUSIONS	211
7.2	Introduction	211
7.3	General conclusion on findings	211
7.3.1	Borohydride synthesized Ag NCs.....	211
7.3.2	Photosynthesised Ag NCs	213
7.3.3	Borohydride-synthesized Cu NCs.....	214
7.3.4	Borohydride-synthesized DNA templated Ag NCs	215
7.3.5	Nuclear magnetic resonance spectroscopy	217
7.4	Reference.....	219
8	APPENDIX.....	220

List of Figures

Figure 1.1: Size-dependent physical properties changes in materials.	2
Figure 1.2: Energy level diagram of metals, semiconductors, and insulators.	5
Figure 1.3: Surface plasmon resonance of nanoparticles in response to excitation energy.	5
Figure 1.4: Size-dependent energy level diagram of metals, semiconductors, and insulators. ...	6
Figure 1.5: Quantum size-dependent classification of materials according to the zone of confinement.	7
Figure 1.6: Energy level diagram showing bandgap.	9
Figure 1.7: Fermi level diagram of metals (conductors), semiconductor, and insulators (broken line representing the Fermi Level).	10
Figure 1.8: Jablonsky diagram showing the fluorescence phenomenon. The blue arrow represents absorption, yellow is the dark-phase internal conversion phase, the red arrow is fluorescence, black (horizontal) arrow represent intersystem crossing and pink arrow is phosphorescence.	11
Figure 1.9: Combined schematic representation of both the fluorescence excitation (blue) and emission (red) spectra.	12
Figure 1.10: Electromagnetic spectrum. Source: Cyberphysics. ⁶⁹	14
Figure 1.11: Component parts and order packing of the emulsion systems comprising the emulsifier (surfactant).	15
Figure 1.12: Water-in-oil emulsion system showing dispersed water droplets in the oil phase.	16
Figure 1.13: (a) Micelle in water continuous phase (b) reversed micelle in oil continuous phase.	17
Figure 1.14: Component parts of an emulsifier. Source: Gcsescience. ¹²⁶	17
Figure 1.15: Processes of micelle formation, Source: Hunter, 1993. ¹⁰⁵	20
Figure 1.16: Schematic diagram of a micelle. Source: European Chemistry Thematic Network. ¹²⁷	21
Figure 1.17: Reverse micelle.	21
Figure 1.18: Non-nucleobase components of DNA (a) phosphate ion (b) sugar. The red hydrogen atom of DNA replacing the OH (hydroxyl group) of ribonucleic acids (RNA), emphasizing its difference from RNA.	23
Figure 1.19: DNA nucleobases (a) cytosine (b) thymine (c) adenine (d) guanine. The atoms in red colour represent the bonding site between the nucleobases and the ribose sugar group.	23

Figure 1.20: (a) pyrimidine (b) purine component ring structure of DNA bases.	24
Figure 1.21: Binding sites (blue asterisk) of the four DNA nucleobases showing points of metal ion (electrophilic) attack. ^{111,128,129,120,130,131,132,133,134,133,135,136,137,138,139,140}	24
Figure 1.22: DNA mononucleotides (a) adenosine (b) cytidine (c) DNA dinucleotide (two mononucleotides combined via the phosphodiester bond).	25
Figure 1.23: DNA polymeric duplex structure showing all detailed component units and bonds.	26
Figure 1.24: (a) Z-form (b) B-form (c) A-form of DNA bases. Source: Berg <i>et al.</i> , 2002. ¹⁰⁴ . 27	27
Figure 1.25: (a) DNA melting into component strands. (b) DNA temperature melting curve (T_m is the melting temperature, with approximately 50 % denaturation).	28
Figure 2.1: Schematic diagram of fluorescence spectrometer.	64
Figure 2.2: Dynamic light scattering instrument's operational schematics.	66
Figure 2.3: Chart of correlation factor (CF) versus time delay.	67
Figure 2.4: Diagram of electrospray ionisation mass spectrometer showing mode of operation.	68
Figure 3.1: Reaction scheme for Ag NCs synthesis by mixing microemulsions (A) $AgNO_3$ and (B) $NaBH_4$ (C) Ag NCs all in microemulsion.	73
Figure 3.2: Plasmon resonance peak of $90 \mu M$ and $1 mM$ Ag NCs in (a) microemulsion (b) aqueous solution.	74
Figure 3.3: UV-visible spectra for (a) $1 mM$ Ag NCs in microemulsion, observed for 96 hours period (b) $90, 150, 250, 500, 750, 1000 \mu M$ Ag NCs in microemulsion.	75
Figure 3.4: Fluorescence spectra for (a) $90 \mu M$ (b) $1 mM$ Ag NCs in microemulsion (c) emulsion only.	76
Figure 3.5: Emission spectra of increasing concentrations of silver nanoclusters (a) at 430 nm; red arrow indicates dropping intensity with increasing concentration of Ag (b) 608 nm.	78
Figure 3.6: (a) Excitation and emission (blue/orange) spectra of silver nanoclusters at 430 nm, with Stokes shift value of 111.5 nm. (b) Schematic representation of data in the form of a Jablonsky diagram.	79
Figure 3.7: Bandgap energy diagram of the Ag NCs samples, adapted from Dolai <i>et al.</i> , 2013. ⁴⁹	80
Figure 3.8: Graph of the relationship between fluorescence intensity at $\lambda_{exc.430 nm}$ vs (a) Ag concentration and (b) ω ($[H_2O]/[AOT]$).	80
Figure 3.9: DLS charts of the intensity of light scattering of water droplets in microemulsion 90 and $1000 \mu M$ Ag NCs samples.	81

Figure 3.10: DLS charts of the intensity of light scattering of water droplets in microemulsion at varying concentrations (90-1000 μM) Ag NCs.	82
Figure 3.11: DLS peak intensity vs ω (AOT concentration).....	83
Figure 3.12: Fluorescence images of emulsion samples of Ag NCs deposited on clean silicon wafers (a), (b), are 90 μM . (c) & (d) are 1 mM samples.....	84
Figure 3.13: TEM images of (a) 90 μM and (b) 1 mM Ag NPs on holey-carbon grid; and particles size distribution histograms (below).	85
Figure 3.14: AFM images (a) 90 μM (b) 1 mM Ag NPs drop-casted on clean silicon wafers. Inset: Probability chart of particles sizes.	86
Figure 3.15: ESI-MS spectrum of both 90 μM and 1 mM Ag NCs corresponding to $[\text{Ag}_4\text{B}_3\text{O}_5\cdot\text{BH}_3\cdot 2\text{H}_2\text{O}]^-$ i.e. $[\text{Ag}_4\text{B}_4\text{O}_7\text{H}_7]^-$	87
Figure 3.16: Calibration curve of number of atoms of silver per cluster (using the 50 nm droplets size obtained from Rayleigh curve fitting) against increasing $[\text{Ag}^+]$ concentration. .	88
Figure 3.17: Fourier transform infrared spectra of (a) 90 μM (b) 1 mM dried samples of Ag NCs on clean silicon wafer. The red asterisks represent some peaks assigned to the surfactant.	90
Figure 3.18: ^{11}B NMR spectrum of $[\text{Ag}_4\text{B}_3\text{O}_5\cdot\text{BH}_3\cdot 2\text{H}_2\text{O}]^-$ aqueous solution at 298 K, with boron trifluoride diethyl etherate, $\text{BF}_3\cdot\text{O}(\text{C}_2\text{H}_5)_2$ as a reference.....	92
Figure 3.19: XPS charts of $[\text{Ag}_4\text{B}_3\text{O}_5\cdot\text{BH}_3\cdot 2\text{H}_2\text{O}]^-$ (a) Boron. See (inset) survey spectrum in Appendix section) (b) Oxygen.	93
Figure 4.1: Photoreduction reaction scheme; (A) is AgNO_3 in microemulsion, (B) is Ag NCs formed in microemulsion at room temperature in a photochemical reactor.....	105
Figure 4.2: Absorbance of photoreduced(a) 90 μM and 1 mM Ag NCs in microemulsion, (b) 90 μM and 1 mM Ag NPs in aqueous solution (control).....	106
Figure 4.3: Emission intensity of (a) 90 μM Ag NCs at 340 nm excitation (Highest peak intensity at 439 nm). (b) Emission intensity for 1 mM Ag NCs at 340 nm excitation by photoreduction of Ag^+ for five hours (highest peak intensity at 453 nm).....	108
Figure 4.4: Emission intensity at 301 nm excitation of photoreducedaqueous solutions (control samples) of Ag NPs (a) 90 μM (peak max at 468 nm) (b) 1 mM Ag NPs (peak max at 470 nm).....	108
Figure 4.5: A plot of emission intensity against time for Ag NCs in microemulsion at peak max of 453 nm (a) 90 μM (b) 1 mM samples.	109
Figure 4.6: A plot of emission intensity against time for Ag NCs in aqueous solution (a) 90 μM (peak max of 468 nm) (b) 1 mM (peak max of 470 nm).....	110

Figure 4.7: Emission intensity at 340 nm excitation for (a) 90 μM AgK. (b) 1 mM AgK of photoreduced microemulsion sample. 440 nm at 423 nm respectively. The label AgK denotes “silver kinetic study”, and the numbers 1, 2,...10 are the number of scans at $\lambda_{\text{exc}}=340$ nm.	112
Figure 4.8: Emission at highest peak intensity (a) at 440 nm for 90 μM (b) at 423 nm for 1 mM Ag NCs.	112
Figure 4.9: Schematic representation of figure 4.9 a&b.	113
Figure 4.10: DLS chart of 90 μM and 1 mM Ag NCs photoreduced in microemulsion with Ag NCs dispersed and water the dispersant phase.	114
Figure 4.11: 90 μM and 1 mM Ag NPs photoreduced from AgNO_3 aqueous solution obtained 24 hours after synthesis.	115
Figure 4.12: (a) Chart of size (diameter) nm with varying Ag NCs (90 - 1000 μM) concentrations at fixed ω . (b) The intensity of scattered at increasing ω	116
Figure 4.13: Droplet diameter of (>100 nm) vs varying ω	116
Figure 4.14: TEM images of photosynthesized Ag NCs in microemulsion (a) 90 μM and (b) 1 mM Ag NCs; particles size analysis histogram is placed below each sample.	118
Figure 4.15: Cyclic voltammograms of (a) 90 μM and (b) 1 mM Ag NCs in microemulsion with 100 mM NaNO_3 with Ag/AgCl reference electrode and scan rate of 0.05 V/s at room temperature.	119
Figure 4.16: Electrospray ionization mass spectrometry spectrum of photosynthesized 90 μM and 1 mM Ag NCs samples.	120
Figure 4.17: ESI-MS spectra of (a) $\text{Ag}_3(\text{H}_2\text{O})\cdot\text{H}_7^-$ (b) $\text{Ag}_4(\text{H}_2\text{O})\text{OH}^-$ (c) $\text{Ag}_3(\text{H}_2\text{O})_9\cdot\text{H}_{11}^-$ and (d) $\text{Ag}_3(\text{H}_2\text{O})_{10}\cdot\text{H}_9^-$. (e) $\text{Ag}_4(\text{H}_2\text{O})\cdot\text{H}_9^-$ (not included).	121
Figure 5.1: Reaction scheme for the synthesis of Cu NCs in microemulsion at ambient temperature (A) copper nitrate (B) sodium borohydride (C) Copper nanoclusters.	127
Figure 5.2: Absorbance spectra of 90 μM and 1 mM Cu NCs (a) in microemulsion (b) aqueous solution. Red arrows indicate the ligand-to-metal charge transfer transition for $[\text{Cu}(\text{H}_2\text{O})_6]^{2+}$ cations.	128
Figure 5.3: Fluorescence emission spectra of (a) 90 μM Cu NCs in microemulsion (b) 1 mM Cu NCs in microemulsion. (Encircled are peaks indicating aggregated particles) (c) 90 μM Cu NCs in aqueous solution, and (d) 1 mM Cu NPs in aqueous solution. Excitation wavelengths are shown in the legends.	129
Figure 5.4: DLS charts of 90 μM and 1 mM Cu NCs in microemulsion	131
Figure 5.5: DLS chart of 90 μM and 1 mM Cu NPs (control) samples in aqueous solution.	132

Figure 5.6: TEM images of (a) $90\ \mu\text{M}$ and (b) $1\ \text{mM}$ Cu samples in microemulsion obtained by drop casting the samples on holey carbon copper grids and drying overnight before TEM imaging.	133
Figure 5.7: AFM images of (a) $90\ \mu\text{M}$ and (b) $1\ \text{mM}$ Cu NPs in microemulsion.(c) 3D image of $90\ \mu\text{M}$ Cu NPs (d) Probability factor chart of particle diameter ($90\ \mu\text{M}$ Cu NPs); (e) 3D image of $1\ \text{mM}$ Cu NPs (f) Probability factor chart of particle diameter ($1\ \text{mM}$ Cu NPs).....	135
Figure 5.8: ESI-MS spectrum of dilute oil-separated $90\ \mu\text{M}$ and $1\ \text{mM}$ Cu NCs in microemulsion solutions; inset is the peak at 575 (experimental and simulated). The red asterisk are peaks ascribed to species of Cu_7 clusters.....	136
Figure 5.9: XPS chart of (a) Boron 1s and (b) oxygen 1s of Cu NPs samples on silicon wafer.	137
Figure 5.10: Fourier transform infrared spectra (a) $90\ \mu\text{M}$ & $1\ \text{mM}$ Cu NPs cartridge oil separated samples (b) $90\ \mu\text{M}$ & $1\ \text{mM}$ Cu NPs in emulsion (c) AOT- containing emulsion only (d) NaBH_4 , all dried samples on silicon chips.....	139
Figure 6.1: Reaction scheme for the reduction of Ag^+ -ssDNA with sodium borohydride in microemulsion droplet.	147
Figure 6.2: Absorbance spectra of DNA1 templated $90\ \mu\text{M}$ and $1\ \text{mM}$ Ag in (a) microemulsion (b) aqueous solution.....	149
Figure 6.3: Absorbance spectra of DNA2 templated $90\ \mu\text{M}$ and $1\ \text{mM}$ Ag^0 in (a) microemulsion (b) aqueous solution.....	149
Figure 6.4: Absorbance spectra of DNA3 templated $90\ \mu\text{M}$ and $1\ \text{mM}$ Ag^0 in microemulsion (a) microemulsion (b) aqueous solution.	150
Figure 6.5: Emission spectra of aqueous solutions of DNA1.	151
Figure 6.6: Emission spectra of aqueous solutions of DNA2.	152
Figure 6.7: Emission spectra of aqueous solutions of DNA3.	152
Figure 6.8: fluorescence emission spectra of (a) $90\ \mu\text{M}$ Ag-DNA1 and (b) $1\ \text{mM}$ Ag-DNA1 in the microemulsion. The encircled set of peaks are thought to be contaminants from the AOT. Spectra (b) & (c) were acquired at emission and excitation slits each set at 2 nm in order to improve the signal to noise quality.....	153
Figure 6.9: fluorescence emission spectra of (a) $90\ \mu\text{M}$ Ag-DNA2 and (b) $1\ \text{mM}$ Ag-DNA2 in the microemulsion.	154
Figure 6.10: fluorescence emission spectra of (a) $90\ \mu\text{M}$ Ag-DNA3 and (b) $1\ \text{mM}$ Ag-DNA3 in the microemulsion.	155

Figure 6.11: fluorescence emission spectra of (a) $90\ \mu\text{M}$ and (b) $1\ \text{mM}$ Ag NCs in the microemulsion.....	157
Figure 6.12: Emission spectra of $90\ \mu\text{M}$ Ag-DNA1 at an Ag: base ratio of 1:4.	158
Figure 6.13: Emission spectra of $90\ \mu\text{M}$ Ag-DNA2 at an Ag: base ratio of 1:5.	158
Figure 6.14: Emission spectra of $90\ \mu\text{M}$ Ag-DNA3 at an Ag: base ratio of 1:6.	159
Figure 6.15: Emission spectra of $180\ \mu\text{M}$ Ag-DNA1 at an Ag: base ratio of 1:2.	161
Figure 6.16: Emission spectra of $217\ \mu\text{M}$ Ag-DNA2 at an Ag: base ratio of 1:2.	161
Figure 6.17: Emission spectra of $255\ \mu\text{M}$ Ag-DNA3 at an Ag: base ratio of 1:2.	162
Figure 6.18: Emission spectra of (a) $90\ \mu\text{M}$ Ag NPs in aqueous solution in the absence of DNA (b) absorbance spectrum of the same $90\ \mu\text{M}$ Ag NP aqueous solution sample. The peaks indicated by red arrows and asterisks are assigned to Raman peaks of water, and the second-order scattering respectively.	162
Figure 6.19: DLS spectra of $90\ \mu\text{M}$ and $1\ \text{mM}$ Ag-DNA1 microemulsion samples.	163
Figure 6.20: DLS spectra of $90\ \mu\text{M}$ and $1\ \text{mM}$ Ag-DNA2 microemulsion samples.	164
Figure 6.21: DLS spectra of $90\ \mu\text{M}$ and $1\ \text{mM}$ Ag-DNA3 solutions in the microemulsion..	164
Figure 6.22: Transmission electron microscopy images of (a&b): $90\ \mu\text{M}$ Ag-DNA1 (c&d) $1\ \text{mM}$ Ag-DNA1.....	166
Figure 6.23: Transmission electron microscopy images of (a&b): $90\ \mu\text{M}$ Ag-DNA2 (c&d) $1\ \text{mM}$ Ag-DNA2.....	167
Figure 6.24: Transmission electron microscopy images of (a&b): $90\ \mu\text{M}$ Ag-DNA3 (c&d) $1\ \text{mM}$ Ag-DNA3.....	168
Figure 6.25: Transmission electron microscopy images of (a): $90\ \mu\text{M}$ Ag ⁰ (f) $1\ \text{mM}$ Ag ⁰ without the ssDNAs.	169
Figure 6.26: Full ESI-MS spectra of (a) Free ssDNA2 (b) $90\ \mu\text{M}$ Ag-DNA2 conjugate (c) $1\ \text{mM}$ Ag-DNA2 in microemulsion. Red asterisks represent DNA signals.....	172
Figure 6.27: Full ESI-MS spectra of (a) Free ssDNA2 (b) $90\ \mu\text{M}$ Ag-DNA2 conjugate (c) $1\ \text{mM}$ Ag-DNA2 in microemulsion. Red asterisks represent DNA signals.....	172
Figure 6.28: Zoomed in ESI-MS spectra at higher m/z (600 – 1300) of (a) Free ssDNA3 (b) $90\ \mu\text{M}$ Ag-DNA3 conjugate (c) $1\ \text{mM}$ Ag-DNA3 in the microemulsion. Red asterisks represent DNA signals.	173
Figure 6.29: Zoomed in ESI-MS spectra at higher m/z (600 – 1300) of (a) Free ssDNA3 (b) $90\ \mu\text{M}$ Ag-DNA3 conjugate (c) $1\ \text{mM}$ Ag-DNA3 in the microemulsion. Red asterisks represent DNA signals.	173

Figure 6.30: Zoomed in ESI-MS spectra for 90 μ M Ag-DNA2 and 3 showing peaks in the region of 465 – 600 m/z [$\text{Ag}_4\text{B}_3\text{O}_5(\text{BH}_3)_2\cdot\text{H}_2\text{O}$] with a m/z value of 591.1. Inset is the matching of the experimental and calculated spectra of the peaks centred at 591.1.....	174
Figure 6.31: ESI-MS spectra of (a) 90 μ M and (b) 1 mM Ag^+ ions in microemulsion.....	174
Figure 6.32: Fluorescence images of Ag-DNA1 (Black-green), Ag-DNA2 (Yellow), and Ag-DNA3 (Orange) in 99 % D_2O solution under UV light.	177
Figure 6.33: ^1H NMR spectra of oligonucleotides a) DNA1 (22-mer) b) DNA2 (29-mer); and c) DNA3 (34-mer). All spectra acquired at 298 K in D_2O with tetramethylsilane (TMS) as a reference. Asterisks are signals from the DNA protecting groups used during the DNA synthesis.	179
Figure 6.34: ^1H NMR spectra of oligonucleotides a) DNA1 (22-mer) b) Ag^+ -DNA1; and c) Ag-DNA1. All spectra acquired at 298 K in D_2O with tetramethylsilane (TMS) as a reference.	180
Figure 6.35: ^1H NMR spectra of oligonucleotides a) a) DNA1 (22-mer); b) Ag^+ -DNA1; and c) Ag-DNA1. All spectra acquired at 298 K in D_2O with tetramethylsilane (TMS) as a reference.	181
Figure 6.36: ^1H NMR spectra of (a) DNA2 (29-mer) oligonucleotide (b) Ag^+ -DNA2 and (c) Ag-DNA2. All spectra acquired at 298 K in D_2O with tetramethylsilane (TMS) as a reference.	184
Figure 6.37: ^1H NMR spectra of a) DNA2 (29-mer) oligonucleotide b) Ag^+ -DNA2 and c) Ag-DNA2. All spectra acquired at 298 K in D_2O with tetramethylsilane (TMS) as a reference.	185
Figure 6.38: ^1H NMR spectra of a) DNA3 (34-mer) oligonucleotide b) Ag^+ -DNA3 and c) Ag-DNA3. All spectra acquired at 298 K in D_2O with tetramethylsilane (TMS) as a reference.	187
Figure 6.39: ^1H NMR spectra of a) DNA3 (34-mer) oligonucleotide b) Ag^+ -DNA3 and c) Ag-DNA3. All spectra acquired at 298 K in D_2O with tetramethylsilane (TMS) as a reference.	188
Figure 6.40: ^{31}P NMR of DNA1 (a) DNA1 only (22-mer) oligonucleotide (b) Ag^+ -DNA1 (c) Ag-DNA1 in D_2O at 298 K in D_2O with 85 % phosphoric acid as a reference.	190
Figure 6.41: ^{31}P NMR of DNA2 (a) DNA2 only (29-mer) oligonucleotide (b) Ag^+ -DNA2 (c) Ag-DNA2 in D_2O at 298 K in D_2O with 85 % phosphoric acid as a reference.	190
Figure 6.42: ^{31}P NMR of (a) DNA3 only (34-mer) oligonucleotide (b) Ag^+ -DNA3 (c) Ag-DNA3 in D_2O at 298 K in D_2O with 85 % phosphoric acid as a reference.	191
Figure 6.43: ^1H NMR spectra of (a) cytidine (b) cytidine_ Ag^+ complex and (c) cytidine_ Ag. All spectra acquired at 298 K in D_2O with tetramethylsilane (TMS) as a reference.	194

Figure 6.44: ^1H NMR spectra of (a) guanosine (b) guanosine $_{\text{Ag}^+}$ complex and (c) guanosine $_{\text{Ag}}$. All spectra acquired at 298 K in D_2O with tetramethylsilane (TMS) as a reference. ...	195
Figure 6.45: ^1H NMR spectra of a) thymidine b) thymidine $_{\text{Ag}^+}$ complex and c) thymidine $_{\text{Ag}}$. All spectra acquired at 298 K in D_2O with tetramethylsilane (TMS) as a reference.	196
Figure 6.46: ^{31}P NMR spectra of a) cytidine b) cytidine $_{\text{Ag}^+}$ complex and c) cytidine $_{\text{Ag}}$ in D_2O at 298 K with 85 % phosphoric acid as a reference.	197
Figure 6.47: ^{31}P NMR spectra of a) thymidine b) thymidine $_{\text{Ag}^+}$ complex and c) thymidine $_{\text{Ag}}$ in D_2O at 298 K with 85 % phosphoric acid as a reference.	198
Figure 6.48: ^{31}P NMR spectra of a) adenosine b) adenosine $_{\text{Ag}^+}$ complex and c) adenosine $_{\text{Ag}}$ in D_2O at 298 K with 85 % phosphoric acid as a reference.	198
Figure 6.49: ^{31}P NMR spectra of a) guanosine b) guanosine $_{\text{Ag}^+}$ complex and c) guanosine $_{\text{Ag}}$ in D_2O at 298 K with 85 % phosphoric acid as a reference.	199
Figure 6.50: Fluorescence spectra of (a) emission spectrum of Ag-DNA1 and (b) excitation spectrum of the emission at 390 nm in 99 % D_2O solution.	200
Figure 6.51: Fluorescence spectra of (a) emission spectrum Ag-DNA2 and (b) excitation spectrum of the emission at 591 nm in 99 % D_2O solution.	201
Figure 6.52: Fluorescence spectra of (a) emission spectrum of Ag-DNA3 and (b) excitation spectrum of the emission at 632 nm in 99 % D_2O solution.	202
Figure 8.1: Pictures of (a) 90 μM and (b) 1 mM Ag NCs in microemulsion synthesized by photoreduction.	220
Figure 8.2: 100 mg reverse-phase silica-based cartridge.	220
Figure 8.3: Rayleigh curve fitting of Ag NCs in microemulsion.	221
Figure 8.4: Rayleigh fit of the photoreduced Ag NCs UV-Vis data.	221
Figure 8.5: XPS spectrum of $[\text{Ag}_4\text{B}_3\text{O}_5\cdot\text{BH}_3\cdot 2\text{H}_2\text{O}]^-$ aqueous solution.	222
Figure 8.6: XPS spectrum of Ag capped by borate, and borane ligand.	223
Figure 8.7: XPS spectrum of Cu NCs capped by borate, and borane ligand.	223
Figure 8.8: ESI-MS of Ag NCs peak at (a) 577 (b) 595. (Top = Simulation, bottom = Experimental).	224
Figure 8.9: ESI-MS spectra of photosynthesized Ag NCs at m/z 467. (Top = Simulation, bottom = Experimental).	225
Figure 8.10: ESI-MS of photoreduced Ag NCs peak at 557. (Top = Simulation, bottom = Experimental).	226
Figure 8.11: ESI-MS spectra of photosynthesized Ag NCs at m/z 467.	227
Figure 8.12: ESI-MS spectra of Cu NCs at m/z 589.	228

Figure 8.13: Expanded ESI-MS spectra of Cu NCs of the peaks at m/z 589.....	229
Figure 8.14: ¹³ C NMR spectrum of DNA1 in 99 % D ₂ O, 308 K.....	230
Figure 8.15: HSQC NMR spectrum of DNA1 in 99 % D ₂ O, 308 K.....	230
Figure 8.16: HMBC NMR spectrum of DNA1 in 99 % D ₂ O, 308 K.....	230
Figure 8.17: ¹³ C NMR spectrum of DNA2 in 99 % D ₂ O, 298 K.....	230
Figure 8.18: COSY NMR spectrum of DNA2 in 99 % D ₂ O, 298 K.....	230
Figure 8.19: HSQC NMR spectrum of DNA2 in 99 % D ₂ O, 298 K.....	230
Figure 8.20: HMBC NMR spectrum of DNA2 in 99 % D ₂ O, 298 K.....	230
Figure 8.21: COSY NMR spectrum of DNA3 in 99 % D ₂ O, 298 K.....	230
Figure 8.22: HSQC NMR spectrum of DNA3 in 99 % D ₂ O, 298 K.....	230
Figure 8.23: HMBC NMR spectrum of DNA3 in 99 % D ₂ O, 298 K.....	230

List of Tables

Table 3.1: DLS samples data for varying ω (and AOT conc.) size and changes in physical parameters.....84

1 CHAPTER ONE

1.1 Background

Nanoparticles (NPs) are materials within in the size range of 1 – 100 nm.^{1,2} These include nanoclusters, which are at the lower end of the nano-scale (<2.0 nm). Nanoclusters (NCs) are therefore much smaller in size and so contain fewer number of atoms, hence, they are regarded as a “cluster of atoms”. They display molecule-like, size-dependent optical properties that distinguishes them from the larger NPs which show metallic properties.

Metal nanoclusters (MNCs) have attracted attention for their unique opto-physical properties. In this light, many optical and biological applications of these nanoclusters are associated with their luminescent properties in relation to their very small nanosizes and consequently their large bandgaps, which allows for radiative electronic transition.^{3,4}

The production of fluorescence in material science is connected with small clusters.⁵⁻⁹ The synthesis and stabilization of these small clusters is challenging, since they are known to grow spontaneously in the absence of stabilizers into larger and more stable nanoparticles with the attendant loss of luminescence. For the purpose of clarity, in this study, metal nanoclusters (MNCs) refer to luminescent metal clusters, and metal nanoparticles (MNPs) are the larger, non-luminescent metal particles. MNPs may also be used as a general term to refer to materials in this 1 – 100 nm region.

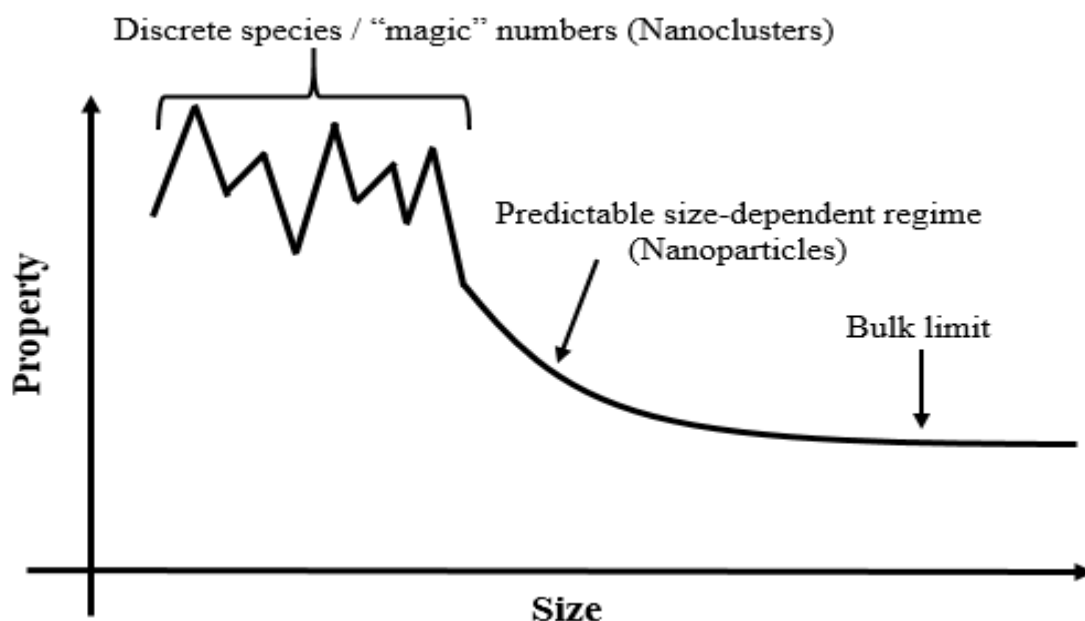


Figure 1.1: Size-dependent physical properties changes in materials.

The diagram in figure 1.1 explains the differences that arise in the physical properties of nanoparticles and nanoclusters on the basis of size variations. Irrespective of the physical property being studied, there are always three regions of the curve obtained. The first, at the upper particles size scale represents bulk materials. The nature of the curve in this region, shows that the properties remain constant and independent of their sizes. But as the particles size decreases from the bulk size, a point is reached where the properties begin to change in response to the size decrease. As the size decrease get to the nanoscale, a gradual change in the physical properties begins. At very small nanosizes (clusters), discrete energy levels are formed and the particles assume molecule-like properties. Addition of a single atom at this point leads to a profound effect on the physical property, to the extent that “magic number” effects are observed.

Thermodynamically speaking, it is unfavourable to have small nanoclusters because of their very high surface-to-volume ratio and energy^{4,10,11,12} which renders them unstable towards aggregation.¹³ Thus in the absence of stabilizers, nanoclusters would irreversibly interact with one another to form larger particles thereby effectively reducing their surface energy.¹⁴ This is represented thermodynamically by equation 1.1.

$$\Delta G = \gamma \Delta A \quad (1.1)$$

where ΔG is the change in Gibbs energy (at constant temperature, pressure and composition) that occurs when the interfacial surface area changes by an amount ΔA . The surface tension γ is defined as:

$$\gamma = \left(\frac{\partial G}{\partial A} \right)_{p,T,n_i} \quad (1.2)$$

As these clusters grow easily into different sizes and shapes over time, there is an increasing variability of physical properties accompanying these size growth^{3,15} as the particles gravitate towards the bulk metals. Hence, the production of luminescent nanoclusters requires very careful control of the reaction conditions and the methods of synthesis, so as to be able to tune the sizes of these clusters in order to obtain specifically desired optical properties for applications.¹⁶

Attempts at stabilizing these particles have led to the application of a varieties of passivating ligands most of which are predominantly organic in nature. Some of these include, sulphur and phosphine ligands, many of which are toxic to both man and the environment. Besides these, polyvalent bio-molecules like DNA have also been employed as stabilizing ligands for nanoclusters.

Besides the problem of consistency in size of the NCs, there is also the issue of consistency in the in the morphology of the MNCs.¹⁷ This is one of the challenges faced by synthetic nanochemists. Microemulsion (ME) systems have recently been employed to provide the type of reaction medium necessary to establish some form of size and morphology control in the synthesis of metal clusters.¹⁸ Through the microemulsion system, it is possible to make monodispersed particles. Microemulsions have also been demonstrated to confer stability against the spontaneous growth of nanoparticles post-synthesis¹⁹ arising from the mutual electrostatic repulsion between the lipophilic end-groups of the surfactant molecules. The need to produce homogeneous MNCs with size-dependent characteristics is crucial to achieve tailor-made sensors.

This exercise is geared towards making metal nanoclusters of a given core size and optical properties according to the concentration of M^{n+} ions present in water droplets of a particular diameter at room temperature and under specific reaction stoichiometry.

1.2 Nanoparticles

Metal nanoparticles have received tremendous attention because of their size-dependent optical properties leading to their applications in optics, optoelectronics, chemical and biological sensing.^{15,16,20} They are renowned for having high surface-to-volume ratio and exhibit remarkable surface activities suitable for application in catalysis^{12,21,22} and surface-enhanced Raman scattering.^{16,23,24} Nanoscience and technology have since burgeoned into a very wide interdisciplinary industry over the years.⁴

1.2.1 Classification

Materials can be classified into metals, semiconductors, and insulators on the basis of electronic conduction and bandgaps (Fig. 1.2). Metals have overlapping energy levels because of the high density of state, hence they form continuous energy bands with no bandgaps. Semiconductors have closely separated (discrete) energy levels and hence small bandgaps. But insulators are associated with much larger bandgaps making it rather impossible to promote electrons from the valence to the conduction bands because of the enormous amount of energy required for this to be accomplished.

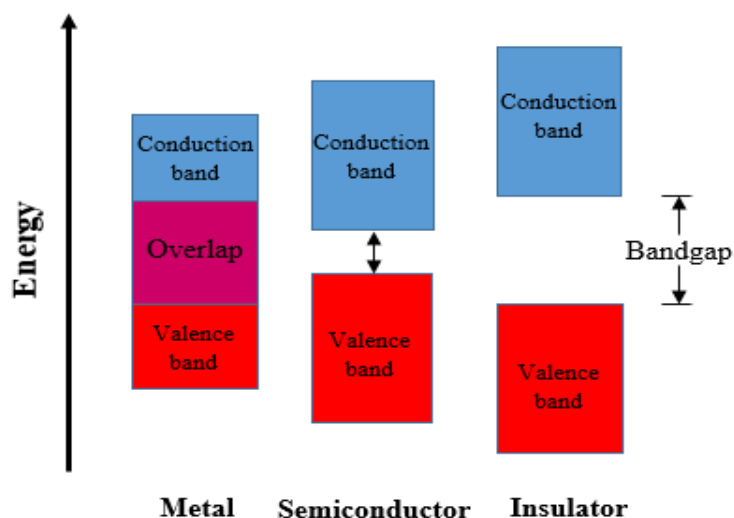


Figure 1.2: Energy level diagram of metals, semiconductors, and insulators.

On the basis of size, metals can be classified into bulk metals, nanoparticles, metal nanoclusters (MNCs), and single atoms. Bulk metals, have free moving (delocalised) electrons from a large number of atoms, due to an increased density of state and the consequent overlap of the electronic energy levels of the valence and conduction bands into a continuous band.³ Metal nanoparticles have sizes typically in the 10 - 100 nm range.³ Although, they contain lesser number of atoms, their properties already tend towards those of the bulk metals.

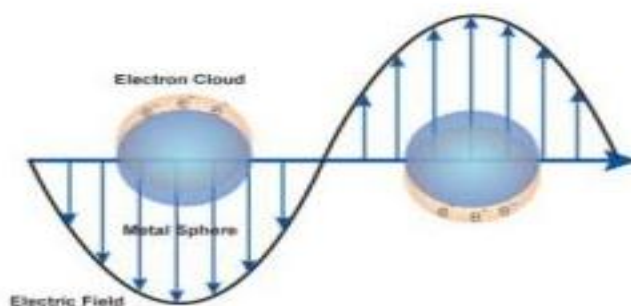


Figure 1.3: Surface plasmon resonance of nanoparticles in response to excitation energy.
Source: Sigma Aldrich.¹²⁴

Metal nanoparticles therefore interact with light of appropriate energy resulting in the collective oscillation of surface electrons (Figure 1.3) in response to the incident photon, a phenomenon known as surface plasmon resonance (SPR).^{1,16,23,25,26}

Further reduction of the sizes of nanoparticles to less than two nanometres (~ 2 nm)^{20,27,28,29} as a consequence of the decrease in the density of state, results in the splitting of the continuous (overlapping) valence and conduction bands, and an energy level gap is thus formed.

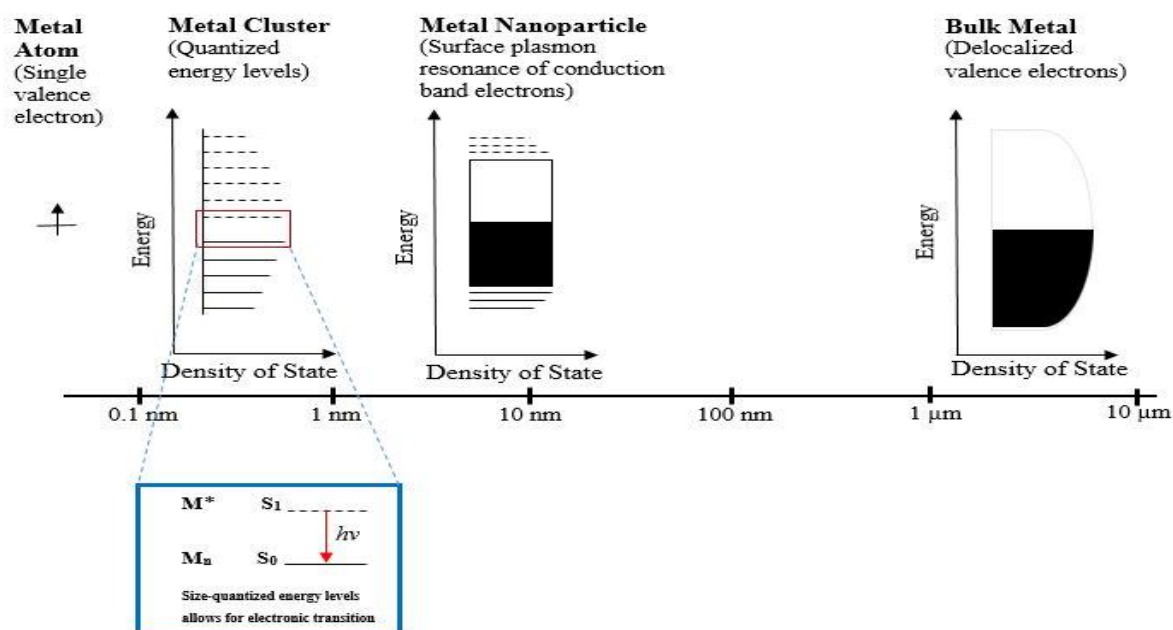


Figure 1.4: Size-dependent energy level diagram of metals, semiconductors, and insulators. Adapted from Isabel Diaz and Robin Ras.¹²⁵

This energy gap is referred to as “bandgap”. The conduction and valence bands are comprised of discrete energy levels. Metal nanoclusters because of their limited number of atoms^{30,31} are characterised by having discrete pockets of energy levels and bandgaps (figure 1.4) Their interactions with light therefore results in electronic transitions from the valence to the conduction band as electrons acquire the requisite energy to cross the “forbidden” bandgap.³²

1.3 Quantum-size effect

As a result of their characteristic small sizes, nanomaterials demonstrate quantum-size confinement properties.³³ Quantum effect is readily explained by the confinement of electron and hole pair in a potential well of very small volume with size corresponding to the Bohr

exciton radius.³³ Perhaps, it is better described by the particle-in-a-box model where a probability of finding a particle is defined by the potential barriers of the box. The energy of the particle can be defined by its mass and quantum number as well as the dimension of the box.³⁴

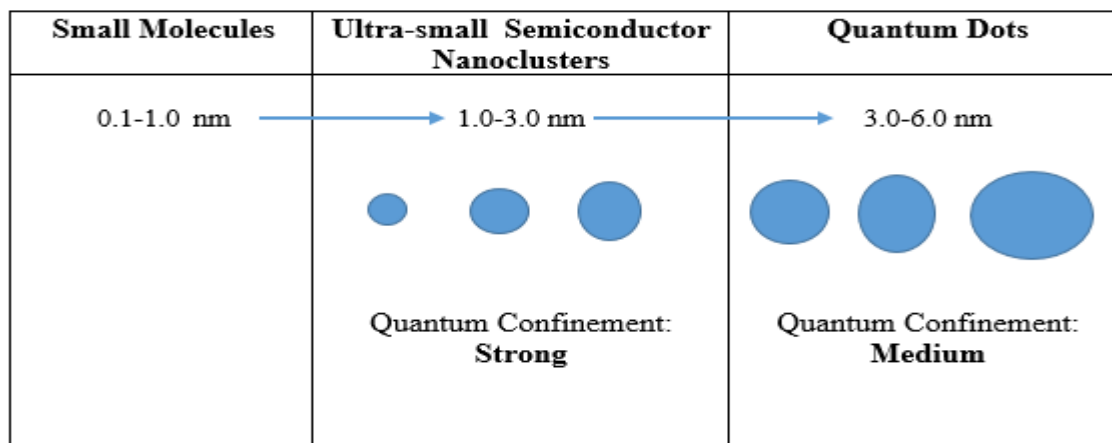


Figure 1.5: Quantum size-dependent classification of materials according to the zone of confinement.

Higher energies of excitation are required as the sizes are reduced and materials become more confined.³⁴ Quantum dots are examples of materials whose sizes (3.0 – 6.0 nm) are typically in the medium zone of confinement (figure 1.5).^{14,31} Hence quantum dots provide an opportunity to study molecule-like properties of materials in the zone of confinement.^{14,31} Nanomaterials typically in the 1.0 – 3.0 nm size scale (figure 1.5) often referred to as ultra-small nanoclusters (USNCs) or as ultra-small quantum clusters, belong to the zone of strong quantum confinement.³⁵⁻⁴⁴ However, the Bohr's radius is dependent on the material in question and varies from material to material, thus every material has its quantum confinement at different sizes.⁴⁵

1.4 Wave Function

Quantum systems are associated with wave function,^{46,47,48} since electrons according to DeBroglie's equation have a dual nature as both a particles and wave. Electrons are therefore associated with wave function which is described by the Schrodinger's equation. This is a complex mathematical function that effectively describes the properties and position of an electron at any given time and space in quantum mechanics.⁴⁹

$$\lambda = \frac{h}{p} \quad (1.3)$$

Equation (1.3), proposed by DeBroglie, relates the wavelike nature of a quantum particle in terms of its wavelength λ to the particle-like nature described by its momentum, p . h is Planck's constant whose value is 6.626×10^{-34} J s.

For a rectangular box of dimension $a \times b \times c$ along each side (the particle-in-a-box model) at an amplitude of zero, the wave function would coincide with the boundary of the box (confinement).⁴⁹ The individual discrete energy levels will be represented by the equation below:⁴⁹

$$E = \frac{h^2 n^2}{2m} \left(\frac{n_1^2}{a^2} + \frac{n_2^2}{b^2} + \frac{n_3^2}{c^2} \right) \quad (1.4)$$

Where **a**, **b**, and **c** represents the dimensions of the box in the x, y and z directions, and **n_j** are integer values, **h** is Plank's constant, while **m** is the mass of the electron.

At these ultra-small sizes, the wave functions of the electrons extend beyond the core of confinement as the kinetic energy of the exciton overcomes the coulombic interactions between the exciton and its hole-pair.⁵⁰ Thereby extending the electron wave function beyond the metal-core^{50, 51} into the bordering ligand monolayer⁵⁰ and possibly coupling with those of their nearest neighbouring atoms.⁵² In this way, excitons are in essence delocalized.⁵³ This delocalization of excitons from the core of confinement causes a reduction of the bandgap and a consequent red shift of emission peak maximum.^{50,51}

As the sizes of the material increase, the wave function become gradually and increasingly less extended. The extent of delocalization also decreases and effectively diminished, lying within the zone of confinement.

1.4.1 Bandgaps

The discontinuation of the energy band between the valence and conduction bands in nanoclusters and semiconductors as the material size decreases open up an energy level gap already described as bandgap (figure 1.6). An inverse relationship exists between bandgap and cluster size (number of atoms), hence, the bandgap varies with cluster size.⁵⁴ Bandgap is actually the difference between the highest energy level of the valence band and the lowest energy level of the conduction band^{54,55} in semiconductors.

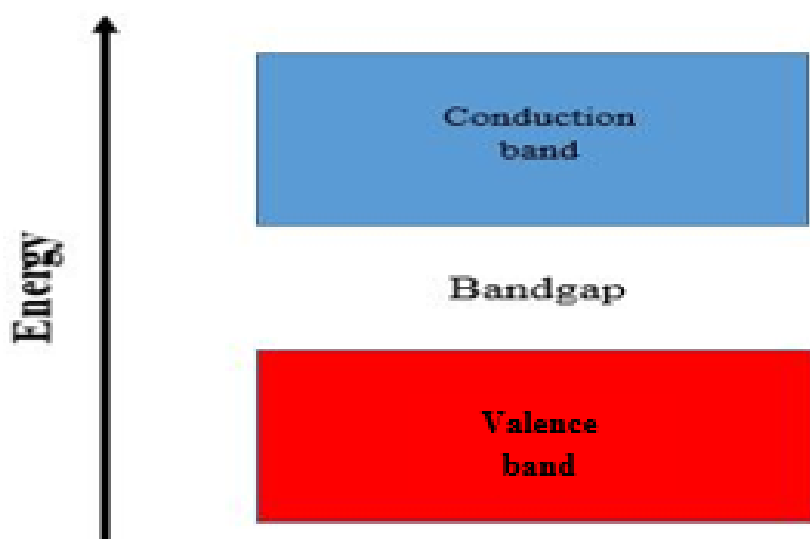


Figure 1.6: Energy level diagram showing bandgap.

Therefore, relatively large energies will be required for the transition of electrons in ultra-small clusters which would correspond to the blue regions of the spectrum of light.

1.5 Fermi Level

The Fermi level, denoted by E_f is described as the highest occupied level at zero Kelvin (0 K) absolute temperature.⁵⁶ In a metal, it is the highest occupied molecular orbital (HOMO) of the solid/nanoparticles/cluster at its ground state. Thermodynamically, it represents the amount of work required to add or remove an electron to or from a material (a body)⁵⁷ also referred to as the chemical or electrochemical potential.⁵⁸ Since electrons cannot exist in the same energy

level at the same time (Pauli's principle), they occupy available lowest energy states and form a sea of Fermi electrons.⁵⁸

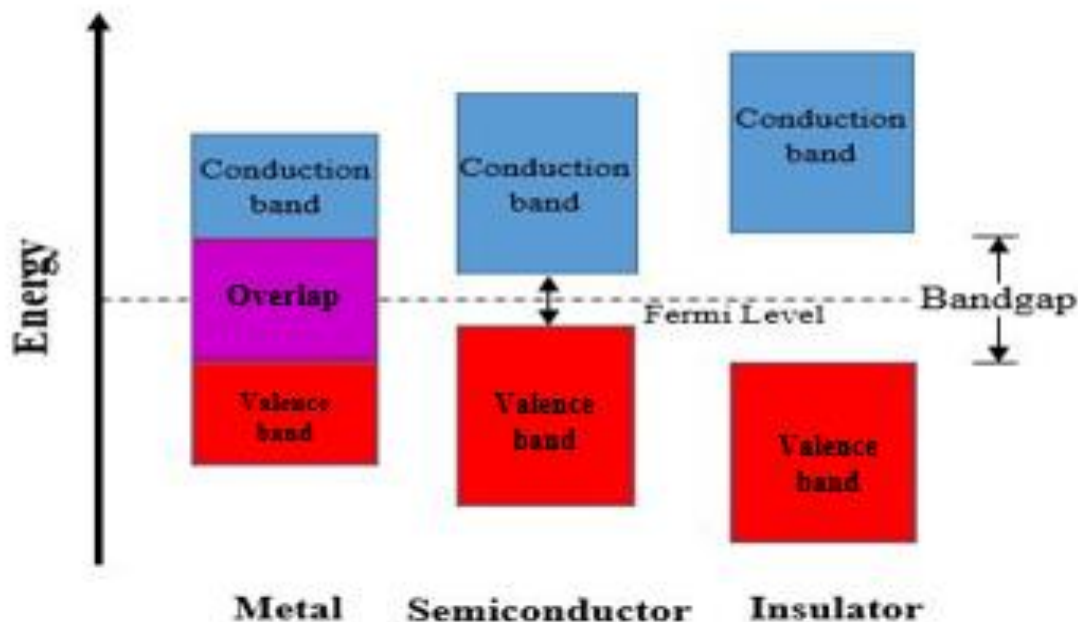


Figure 1.7: Fermi level diagram of metals (conductors), semiconductor, and insulators (broken line representing the Fermi Level).

The level at the top of this sea of electrons is called the Fermi level (figure 1.7). Below this level, electrons do not have enough energy to go above it.⁵⁵ But at a higher temperature and with sufficient energy, electrons can be moved above the Fermi Level onto the conduction band. In metals, the Fermi level lies in either of the two overlapping valence or conduction band. It lies at the centre of the bandgap for semiconductors (intrinsic).⁵⁵ The bandgaps of metal nanoclusters are similar to those of semiconductors hence in many contexts they are referred to as semiconductor nanoclusters (particles) (SNCs).⁵⁹⁻⁶²

1.6 Fluorescence

The absorption of photons of energy by a material, leading to electronic excitation and transitions to an excited state higher energy level, where the exciton undergoes stages of vibrational relaxation, before eventually returning to the ground state energy level by the loss of the loss of residual energy through re-emission is generally known as photoluminescence; this comprises fluorescence and phosphorescence⁶³ (see figure 1.8 below). Whereas

fluorescence is characteristically more transient in comparison with the phosphorescence, which spans much longer times (between 10^3 to 10^0 seconds or even longer) arising from intersystem crossing,^{64,65} which corresponds to a transition between states of different spin (the triplet excited state and the singlet ground state). The process involves simultaneously flipping the spin of an electron as well as emitting a photon and is less likely than fluorescence which involves a transition between states of the same spin (S_1 and S_0).

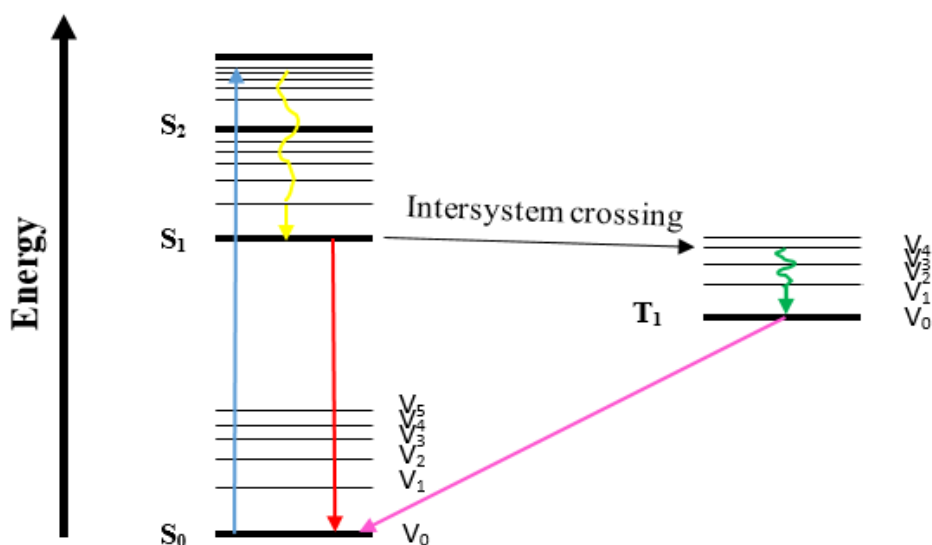


Figure 1.8: Jablonsky diagram showing the fluorescence phenomenon. The blue arrow represents absorption, yellow arrow represents dark-phase internal conversion phase, red is fluorescence, black (horizontal) represents intersystem crossing and pink is phosphorescence.

Fluorescence occurs when light energy at relatively short wavelengths, is absorbed by a substance and results in the projection of electrons from the ground state to the excited state level and undergoes a process of vibrational relaxation (a non-radiative (dark phase)) resulting in some energy loss, and subsequently returning back to the ground state by losing its residual energy through re-radiation of light of longer wavelengths (figure 1.8).^{64,65} Fluorescence is characterized by light absorption in femtoseconds (10^{-15} sec) time frame and re-emission of residual light at longer wavelengths in pico- to nanoseconds (10^{-12} to 10^{-9} sec) later,^{64,65,66} with an average lifetime of 10^{-8} sec in the excited state.⁶⁵

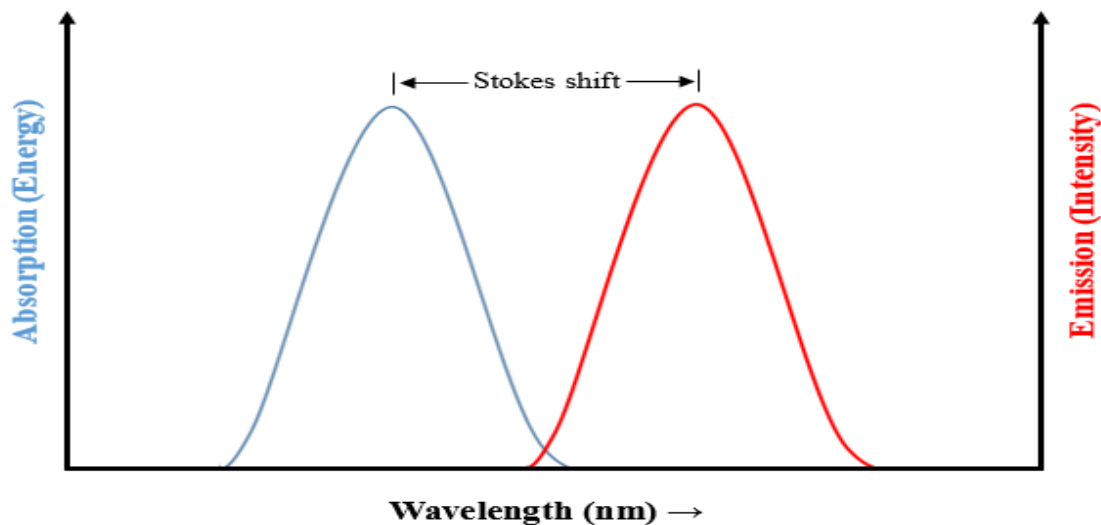


Figure 1.9: Combined schematic representation of both the fluorescence excitation (blue) and emission (red) spectra.

The absorption and emission energies and spectra of a molecule are its unique identity, thus, its absorption and emission spectra are of great analytical significance.⁶¹ Fluorescence spectrometer measures the intensity of the emitted light which is related to the concentration of the sample.⁶¹

Both the absorbance and emission bands maybe mirror images of themselves if an exciton is excited from the singlet ground state (S_0) to the singlet excited state (S_1) and then returns back to the S_0 , so long as there is a weak solvent and fluorophores interaction. This is referred to as the mirror-image rule (figure 1.9).^{61,65}

1.7 Electromagnetic radiation and spectrum

Electromagnetic radiation is a combination of electric and magnetic wave oscillating at the speed of light through space, carrying quanta (photons) of energy and momentum with which it interacts with matter.⁶⁷ The interaction between electromagnetic radiation and matter has become the basis of the study and characterization of matter in the field of science known as spectroscopy.⁶⁷ This interaction results in certain peculiar physical changes in matter in relation to the absorption of quanta of electromagnetic energy.⁶⁸ The quantized energy of a photon at higher frequencies are related to each other by equation 1.5 presented below:

$$E = hf \quad (1.5)$$

E is the energy of a photon, h is the Planck's constant, and f is frequency.

The properties of the electromagnetic radiation are described by its frequency and wavelength. Its speed of propagation is also related both to its frequency and wavelength by the equation 1.6:

$$c = \lambda f \quad (1.6)$$

c is the speed of the electromagnetic wave, λ is the wavelength, and f is frequency. From the above equation, frequency is inversely proportional to wavelength; equation 1.6 therefore becomes:

$$f = \frac{c}{\lambda} \quad (1.7)$$

Equation (1.4) above can be rewritten as:

$$E = \frac{hc}{\lambda} \quad (1.8)$$

1.7.1 Electromagnetic Spectrum

The electromagnetic spectrum is an array of the different components of the electromagnetic wave in the order of their increasing wavelengths. According to the increasing wavelengths, electromagnetic spectrum is classified into: gamma ray, x-ray, ultra-violet, visible, infra-red, microwave, and radio waves (see figure 1.10 below).

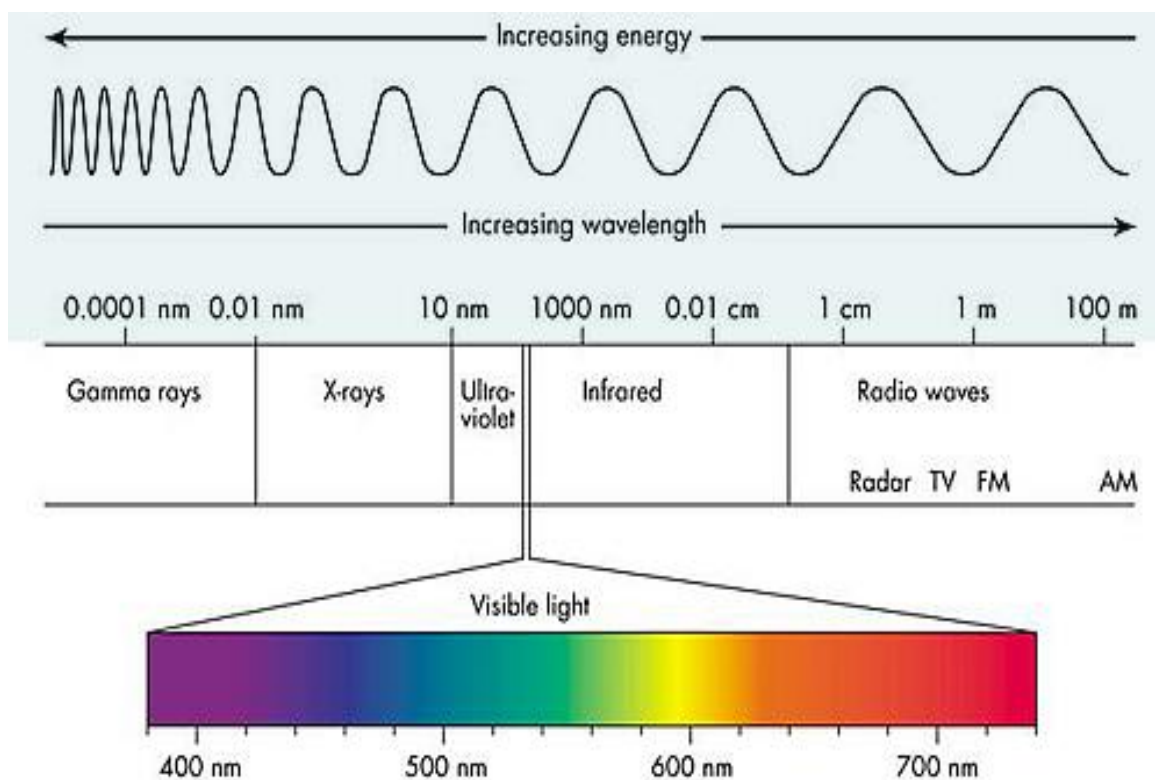


Figure 1.10: Electromagnetic spectrum. Source: Cyberphysics.⁶⁹

From equation 1.8 above, energy is inversely proportional to wavelength. Thus, those components of the electromagnetic wave with shorter wavelengths have characteristically more energy and so are able to affect matter more drastically, causing ionisation and heat.^{68,70} Whereas, those components with longer wavelengths possess comparatively less dramatic energy and do not result in ionisation when interacting with matter.^{68,71-74} Interaction between high energy ionising radiation results in chromosome damage in living cells.^{73,75-80}

Molecular spectroscopy is concerned with studying the interactions of the non-ionising energy with matter, which results in the excitation, translation, vibration, and rotation of electrons, bonds, molecules and nuclei upon absorption of the requisite photons of light energy.^{61,65} The total energy of the system can be represented by the equation:^{61,65}

$$E_{\text{total}} = E_{\text{translation}} + E_{\text{vibrational}} + E_{\text{rotational}} + E_{\text{electronic}} + E_{\text{electronic spin orientation}} + E_{\text{nuclear spin orientation}} \quad (1.9)$$

1.8 Emulsion

Emulsion is a dispersion of an insoluble liquid in another.^{81,82} An example is water in oil. Since emulsions comprise of two immiscible liquids, therefore, they are not stable (do not mix), and often phase-separate from each other (figure 1.11).^{83,84} Such phase-separated emulsions are described as “broken”.^{85,86} The stability of emulsions depend on the inherent physico-chemical properties of the component liquids, such as pH, temperature, viscosity, size of droplets, and electrostatic interactions.^{81,87,88,89} However, the introduction of substances called surfactants, or emulsifiers, help bring stability to emulsion systems^{81,85} by reducing the interfacial energy between the immiscible liquids.^{84,90} The sizes of the dispersed-droplets in emulsion systems are in the region of hundred to tens of micrometres.^{84,85}

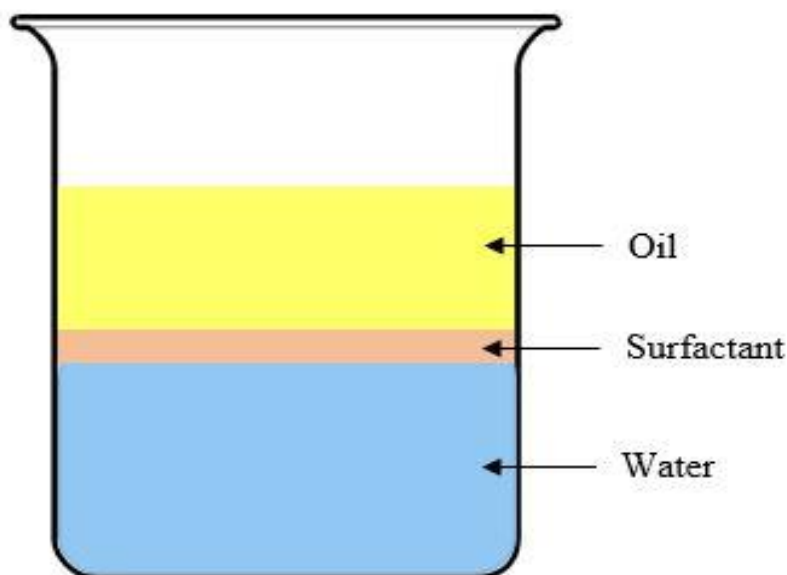


Figure 1.11: Component parts and order packing of the emulsion systems comprising the emulsifier (surfactant).

Density differences between the two phases of an emulsion system may cause the dispersed droplet phase to rise or drop in the medium, a process known as creaming and sedimenting.⁸⁵ Creaming is said to occur when the dispersed phase has a density less than that of the continuous phase, and the reverse being the case for sedimentation to occur.^{85,88} Sedimentation may occur where the droplet size exceeds 5 μm .⁸⁵ The movement of droplets is predominantly controlled by the sizes of the inherent colloidal droplets.^{84,86}

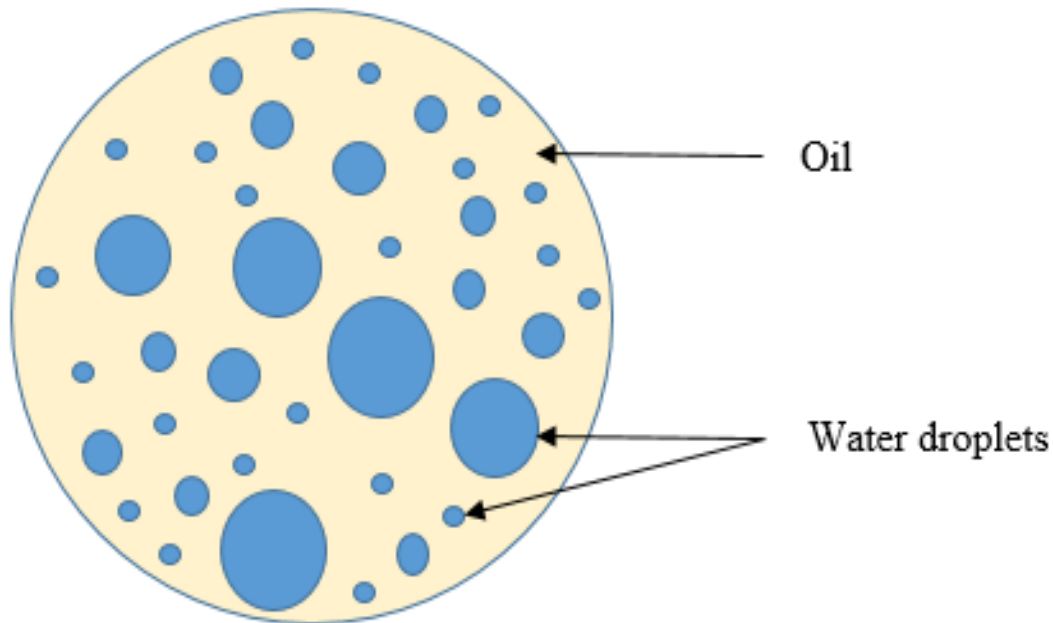


Figure 1.12: Water-in-oil emulsion system showing dispersed water droplets in the oil phase.

At droplet sizes below 5 μm , Brownian motion predominates, and such systems are characteristically stable (figure 1.12).⁸⁵ There are two types of emulsion systems basically, depending on which of water or oil is the dispersed or continuous phase. These are: the water-in-oil, or the oil-in-water emulsion, denoted by w/o and o/w respectively (figure 1.13).^{85,90} Examples of oil-in-water emulsion are fat globules in water, while milk and butter are examples of water dispersed in oil (water-in-oil).^{90,91}

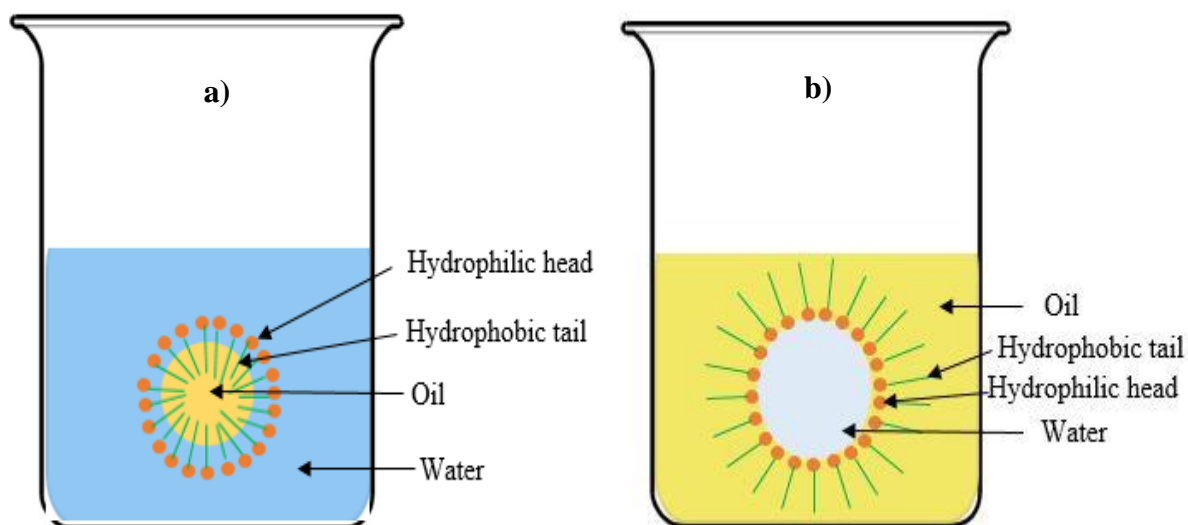


Figure 1.13: (a) Micelle in water continuous phase (b) reversed micelle in oil continuous phase.

1.9 Role of Emulsifiers

Two important factors govern and describe the role of emulsifiers in emulsion systems. These are the hydrophilic (water-loving) and hydrophobic (water-hating) factors. Emulsions have already been described as a mixture of oil and water dispersions. Oil is hydrophobic, and water the hydrophilic, the reason these liquids do not readily associate.⁸¹ But with the aid of an emulsifier, they can be made to “mix” by forming interfacial “wall” around droplets and reducing their surface energies.^{86,87} This also prevents coalescence of droplets, and ensuring thermodynamic stability.^{10,11,87, 92}

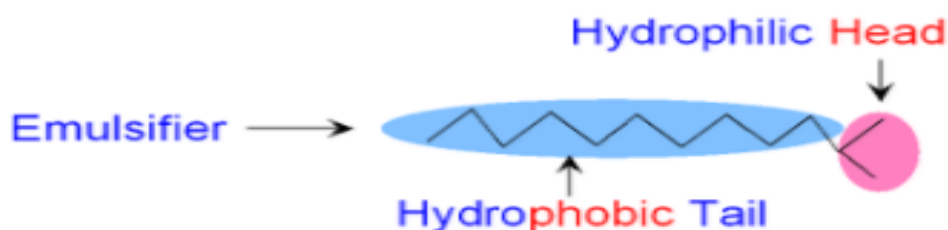


Figure 1.14: Component parts of an emulsifier. Source: Gcsescience.¹²⁶

An emulsifier (or surfactant) is a substance with an amphiphilic (hydrophilic and hydrophobic head and tail) groups (figure 1.14), which enables it to associate easily with both water and oil phases of the emulsion,⁸¹ to form a colloidal solution.⁸⁴ Emulsifier are therefore the third component of the emulsion system. Its polar head is typically attracted towards water and other polar solvents, and the tail usually of long hydrocarbon chain is attracted to the oil phase.

Depending on the balance between the hydrophilic and lipophilic (hydrophobic) components, also known as HLB (hydrophilic and lipophilic balance) whose value represents the measure of the size and strength of these component parts.^{90,93} An HLB value of 1-6 gives rise to w/o emulsion, whereas, values above 8 produce o/w emulsions.⁹⁰ Therefore, depending on the packing capability of the emulsifier as represented by the HLB value, either of the (w/o) and (o/w) types may be formed.⁸⁴ The packing capability determines the tendency of the emulsifier molecules forming an interfacial-monolayer and curving around the water or oil to form droplets, or indeed remaining unaffectedly planar⁸⁴ as the case may be (see figure 1.11). In this way, hydrophilic emulsifiers give rise to o/w emulsions while lipophilic ones produce w/o emulsions.⁸⁴

Pickering⁹⁴ also used the idea of the extent to which the surfactant particles are wetted by either of the two composing liquids in the emulsion to demonstrate what type of emulsion was formed. According to him, if the particles of the emulsifier are more wetted by the oil, then a water-in-oil emulsion was formed; and the reverse (o/w) if the emulsifier particles were better wetted by water.⁹⁴

Since phase-separation of the liquid components of the emulsion is a thermodynamic response to lower the surface energy between immiscible liquids,⁸⁴ therefore to maintain the balance in the stability of emulsions, energy would be required by way of constant agitation of the system, or the incorporation of surfactants to overcome this energy need⁸⁴ without which the system reverts back to phase separation.^{95,96}

1.10 Microemulsion

Emulsions are classified according to the size of the dispersed droplets they contain^{84,85} and by their kinetic stability.⁸⁶ Bucak and Rende classified emulsions as those whose dispersed phase comprised of particles between 0.1 to 10 μm . A size range of 30 to 100 nm dispersed droplets is classified as miniemulsion. Microemulsion then are those with dispersed droplets sizes between 1 to 30 nm⁸⁴ or 5 – 50 nm according to Capek⁸⁷ and Eastoe.⁹⁷

Due to their droplet size, microemulsions comprise of droplet particles which undergo Brownian motion and are essentially stabilized by their inherent small droplet size as well as by electronic repulsion of surfactant molecules, hence require no agitation. Microemulsions are thermodynamically very stable, isotropic, colloidal mixtures of water, oil, and emulsifier.^{84,89,98}

1.10.1 Thermodynamic stability

Considering that microemulsion contain small dispersed droplets in a dispersion medium, then the entropy change for the dispersed droplets can be represented by equation 1.10.^{97,99}

$$\Delta S_{\text{conf}} = -nk_B [\ln\phi + \{(1 - \phi)/\phi\}\ln(1 - \phi)] \quad (1.10)$$

Where n is the number of dispersed phase droplets, ϕ is volume fraction of the dispersed phase, and k_B is the Boltzmann constant. According to Tadros¹⁰⁰ the Gibb's free energy equation can be expressed as:¹⁰⁰

$$\Delta G_{\text{form}} = \Delta A\gamma - T\Delta S \quad (1.11)$$

ΔG is the Gibb's free energy, γ is the surface tension of the interface, ΔA is the change in interfacial area (where A is the area of a sphere, $A = 4\pi r^2$), of interface, and T is the absolute

(Kelvin) temperature, ΔS is the entropy change. Equation 1.11 therefore represents the sum of the area of interface, and the entropy of the droplet.¹⁰⁰

Since there is an increase in entropy of the system by the dispersal of droplets, the entropy term ΔS is therefore positive. In order for the microemulsion system to be stable there has to be a concomitant reduction of the surface tension (γ) of the interface.⁹⁷ This is where the surfactant comes in. The ability of the surfactant to cause the reduction of the interfacial surface tension to a significantly low value, so as to obtain a negative Gibb's free energy change is crucial for the thermodynamic stability of the microemulsion system. This can be achieved if the surfactant can significantly reduce the interfacial surface tension so that the energy component ($\Delta A\gamma$) is significantly reduced to a small positive value and ΔG becomes negative.

Two-tailed^{97,101,102} and some non-ionic¹⁰³ surfactants have been observed to have an advantage over the single-tailed in being able to reduce the interfacial surface tension to such low values necessary to achieve thermodynamic stability of microemulsion systems.^{97,101,102,103} The single-tailed surfactant is limited in this respect because they reach the critical micelle concentration (CMC) before they are able to attain the low interfacial surface tension, hence, they often require a co-surfactant.⁹⁷

1.11 Micelles

Surfactant are surface active agents. They act on the surfaces of the liquid by lowering the surface tension (section 1.10.1).⁸⁴ As the surfactant concentration increases, the number of molecules on the surface of the monolayer increases correspondingly, until it reaches a state whereby some of these molecules become progressively solubilized into the water medium.^{84,104} Further increases in surfactant concentration, results in an increase in the number of the “solubilized” surfactant molecules (figure 1.15).^{84,104}

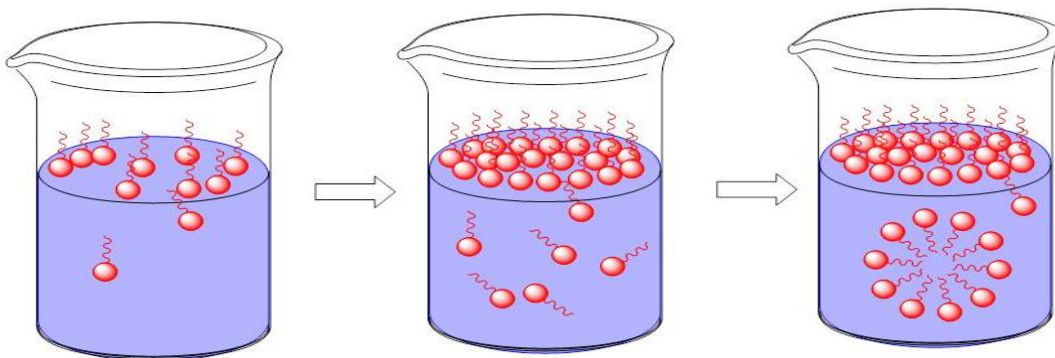


Figure 1.15: Processes of micelle formation. Source: Hunter, 1993.¹⁰⁵

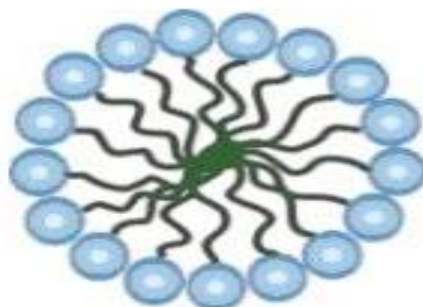


Figure 1.16: Schematic diagram of a micelle. Source: European Chemistry Thematic Network.¹²⁷

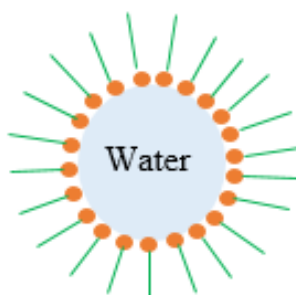


Figure 1.17: Reverse micelle.

This process continues until the concentration of the solubilized molecules reaches what is described as the CMC and micelles are formed (figure 1.16) in aqueous solution whose orientation depend on the hydrophilic environment of the liquid. Usually, the first micelle aggregates formed are spherical in geometry (figure 1.15 and 1.16).⁸⁴ Above this CMC, further increments in surfactant concentration result in the addition (solubilisation) of more emulsifier molecules onto the spherical micelles in the aqueous medium which grows further into larger, non-spherical morphology while the concentration at the monolayer of the liquid, remains relatively constant.⁸⁴

In the water-in-oil emulsion (oil as the dispersed phase), the surfactant molecules typically form reverse micelles with the hydrophilic head forming a layer of aggregates around the water droplets (curving towards water) according to the hydrophilic/hydrophobic and wetting properties of the surfactant. The polar head-groups tend towards the water pool and the hydrophobic tail align with the oil phase forming reverse (or inverted) micelles (figure

1.17).^{84,94} Thus, being better wetted by the oil than by the water, and also having a larger contact angle, (between the surfactant molecules and the oil) the orientation of the surfactant molecules favours the oil phase. According to Tanford, the reverse micelle formation is driven by the hydrophobic effect.¹⁰⁶ Reverse micelles are also known to have a diameter of between 2 – 20 nm according to Eastoe *et al.*,⁹⁸ and Walde *et al.*¹⁰⁷

1.12 Deoxyribonucleic acids, DNA

Deoxyribonucleic acid (DNA) is a polymeric molecule which exists naturally in chromatin in the nucleus of eukaryotic cells.^{108,109} It contains the transmitted generic codes necessary for the development and proper functioning of living organisms.¹¹⁰ DNA is primarily composed of three chemical groups of phosphate, sugar (ribose), and nitrogen-containing bases.¹⁰⁹ The first two groups make up the DNA backbone^{59,109-111}, giving it the rigid structure. The nitrogenous bases make up the centre of the molecule.^{109,112} DNA contains four types of nitrogenous bases viz: adenine (A), cytosine (C), guanine (G), and thymine (T).^{108,109,112} It is different from ribonucleic acids (RNA) by having the oxygen atom belonging to the hydroxyl group of the second carbon atom (C2) in the ribose sugar removed in DNA. This is the reason for the prefix (Deoxy-) in the name deoxyribonucleic acids. Besides, it is also different from RNA by the replacement of one of the nucleobases of RNA, uracil (U) by thymine in DNA.^{108,109,112}

1.12.1 Structure and nomenclature of DNA

As has already been mentioned, DNA is composed of these component units: a phosphate, a ribose sugar, and nitrogenous bases with the following chemical structures (figure 1.18 and 1.19):

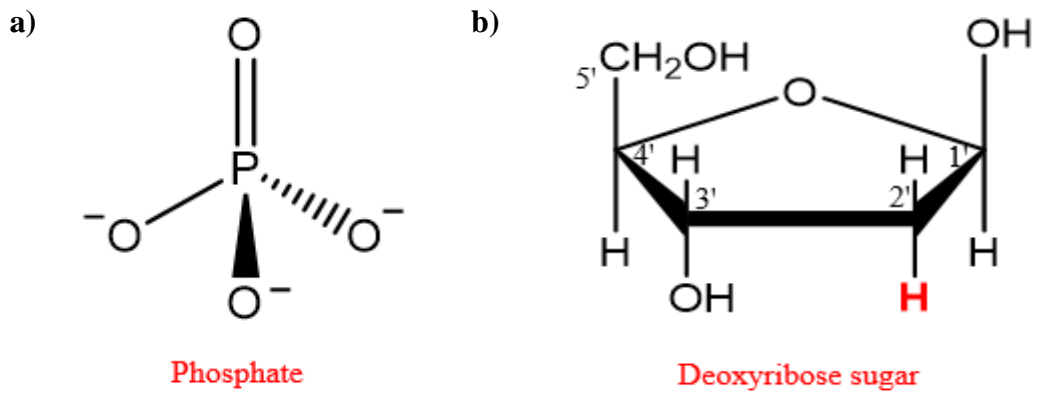


Figure 1.18: Non-nucleobase components of DNA (a) phosphate ion (b) sugar. The red hydrogen atom of DNA replacing the OH (hydroxyl group) of ribonucleic acids (RNA), emphasizing its difference from RNA.

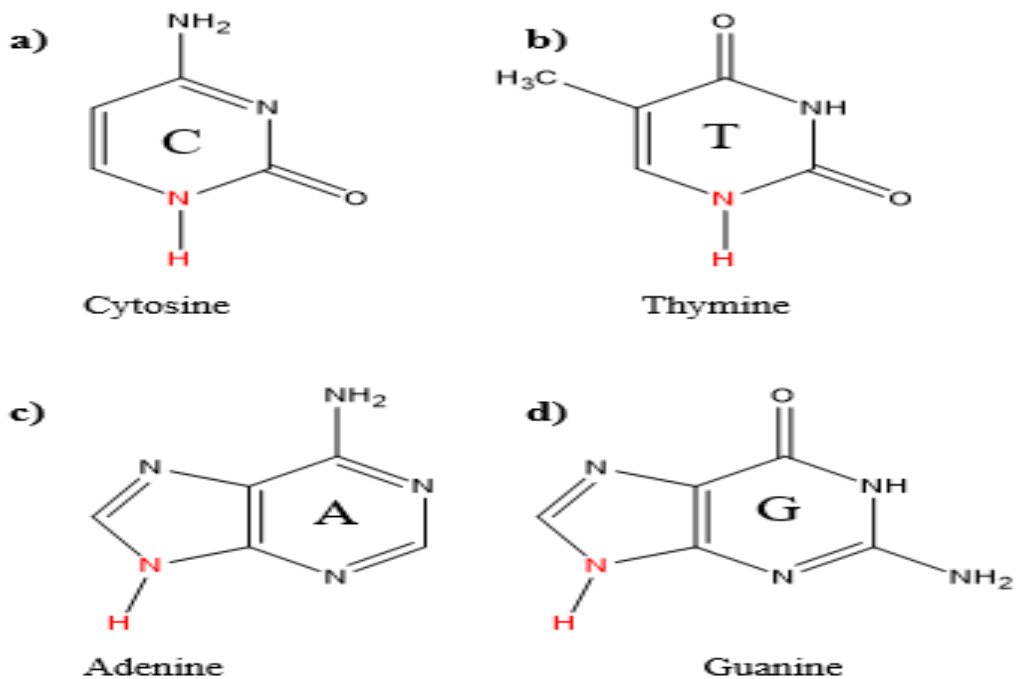


Figure 1.19: DNA nucleobases (a) cytosine (b) thymine (c) adenine (d) guanine. The atoms in red colour represent the bonding site between the nucleobases and the ribose sugar group.

According to their chemical structures, these nitrogenous bases can further be classified into two groups: the first, is a pyrimidine group, and the second is a purine group consisting of a pyrimidine ring combined with an imidazole ring (figure 1.20).

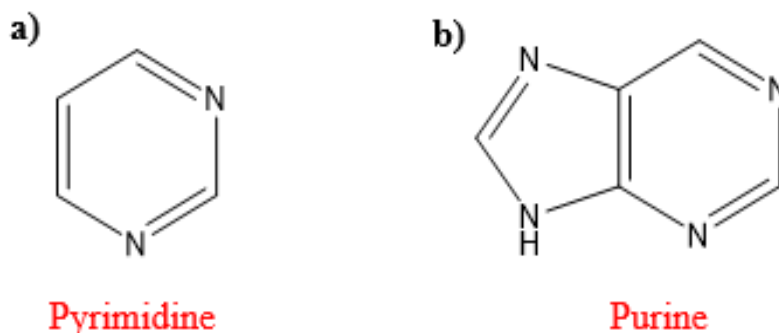


Figure 1.20: (a) pyrimidine (b) purine component ring structure of DNA bases.

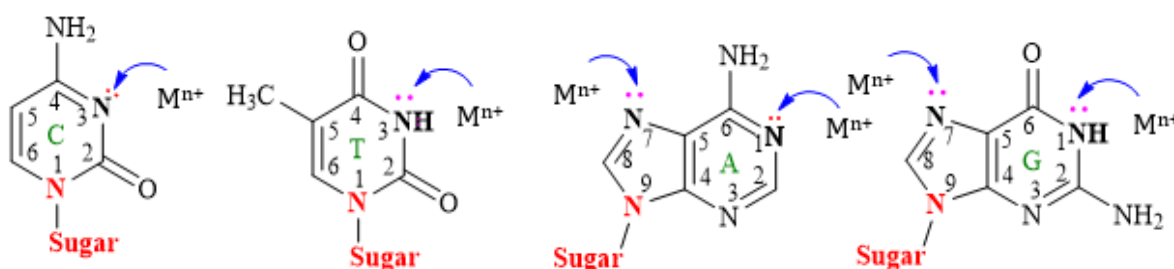


Figure 1.21: Binding sites (pink/red lone pair of electrons) of the four DNA nucleobases showing points of metal ion (electrophilic) attack.^{111,128-140}

The pyrimidine is a single, six-membered ring bearing two nitrogen atoms at the 1 and 3 positions, whereas the purine structure has a five-membered imidazole ring attached to the six-membered pyrimidine ring with a total of four nitrogen atoms at the 1, 3, 7 and 9 positions (figure 1.21).

A DNA nucleobase binds to a ribose sugar molecule (without the phosphate group) to form a nucleoside.^{108,113,114} A combination of the phosphate, ribose sugar, and nucleobase is referred to as a nucleotide.^{108,109,113,115} This forms the monomeric unit of DNA known also as a mononucleotide (figure 1.22 a&b).

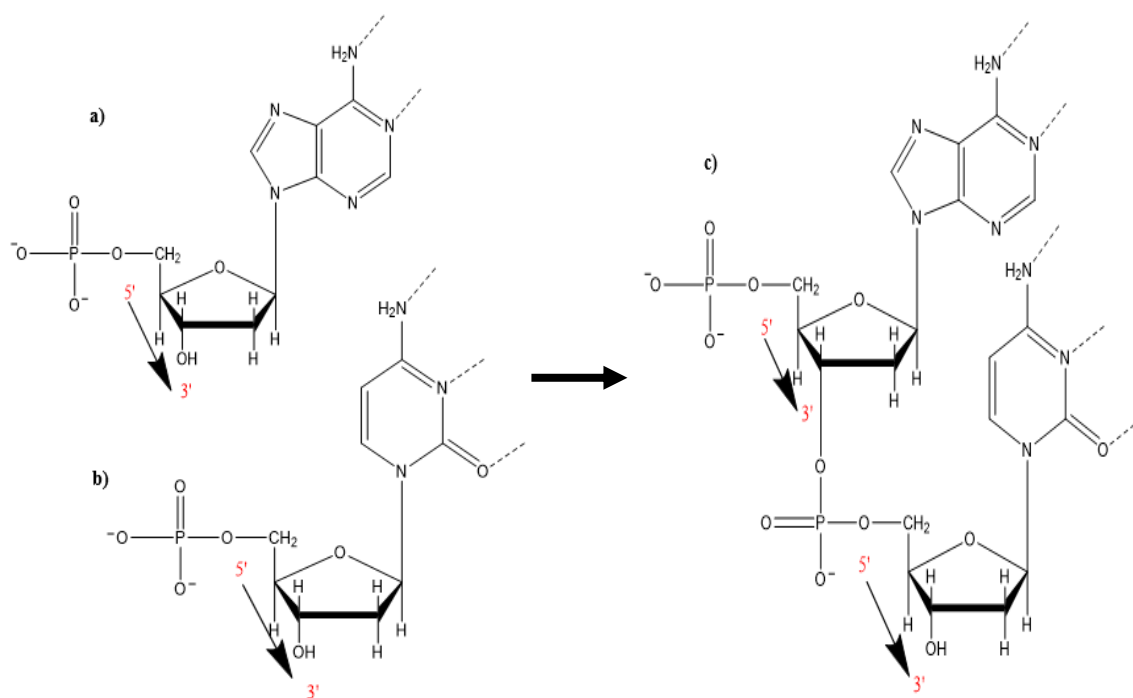


Figure 1.22: DNA mononucleotides (a) adenosine (b) cytidine (c) DNA dinucleotide (two mononucleotides combined via the phosphodiester bond).

Thus, a combination of two mononucleotides containing two different bases involves the linking of a phosphate group of one mononucleotide already bonded to its sugar group at the **C5** position, to another sugar group of the other mononucleotide at the **C3** position to form a dinucleotide. This is a condensation reaction process which leads to the loss of water (H_2O) molecule. In a similar way, DNA trimers, tetramers are formed.¹¹³ This eventually gives the linking pattern now known as the 5'-3' geometry^{112,113,115} in the DNA molecule with net negative charges.

But DNA exists naturally as a duplex molecule containing two intertwined strands in a helical structure.^{108,115} Each individual strand is ordered in exactly the opposite direction of the other to form an antiparallel orientation (reverse 5'-3' and 3'-5') often referred to as the “plus” and “minus” or “direct” and “reverse” forms^{108,113,115} or simply as 3prime to 5prime.¹¹⁶ These antiparallel strands carrying surplus negative ions give DNA its known hydrophilic properties which makes it dissolve readily in polar solvents.^{112,113,115} However, the centre of the molecule comprising the nucleobases is hydrophobic,¹¹⁵ arising from its methyl (CH_3) containing base groups.¹¹³

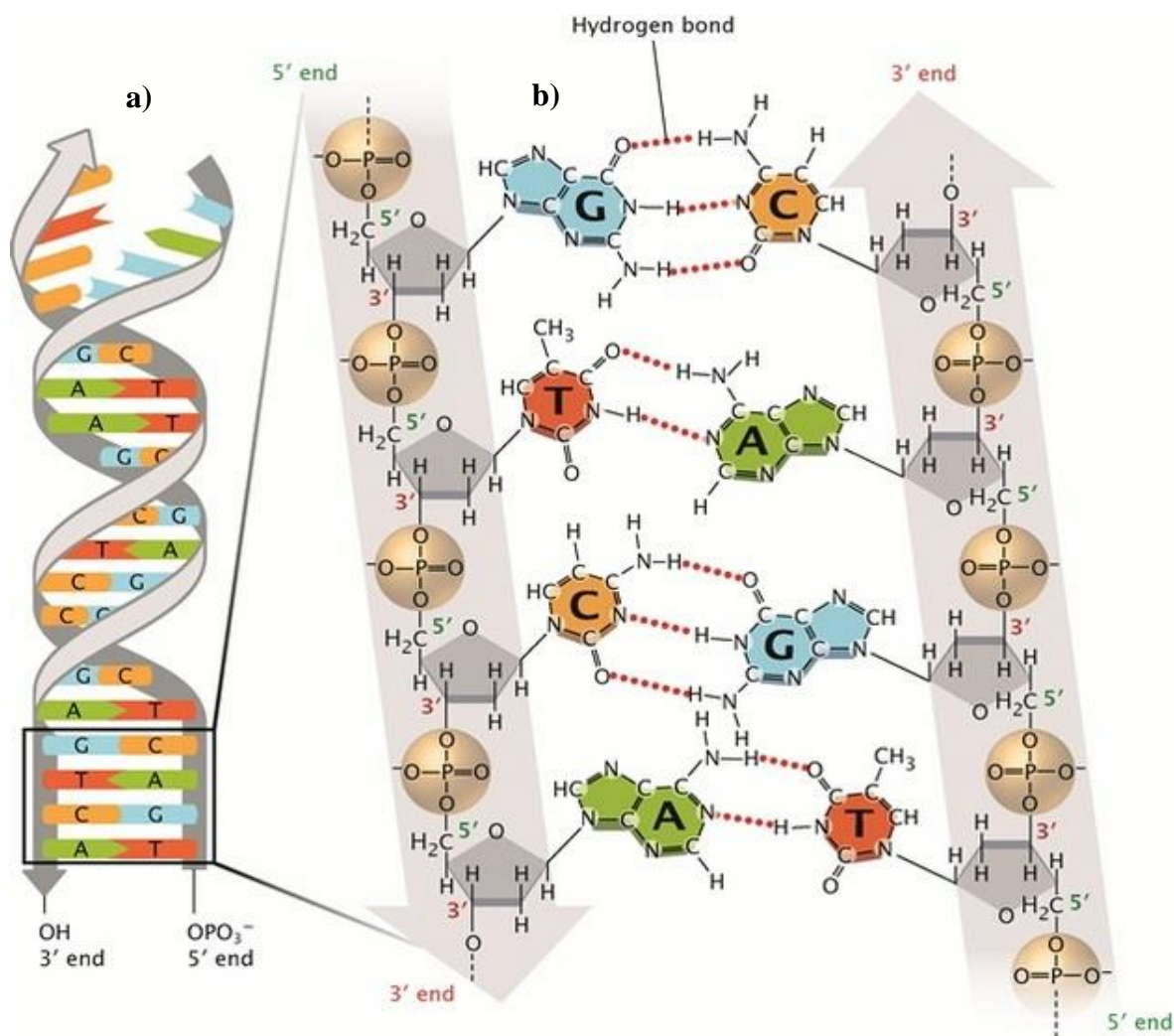


Figure 1.23: DNA polymeric duplex structure showing all detailed component units and bonds.
Source: © 2013 Nature Education: Pray, 2006.¹¹⁷

The resulting duplex (figure 1.23) with a diameter of 20 Å has a pair of complementary (Watson and Crick's) bases: A-T, and C-G respectively, with each base pairs connected by a number of hydrogen bonds.^{113,115} These hydrogen bonds together with base stacking effectively hold the strands together in a DNA duplex.¹¹⁸ Two hydrogen bonds connect the adenine of one strand to thymine of the other complementary strand. Between cytosine of one strand and guanine of the other, there are three hydrogen bond interactions.^{112,113} Each set of base pairs are separated from the other by a space of 3.4 Å (minor groove), with a distance of 34 Å between two major grooves (known as a helical turn) corresponding to a combination of 10 base pairs (i.e., 3.4 Å x 10)¹¹³ in a molecule of 2 nm diameter.¹¹⁵

1.12.2 Forms of DNA

Three basic forms of DNA have been classified, these are the **A**, **B**, and **Z**-forms,^{113,114,115,119} this is because DNA can assume a number of structural forms (figure 1.24).¹¹⁸ The A-form looks closely like the B-form, but is less hydrated (according to X-ray diffraction studies)¹¹⁸ occurring with less than 75 percent humidity since fewer water molecules are bound to the phosphate and sugar hydrophilic groups.¹¹⁸ The A-form of DNA does not exist in living cells.¹¹³ The B-form is the most commonly found DNA duplex which exist in living cells^{113,115} and is much longer than the A-form.¹¹⁸ Third, is the one groove Z-form with the phosphate groups packed more closely together, is formed when DNA temporarily flips from the B-form to the Z-form in vivo during transcription.^{109, 113} The Z-form is also different in having a left-handed duplex helix, with a zig-zag phosphate backbone conformation.^{113,118}

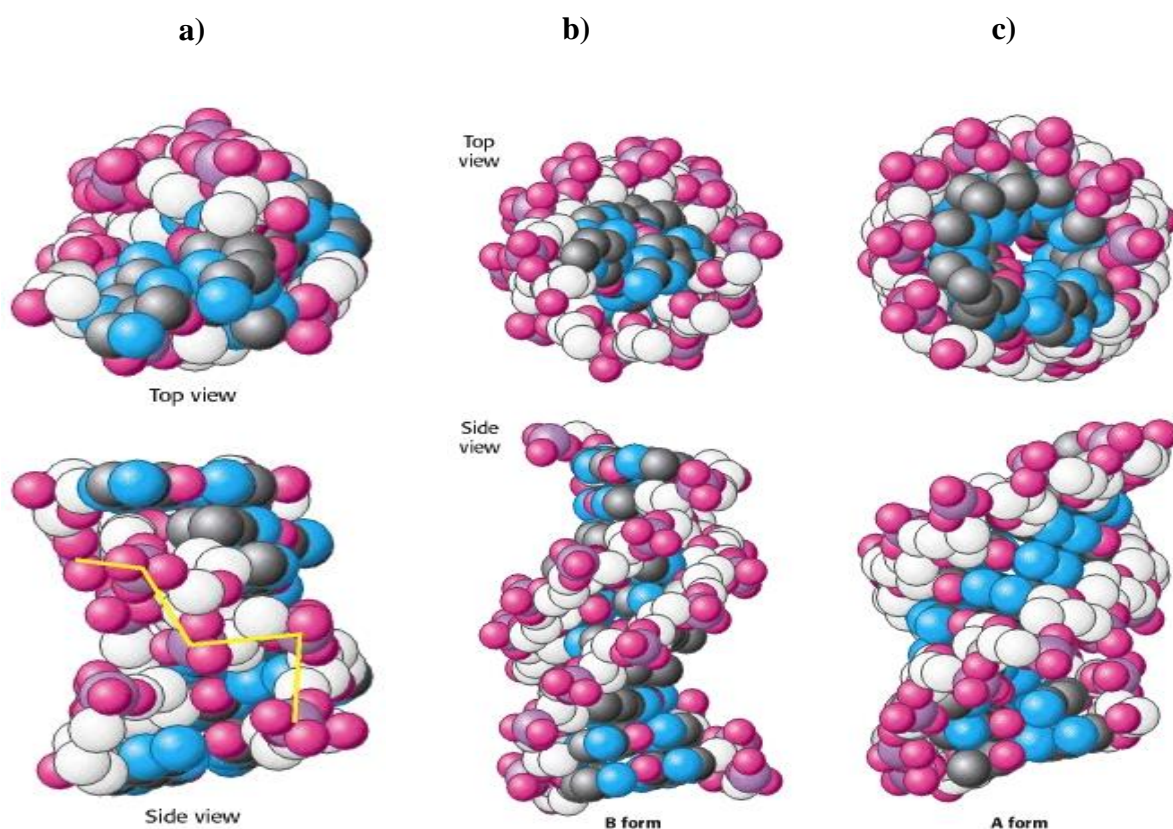


Figure 1.24: (a) Z-form (b) B-form (c) A-form of DNA bases. Source: Berg *et al.*, 2002.¹⁰⁴

Other forms of DNA are the single-stranded, duplex (already discussed), triplex, and quadruplex DNAs each of which contains one, two, three, and four strands accordingly as well as other complex motifs.

1.12.3 Denaturation and renaturation

When duplex DNA is isolated externally from the cell or made synthetically and studied *in vitro*, the component strands can be dissociated by breaking the composing hydrogen bonds between stacked bases and the subsequent destacking of the base pairs. This is known as denaturation or melting which can happen under the conditions of increasing temperature, pressure, pH, and mechanical agitation, the concentration of ions (Na^+ , K^+ , Ca^{2+}) as well as organic solvents like formamide and dimethylsulfoxide.^{113,120,121} When DNA duplex molecule denatures, two separate strands (single-stranded DNAs) are formed, and the strands attain random-coil conformations having lost their “rigid” duplex conformation (figure 1.25a).¹²² This usually leads to a rise in absorbance intensity and a red shift of the absorption peak max.^{113,123}

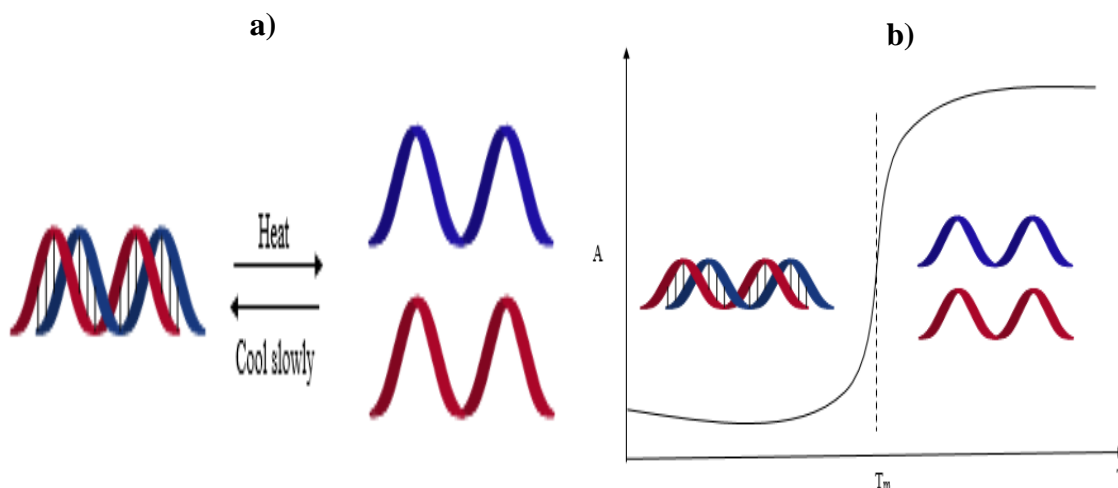


Figure 1.25: (a) DNA melting into component strands. (b) DNA temperature melting curve (T_m is the melting temperature, with approximately 50 % denaturation).

Renaturation occurs when the temperature is reduced (cooling) and the hitherto dissociated single strands recombine to form the duplex in a hybridisation process known as renaturation¹²² at a temperature below the T_m (Figure 1.25b). If the DNA solution is allowed to cool very slowly, then it is possible to obtain the original duplex, otherwise, a new duplex molecule may result.¹²⁰⁻¹²³ This reversible process is essential for DNA transcription, replication, and in polymerase chain reactions.¹²¹⁻¹²³

1.13 Reference

- 1 L. Mulfinger, S. D. Solomon, M. Bahadory, A. V. Jeyarajasingam, S. a. Rutkowsky and C. Boritz, *J. Chem. Educ.*, 2007, **84**, 322–325.
- 2 I. Hussain, Singh, N.B. Singh, A. E., *Biotechnol Lett*, 2016, **38**, 545–560.
- 3 K. Nordlund, *Introduction to Nanoscience*, 2005, 1-24.
- 4 A. Alagarasi, PhD Thesis, Introduction to Nanomaterials, 2006.
- 5 H. Yang, Y. Wang, H. Huang, L. Gell, L. Lehtovaara, S. Malola, H. Häkkinen and N. Zheng, *Nat. Commun.*, 2013, **4**, 1–8.
- 6 S. M. Copp, D. Schultz, S. Swasey, J. Pavlovich, M. Debord, A. Chiu, K. Olsson and E. Gwinn, *J. Phys. Chem. Lett.*, 2014, **5**, 959–963.
- 7 L. A. Peyser, *Science (80-.)*, 2001, **291**, 103–106.
- 8 L. A. Peyser, T. H. Lee and R. M. Dickson, *J. Phys. Chem. B*, 2002, **106**, 7725–7728.
- 9 J. Zheng, P. R. Nicovich and R. M. Dickson, *Annu. Rev. Phys. Chem.*, 2007, **58**, 409–431.
- 10 I. R. Barnes, G. T, and Gentle, *An Introduction to Interfacial Science*, Oxford University Press, 2005.
- 11 K. Jensen, *Projekter.Aau.Dk*, 2009.
- 12 B. Akbari, M. P. Tavandashti and M. Zandrahimi, *Iran. J. Mater. Sci. Eng.*, 2011, **8**, 48–56.
- 13 B. G. Ershov, *Russ. Chem. Bull.*, 1999, **48**, 1–15.
- 14 I. Díez and R. H. A. Ras, *Nanoscale*, 2011, **3**, 1963.

- 15 R. Fournier, *J. Chem. Phys.*, 2001, **115**, 2165–2177.
- 16 L. del Valle Carrandi, *Slides*, 2008, 1-20.
- 17 E. G. Gwinn, P. O'Neill, A. J. Guerrero, D. Bouwmeester and D. K. Fygenson, *Adv. Mater.*, 2008, **20**, 279–283.
- 18 M. P. Lisiecki, I Pileni, *J. Am. Chem. Soc.*, 1993, **115**, 3837–3896.
- 19 G. H. Woehrle, L. O. Brown and J. E. Hutchison, *J. Am. Chem. Soc.*, 2005, **127**, 2172–2183.
- 20 B.-C. Ye, Bang-Ce, Zhang, Min, Yin, *Nano-Bio Probe Design and Its Application for Biochemical Analysis*, SpringerBriefs in Molecular Science, 2012, 1-938.
- 21 R. A. Salkar, P. Jeevanandam, S. T. Aruna, Y. Koltypin and A. Gedanken, *J. Mater. Chem.*, 1999, **9**, 1333–1335.
- 22 T. Sun and K. Seff, *Chem. Rev.*, 1994, **94**, 857–870.
- 23 H. Wei, D. Ratchford, X. E. Li, H. Xu and C.-K. Shih, *Nano Lett.*, 2009, **9**, 4168–4171.
- 24 I. Nabiev, A. Baranov, I. Chourpa, a Beljebbar, G. D. Sockalingum and M. Manfait, *J. Phys. Chem.*, 1995, **99**, 1608–1613.
- 25 J. M. Gorham, R. I. MacCuspie, K. L. Klein, D. H. Fairbrother and D. Holbrook, *J. Nanoparticle Res.*, 2012, **14**, 1-16.
- 26 S. Noordeen, K. Karthikeyan and M. A. N. Parveen, *Int. J. Eng. Res. Technol.*, 2013, **2**, 388–397.
- 27 A. M. Angulo and C. Noguez, *J. Phys. Chem. A*, 2008, **112**, 5834–8.
- 28 J. Sharma, R. C. Rocha, M. L. Phipps, H.-C. Yeh, K. A. Balatsky, D. M. Vu, A. P. Shreve, J. H. Werner and J. S. Martinez, *Nanoscale*, 2012, **4**, 4107–10.

- 29 A. Latorre, R. Lorca, F. Zamora and Á. Somoza, *Chem. Commun. (Camb)*., 2013, **49**, 4950–2.
- 30 J. Xie, Y. Zheng and J. Y. Ying, *J. Am. Chem. Soc.*, 2009, **131**, 888–889.
- 31 W. Y. Chen, G. Y. Lan and H. T. Chang, *Anal. Chem.*, 2011, **83**, 9450–9455.
- 32 Z. Dilli, in *ENEE*, 2008, pp. 1–8.
- 33 F. Bertorelle, R. Hamouda, D. Rayane, M. Broyer, R. Antoine, P. Dugourd, L. Gell, A. Kulesza, R. Mitric and V. Bonacic-Koutecky, *Nanoscale*, 2013, **5**, 5637–5643.
- 34 N. C. Anderson, *the Surface Chemistry of Metal Chalcogenide Nanocrystals*, PhD Thesis, 2014, University of Cumbria, USA.
- 35 H. Xu and K. S. Suslick, *Adv. Mater.*, 2010, **22**, 1078–1082.
- 36 T. Udayabhaskararao, M. S. Bootharaju and T. Pradeep, *Nanoscale*, 2013, **5**, 9404–11.
- 37 Y. Sun and K. Balasubramanian, *J. Phys. Chem. C*, 2011, **7**, 20380–20387.
- 38 Y. Negishi, N. K. Chaki, Y. Shichibu, R. L. Whetten and T. Tsukuda, *J. Am. Chem. Soc.*, 2007, **129**, 11322–11323.
- 39 K. Xavier, P. L., Chaudhari, A. Baksi and T. Pradeep, *Nano Rev.*, 2012, **3**, 1–16.
- 40 K. Chaudhari, P. L. Xavier and T. Pradeep, *ACS Nano*, 2011, **5**, 8816–8827.
- 41 S. Kumar, M. D. Bolan and T. P. Bigioni, *J. Am. Chem. Soc.*, 2010, **132**, 13141–13143.
- 42 L. D. Menard, S. P. Gao, H. Xu, R. D. Twisten, A. S. Harper, Y. Song, G. Wang, A. D. Douglas, J. C. Yang, A. I. Frenkel, R. G. Nuzzo and R. W. Murray, *J. Phys. Chem. B*, 2006, **110**, 12874–12883.
- 43 I. Chakraborty, T. Udayabhaskararao and T. Pradeep, *Chem. Commun.*, 2012, **48**, 6788.

- 44 I. Díez, M. Pusa, S. Kulmala, H. Jiang, A. Walther, A. S. Goldmann, A. H. E. Müller, O. Ikkala and R. H. A. Ras, *Angew. Chemie - Int. Ed.*, 2009, **48**, 2122–2125.
- 45 L. E. Brus, *J. Chem. Phys.*, 1984, **80**, 4403.
- 46 E. Schrödinger, *Phys. Rev.*, 1926, **28**, 1049.
- 47 T. Pusey, M. F., Barrett, J. & Rudolph, *Nat. Phys.*, 2012, **8**, 475–478.
- 48 Z. Merali, *Nature*, 2015, **521**, 278–280.
- 49 M. L. H. Green, *J. Organomet. Chem.*, 1995, **500**, 127–148.
- 50 E. A. Knowles, K. E., Tice, D. B., McArthur, E. A., Solomon, G. C., Weiss, *J. Am. Chem. Soc.*, 2009, **132**, 1041–1050.
- 51 J. G. Kamat, Prashant V., Tvrdy, Kevin., Baker, David R., and Radich, *Chem. Rev.*, 2010, **110**, 6664–6688.
- 52 A. Koole, R., Liljeroth, P., de Mello Donegá, C., Vanmaekelbergh, D., Meijerink, *J. Am. Chem. Soc.*, 2006, **128**, 10436–10441.
- 53 R. Wu, Z., and Jin, *Nano Lett.*, 2010, **10**, 2568–2573.
- 54 D. Schmid, G., and Fenske, *Phil. Trans. R. Soc.*, 2010, **368**, 1207–1210.
- 55 E. Schmickler, W., and Santos, *Interfacial Electrochemistry*, Springer-Verlag, Heidelberg, 2010, 1-267.
- 56 F. H. Cardona, M. and Pollack, *Phys. Rev.*, 1966, **142**, 530.
- 57 M. R. A. Shegelski, *Solid State Commun.*, 1986, **58**, 351–354.
- 58 C. Kittel, *Introduction to Solid State Physics*, 7th edn., 1996.
- 59 M. G. Warner and J. E. Hutchison, *Nat. Mater.*, 2003, **2**, 272–277.

- 60 W. Song, C. Lau and J. Lu, *Analyst*, 2012, **137**, 1611.
- 61 R. J. Albani, *Principles and Applications of Fluorescence Spectroscopy*, Blackwell Publishing, Oxford, 2007, 1-27.
- 62 X. Yuan, M. I. Setyawati, A. S. Tan, C. N. Ong, D. T. Leong and J. Xie, *NPG Asia Mater.*, 2013, **5**, 39.
- 63 Perkin Elmer, *Microchem. J.*, 2000, **65**, 353.
- 64 R. J. Albani, *Structure and Dynamics of Macromolecules: Absorption and Fluorescence Studies*, Elsevier Science, First Edit., 2004.
- 65 J. R. Lakowicz and B. R. Masters, *J. Biomed. Opt.*, 2008, **13**, 29901.
- 66 G. G. Guilbault, *Practical Fluorescence*, Marcel Dekker, New York, Second Edi., 1990, 826.
- 67 A. Mehta, *Pharmchange.Info*, 2011, online webpage.
- 68 A. Ahlbom and M. Feychting, *Br. Med. Bull.*, 2003, **68**, 157–165.
- 69 Cyberphysics, *Cyberphysics.com*, 2017.
- 70 D. R. Lide, *eBook*, 2003, 3485.
- 71 M. P. Little, *Br. Med. Bull.*, 2003, **68**, 259–275.
- 72 E. M. Thomas, *Optical propagation in linear media : atmospheric gases and particles, solid state components, and water*, 2006.
- 73 E. S. Gilbert, *Int. J. Radiat. Biol.*, 2009, **85**, 467–482.
- 74 D. H. Staelin, A. ~W. Morgenthaler and J. A. Kong, *Electromagnetic Waves*, InTech, First., 1994.

- 75 J. L. Tucker, J.D., Ramsey, M.J. Lee, D.A. Minkler, *Int J Radiat Biol.*, 1993, **64**, 27–37.
- 76 J. R. Tucker, J.D. Senft, *Radiat Res.*, 1994, **140**, 31–36.
- 77 T. Matsuoka, A., Tucker, J.D. Hayashi, M. Yamazaki, N. Sofuni, *Mutagenesis.*, 1994, **9**, 151–155.
- 78 J. D. Spruill, M.D. Nelson, D.O. Ramsey, M.J. Nath, J. Tucker, *Radiat Res.*, 2000, **153**, 110–121.
- 79 C. R. Johnson, K.L. Brenner, D.J. Nath, J. Tucker, J.D. Geard, *Biol., Int J Radiat*, 1999, **75**, 131–141.
- 80 J. D. Johnson, K.L. Brenner, D.J. Geard, C.R. Nath, J., Tucker, *Radiat Res.*, 1999, **152**, 1–5.
- 81 L. Foist, Emulsion: Definition & Examples *Study.com*, 2017.
- 82 V. Preziosi, A. Perazzo, S. Caserta, G. Tomaiuolo and S. Guido, *Chem. Eng. Trans.*, 2013, **32**, 1585–1590.
- 83 R. Hiemenz, P. C. and Rajagopalan, *Principles of Colloid and Surface Chemistry*, Marcel Dekker, New York, 3rd Editio., 1997.
- 84 D. Bucak, S. and Rende, *Colloid and Surface Chemistry: A laboratory guide for exploration of the nano world*, CRC Press, Taylor & Francis Group, Boca Raton, 1st edn., 2014.
- 85 A. Pietrini, Biochemical reactions in Micro and Nanocompartments, PhD Thesis, *Swiss Federal Institute of Technology, Zurich*, 2003.
- 86 K. Edler, *PetroWiki OnePetro, Soc. Pet. Eng.*, 2015, 1–17.
- 87 R. Pichot, Stability and Characterisation of Emulsions in the presence of Colloidal

- Particles and Surfactants PhD *Thesis*, 2010, 1–219.
- 88 A. R. Taherian, P. Fustier and H. S. Ramaswamy, *J. Food Eng.*, 2006, **77**, 687–696.
- 89 P. G. De Gennes and C. Taupin, *J. Phys. Chem.*, 1982, **86**, 2294–2304.
- 90 J. P. Clarks, *Food Technol.*, 2013, **67**.
- 91 G. A. Volkov, *Liquid Interfaces In Chemical, Biological And Pharmaceutical Applications: Surfactant Science.*, CRC Press, 2001.
- 92 K. Lu, *Ceram. Int.*, 2008, **34**, 1353–1360.
- 93 W. C. Griffin, *J. Soc. Cosmet. Chem.*, 1984, **5**, 249–256.
- 94 S. U. Pickering, *J. Chem. Soc. Trans.*, 1907, **91**, 2001–2021.
- 95 D. G. Haase, M. F., D. Grigoriev, H. Moehwald, B. Tiersch, and Shchukin, *J. Phys. Chem. C*, 2010, **114**, 17304–17310.
- 96 D. G. Haase, M. F., D. Grigoriev, H. Moehwald, B. Tiersch, and Shchukin, *Langmuir*, 2010, **27**, 2010b.
- 97 J. Eastoe, *Surfactant Chemistry*, 2003, 1-134.
- 98 J. Eastoe, M. J. Hollamby and L. Hudson, *Adv. Colloid Interface Sci.*, 2006, **128–130**, 5–15.
- 99 J. T. G. Overbeek, *Faraday Discuss. Chem. Soc.*, 1978, **65**, 7–19.
- 100 B. Tadros, Th. F. Vincent, *Encycl. Emuls. Technol.*, 1980, 1, 281.
- 101 H. K. Shinoda, *J. Colloid Interface Sci.*, 1980, **75**, 601–606.
- 102 S. J. Chen, D. F. Evans and B. W. Ninham, *J. Phys. Chem.*, 1984, **88**, 1631–1634.

- 103 G. Kahlweit, M. Strey, R. Busse, *J. Phys. Chem.*, 1990, **94**, 3881–3894.
- 104 V. T. Liveri, *Controlled Synthesis of Nanoparticles in Microheterogeneous Systems.*, 2006, vol. 45, 6949-6950.
- 105 R. J. Hunter, *Foundations Of Colloid Science.*, Oxford University Press, United Kingdom, 1993.
- 106 C. Tanford, *The Hydrophobic Effect: Formation of Micelles and Biological Membranes.*, John Wiley & Sons, New York, 1973.
- 107 P. L. Walde, P. Giuliani, A. M. Boicelli, C. A. Luisi, *Chem. Phys. of Lipids*, 1990, **53**, 265–288.
- 108 C. F. A. Bryce and D. Pacini, *Biochem. Soc.*, 1998, 1–70.
- 109 S. G. Davenport, *Anatomy and Physiology Text and Laboratory Workbook*, Link Publishing, 2006.
- 110 R. V. Prigodich, J. Casas-finet, K. R. Williams, W. Konigsberg and J. E. Coleman, *Biochemistry*, 1984, **23**, 522–529.
- 111 K. Lavaee, Parirokh., Eshtiagh-Hosseini, Hossein., HousaindokhtJoel, Mohammad Reza., Mague, J. T., Esmaeili, Abbas Ali., Abnous, *J. Fluoresc.*, 2016, **26**, 333–344.
- 112 D. Swigon, *Mathematics of DNA Structure, Function and Interactions*, Benham, C., 2009, vol. 150.
- 113 J. L. Huret, DNA: molecular structure. *Atlas Genet Cytogenet Oncol Haematol*. September 2006, **1**, 112–123.
- 114 D. R. Kearns, *CRC Crit Rev Biochem*, 1984, **15**, 237–290.
- 115 C. R. Calladine, H. R. Drew, B. F. Luisi and A. A. Travers, *Understanding DNA: The Molecule and How it Works: Third Edition*, 2004.

- 116 J. Clark, *DNA Structure*, 2007, Chemguide.co.uk
- 117 L. A. Pray, Discovery of DNA structure and function: Watson and Crick. *Nature Education*, 2008, 1(1):100.
- 118 L. Berg, J.M., Tymoczko, J. L., Stryer, *Biochemistry*, W H Freeman, New York, Fifth Edit., 2002.
- 119 S. K. Pal, L. Zhao and A. H. Zewail, *Proc. Natl. Acad. Sci. U. S. A.*, 2003, **100**, 8113–8118.
- 120 G. Liu, Y. Shao, F. Wu, S. Xu, J. Peng and L. Liu, *Nanotechnology*, 2013, **24**, 15503.
- 121 F. Liu, E. Tøstesen, J. K. Sundet, T. K. Jenssen, C. Bock, G. I. Jerstad, W. G. Thilly and E. Hovig, *PLoS Comput. Biol.*, 2007, **3**, 0874–0886.
- 122 N. Sturm, *Nucleotides: Composition and Structure*, 2014, Chemistry.gravitywaves.com.
- 123 G. Khandelwal and J. Bhyravabhotla, *PLoS One*, 2010, **5**, 1–9.
- 124 S. Aldrich, *Azonano.com*, 2017.
- 125 R. H. A. Díez, Isabel Ras, in *Advanced Fluorescence Reporters in Chemistry and Biology II*, ed. A. P. Demchenko, 10.1007/978-3-642-04701-5, Springer, Berlin, Heidelberg, Second., 2010, pp. 307–332.
- 126 Gcsescience.com, Product from oil, 2015.
- 127 D. Avitabile, Gustavo. Caruso, Ugo. Maglio, Giovanni. Merlino, Antonello. Picone, *Univ. 'Federico II' Naples, Italy Dep. Chem. Eur. Chem. Themat. Network*.
- 128 S. M. Swasey, L. E. Leal, O. Lopez-Acevedo, J. Pavlovich and E. G. Gwinn, *Sci. Rep.*, 2015, 5:10163.

- 129 P. R. O'Neill, L. R. Velazquez, D. G. Dunn, E. G. Gwinn and D. K. Fygenson, *J. Phys. Chem. C*, 2009, **113**, 4229–4233.
- 130 D. W. Gibson, M. Beer and R. J. Barnett, *Biochemistry*, 1971, **10**, 3669–3679.
- 131 B. Lippert, *Coord. Chem. Rev.*, 2000, **200–202**, 487–516.
- 132 N. Santamaría-Díaz, J. M. Méndez-Arriaga, J. M. Salas and M. A. Galindo, *Angew. Chemie - Int. Ed.*, 2016, 6170–6174.
- 133 S. Dai, X. Zhang, T. Li, Z. Du and H. Dang, *Appl. Surf. Sci.*, 2005, **249**, 346–353.
- 134 C. M. Ritchie, K. R. Johnsen, J. R. Kiser, Y. Antoku, R. M. Dickson and J. T. Petty, *J. Phys. Chem. C*, 2007, **111**, 175–181.
- 135 T. Vosch, Y. Antoku, J.-C. Hsiang, C. I. Richards, J. I. Gonzalez and R. M. Dickson, *Proc. Natl. Acad. Sci. U. S. A.*, 2007, **104**, 12616–21.
- 136 R. M. Richards, C.I. Choi, S. Hsiang, J.C. Antoku, Y. Vosch, T. Bongiorno, A. Tzeng, Y.L. Dickson, *J Am Chem Soc.*, 2008, **130**, 5038–9.
- 137 J. T. Sengupta, B. Ritchie, C. M. Buckman, J. G. Johnsen, K. R. Goodwin, P. M. Petty, *J. Phys. Chem. C*, 2008, **112**, 18776–18782.
- 138 R. M. Patel, S. A. Richards, C. I. Hsiang, J.-C. Dickson, *J. Am. Chem. Soc.*, 2008, **130**, 11602–11603.
- 139 V. Soto-Verdugo, H. Metiu and E. Gwinn, *J. Chem. Phys.*, 2010, **132**.
- 140 G. L. Eichhorn, *Inorganic Chemistry*, Elsevier, 1973.

2 CHAPTER TWO

2.1 EXPERIMENTAL

2.2 Introduction

This chapter provides experimental details, the various types of chemical reagents used throughout the course of this project, together with details of the companies from which they were bought, and their individual state of purity prior to their use for experiments. It includes also the different instrumental tools of analysis, their respective manufacturers, and the specific operational settings under which they were used. Furthermore, the specific experiments and experimental conditions which were undertaken in the course of this exercise, and the subsequent methods of characterization employed are all carefully and systematically reported. Finally, the theoretical principles guiding some of the instrumental tools for analyses are also explained.

2.3 Materials

2.1.1 Silver nitrate (AgNO_3 , 99 %) (D1685-100G) was bought from Sigma-Aldrich, USA. Sodium borohydride (NaBH_4 , 99 %) (213462-25G) also from Sigma-Aldrich, USA. Sodium bis (2-ethyl hexyl) sulfosuccinate (AOT) ($\text{C}_{20}\text{H}_{37}\text{NaO}_7\text{S}$) (D1685-100G) bought from Sigma-Aldrich, USA. 2, 2, 4-trimethylpentane (Isooctane, 99.8 %) (360066-1L) a product of Sigma-Aldrich, Germany. Oligonucleotides (**DNA1**, 22-mer: 5'-TGACTAAAAACCCTTAATCCCC-3'; **DNA2**, 29-mer: 5'-AGTCACCCCAACCTGCCCTACCACGGACT-3'; **DNA3**, 34-mer: 5'-GGCAGGTTGGGGTGACTAAAAACCCTTAATCCCC-3') all products of Eurofins Genomics, Ebersberg, Germany. Copper nitrate trihydrate ($\text{Cu}(\text{NO}_3)_2 \cdot 3\text{H}_2\text{O}$, 98 %) product of Fluka Chemika, United Kingdom. Calf thymus DNA (Type 1, highly polymerized) (D1501-

1G), a product of Sigma-Aldrich, USA. Deuterium oxide (D₂O 99.96 %), Sigma-Aldrich, a product of USA. Adenosine 5'-monophosphate disodium salt ($\geq 99\%$), guanosine 5'-monophosphate disodium salt hydrate ($\geq 99\%$), cytidine 5'-monophosphate disodium salt ($\geq 99\%$), thymidine 5'-monophosphate disodium salt hydrate ($\geq 99\%$); nucleotides all products of Sigma-Aldrich. Agarose was bought from Melford Biolaboratories Ltd., Ipswich, UK. 1 kilobase+ DNA ladders were purchased from Thermo Scientific. All chemicals were used as purchased without further treatment. Nanopure water obtained from, Millipore Diamond Barnstead series 1370, model D11931, operated at 100-240V, with a resistivity of 18.2 M Ω -cm. HC330Cu, Holey carbon film on 300 mesh copper, a product of EM Resolutions limited Essex, United Kingdom. P-type silicon (111) wafer from Virginia Semiconductors, Virginia, USA. Resprep SPE (solid phase extraction) cartridges (see Appendix fig. 8.2) by Thames Restek, Pennsylvania, USA, with a bonded reverse phase hydrophobic silica-based adsorbent for extracting non-polar materials from polar matrices.¹ It has a tube size of 1 mL, C18 (high load, endcapped), with a bed weight of 100 mg. 500 μ L Hellma micro-quartz cuvette with all four clear sides (path length - 10 mm).²

2.4 Instrumentations

2.4.1 Ultraviolet-Visible Spectrophotometer (UV-Vis spectrophotometer):

UV-Vis absorption spectra of the Ag NCs were obtained using Varian Cary 100 Bio spectrophotometer with a tungsten halogen visible source, and a deuterium arc ultraviolet lamp. The detector was an R928 (PMT) photomultiplier detector, the maximum scan range was 190 – 900 nm, using a 500 μ L quartz microcuvette (Hellma UK Ltd).

2.4.2 Fluorescence Spectrophotometer:

Fluorescence emission and excitation spectra were recorded with a SPEX FluoroMaxTM spectrofluorimeter instrument, New Jersey, USA. The excitation source was an ozone-free xenon lamp. A photomultiplier served as emission detector and there was also a photodiode reference detector. The emission/excitation range was 200-950 nm in wavelength and optimized in the ultraviolet and visible regions.

2.4.3 Confocal microscopy:

The fluorescence microscope images were obtained using ZEISS Axioskop2 plus model instrument with 100 W halogen lamp for transmitted light and 50 W HBO mercury short-arc lamp reflected fluorescence light source, with a power supply rated at 100 – 240 V.

2.4.4 Dynamic Light Scattering (DLS):

Particle size measurements were obtained using a Malvern high-performance particle-sizer (HPPS) incorporating non-invasive backscatter technology (NIBS) technology dynamic light scattering instrument. The laser was He-Ne device, 3.0mW, wavelength of 633nm, and an avalanche photodiode served as the detector. The instrument was equipped with a silicon photodiode laser monitor, and a thermo-electric Peltier heater/cooler element. The instrument runs on 90 – 240 V power supply.

2.4.5 Atomic Force Microscopy (AFM):

AFM images were by Bruker MultiMode 8 High-Performance AFM instrument, with High-Speed ScanAsyst operated at peak force tapping mode using NanoProbe tips (Veeco Inc.). Data obtained were analyzed using Gwyddion 2.41 software.

2.4.6 Transmission Electron Microscopy (TEM):

The Philips CM 100 transmission electron microscope with 40 – 100 kV tungsten filament, with a single-tilt goniometer stage, a compusstage, and high-resolution digital image capture. Data obtained were further processed by ImageJ software (NIH, Maryland, USA).

2.4.7 Electrospray Ionisation Mass Spectrometry (ESI-MS):

A Waters LCT Premier Electrospray ionization mass spectrometer with Masslynx™ 4.1 software was used. The instrument has a time of flight (TOF) analyzer and a microchannel plate (MCP) detector. A mains power supply of 100/240 V runs the instrument, and *leucine enkephalin* is the reference sample. The University of Manchester, United Kingdom, mass spectrometer software tool: <http://fluorine.ch.man.ac.uk/research/mstool2.php> was used for data analysis and simulations of spectra.

2.4.8 X-ray Photoelectron Spectroscopy (XPS):

X-ray photoelectron spectroscopy data of the samples were taken on a Kratos AXIS Nova instrument (Kratos Analytical), Manchester, United Kingdom at the NEXUS facility, Newcastle University, UK. It has an aluminum $K\alpha$ ($AlK\alpha$) monochromatic x-ray source, with an x-ray energy of 1486.6 eV and a delay-line detector (DLD) comprising of multichannel plates above two delay-line orthogonal plates in association with electronic control units. It runs at a source voltage/current/power rating of 15 kV/15 mA/225 W. CasaXPS software (casaxps.com) was used to process and analyze the data.

2.4.9 Infrared Spectroscopy:

Infrared spectroscopy data were taken using an IRAffinity – 1S Fourier Transform Infrared Spectroscopy, Shimadzu Corporation, Japan. 220/230/240 V~ 50/60 Hz, 150 VA power specification with LabSolutions IR series software. It has a high-energy ceramic light source, a He-Ne laser for the interferometer, and a DLATGS (Deuterated Lanthanum α -Alanine doped TriGlycine Sulphate) detector with temperature control mechanism.

2.4.10 Nuclear magnetic resonance (NMR):

The spectrometers used were a Bruker 500 and 700 MHz Avance III HD with 11.7 Tesla spectrometer for the 500 MHz, an auto-sampler, with 5 and 10 mm probes range for virtually all active NMR nuclei; and the 16.4 Tesla spectrometer, with triple resonance nitrogen-cooled TCI Prodigy cryoprobe covering the 1H , ^{13}C , ^{15}N , and ^{19}F nuclei for the 700 MHz instrument.³ Chemical shifts are reported in ppm referenced to TMS (trimethylsilane) for the 1H spectra acquired on the 700 MHz instrument, run with suppression of the H_2O frequency, with $dl = 2s$ and a 90-degree pulse angle, at a sweep width of 16 ppm and offset of 4.7 ppm. While the ^{31}P spectra were obtained from the 500 MHz instrument operating at 202.46 MHz with an external reference of 85 % phosphoric acid (H_3PO_4). An HMBC (heteronuclear multiple bond correlation) pulse sequence with optimization of $J = 8$ Hz was used for the ^{31}P - 1H correlation experiments.

2.4.11 Rayonet Photochemical Reactors:

The photoreaction experiments were done in the Rayonet ultraviolet photoreactor by The South New England Ultraviolet Company, Connecticut, USA. It has an A.C power source of 120 V, 50/60 Hz, and a mercury source light with major emission wavelength of 254 nm.

2.4.12 EmStat³ Electrochemical Interface:

Cyclic voltammetry data were taken with PSTrace 4.7 software using EmStat³ interphase by PalmSens BV, Electrochemical Sensor Interfaces, Netherlands.

2.4.13 Electrophoresis:

Electrophoresis analysis was done in BIO-RAD wide mini-sub cell GT gel box, powered by Hoefer Mighty Slim SX 250 system, with an output of 250 V, 200 mA, a product of Hoefer Pharmacia Biotech Inc. CA, USA. Images were obtained using UVITEC UVI-UV.BOX/1 model comprising transilluminator and 1.4-megapixel scientific grade CCD camera with SONY chip, and an emission filter for use with ethidium bromide (EtBr) and other fluorophores that emit in the 590 nm range; with UVIpromW advanced image analysis software (UVIpromW version 11.02 for windows, © 1999 - 2003).

2.5 Synthesis of silver (I) complex with ssDNA1 (22-mer) and reduction with sodium borohydride.

0.5 mL 90 μ M aqueous AgNO₃ solution was added to another 0.5 mL aqueous 15 μ M ssDNA1 and mixed by vortexing for 2 minutes then kept in the dark for 20 - 30 minutes. It was reduced afterward with 0.5 mL equimolar (90 μ M) aqueous NaBH₄ solution, shaken vigorously and then stored at room temperature in the dark for 24 hours.⁴

2.5.1 Absorbance and fluorescence determinations

40 μ L of the synthesized Ag/ssDNA1 complex was pipetted into a 500 μ L micro-quartz cuvette and made up to the “meniscus” with nanopure water for optical measurements.

2.6 Synthesis of silver (I) complex with ssDNA2 (29-mer) and reduction with sodium borohydride.

To an aqueous solution of 0.5 mL (15 μ M) ssDNA2 in a glass vial, 90 μ M (0.5 mL) aqueous AgNO₃ solution was added and mixed for two minutes, then stored in the dark for another 20 minutes, before being reduced by equimolar 0.5 μ L aqueous solutions of NaBH₄. The resulting solution was mixed for two minutes and then stored in the dark for 24 hours.

2.6.1 Absorbance and fluorescence measurements

40 μL of the synthesized Ag/ssDNA2 complex was pipetted into a 500 μL micro-quartz cuvette and made up to the mark with nanopure water for optical measurements.

2.7 Synthesis of silver (1) complex with ssDNA3 (34-mer) and reduction with sodium borohydride.

15 μM (0.5 mL) aqueous ssDNA3 and 0.5 mL 90 μM aqueous AgNO_3 solutions mixed by vortexing for 2 minutes and kept in the dark for 30 minutes before being reduced afterwards by 0.5 mL equimolar (90 μM) aqueous NaBH_4 solution; shaken vigorously and then stored at room temperature in the dark for 24 hours.

2.7.1 Absorbance and fluorescence measurements

Absorbance and fluorescence measurements were taken as explained in preceding sections above.

2.8 Synthesis of silver nanoclusters in microemulsion

90 μM Ag NCs

0.2223 g AOT was dissolved in 5 mL isooctane in a clean 50 mL beaker by sonication and the resulting solution shared into two equal portions in separate 15 mL clean glass vials. Then 90 μM equivalent 45 μL aqueous solutions of AgNO_3 and NaBH_4 were each prepared and poured into either of the two AOT/isooctane solutions to form two $\text{AgNO}_3/\text{AOT}/\text{isooctane}$ and $\text{NaBH}_4/\text{AOT}/\text{isooctane}$ microemulsions. A clean magnetic stirrer was inserted in the former on a magnetic plate while the other portion of $\text{NaBH}_4/\text{AOT}/\text{isooctane}$ is added within 30 seconds. The solution is kept on the stirrer for another five minutes at 450-500 rpm until any resulting colour change becomes stable.

1 mM Ag NCs

1.1114 g AOT was dissolved in 18 mL isooctane by sonication, share the resulting solution into two equal portions in separate 30 mL clean glass vials. Then prepare 1 mM equimolar 450 μL aqueous solutions of AgNO_3 and NaBH_4 each in separate vials and add to either of the portions

of AOT/isooctane earlier prepared. Insert a clean magnetic stirrer and proceed as in the section above for the $90\ \mu\text{M}$ Ag NCs sample.

2.8.1 Absorbance and fluorescence determinations for $90\ \mu\text{M}$ and $1\ \text{mM}$ silver nanoclusters in microemulsion

Absorbance readings for the samples were obtained after synthesis by withdrawing $500\ \mu\text{L}$ aliquots into the $500\ \mu\text{L}$ micro cell quartz cuvette and then ran in the UV-Vis spectrophotometer with isooctane as background.

Fluorescence data were obtained for both samples scanning from 280-750 nm, exciting at 280, 300, 320, 340, 360, 380, 400, 420 nm.

2.8.2 Dynamic light scattering (DLS) measurement of $90\ \mu\text{M}$ and $1\ \text{mM}$ silver nanoclusters in microemulsion

$200\ \mu\text{L}$ portion of each samples was taken for DLS measurement of the droplet size and measurement were taken at $25\ ^\circ\text{C}$. Several repeating scans were done and readings recorded.

2.8.3 Fourier Transform Infra-red (FTIR) analysis of $90\ \mu\text{M}$ and $1\ \text{mM}$ Ag NCs in microemulsion

$10\ \mu\text{L}$ solution of each sample was pipetted onto a piranha-cleaned silicon wafer and dried overnight prior to analysis.

2.8.4 Atomic force microscope imaging of $90\ \mu\text{M}$ and $1\ \text{mM}$ silver nanoclusters in microemulsion

The as-synthesized (Restek cartridge separated) samples were dotted on $1\ \text{cm}^2$ area silicon wafer, pre-cleaned by soaking for 15 minutes in 3:1 ($\text{H}_2\text{SO}_4:\text{H}_2\text{O}_2$) acid piranha solution and then rinse off thoroughly with copious amounts of deionized water before drying with N_2 gas.

The samples were allowed to dry overnight and then analysed on the AFM instrument.

2.8.5 Fluorescence microscope imaging of $90\ \mu\text{M}$ and $1\ \text{mM}$ Ag NCs samples

The same samples for AFM above were used for photoluminescence imaging.

2.8.6 Transmission Electrons Microscopy (TEM) of 90 μM and 1 mM Ag NCs samples

TEM images of the samples spotted and dried on clean carbon grid supported on copper disk (holey carbon) were obtained.

2.8.7 Separation of aqueous from the organic phase liquid in the emulsion system using a restek chromatography cartridge

ESI-MS analysis of the microemulsions was not possible directly on the as-prepared samples because of the large concentration of isooctane and AOT. The aqueous phase was therefore separated using a Restek chromatography cartridge, Restek Corporation, U.S.A.

To separate the aqueous from the organic phase in the microemulsion, 500 μL (or 1 mL) of the 90 μM Ag NCs sample was pipetted into a clean separating funnel mounted on a retort stand and another 500 μL deionized water was added to it to achieve phase separation. This was allowed to stand for 3-5 minutes before withdrawing the aqueous phase (denser of the two) at the bottom of the flask into a clean glass vial.

The cartridge was fitted with a plastic cork into a Buckner funnel connected to a vacuum pump. Then 1 mL deionized water was put into the cartridge and then eluted with the help of the vacuum pump into a small glass vial earlier inserted in the conical flask. This process is called *conditioning*.¹

Next pipette 1 mL of the water phase (denser fraction) from the separation flask into the cartridge and allow to elute slowly under vacuum (one drop at a time) until no more clear droplets are left, without allowing white surfactant froths.

2.8.8 Electrospray ionization mass spectrometry (ESI-MS) analysis of 90 μM and 1 mM Ag NCs samples

1 μL of the cartridge separated samples were diluted in 199.0 μL water at a dilution factor of 1:200 (and 1:1000 for the 1 mM sample) and spectra run in the ESI-MS instrument with nanopure water as solvent background. Deionized water was obtained from a Barnstead NanopureTM purification train (model DH 931), Barnstead International, Dubuque, Iowa, USA) with nominal 18.2 M Ω cm resistivity.

2.8.9 X-ray photoelectron microscopy (XPS) of 90 μM and 1 mM samples

2 μL drops of these samples were deposited on acid-piranha cleaned silicon wafer (1 cm^2 area), covered up in a petri dish and allowed to dry overnight before XPS analysis.

2.8.10 Boron NMR analysis of 1 mM Ag NCs prepared by microemulsion

About 2 mL of the as-synthesized Ag NCs was pipetted into a separating funnel and 1 mL nanopure added to achieve phase separation. The resulting denser aqueous phase was passed through the restek cartridge and eluted with 1 mL water.

1.5 mL of the resulting eluent was put in the NMR tube and analyzed for ^{11}B in the 500 MHz instrument at 298 K and with boron trifluoride diethyl etherate, $\text{BF}_3 \cdot \text{O}(\text{C}_2\text{H}_5)_2$ as a reference.

2.9 Syntheses of aqueous solutions of silver nanoparticles (no microemulsion)

90 μM Ag NPs

45 μL (90 μM) aqueous solutions of AgNO_3 and another 45 μL (90 μM) aqueous NaBH_4 solution were both prepared from their stocks solutions. Then the 45 μL NaBH_4 was carefully added to the aqueous AgNO_3 solution in an Eppendorf tube with gentle shaking to form a pale yellow coloured solution of Ag NPs.

1 mM Ag NPs

In a similar way, 450 μL (1 mM) aqueous solutions of AgNO_3 and NaBH_4 were made from their stock solutions. Again, the NaBH_4 was carefully added to the AgNO_3 solution to reduce Ag^+ ions to Ag NPs giving a rich yellow solution.

2.9.1 Absorbance and fluorescence of 90 μM and 1 mM aqueous solutions (control) (No microemulsion)

Absorbance readings for the control samples were measured after syntheses by withdrawing 10 μL aliquot portion into the 500 μL micro cell quartz cuvette and then ran in the UV-Vis spectrophotometer with water as background.

Fluorescence data was obtained for the $90\ \mu\text{M}$ and $1\ \text{mM}$ aqueous solutions, scanning from 280-750 nm, exciting at 280, 300, 320, 340, 360, 380, 400, 420 nm.

2.9.2 Dynamic light scattering (DLS) measurement of $90\ \mu\text{M}$ and $1\ \text{mM}$ aqueous solutions (control) samples

200 μL portion of the $90\ \mu\text{M}$ and 100 μL of the $1\ \text{mM}$ samples (made up to 200 μL with water) were taken for DLS measurement of particle sizes. All measurements were taken at $25\ ^\circ\text{C}$ using micro-quartz cuvette. Several repeated scans were done and readings recorded accordingly.

2.9.3 Infra-red analyses of $90\ \mu\text{M}$ and $1\ \text{mM}$ aqueous solutions (control) samples

These also followed similar protocol as with the microemulsion samples.

2.10 90 and $900\ \mu\text{L}$ water in oil microemulsions (in 5 and $18\ \text{mL}$ oil, no analytes) – (control samples)

90 and $900\ \mu\text{L}$ water were added to 5 and $18\ \text{mL}$ isooctane solutions containing 0.2223 and $1.1114\ \text{g}$ (AOT) respectively to form microemulsions containing neither AgNO_3 nor NaBH_4 .

2.10.1 Absorbance and fluorescence of 90 and $900\ \mu\text{L}$ water in oil microemulsions (control) samples

$500\ \mu\text{L}$ of these microemulsion control samples were studied under the UV-Vis and fluorescence spectrophotometers to observe any optical properties with isooctane as background (for the UV-Vis) as was done with the analyte-containing samples.

2.11 Syntheses of 90 , 150 , 250 , 500 , 750 , and $1000\ \mu\text{M}$ Ag NCs in $5\ \text{mL}$ microemulsion (at fixed ω values)

Omega (ω) is the coefficient of the ratio of the molar concentration of water to that of the surfactant.

Six different solutions of AOT/isooctane each containing $0.2223\ \text{g}$ AOT in $5\ \text{mL}$ isooctane were prepared with each equally shared into two portions of $2.5\ \text{mL}$ after dissolution. Then six portions of AgNO_3 in the following concentrations 90 , 150 , 250 , 500 , 750 , and $1000\ \mu\text{M}$ each in separate $45\ \mu\text{L}$ aqueous solutions of water were subsequently prepared and poured into

separate (2.5mL) AOT/isooctane solutions, until we have six different 45 μL aqueous solution concentrations of AgNO_3 in six 2.5 mL of AOT/isooctane solutions each. Similarly, another six sets of aqueous solutions of NaBH_4 with same concentration range as above (90, 150, 250, 500, 750, and 1000 μM) in 45 μL water in 2.5 mL isooctane solutions each per concentration type were prepared. These were used to reduce their corresponding pair of Ag^+ ion solution (in a 1:1 molar ratio) to form Ag NCs in microemulsion at room temperature by mixing both reagents and stirring with a magnetic stirrer at 450-500 rpm for 5 minutes until any resulting colour change becomes stable.

2.11.1 Absorbance and fluorescence determinations for 90, 150, 250, 500, 750, and 1000 μM Ag NCs in 5 mL microemulsion

Absorbance readings for the sample were obtained after synthesis by withdrawing 500 μL aliquots into the 500 μL micro cell quartz cuvette and then ran in the UV-Vis spectrophotometer with isooctane as background.

Fluorescence data were obtained for both samples scanning from 280-750 nm, exciting at 280, 300, 320, 340, 360, 380, 400, 420 nm.

2.11.2 Dynamic light scattering (DLS) measurement of 90, 150, 250, 500, 750, and 1000 μM Ag NCs in 5 mL microemulsion

200 μL portion of the sample was taken for DLS measurement of the droplet size and measurement were taken at 25 °C. Several repeating scans were done and readings recorded.

2.11.3 Fourier Transform Infra-red analyses of 90, 150, 250, 500, 750, and 1000 μM Ag NCs in 5 mL microemulsion

Infra-red analyses of these clusters were undertaken by spotting 20 μL of the individual oil separated samples on cleaned (1x1 cm^2) silicon wafer and allowing them to dry overnight before analyses.

2.12 Syntheses of 90, 150, 250, 500, 750, and 1000 μM Ag NCs in microemulsion (at varied ω values)

90, 150, 250, 500, 750, and 1000 μM Ag NCs were prepared in 5.0, 7.5, 10.0, 12.5, 15.0, 18.0 mL isooctane with 10, 12, 14, 16, 18, 20 ω -values respectively, in six different microemulsion

systems. These were all prepared in similar ways as in section 2.13.0 above only that in this case, the ω -values (and [AOT]) for each sample type is different; as well as the reaction volumes, whilst maintaining the same 1:1 stoichiometric ratio of $[\text{Ag}^+]$ and $[\text{BH}_4^-]$ in all the reactions.

2.12.1 Absorbance and fluorescence determinations.

These were taken in exactly the same way as in section 2.13.1 above again with isooctane as background.

2.12.2 Dynamic light scattering (DLS) measurement.

200 μL portion of the sample was taken for DLS measurement of the droplet size at 25 °C. Several repeating scans were taken for each sample and readings recorded before being plotted out on Microsoft Excel.

2.13 Photochemical syntheses of 90 μM and 1 mM Ag NCs by reduction of Ag^+ ions in microemulsion

90 μM Ag NCs sample

90 μM AgNO_3 in 90 μL aqueous solution was prepared from stock 1 mM solution and then added to 5 mL isooctane solution, containing 0.2223 g (0.0005 M) AOT.

1 mM Ag NCs sample

Similarly, 1 mM AgNO_3 in 900 μL aqueous solution was prepared from stock 1 M solution and added to 18 mL isooctane solution containing 1.1114 g (0.0025 M) AOT to form 1 mM aqueous microemulsion.

Both samples were then subjected to UV-light illumination in a photochemical reactor for 6-10 hours.

2.13.1 Absorbance and fluorescence measurements of 90 μM and 1 mM Ag NCs samples

500 μL aliquots of both samples were taken every 1-hour intervals for UV-Vis and fluorescence analyses. Data obtained is recorded and plotted out in Microsoft Excel.

2.13.2 Dynamic light scattering measurements of 90 μM and 1 mM Ag NCs samples

Samples particles sizes were observed on the DLS as with the borohydride reduced analogues.

2.13.3 Electrospray ionisation mass spectrometry (ESI-MS) 90 μM and 1 mM Ag NCs samples

Molecular mass and form μLa of the samples were obtained from the ESI-MS using the dilution factor of 1:200 for the 90 μM sample, and 1:1500 for the 1 mM sample.

2.13.4 Transmission electron microscopy (TEM) of the photoreduced samples

TEM images of the photoreduced samples were obtained in a similar way as the NaBH_4 reduced emulsion samples after separation with the restek cartridge.

2.13.5 Photoluminescence imaging of photoreduced microemulsion samples

Again, these were obtained by drying the samples on clean silicon chips prior to fluorescence imaging under similar conditions as was the case with the borohydride reduced samples.

2.14 Synthesis of aqueous solutions of 90 μM and 1 mM Ag NPs (without microemulsion) by photochemical reduction

5 mL solutions each of 90 μM and 1 mM AgNO_3 were prepared from 1 mM and 1 M stock solutions in aqueous medium only (without microemulsion) and photoreduced in the photochemical reactor for a period of 8 hours duration.

2.14.1 Absorbance and fluorescence measurements of aqueous (control) photoreduced samples

Absorbance data was obtained by withdrawing 500 μL portions of 90 μM and 1 mM AgNO_3 control samples every one-hour interval for 8 hours period to observe the growth of the Ag NPs being formed.

Fluorescence data for these control samples were taken at the end of the photoreduction process by scanning from 280-750 nm, exciting at 280, 300, 320, 340, 360, 380, 400, 420 nm.

2.14.2 DLS measurement of particles sizes

Silver nanoparticles sizes of the aqueous samples were obtained by dynamic light scattering method in 200 μL volumes.

2.14.3 Electrochemical Cyclic voltammetry (CV) measurement

For cyclic voltammetry measurements, 100 mM sodium nitrate (NaNO_3) salt was added to each of the 90 μM and 1 mM AgNO_3 aqueous solutions to improve their conductivity. A simple electrochemical setup was made with Ag/AgCl reference electrode, platinum working electrode, and the platinum wire counter electrode. Data were obtained by the use of PSTrace 4.6 software, scanning from -0.5 to 0.5 Volts and back, with a scan rate of 0.05 V/s.

A control cyclic voltammetry measurement of control samples containing no AgNO_3 (analyte) but just 5 mL nanopure water with only 100 mM NaNO_3 .

Data were recorded and analysed with Microsoft Excel (2013 version).

2.15 Kinetic study of the rate of formation of Ag NCs in microemulsion

90 μM and 1 mM Ag NCs were prepared in separate microemulsion systems as previously described. Immediately the borohydride portion was added and shaken, 500 μL portions were quickly transferred into the cuvette and placed on the fluorimeter already set to run. The instrument was pre-set at an excitation wavelength of 340 nm (wavelength of highest intensity) and seven repeated scans were taken for either sample at this wavelength over the next one hour.

Data were retrieved and plotted out using Microsoft Excel (2013 version).

2.16 Electrospray mass spectrometry analysis of Ag^+ ions in microemulsion without photoreduction (control)

Both 90 μM and 1 mM Ag^+ ions solutions of 90 and 900 μL were prepared from their stock solutions and added to 5 and 18 mL isoctane solutions containing 0.2223 and 1.1114 g AOT respectively. These were then oil separated in a separating funnel and then through the restek cartridge before aliquots of both samples were taken at a dilution factor of 1:1000 and 1:2000 for ESI-MS analyses.

2.17 Syntheses of 90 μM and 1 mM Ag NCs on ssDNA1 (1:4) in microemulsion

90 μM sample

90 μM Ag NCs was prepared on ssDNA1 (22-mer) ligand in 5 mL microemulsion. 0.2223 g AOT was dissolved completely in 5 mL isooctane and the resulting solution shared into two portions, 2.5 mL each. Then 90 μM aqueous AgNO_3 in 45 μL volume was obtained from a stock 1 mM AgNO_3 solution and added to one of the 2.5 mL AOT/isooctane solutions, Then, 10 μL solution of 15 μM ssDNA1 was added to it, and properly wrapped up with aluminium foil, shaken and allowed to stand in the dark for 30 minutes. Afterward, a magnetic stirrer was inserted into it and placed on a magnetic plate set at 450 rpm and reduced with the other (second 2.5 mL) microemulsion portion containing 90 μM NaBH_4 in 35 μL aqueous solution. This was stirred with the magnetic stirrer on the magnetic plate for ~5 minutes and then incubated for 24 hours in the dark.

1 mM Ag NCs sample

The 1 mM Ag NCs on ssDNA1 was prepared similarly, from 1 M aqueous stock AgNO_3 solution, 450 μL containing 1 mM AgNO_3 solution was made, by adding 100 μL 167 μM ssDNA1 solution, and then reducing with 350 μL , 1 mM NaBH_4 solution, in 18 mL isooctane in which 1.1114 g (0.0025 M AOT) had previously been dissolved.

2.17.1 UV-Vis and fluorescence measurements

500 μL of the as-synthesized 90 μM and 1 mM Ag NCs on ssDNA1 was taken for UV-Vis and fluorescence measurements.

2.17.2 Dynamic light scattering measurements

100 μL aliquots of the samples were withdrawn and diluted with another 100 μL nanopure water for DLS measurement.

2.17.3 Fluorescence microscope imaging

Aliquots of the cartridge separated samples were deposited on piranha pre-cleaned silicon chip and dried overnight before imaging on the instrument.

2.17.4 Transmission electron microscope imaging

About 2 μL oil-separated solution of both samples were spotted on different new holey carbon grids (EM Resolutions Ltd., Sheffield, UK) and allowed to dry prior to TEM imaging.

2.17.5 Electrospray ionization mass spectrometry measurement

From the restek cartridge oil-separated 90 μM sample, 200 μL solutions were prepared by taking 1 μL sample and adding in 199 μL water (dilution factor of 1:200) for electrospray mass spectrometry analysis.

1 μL of the 1 mM Ag NPs on ssDNA1 was diluted up to 1000 μL with water (1:1000) for mass spectrometry analysis of the cartridge oil-separated sample.

2.18 Syntheses of 90 μM and 1 mM Ag NPs on ssDNA1 (1:4) in aqueous solution (control)

(a) 90 μM and Ag NPs on ssDNA1 (1:4) in aqueous solution

From 1 mM stock AgNO_3 solution, 90 μM AgNO_3 (500 μL) solution was made to which another 500 μL of 15 μM ssDNA1 solution was added then shaken, wrapped up in aluminum foil and allowed to stand in the dark for 30 minutes before being reduced with 90 μM 500 μL aqueous NaBH_4 solution. Shaken yet again and allowed to stand in the dark for 24 hours.

The 1 mM Ag NPs on ssDNA1 was prepared similarly, from 450 μL (1 mM AgNO_3 solution), 100 μL 167 μM ssDNA1 solution, and 1 mM NaBH_4 in 350 μL solution, in 18 mL isooctane in which 1.1114 g (0.0025 M AOT) had previously been dissolved.

2.18.1 UV-Vis and fluorescence measurements

10 μL each of the as-synthesized 90 μM and 1 mM Ag NPs on ssDNA1 (controls) were made up to 500 μL in the quartz cuvette and taken for measurement on the UV-Vis and fluorescence instruments.

2.18.2 Dynamic light scattering measurements

100 μL aliquots of the two samples were separately withdrawn and diluted with another 100 μL nanopure water for DLS measurement.

2.18.3 Fluorescence microscope imaging

2 μL aliquots of the samples are deposited on a pre-cleaned silicon chip and dried overnight before imaging on the instrument.

2.18.4 Transmission electron microscope imaging

About 2 μL solution of the sample was spotted on the new holey-carbon grid and allowed to dry prior to imaging.

2.18.5 Electrospray ionization mass spectrometry measurement

1 μL of the 180 μM aqueous sample in 199 μL nanopure water (dilution factor of 1:200) was prepared for electrospray mass spectrometry analysis.

2.19 Syntheses of 90 μM and 1 mM Ag NCs on ssDNA2 (1:5) in microemulsion

A 90 μL solution containing 90 μM Ag NCs was prepared on ssDNA2 (29-mer) template in 5 mL microemulsion. Again as in the synthesis of 90 μM Ag NCs in 5 mL microemulsion in section 2.9.0; 0.2223 g AOT was dissolved completely in 5 mL isooctane and then shared into two equal portions (2.5 mL each). Then 90 μmole AgNO_3 in 45 μL was obtained from a stock 1 mM AgNO_3 solution and added to one of the 2.5 mL AOT/isooctane solutions, 10 μL solution of 15 μM ssDNA2 was added to it. This was then properly wrapped up with aluminum foil, shaken and allowed to stand in the dark for 20 minutes before being reduced with 35 μL (90 μM NaBH_4) previously prepared in the other (second 2.5 mL) portion of the AOT/isooctane solution. The resulting solution was stirred with the aid of a magnetic stirrer on a magnetic plate set at 450 rpm for 3-5 minutes, and then incubated for 24 hours.

The 1 mM Ag NCs on ssDNA2 was prepared similarly, from 450 μL (1 mM AgNO_3 solution), 100 μL 167 μM ssDNA2 solution, and 1 mM NaBH_4 in 350 μL solution, in 18 mL isooctane in which 1.1114 g (0.0025 M AOT) had previously been dissolved.

2.19.1 UV-Vis and fluorescence measurements

500 μL of the as-synthesized 90 μM and 1 mM Ag NCs on ssDNA3 was taken for UV-Vis and fluorescence measurements.

2.19.2 Dynamic light scattering measurements

100 μL aliquots of the samples were withdrawn and diluted with another 100 μL nanopure water for DLS measurement.

2.19.3 Fluorescence microscope imaging

Aliquots of the cartridge separated samples were deposited on a pre-cleaned silicon chip and dried overnight before imaging on the instrument.

2.19.4 Transmission electron microscope imaging

About 2 μL oil separated solution of the samples were spotted on new holey carbon grid and allowed to dry prior to TEM imaging.

2.19.5 Electrospray ionization mass spectrometry measurement

From the restek cartridge oil separated 90 μM Ag NCs on ssDNA2 sample, 200 μL solution was prepared by adding 1 μL sample in 199 μL nanopure water (dilution factor of 1:200) and for electrospray mass spectrometry analyses.

1 μL of the 1 mM Ag NCs on ssDNA2 was diluted up to 300 μL with water (1:300) for mass spectrometry analysis of the cartridge oil-separated sample.

2.20 Syntheses of 90 μM and Ag NPs on ssDNA2 in aqueous solution (control)

(a) 90 μM and Ag NPs on ssDNA2 (1:5) in aqueous solution

From 1 mM stock AgNO_3 solution, 90 μM AgNO_3 (500 μL) solution was obtained to which 500 μL of 15 μM ssDNA2 solution was added well shaken, wrapped up in aluminium foil and allowed to stand in the dark for 30 minutes before being reduced with 90 μM 500 μL aqueous NaBH_4 solution. Shaken yet again and allowed to stand in the dark for 24 hours.

2.20.1 UV-Vis and fluorescence measurements

10 μL each of the as-synthesized Ag NPs on ssDNA2 (controls) were made up to 500 μL in the quartz cuvette and taken for measurement on the UV-Vis and fluorescence instruments.

2.20.2 Dynamic light scattering measurements

100 μL aliquots of the samples were withdrawn and diluted with another 100 μL nanopure water for DLS measurement.

2.20.3 Fluorescence microscope imaging

Aliquots of the samples are deposited on a pre-cleaned silicon chip and dried overnight before imaging on the instrument.

2.20.4 Transmission electron microscope imaging

About 2 μL solution of the sample was spotted on new holey carbon grid and allowed to dry prior to TEM imaging.

2.20.5 Electrospray ionisation mass spectrometry measurement

200 μL solution of and 217 μM samples obtained by adding 1 μL sample in 199 μL nanopure water (dilution factor of 1:200) was prepared for electrospray mass spectrometry analysis.

2.21 Syntheses of 90 μM and 1 mM Ag NCs on ssDNA3 (1:6) in microemulsion

Dissolve 0.2223 g (AOT) in 5 mL isooctane and divide into two equal portions. Then pour 45 μL aqueous solution of 90 μM AgNO_3 to one of the two portions of AOT/isooctane portions and add 10 μL 15 μM ssDNA3, shake vigorously and keep in the dark for 30 minutes. This was later reduced with 90 μM NaBH_4 35 μL aqueous solution and stored away to age in the dark for 24 hours.

The 1 mM Ag/ssDNA3 NCs sample was again prepared in a similar manner as in section 2.20.0 for 1 mM Ag/ssDNA2 NCs in microemulsion.

2.21.1 UV-Vis and fluorescence measurements

500 μL of the as-synthesized Ag NCs on ssDNA3 was taken for UV-Vis and fluorescence measurements.

2.21.2 Dynamic light scattering measurements

100 μL aliquots of the samples were withdrawn and diluted with another 100 μL nanopure water for DLS measurement.

2.21.3 Fluorescence microscope imaging

An aliquot of the cartridge oil-separated sample is deposited on a pre-cleaned silicon chip and dried overnight before imaging on the instrument.

2.21.4 Transmission electron microscope imaging

About 1 μL solution of the oil-separated sample was spotted on new holey carbon grid and allowed to dry prior to TEM imaging.

2.21.5 Electrospray ionisation mass spectrometry measurement

200 μL solution obtained by adding 199 μL nanopure water to 1 μL portion of the cartridge eluted sample (dilution factor of 1:200) of both 90 μM and 1 mM samples were prepared for analyses on electrospray mass spectrometer.

2.22 Syntheses of aqueous Ag NPs on ssDNA3 (control) sample solutions

(a) 90 μM and Ag NPs on ssDNA3 (1:6)

90 μM Ag NPs were templated on ssDNA3 in exactly the same way as that of ssDNA2 in section 2.21.0.

2.22.1 UV-Vis and fluorescence measurements

10 μL each of the as-synthesized Ag NPs on ssDNA3 (controls) samples were made up to 500 μL in the quartz cuvette and taken for measurement on the UV-Vis and fluorescence instruments.

2.22.2 Dynamic light scattering measurements

100 μL aliquots of the samples were withdrawn and diluted with another 100 μL nanopure water for DLS measurement.

2.22.3 Fluorescence microscope imaging

Aliquots of the samples are deposited on a pre-cleaned silicon chip and dried overnight before imaging on the instrument.

2.22.4 Transmission electron microscope imaging

About 1 μL solution of the sample was spotted on new holey carbon grid and allowed to dry prior to TEM imaging.

2.22.5 Electrospray ionisation mass spectrometry measurement

200 μL solution of the 255 μM sample obtained by adding 1 μL sample in 199 μL nanopure water (dilution factor of 1:200) was prepared for electrospray mass spectrometry analysis.

2.23 Gel electrophoresis experiment of the microemulsion synthesized Ag NCs on ssDNAs

The oil separated cartridge eluents were loaded onto a 1 % agarose gel earlier prepared. 1x Tris/Borate/EDTA (TBE) and 50: 50 EDTA were used as running and loading buffers respectively, in the presence of 6x loading dye comprising 2.5 % Ficoll-400, 11 mM EDTA, 3.3 mM Tris-HCl (pH 8.0 at 25 °C), 0.017 % sodium dodecyl sulfate (SDS) and 0.015 % bromophenol blue.

The apparatus was then connected to a voltage source set to run at 100 V, 100 mA, and 10 W for 1 hour. Afterward, the gel was removed and post-stained with 1 $\mu\text{g}/\mu\text{L}$ solution of ethidium bromide, then placed under the ultraviolet transilluminator of 314 nm fixed wavelength.

2.24 Synthesis of ssDNA1 in deuterated water for ^1H , ^{13}C , ^{31}P NMR, COSY, HSQC, and HMBC analyses

0.8 mL D_2O was added to a sample vial containing 193 *n*moles ssDNA1 salt under argon gas to form 0.241 mM (5.31 mM base concentration) concentration of the ssDNA1 solution. This was carefully transferred to a mini NMR tube for NMR analyses.

2.24.1 Addition of Ag⁺ ions to the ssDNA template

0.0850 g AgNO₃ salt was weighed out and dissolved in 0.5 mL D₂O to give a 1 M stock solution. From this, 1.33 mM AgNO₃ solution in 100 μL D₂O was prepared and added directly under argon gas to 0.4 mL (0.241 mM ssDNA1) solution earlier prepared so as to have a 1:4 ratio of Ag: ssDNA1. This solution was then wrapped up in with aluminium paper and the lid wrapped as well with paraffin film to reduced atmospheric moisture addition, then shaken vigorously for 2 minutes before standing in the dark for 20 minutes prior to ¹H, ¹³C, and ³¹P NMR analyses.

2.24.2 Reduction of Ag⁺ssDNA1 complex with NaBH₄

1 M stock NaBH₄ solution was made in 125 μL D₂O, from which 1.33 mM NaBH₄ in 100 μL D₂O solution was then prepared.

The 1.33 mM equivalent portion of NaBH₄ was added to the Ag⁺ssDNA1 solution whilst flushing with Argon gas in order to reduce the Ag⁺ ions to Ag⁰. The resulting solution was again placed in the NMR tube for ¹H, ¹³C, and ³¹P NMR analyses.

2.25 Synthesis of Ag⁺/ssDNA2 in deuterated water for ¹H, ³¹P, and ¹³C NMR analyses

0.4 mL D₂O was added to a sample vial containing 87 nmoles ssDNA2 salt under argon gas to form 0.218 mM (6.308 mM base concentration) concentration of the ssDNA2 solution. This was carefully transferred to a mini NMR tube for ¹H, ¹³C, ³¹P and other NMR analyses.

2.25.1 Addition of Ag⁺ to the ssDNA2 template

0.0850 g AgNO₃ salt was weighed out and dissolved in 0.5 mL D₂O to give a 1 M stock solution. From this, 1.262 mM AgNO₃ solution in 100 μL D₂O was prepared and directly added under argon gas to 0.4 mL (0.218 mM ssDNA2) solution earlier prepared so as to have a 1:5 base ratio of Ag: ssDNA2. This solution was wrapped up in aluminium foil after sealing the lid with paraffin film to eliminate atmospheric moisture, then shaken vigorously for 2 minutes before standing in the dark for 20 minutes prior to ¹H, ¹³C, and ³¹P NMR analyses.

2.25.2 Reduction of Ag⁺ssDNA2 complex with NaBH₄

1 M stock NaBH₄ solution was made in 125 μL D₂O, from which 1.262 mM NaBH₄ in 100 μL D₂O solution was then prepared.

The 1.262 mM equivalent portion of NaBH₄ was added to the Ag⁺/ssDNA2 solution whilst flushing with Argon gas in order to reduce the Ag⁺ ions to Ag⁰. The resulting solution was again placed in the NMR tube for ¹H, ¹³C, and ³¹P NMR analyses.

2.26 Synthesis of Ag NCs/ssDNA3 by reduction with NaBH₄ in deuterated water for ¹H, ³¹P, and ¹³C NMR analyses

0.4 mL D₂O was added to a sample vial containing 67.9 nmoles ssDNA3 salt under argon gas to form 0.170 mM (5.772 mM base concentration) concentration of the ssDNA3 solution. This was carefully transferred to a mini NMR tube, sealed with paraffin film and taken for ¹H, ¹³C, and ³¹P NMR analyses.

2.26.1 Addition of Ag⁺ ions to the ssDNA3 template

0.0850 g AgNO₃ salt was weighed out and dissolved in 0.5 mL D₂O to give a 1 M stock solution. From this, 0.962 mM AgNO₃ solution in 100 μL D₂O was prepared and added directly under argon gas to 0.4 mL (0.170 mM ssDNA3) solution earlier prepared so as to have a 1:6 ratio of Ag: ssDNA3. This solution was then wrapped up in with aluminium paper and the lid wrapped as well with paraffin film to reduced atmospheric moisture addition, then shaken vigorously for 2 minutes before standing in the dark for 30 minutes prior to ¹H, ¹³C, and ³¹P NMR analyses.

2.26.2 Reduction of Ag⁺ssDNA3 complex with NaBH₄

1 M stock NaBH₄ solution was made in 125 μL D₂O, from which 0.962 mM NaBH₄ in 100 μL D₂O solution was then prepared.

The 0.962 mM equivalent portion of NaBH₄ was added to the Ag⁺ssDNA1 solution whilst flushing with argon gas in order to reduce the Ag⁺ ions to Ag⁰. The resulting solution was again placed in the NMR tube for ¹H, ¹³C, and ³¹P NMR analyses.

2.27 Syntheses of Ag NPs on adenosine, cytidine, guanosine, and thymidine 5'-monophosphate disodium salts in D₂O.

1 mg (0.0010 g) of each nucleotide salt was dissolved in 1 mL D₂O to form stock solutions of 2.56, 2.72, 2.46, 2.73 mM of adenosine, cytidine, guanosine, and thymidine respectively. From each of these, 0.256, 0.272, 0.246, and 0.273 mM accordingly were reacted with appropriate portions (0.128, 0.136, 0.123, & 0.683 mM) Ag⁺ concentration in a 1: 2 Ag: base ratio. These

were studied by ^1H , ^{13}C , ^{31}P NMR analyses after shaking for 2 minutes and then allowed to stand wrapped in aluminium foil-paper in a dark cupboard for 30 minutes.

They were subsequently reduced with equivalent portions of NaBH_4 in D_2O solution in a 1:1 $\text{Ag}^+:\text{BH}_4^-$ ratio before repeating the ^1H , ^{13}C , ^{31}P and other NMR analyses. All reactions took place under gentle air flushing with argon gas.

2.28 Syntheses of Cu NCs in microemulsion

90 μM Cu NCs

Again, 0.2223 g AOT dissolved in 5 mL isooctane and then shared into two equal portions in two separate glass vials, after which 45 μL aqueous solution containing 90 μM $\text{Cu}(\text{NO}_3)_2$ was added to one of the two portions of the AOT/isooctane solutions. 45 μL aqueous NaBH_4 solution containing 90 μM was poured into the other glass vial of 2.5 mL AOT/isooctane solution. Insert a magnetic stirrer into the $\text{Cu}(\text{NO}_3)_2$ containing vial and place on a magnetic plate set at 450 rpm, before reducing with the 90 μM NaBH_4 in microemulsion and stirred for 3-5 minutes before being taken down.

1 mM Cu NCs

Dissolve 1.1114 g AOT in 18 mL isooctane and divide into two equal portions of 9 mL in two separate 30 mL glass vials. Then, from 1 M aqueous stock $\text{Cu}(\text{NO}_3)_2$ solution, 1 mM $\text{Cu}(\text{NO}_3)_2$ in 450 μL solution was prepared and added to one of the 9 mL AOT/isooctane solutions. Another 1 mM aqueous NaBH_4 solution in 450 μL was added to the second 9 mL AOT/isooctane solution. This was used to reduce the Cu^{2+} ions by mixing the two microemulsions together and stirring with a stirrer on a magnetic plate at 450 rpm for 3-5 minutes.

2.28.1 UV-Vis and fluorescence measurements

500 μL of the sample was put in the quartz cuvette and its optical density measured in the UV-Vis instrument with isooctane as background.

Fluorescence measurement was taken of the 500 μL sample in the quartz microcuvette at the following excitation wavelengths: 280, 300, 320, 340, 360, 380, 400, 420, 440, 460, 480, and 500 nm, scanning from 280-750 nm.

2.28.2 Dynamic light scattering measurements

200 μL of the samples were taken for DLS measurement.

2.28.3 Fluorescence microscope imaging

Portions of the oil-separated Cu NCs were deposited on clean silicon chips and dried overnight before imaging on the instrument.

2.28.4 Transmission electron microscope imaging

1 μL of the oil-separated samples was dropped on new holey carbon grid and allowed to dry prior to TEM imaging.

2.28.5 Fourier transform infrared (FTIR) measurement

Dry samples on clean silicon wafers were used for infrared measurement.

2.28.6 Electrospray ionization mass spectroscopy measurement

Aliquots of the cartridge separated Cu NCs sample in a 1:100 μL dilution factor was taken for ESI-MS measurement.

2.29 Syntheses of 90 μM and 1 mM aqueous solutions of Cu NPs (control)

90 μM Cu NPs

45 μL of 90 μM aqueous $\text{Cu}(\text{NO}_3)_2$ solution was prepared and then reduced with another 45 μL equimolar aqueous portion of NaBH_4 solution to form 90 μM Cu NPs.

1 mM Cu NPs

1 mM aqueous $\text{Cu}(\text{NO}_3)_2$ in 450 μL solution was reduced with another 1 mM aqueous NaBH_4 solution to form Cu NPs in aqueous solution.

2.29.1 Absorbance and fluorescence measurements of the 90 μM and 1 mM Cu NPs control samples

10 μL aliquot portion of the samples were put in 500 μL micro cell quartz cuvette and then ran in the UV-Vis spectrophotometer with water as background.

Fluorescence data was obtained for the $90\ \mu\text{M}$ and $1\ \text{mM}$ aqueous solutions, scanning from 280-750 nm, exciting at 280, 300, 320, 340, 360, 380, 400, 420 nm.

2.29.2 Dynamic light scattering (DLS) measurement of $90\ \mu\text{M}$ and $1\ \text{mM}$ Cu NPs aqueous solutions (control) samples

200 μL portion of the $90\ \mu\text{M}$ and $1\ \text{mM}$ samples were taken for DLS measurement of particle sizes. All measurements were taken at $25\ ^\circ\text{C}$ micro-quartz cuvette, and several repeating scans were done.

2.29.3 Infra-red analyses of $90\ \mu\text{M}$ and $1\ \text{mM}$ Cu NPs aqueous solutions (control) samples

These also followed similar protocol as with the microemulsion samples.

2.30 Principles of instrumental methods of analyses

2.30.1 Fluorescence spectroscopy

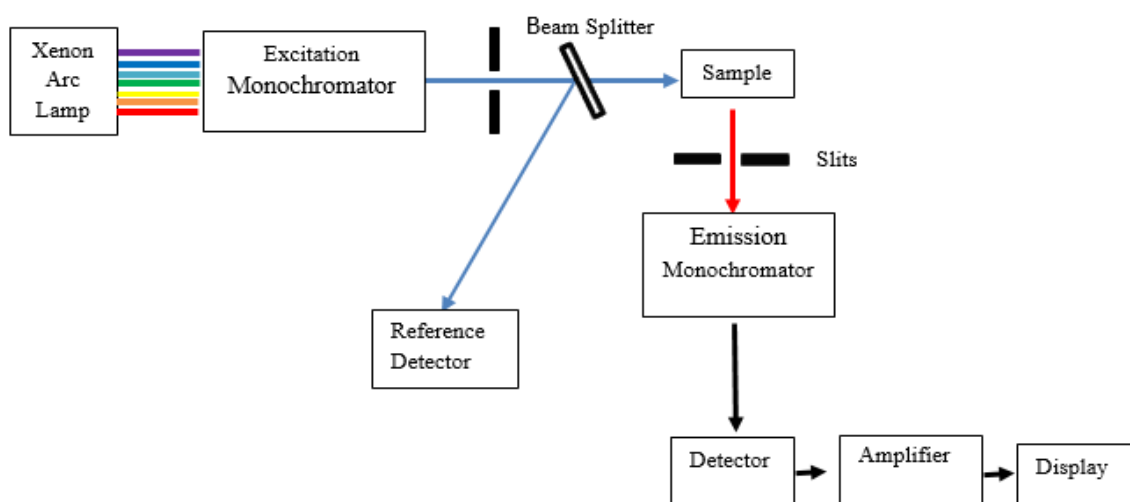


Figure 2.1: Schematic diagram of fluorescence spectrometer.

Once the instrument is turned on and the necessary experimental parameters are set up at a given excitation wavelength, light from the xenon bulb source streams through the first (excitation) monochromator which allows light at the set wavelength of excitation to pass

through the slit and onto the beam splitter (figure 2.1). At the beam splitter, some of this light is reflected off and recorded by the *reference detector*, this allows correction for the variation of source intensity with wavelength. The rest is transmitted through to the sample in the sample cell (cuvette). For this reason, fluorescence excitation spectra are usually corrected for distortions caused by spectral variations in the transmittance/reflectance ratio of the beam splitter.⁵ The sample fluorophores are thus excited to the higher singlet excitation state, then undergo levels of vibrational relaxation with consequent loss of energy, before eventually returning to the ground state by losing excess excited energy through fluorescence.⁶ The fluorescence emission passes through another slit to the emission monochromator and to the detector, then to the amplifier from where a digital program converts this to a spectrum before it is displayed on the monitor.

2.30.2 Dynamic light scattering

This uses the He-Ne laser as its light source with a wavelength of 633 nm.⁷ The instrument sends a laser jet at this wavelength through the attenuator to the sample in the cuvette whose particles diameters are to be measured. The attenuator controls the amount of light entering the sample according to how dilute or concentrated the sample solution is. As the light hits the sample particles which are in constant Brownian motion in solution, the incident light is scattered according to their individual sizes.⁷ Smaller particles move faster and the light intensity fluctuations are of higher frequency. Analysis of the fluctuations gives the diffusion coefficient of the particle.⁸ Hence, the hydrodynamic radius of the particles are linked to the viscosity, refractive index, and temperature of the sample solution and cuvette as shown in the Stokes-Einstein equation:

$$D_{hyd} = \frac{kT}{6\pi\eta D} \quad (2.1)$$

D_{hyd} is the hydrodynamic radius, k is Boltzmann constant, T is absolute (Kelvin) temperature, η is solvent viscosity, and D is diffusion coefficient.

The scattered light, which is the attenuation of the incident light is collected through a converging lens by a photodiode detector placed either at 90 or 173-degree angle to the incident light (figure 2.2 below). The intensities of light scattering and the frequency of fluctuation with

time of the light intensity by the various individual particles are correlated by the Correlator which uses a software to display the data.

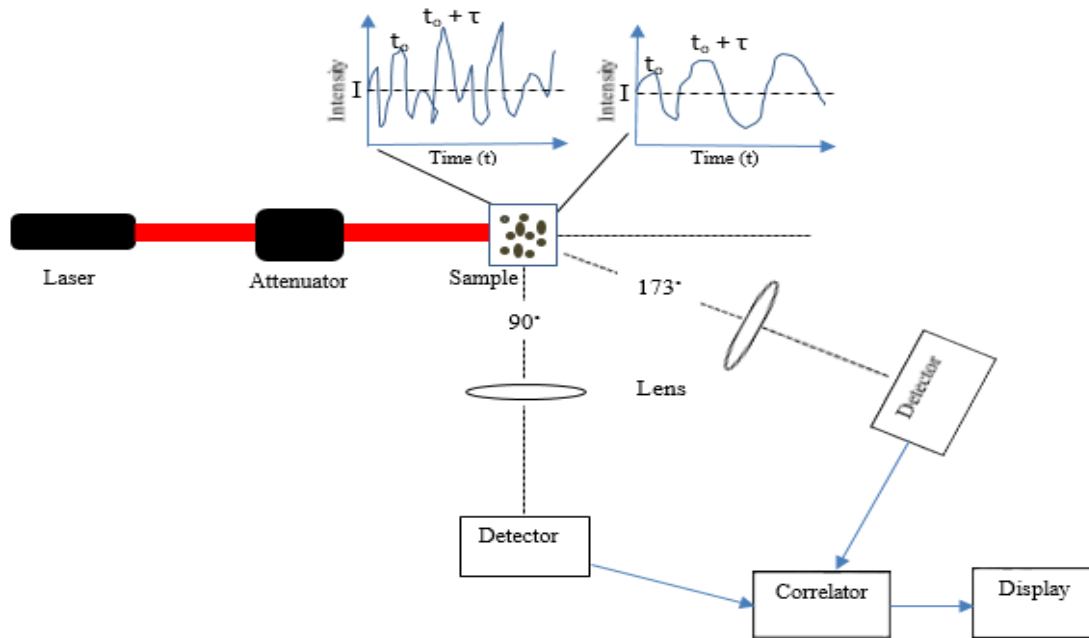


Figure 2.2: Dynamic light scattering instrument’s operational schematics.

Characteristically, the frequency of the fluctuations of the intensities the scattered light with time is higher for smaller particles, and lower for the larger (see the graphs in figure 2.2). The instrument works by measuring the fluctuations in the intensities of the scattered light against time at a time t_0 and at another short time interval of τ later; and then calculates the correlation function (CF) from the equation below:

$$\left\langle \frac{I(t_0) \cdot I(t_0 + \tau)}{I^2(t)} \right\rangle = CF \quad (2.2)$$

A plot of the CF against the log of the time delay is made as shown below:

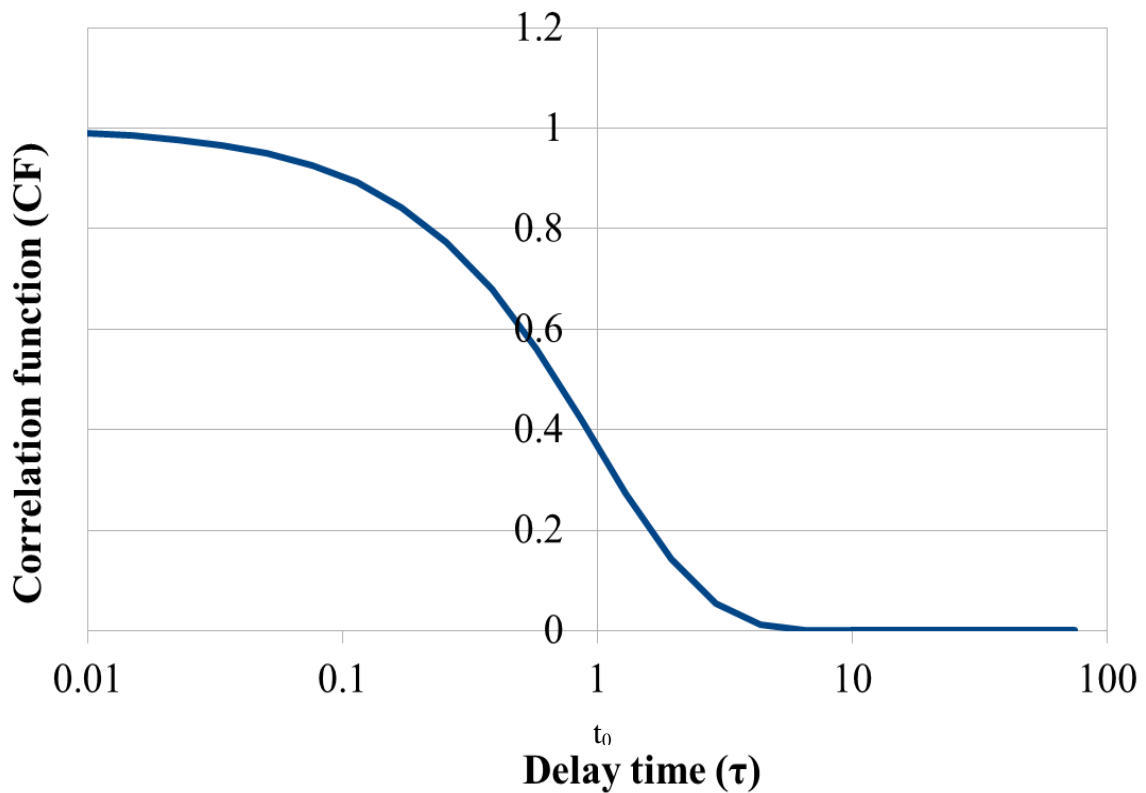


Figure 2.3: Chart of correlation factor (CF) versus delay time.

With the curve in figure 2.3 (above) corresponding to $e^{-\tau/t_0}$. Several repeated light scattering intensity measurements are made at different time delays and the instrument tries to fit these to the CF curve. Each of these cumulatively combines to form a Gaussian curve distribution for the particles of a given size. Thus, a polynomial expression is obtained for CF in the form of:⁹

$$CF = \mathbf{a}_0.e^{-\tau/t_0} + \mathbf{a}_1.e^{-\tau/t_1} + \mathbf{a}_2.e^{-\tau/t_2} + \mathbf{a}_3.e^{-\tau/t_3} + \mathbf{a}_4.e^{-\tau/t_4} \dots \dots \mathbf{a}_n.e^{-\tau/t_n} \dots \dots (2.3)$$

Where \mathbf{a} is particle type, τ is a time delay, $t_{0, 1, 2, \dots, n}$ is time at different constants for exponential decay corresponding to different size particles. For example, t_1 means particle 1 is fast and small.

The instrument's software collects all the t 's and plots them as a size distribution.

2.30.3 Electrospray ionisation mass spectrometry

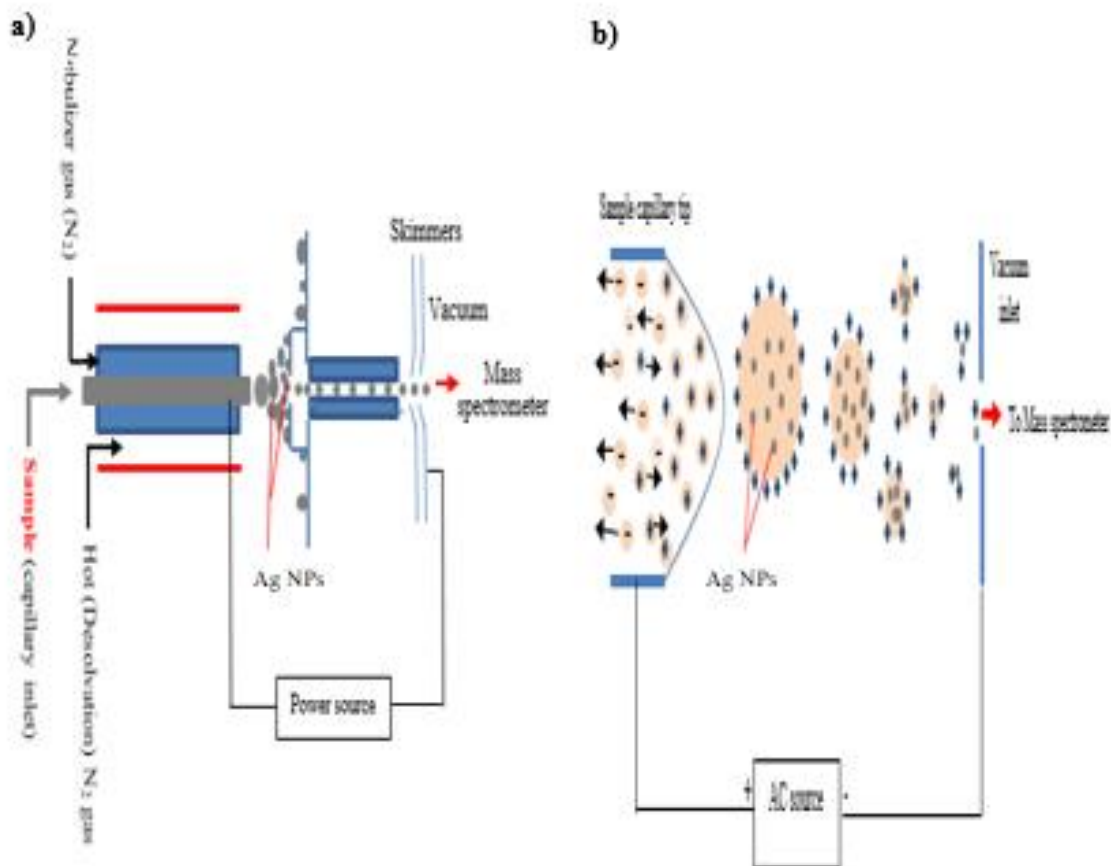


Figure 2.4: Diagram of electro spray ionisation mass spectrometer showing mode of operation.

This is a *soft* ionisation¹⁰ mass spectrometry method in that very little or no fragmentation of the molecule occurs. It is effective because it produces multiply charged molecular ions and hence allows for large macromolecules to be analysed.¹⁰

It works in either positive or negative mode according to the chosen electrical field applied (i.e. either +ve or -ve). The sample is fed through the capillary tube (figure 2.4) and with the help of an electric voltage, the liquid carrying the sample is dispersed into a fine aerosol. The high pressured nebulizer gas, in this case, is inert N₂ gas, further assist in dispersing the sample from the capillary tip into a mist. In order to decrease the droplet size, charged conducting groups like H⁺ and Na⁺ are usually added. Therefore, as the nebulized droplets reach their maximum size and number of charges as permitted by Rayleigh limit, the surface tension increases and the coulombic force eventually overcomes the surface tension of the evaporating solvent.¹⁰ At this point, the droplets explode into smaller, more stable droplets containing fewer analytes and charges. Hot inert N₂ gas is passed into the chamber to cause the evaporation of the aerosolized

sample-solvent thus leaving the analytes in the gaseous phase with different charges. These then move into the vacuum chamber and onto the mass analyser, in this case, the time of flight analyser, which separates the ions according to their respective molecular masses. They then move on to the detector where a software converts the signals into a mass spectrum according to the intensities of their relative abundance and their mass-to-charge ratios.

2.31 Reference

1. <http://restek.com/catalog/view/1709>
2. <http://www.sigmaaldrich.com/catalog/product/sigma/z600822?lang=en®ion=GB>
3. C. Wills, 2016, NMR Laboratory Training Guide, Newcastle University, UK.
4. J. T. Petty, J. Zheng, N. V. Hud and R. M. Dickson, *J. Am. Chem. Soc.*, 2004, **126**, 5207–5212.
5. K. D. Mielenz, *Appl. Opt.*, 1979, **18**, 4134-4137.
6. B. Valeur, *Molecular fluorescence: principles and applications*, 2001, Wiley-VCH, Verlag GmbH, ISBN: 3-527-60024-8 (Electronic).
7. Malvern instruments High-performance particle sizer-The first system to combine High sensitivity with a high concentration capability.
<http://www.instrumentation/malvernpps.pdf>
8. Malvern, 2012, Inform: White Paper; A Basic Guide to particle Characterization. Malvern Instruments Limited, Worcestershire, UK.
9. P. Russo, 2012, DLS_minicourse.doc. <http://macro.Isu.edu/howto>
10. Walters Micromass LCT Premier Mass Spectrometer: Operator's Guide, Waters, Milford, MA. <https://www.instrumentation/waterslctpremiermassspectrometer.pdf>

3 CHAPTER THREE

3.1 RESULTS AND DISCUSSION I

3.2 Synthesis and Characterization of silver nanoclusters (Ag NCs) in Microemulsion

3.3 Introduction

This chapter focuses on the synthesis and characterization of silver nanoclusters (Ag NCs) from silver nitrate (AgNO_3) solution by reduction at room temperature, with equivalent portion of sodium borohydride (NaBH_4) solution in microemulsion, using sodium bis-(2-ethyl hexyl)sulfosuccinate (AOT) as stabiliser.

Samples of $90 \mu\text{M}$ and 1 mM silver nanoclusters were synthesized in two different experiments in microemulsion at room temperature, containing different concentrations of surfactant, water and oil (see Experimental Chapter (Two)). NaBH_4 was chosen for its strength as a reducing agent,^{1,2,3,4} leading to the rapid production of Ag NCs without the requirement of heat, to produce small, monodispersed nanoclusters.

A microemulsion system was used in order to control the reaction by restricting the reactants into small thermodynamically stable (nano/micro-sized) water droplets, often referred to as nanoreactors.⁵ Thereby avoiding the randomized bulk reduction of Ag^+ ions in aqueous solution which quickly results in the growth of large non-fluorescent nanoparticles in the absence of stabilizers.^{1,6,7,8}

A number of Ag NPs of diverse Ag-core sizes have been reported in the literature over the last decade. Suarez and co-workers⁹ in 2007 documented the synthesis and characterization of monolayer-protected Ag NCs in microemulsion by reducing aqueous solution of AgNO_3 with a solution of sodium hypophosphate monohydrate ($\text{NaH}_2\text{PO}_2 \cdot \text{H}_2\text{O}$). ESI-MS results indicated the formation of Ag_3O_2 , Ag_5 , and Ag_9 which were fluorescent. In 2010, Udayabaskararao and

Pradeep reported the syntheses and characterization of Ag₇ and Ag₈ clusters by the reduction of AgNO₃ solution with NaBH₄ in the presence of mercaptosuccinic acid as ligand to produce fluorescent Ag₇(H₂MSA)₇ and Ag₈(H₂MSA)₈ (H₂MSA: mercaptosuccinic acid).¹⁰ They followed this up with the solid-state synthesis of an Ag₉ cluster, again with mercaptosuccinic acid as capping ligand. Baksi *et al.* 2014, synthesized Ag₁₁- glutathione cluster (Ag₁₁(SG)₇) (SG:glutathionate) from the reduction of AgNO₃ with NaBH₄ in the presence of the tripeptide, glutathione (GSH) to produce fluorescent Ag NCs.¹¹ Recently in 2015, Buceta and co-workers announced the synthesis and characterization of Ag₂ and Ag₃ clusters on DNA template,¹² this in their opinion being the first synthesis and characterization of specific Ag cluster size stabilized by DNA using an electrochemical technique without the use of surfactants or capping agents. In a pioneering work in 2004, Petty *et al.*,¹³ documented the successful synthesis of Ag₂ to Ag₈ NCs templated on a 12-mer DNA by reduction with NaBH₄ in aqueous solution. However, the need to prepare tailor-made Ag NCs of a given cluster size and optical properties suited for specific applications remains a major challenge. Ag NCs with unique optical properties find applications in optoelectronics, catalysis as well as nano-biophysical research¹⁴⁻²⁹ catalysis^{30,31,32} electronics³³ photonics³⁴ biological tagging²⁷ and surface-enhanced Raman scattering.^{35,36,37}

3.4 Aims

This chapter aims at exploring the synthesis of precise-size (of a given cluster size) fluorescent silver nanoclusters suitable for specific applications by careful control of the reactants concentrations and the reaction stoichiometry, as well as temperature, and the droplets size, with the view to producing ultra-small, precise-size, fluorescent Ag NCs passivated by inorganic ligands, instead of DNA, thiol- or phosphorus-containing organic ligands.

3.5 Microemulsion reaction scheme for Ag NCs synthesis

Ultra-small Ag NCs were produced by dissolving appropriate amounts of AgNO₃ and NaBH₄ salts in a given volume of deionized water to obtain stock solutions from which 90 μM and 1 mM of the AgNO₃ and NaBH₄ were obtained by serial dilution. Each of the reagents was put into two different isooctane solutions, containing dissolved AOT surfactants to obtain water-in-oil microemulsions. These were then mixed together (figure 3.1 below) and stirred for five

minutes at about 500 revolutions per seconds (rps) on a magnetic stirrer with the aid of a clean stir bar inserted into the mixture (see Experimental Chapter (Two)).

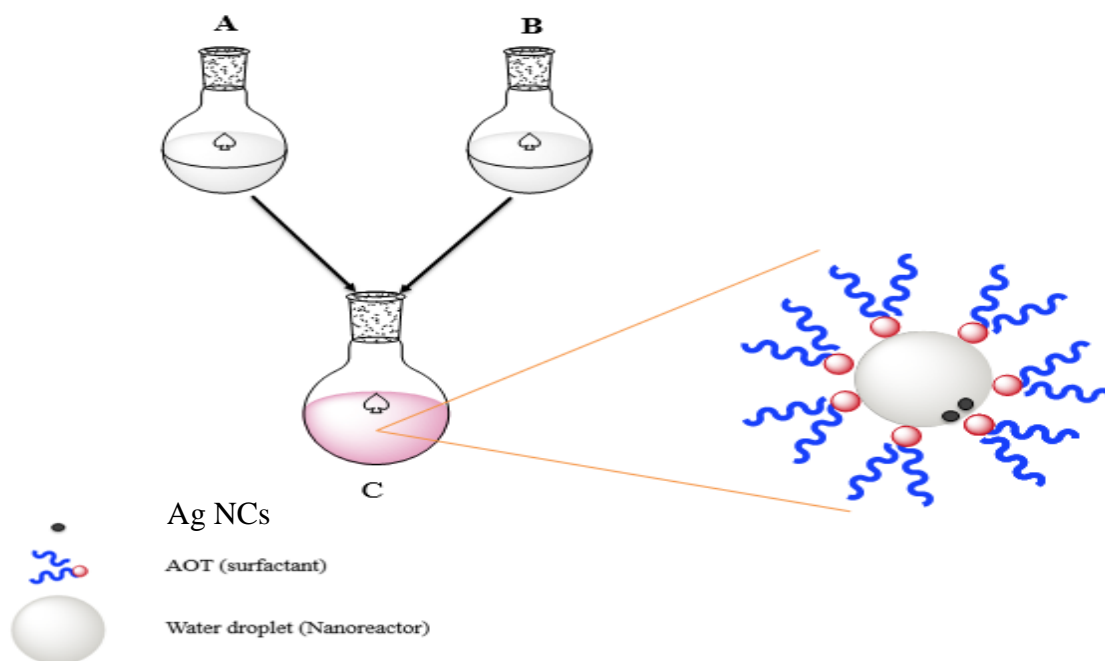


Figure 3.1: Reaction scheme for Ag NCs synthesis by mixing microemulsions (A) AgNO₃ in oil + water + AOT, and (B) NaBH₄ in oil + water + AOT (C) Ag NCs all in microemulsion.

3.6 Ultraviolet-visible spectroscopy

Figure 3.2a is a typical spectrum showing surface plasmon resonance (SPR) peaks of metallic silver nanoparticles obtained from the reduction of Ag⁺ ions by sodium borohydride in aqueous solution. It is apparent that the intensity of the plasmon resonance peak increases with increasing Ag NPs concentration. The pictures inset further highlight the difference in the concentration of the Ag NPs in aqueous solution.

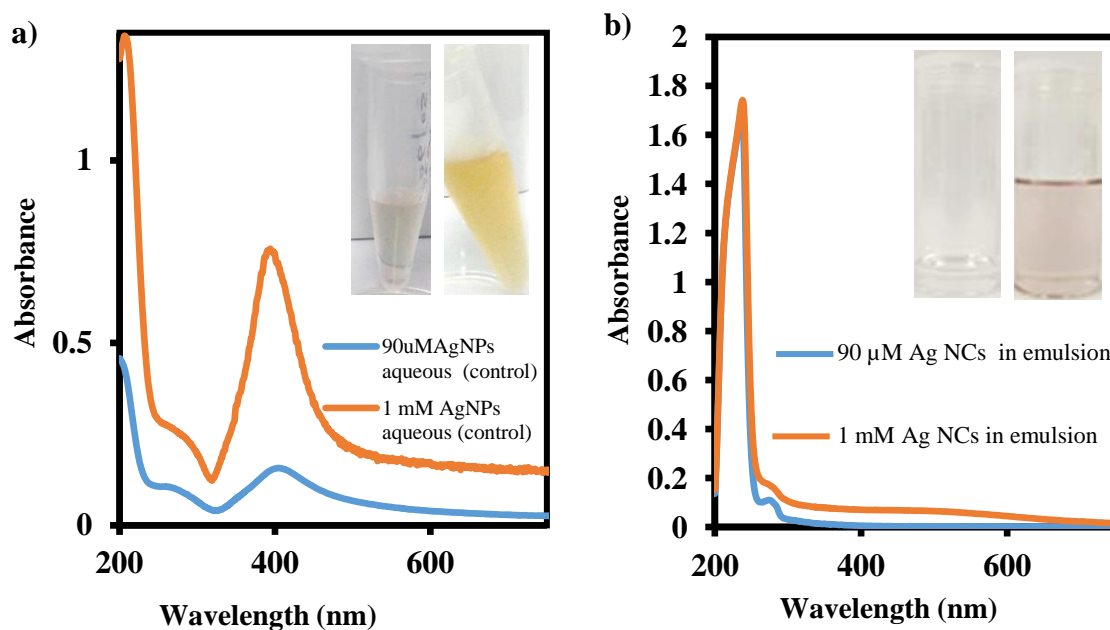


Figure 3.2: Plasmon resonance peak of $90\ \mu\text{M}$ and $1\ \text{mM}$ Ag NCs in (a) samples synthesized in bulk aqueous solution (not microemulsion system) (b) microemulsion-synthesized samples.

Figure 3.2b is the UV-Vis spectra of the $90\ \mu\text{M}$ and $1\ \text{mM}$ Ag NCs microemulsion samples. Inset is the picture of both samples, the near colourless (left) is the $90\ \mu\text{M}$ sample, and the $1\ \text{mM}$ is the pink sample on the right. The spectra of both samples do not show the usual resonance plasmon band of large metallic Ag NPs. This demonstrates that we have not produced large Ag NPs, rather, it indicates that small clusters of Ag have been synthesized. Silver nanoparticles (Ag NPs) are known for their characteristic resonance plasmon peak around 420-430 nm.^{11,13,38-40} The phenomenon of surface plasmon resonance (SPR) is consistent with large Ag NPs which contains more than 20 or 30 silver atoms^{41,42} with no bandgap, which are expectedly nonfluorescent.

The reduction of Ag (I) ions in water-in-oil microemulsion system ensured that small Ag NCs were formed, comprising of fewer than 10 atoms of silver.^{2,43} These Ag NCs were also prevented from aggregating to large NPs by the restriction proffered by the water droplets. This is why the prominent SPR band usually observed in the bulk phase was not observed in the UV-Vis spectra of the emulsion-synthesized samples as can be seen in figure 3.2b. However, under the same reaction conditions but this time in the aqueous bulk phase (without the emulsion system) the intense SPR peaks is prominent in the spectra of the samples (figure 3.2a), this is typical of large nonfluorescent Ag NPs which are known for their yellow colouration.⁴⁴

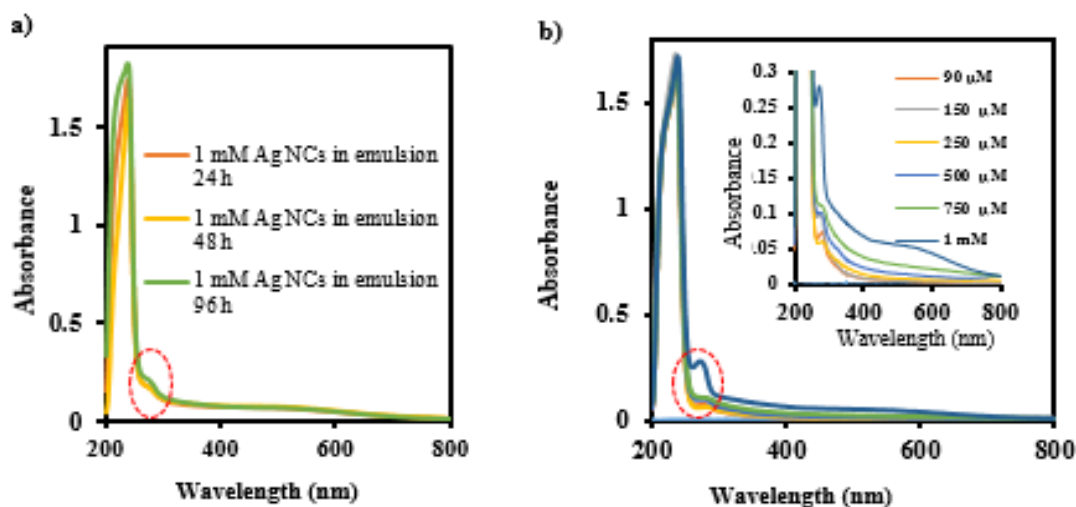


Figure 3.3: UV-Visible spectra for (a) 1 mM Ag NCs in microemulsion, observed for 96 hours period (b) 90, 150, 250, 500, 750, 1000 μM Ag NCs in microemulsion.

Figure 3.3a shows the change in the UV-Visible absorbance band of the 1 mM Ag NPs for a period of 96 hours post-synthesis in order to investigate the effect of ageing on the absorbance intensity of the surface plasmon peak. This showed a marginal increase in intensity over the course of time, suggesting that particles may be aggregating.

Meanwhile, increases in the concentration of silver ions [Ag^+] in the droplets of the emulsion system led to a corresponding increase in the concentration of the resulting Ag clusters as was represented by the resulting absorbance values which can be seen inset in figure 3.3b (above).

Both samples synthesized by the microemulsion method, and the bulk (aqueous) system show a peak at approximately 280-290 nm (encircled in red in Figure 3.3a&b). This peak is attributed to Ag_4^{2+} clusters reportedly formed immediately following the addition of NaBH_4 by Petit *et al.*⁴⁵ This usually appeared even before the onset of the plasmon band at 400 nm, and gradually diminishes in intensity as the 400 nm plasmon band intensity increased with time. The appearance of this peak according to Petit and co-workers¹¹ is indicative of the formation of this Ag_4^{2+} soon after mixing the reactants.

3.7 Fluorescence

It has already been reported that nanoparticles of silver and gold usually larger than the Fermi wavelength of an electron (~ 0.5 nm) would not be expected to fluoresce.^{14,46} Therefore having shown already by the absence of a resonance plasmon peak (absorption above), it becomes necessary to demonstrate that small nanoclusters have been made by observing their fluorescence properties.

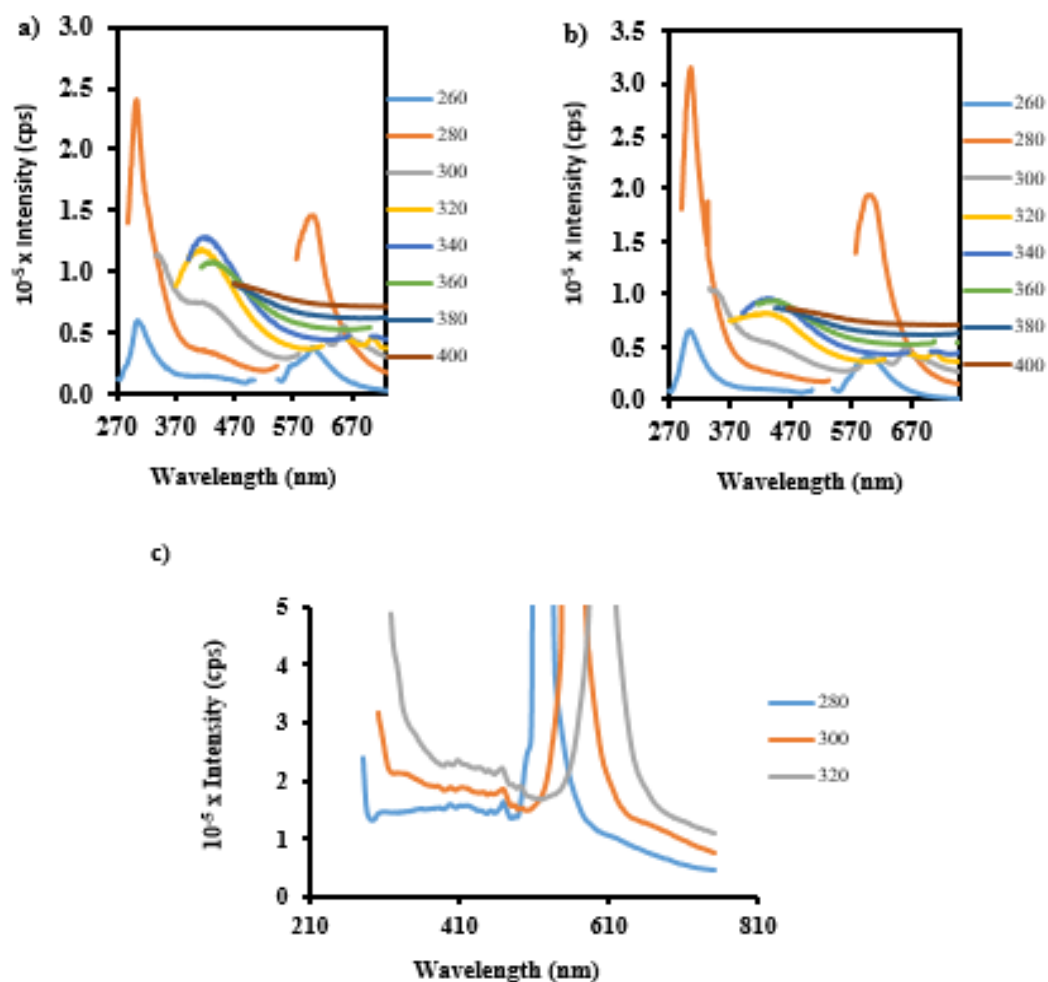


Figure 3.4: Fluorescence spectra for (a) $90 \mu\text{M}$ (b) 1 mM Ag NCs in microemulsion at $\lambda_{\text{exc.}} = 280 - 400$ nm. Raman peaks and the second order scattering have been removed. (c) Emulsion only (no AgNO_3 and NaBH_4) excited at $\lambda_{\text{exc.}} = 280 - 320$ nm, containing Raman and second order scattering peaks respectively.

The emission intensities of the $90 \mu\text{M}$ and 1 mM concentration samples of Ag NCs were studied by scanning over a wide range of excitation wavelengths, from 260 - 700 nm at consecutive increments of 20 nm. Results in figures 3.4(a) & (b) show that both microemulsion samples

fluoresce. However, above 400 nm excitation wavelength, no fluorescence was observed. Samples notably produced blue fluorescence, consistent with small NCs within the zone of confinement usually with large bandgaps.^{47,48} This indicates that light whose energies fall within the ultraviolet region was absorbed, leading to the translation of excited electrons (excitons) from the highest occupied molecular orbital (HOMO) to the lowest unoccupied molecular orbital (LUMO). The absorption of light energy from the ultraviolet region gives a further indication of the size of these silver nanoclusters, since the size and by extension the number of atoms in the cluster, correlate with the magnitude of the bandgap.⁴⁹ A large HOMO – LUMO gap is a characteristic of ultra-small NCs which, according to Zeiger,⁵⁰ is one factor together with closed electronic shells, are related to their stability. Figure 3.4(c) is the spectrum of the emulsion only (without the analytes), this is the control sample. The large cut off peaks are the second order scattering (between 410 – 700 nm).

Generally, three emission peak distributions are indicated in the emission spectra of the samples at 305, 430, and 607 nm respectively. A formula reported by Buceta et al,¹² relates cluster size with the emission wavelength in equation 3.1 below:

$$N = \left(\frac{E_F}{E_g} \right)^3 \quad (3.1)$$

Where E_F and E_g are the Fermi level (5.4 eV for bulk Ag) and the HOMO–LUMO energy bandgap, respectively.¹²

By this formula (3.1) therefore, the three emission bands in the spectra above correspond to two, six, and eighteen atoms of silver respectively. The latter (eighteen) is considered to be aggregates/coalescents of the smaller clusters. Based on the intensity values (counts per second) of these bands, the Ag_2 clusters emitting at ~305 nm (bandgap of 4.1 eV) in Figure 3.4a and 3.4b are obviously higher in concentration. The sharp nature of the 305 nm (Ag_2) emission band shows that these clusters are better passivated.

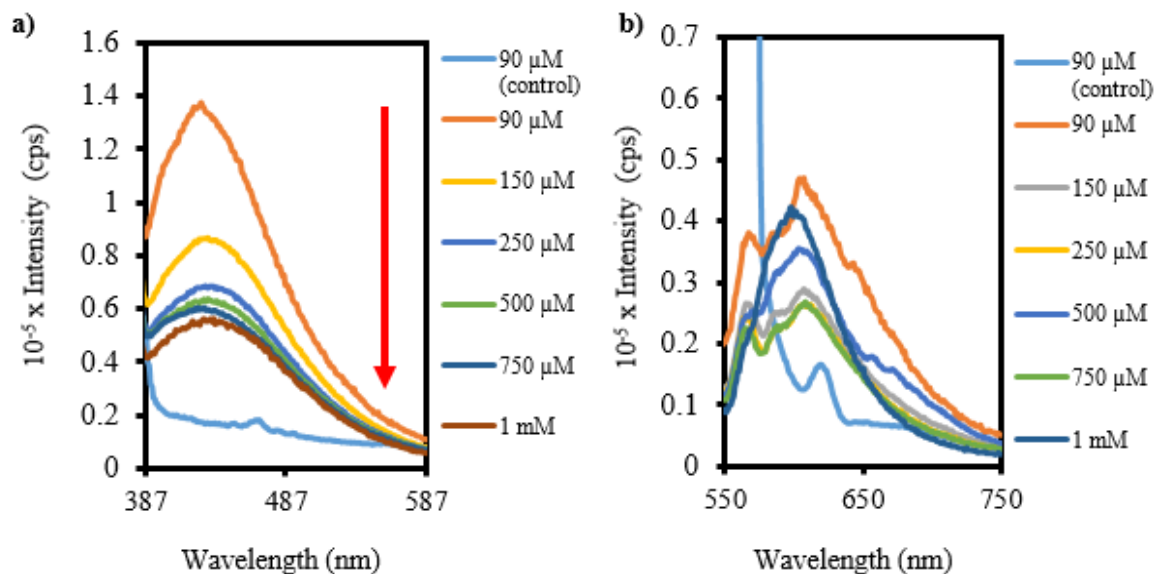


Figure 3.5: Emission spectra of increasing concentrations of silver nanoclusters ($\lambda_{exc.} = 340$ nm) centred at (a) 430 nm (red arrow indicates decreasing intensity with increasing concentration of Ag) (b) 608.

Furthermore, in order to understand the effect of increasing concentration of Ag ions on fluorescence and fluorescence intensity, microemulsion samples of 90, 150, 250, 500, 750, 1000 μM and the 90 μM aqueous (control) sample were studied. Intensities at two distinct emission wavelengths of 430 and 608 nm were monitored and plotted out in figures 3.5 (a) & (b) above. From these spectra, it can be deduced that the emission intensity decreases with increasing [Ag]. This is obviously the case in figure 3.5(a) whose trend of decreasing emission intensity corresponds with increasing concentrations of Ag. That is, there is an inverse relationship between fluorescence intensity and concentration of silver nanoclusters.⁵¹ This inverse relationship is also associated with the inner-filter effect.^{52,53,54} This trend was not exactly replicated in the emission intensities of the band at 608 nm (figure 3.5b), possibly because these 608 nm emission bands are thought to be associated with aggregated particles. Nonetheless, the least concentrated sample (90 μM) yet again recorded the highest intensity at 608 nm.

Very pertinent to note in figures 3.5a&b is the emission intensities of the 90 μM aqueous (control) sample at these (430 and 608 nm) observed wavelengths. There was apparently no fluorescence emission from this (control) sample when compared with the microemulsion

samples. Rather in fig. 3.5b, what was observed in this case looks seemingly like the Raman peak for water⁵⁵.

Meanwhile, with further interest in the emission at 430 nm, an excitation study was undertaken to ascertain the exact wavelength(s) of absorption responsible for this emission (figure 3.6a). It was observed that the emission at 430 nm was occasioned by the absorption of light energy at 318.5, 346.5, and 381.5 nm (3.90, 3.58, 3.25 eV) respectively. These imply electron transitions from different electronic states of the NCs' valence band to the conduction band.

A large Stokes shift value of 111.5 nm was observed for the clusters. This Stokes shift is an indication of deep energy trapped states, an observation which is consistent with incomplete metal-core surface passivation by capping ligands.^{11,56,57} Therefore, improving the surface passivation around the clusters would translate to an increase in quantum yield (ϕ_f) and applicability. The relatively narrow emission bandwidth of these clusters gives it an advantage in it being used as sensors over the usually very broad emission bands of DNA-templated nanoclusters of approximately 200 nm bandwidth.⁵⁸

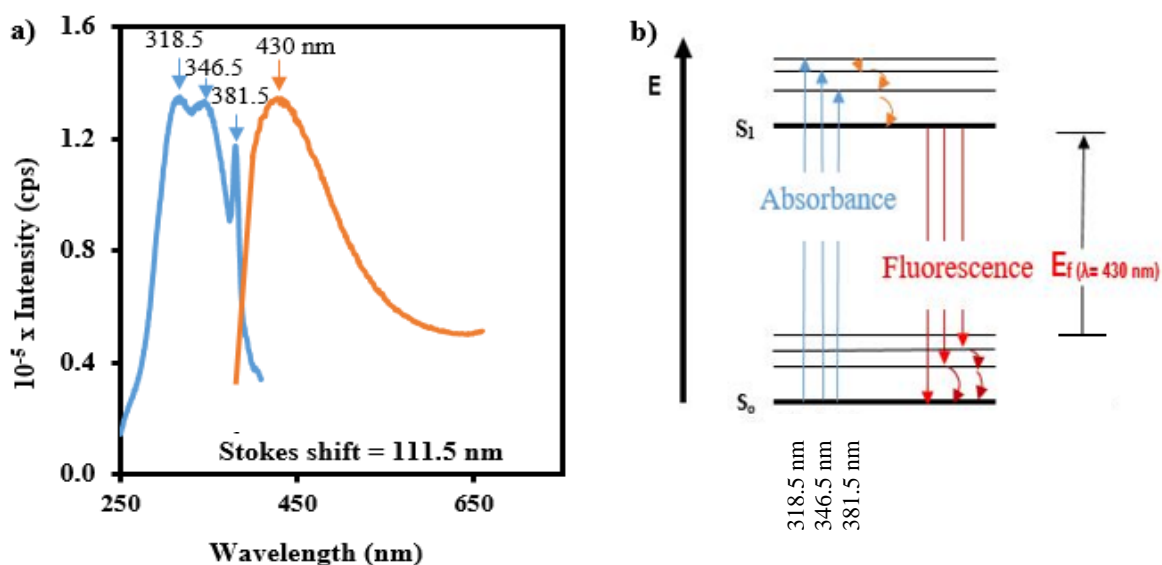


Figure 3.6: (a) Excitation and emission (blue/orange) spectra of silver nanoclusters at 430 nm, with Stokes shift value of 111.5 nm. (b) Schematic representation of data in the form of a Jablonsky diagram.

Figure 3.6b shows the stages of absorption of light energy at 318.5, 346.5, and 381.5 nm which may correspond to electronic state transitions of electrons from different orbitals of the HOMO to the LUMO; followed by a series of nonradiative vibrational relaxations and the eventual

return to the ground (singlet) state accompanied by the release of photons of light energy in the form of fluorescence with an (emission) energy of 2.88 eV (~ 2.9 eV) corresponding to 430 nm.

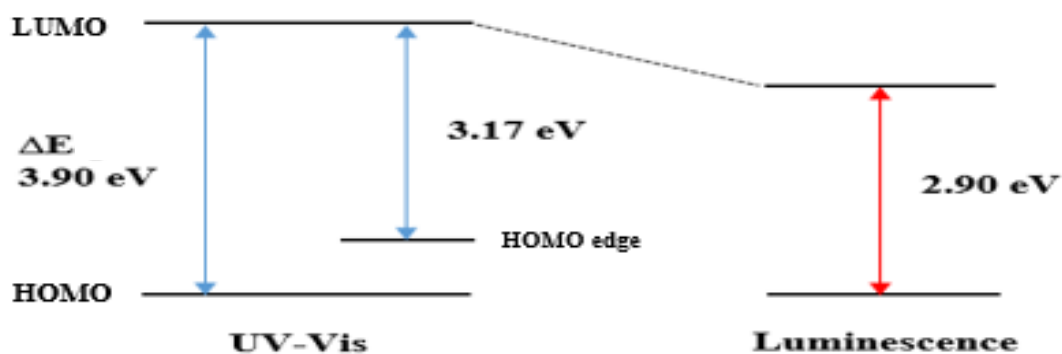


Figure 3.7: Bandgap energy diagram of the Ag NCs samples, adapted from Dolai *et al.*, 2013.⁴⁹

These NCs show the highest energy absorbance at 318.5 nm (~ 3.90 eV) as earlier reported in the preceding paragraph, and an absorption (HOMO) band edge of 391.5 nm (3.17 eV) (figure 3.7). It also has a bandgap of 2.88 eV as earlier stated.

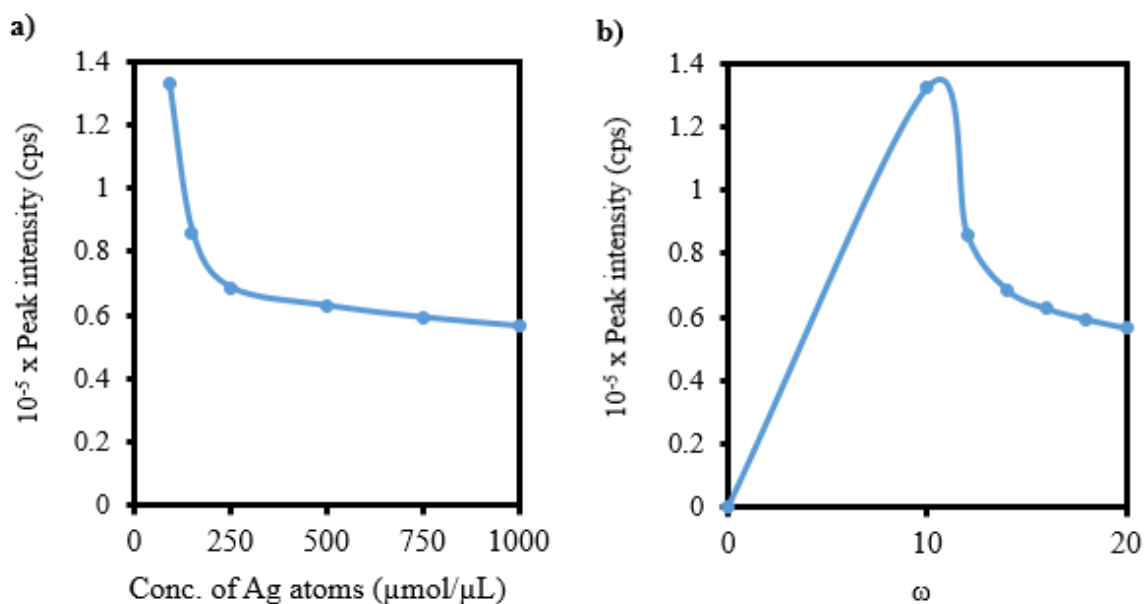


Figure 3.8: Graph of the relationship between fluorescence peak intensity centred at 430 nm vs (a) Ag concentration and (b) $\omega = ([\text{H}_2\text{O}]/[\text{AOT}])$.

The decreasing pattern of fluorescence intensity with rising Ag ion concentration is made clearer in figure 3.8a. For an increase in Ag atom concentration from $90 - 1000 \mu\text{M}$ (increase factor of 11 times), there was a concomitant decrease in intensity by a factor of 2.5 times the emission value of the $90 \mu\text{M}$ sample. Thus, intensity is expected to further decrease as concentration increases, until a near plateau state is reached at high concentrations where presumably clusters are no longer being formed but increasingly larger non-fluorescent Ag NPs.

On the other hand, when the fluorescence intensity was measured against the increasing ω -values to see how this varied with the other in terms of the emission intensity maximum (Fig. 3.8b), emission intensity rose to a maximum at an ω -value of 10, before dropping down consistently to a minimum at an ω -value of 20. This indicated that a ω -value of 10 maybe the most efficient for preparing these Ag NCs in the microemulsion. ω is the ratio of the concentration of water to that of the surfactant in the emulsion system and dictates the size of the droplet.^{5,59}

3.8 Dynamic light scattering studies

It is difficult to measure directly the particles size of the nanoclusters in the microemulsion. However, it is rather more plausible to obtain the hydrodynamic diameter of the water droplets in the emulsion system.

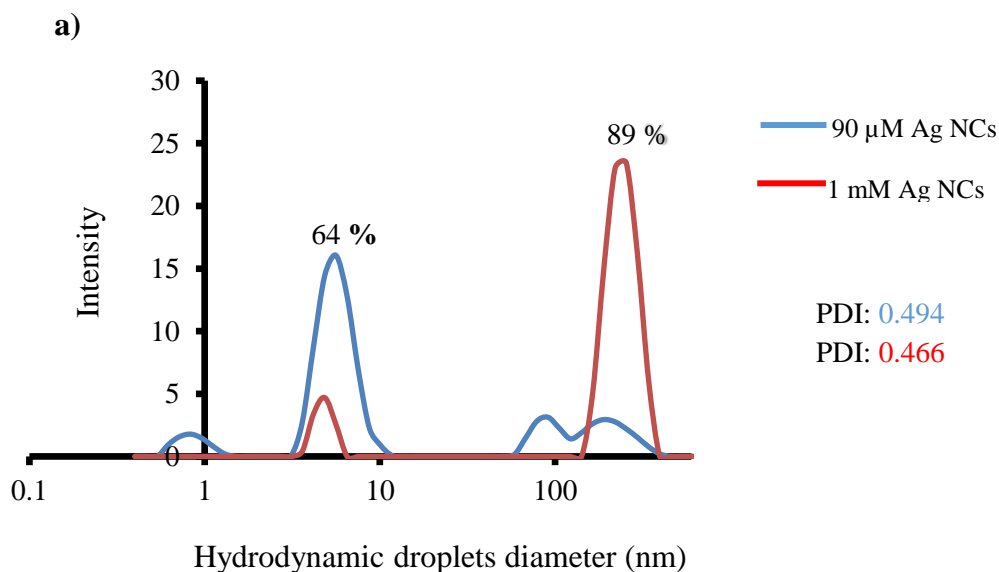


Figure 3.9: DLS charts of the intensity of light scattering of water droplets in microemulsion 90 and $1000 \mu\text{M}$ Ag NCs samples.

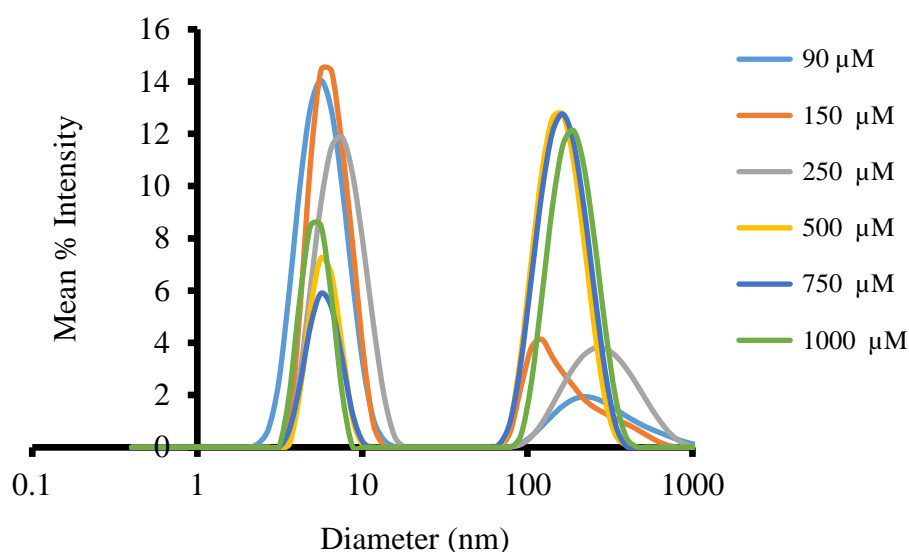


Figure 3.10: DLS charts of the intensity of light scattering of water droplets in microemulsion at varying concentrations (90-1000 μM) Ag NCs.

Table 3.1: DLS samples data for varying ω (and AOT conc.) size and changes in physical parameters.

S/No.	ω	Diameter / nm	Intensity (Peak 1) %	Intensity (Peak 2) %	Conc. (AOT) / M
1	10	5.615	16.06	1.183	0.0005
2	12	5.615	11.41	4.393	0.0007
3	14	5.615	11.16	3.954	0.0010
4	16	11.70	4.246	8.337	0.0017
5	18	13.55	5.856	11.11	0.0022
6	20	4.849	4.694	24.44	0.0025

In figure 3.9, two particles size distributions were obtained: one with an average size of 5 nm and the other ranging between 100-255 nm. It is thought that the former are reverse micelles, and the latter, water droplets.^{60,61} The 5 nm particles size consist of approximately 65 % of the 90 μM sample distribution, while the 100-255 nm size range accounted for approximately 90

% of the 1 mM sample distribution. Rayleigh fitting of the UV-Vis data for both the 90 μM and 1 mM samples to the theory, gave a droplet size of \approx 50 nm (see Appendix fig. 8.3). Hence, it

was considered that the 100-250 nm maybe a group of coalesced droplets. Therefore, the ω value of 20, and its surfactant concentration (0.0025 M) was regarded as being ideal in terms of having $\approx 90\%$ of the droplets being in this (100-250 nm) size range (figure 3.9). In both the 90 μM and 1 mM samples, the 100-255 nm size dimension was considered to be the reaction centre for the synthesis of Ag NCs, since the 5 nm reverse micelles may not contain enough concentration of Ag^+ ions to form Ag NCs, bearing in mind its volume.

Figure 3.10 confirmed the earlier observation in figure 3.9 that two particles size distribution were observed irrespective of the ω -value and surfactant concentration (see table 3.1). Also in table 3.1, as the ω -values increased and AOT concentration rose from 0.0005 to 0.0025 M, the trends in the intensities of the scattered light reversed after an ω -value of 14 in favour of the larger 100-200 nm particles (peak 2) as the percentage proportions of this larger particle size increased.

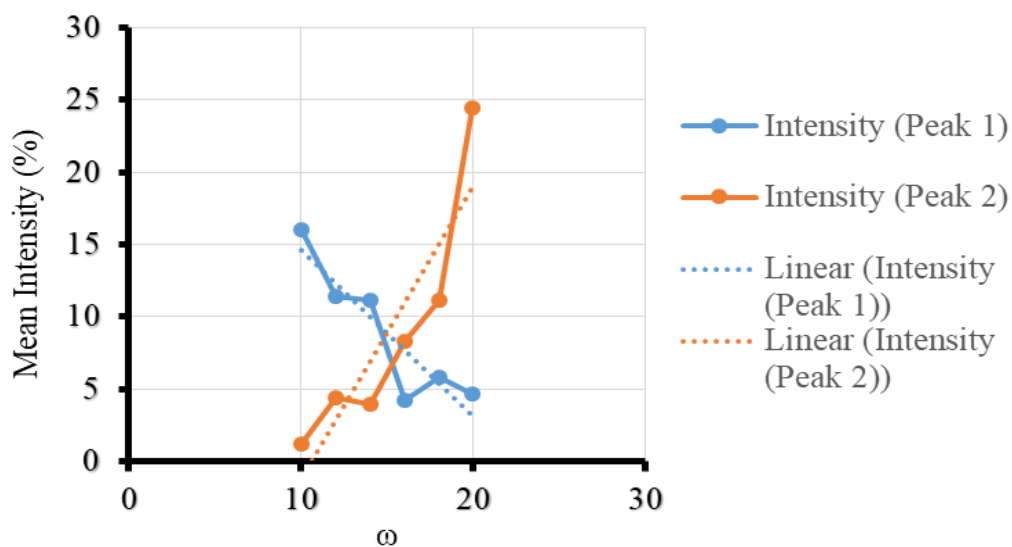


Figure 3.11: DLS peak intensity vs ω (AOT concentration).

A plot of peak intensity (for peaks 1 and 2), vs ω -values in table 3.1 above, show a good trend between intensity and ω (increasing AOT concentration) (figure 3.11). It is apparent from table 3.1, that whereas the intensity of the scattered light by mobile “particles” of the 5 nm dimension (peak 1) decreased with rising ω -values, the intensities of the scattered light by the > 100 nm size “particles” of peak 2 increased with increasing ω -values. This further strengthens our proposition that the Ag NCs are more likely to be resident in the larger droplets (Peak 2).

Closer observation of the values of the reverse micelle diameter at the 5 nm region for both the $90\ \mu\text{M}$ and $1\ \text{mM}$ samples (see table 3.1), shows a contraction in reverse micelle size (4.85 nm) for the $1\ \text{mM}$ sample from 5.62 nm in the $90\ \mu\text{M}$. This has been attributed to the effect of increased concentration of monolayer-forming surfactant molecules around the water droplets. This is thought to be responsible for the shrinking effect observed in the $1\ \text{mM}$ droplet-size at the 5 nm region. Similar observation was reported by Pietrini.⁵

3.9 Fluorescence microscopy

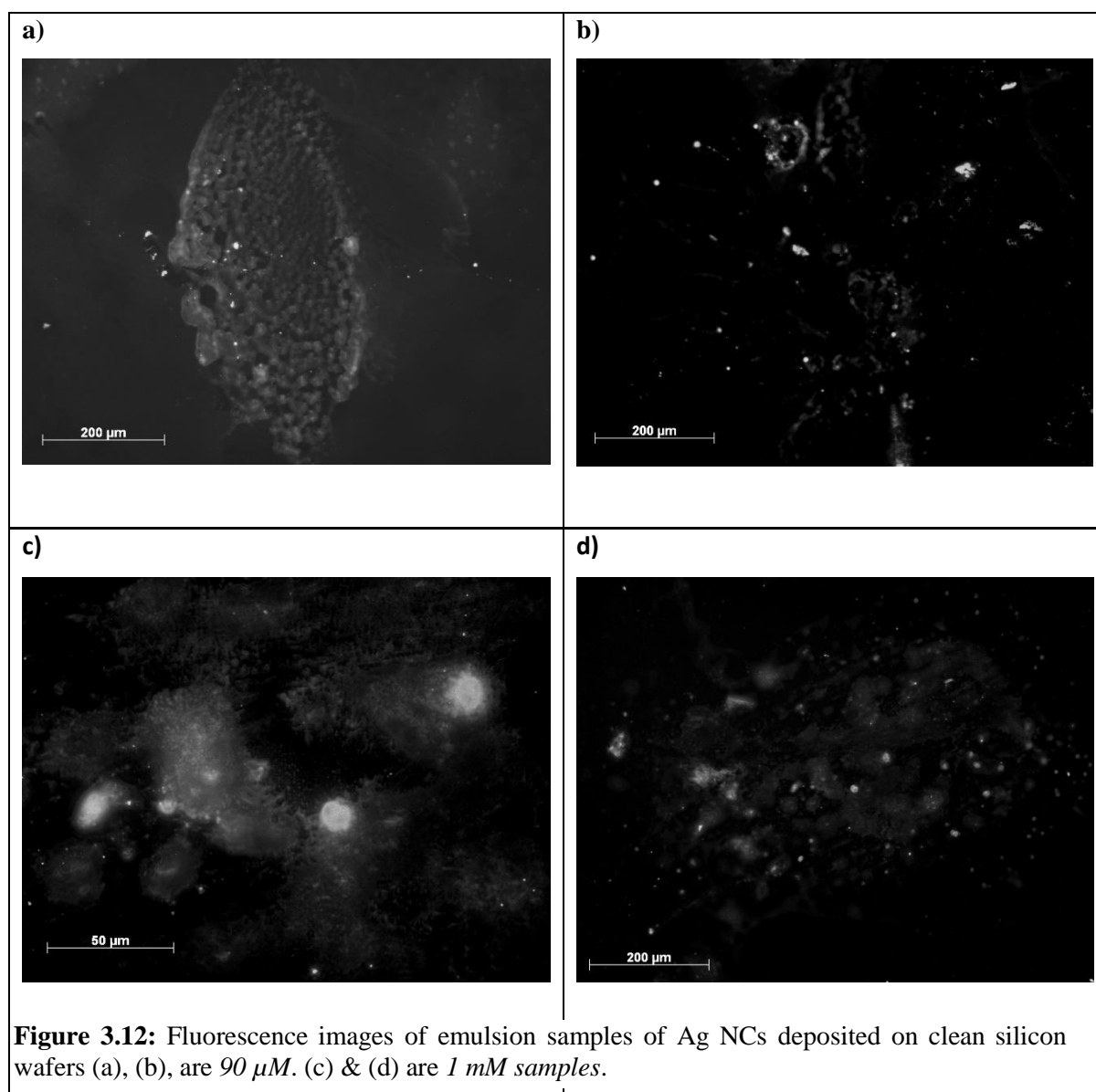


Figure 3.12: Fluorescence images of emulsion samples of Ag NCs deposited on clean silicon wafers (a), (b), are $90\ \mu\text{M}$. (c) & (d) are $1\ \text{mM}$ samples.

Emission properties of the Ag NCs were further studied by fluorescence microscopy, having excitation and emission wavelengths of 365 and 420 nm respectively and an exposure time of 52 s and 47 s for the $90\ \mu\text{M}$ and $1\ \text{mM}$ respectively. Images obtained (figure 3.12 above) show

fluorescence from both samples. These demonstrate that the samples contain luminescent Ag NCs as anticipated.

3.10 Transmission electron microscopy (TEM)

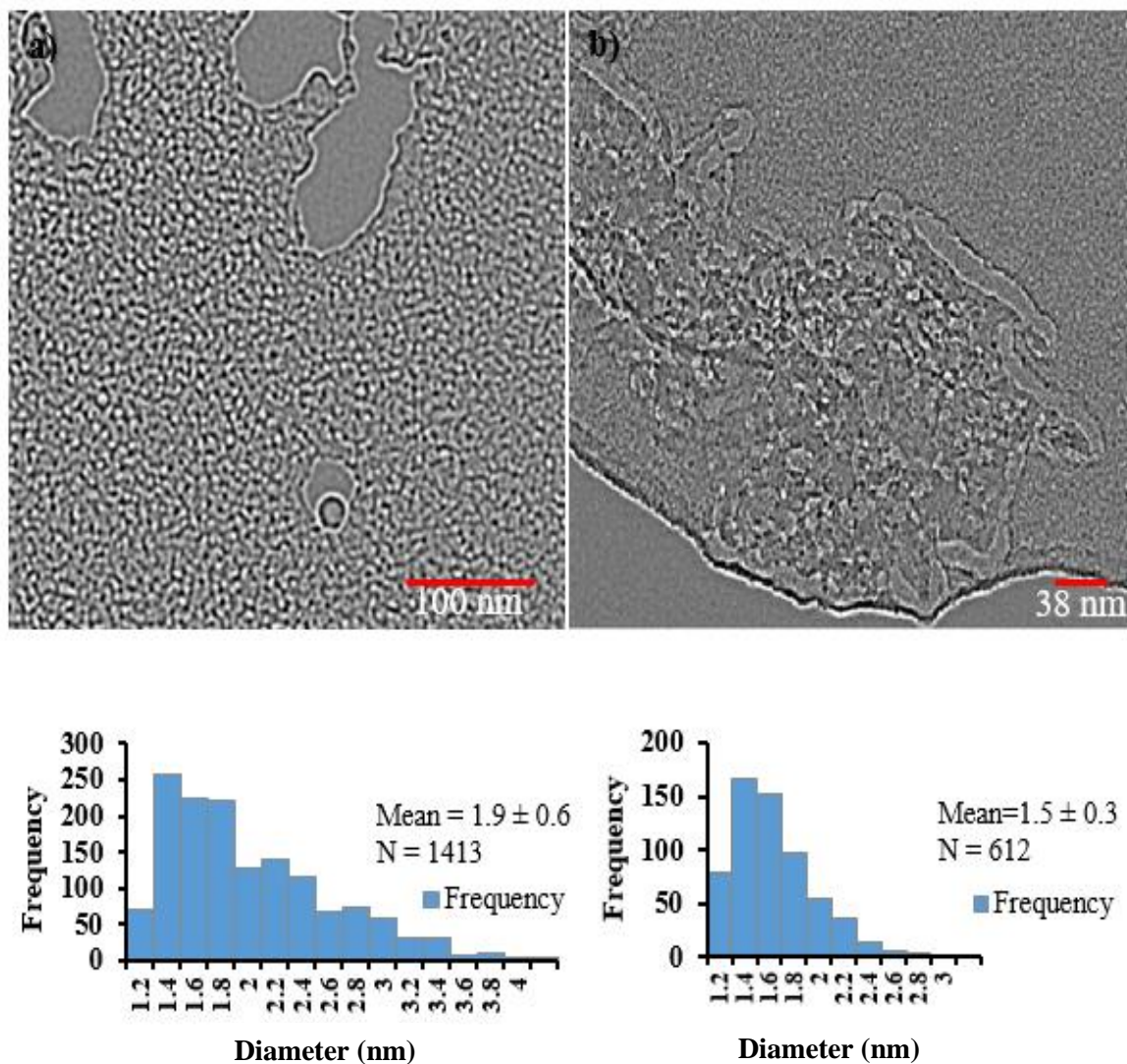


Figure 3.13: TEM images of (a) 90 μM and (b) 1 mM Ag NPs on holey-carbon grid; and particles size distribution histograms (below).

TEM images and particles size distribution of the samples are displayed in figure 3.13 above, showing Ag NPs enmeshed between surfactant molecules. Some of these particles can be observed lined along the fringes of the samples on the carbon grid in figure 3.13b. Statistical analyses of these particles sizes revealed mean diameters of 1.5 ± 0.3 nm for the 90 μM and 1.9 ± 0.6 nm for the 1 mM samples. A modal particles size of 1.4 nm for both samples was recorded

as can be seen in the histograms of both samples. Indicating that the bulk of the particles is of this 1.4 nm size going by the frequency counts, even though other larger particles sizes above that were also observed which are considered to be indications of coalescence/aggregation. The process of drying up the samples after spotting on the grids prior to measurement may further promote aggregation. Besides, there is also the issue of the instrument's limitation to precisely differentiate particles of less than 0.3 nm size differences; besides, the NCs are also known to melt under the intense electron beam.^{62,63} Meanwhile, the average Ag NCs diameter of 1.4 nm obtained in this study are close to the less than 2.0 nm size obtained for Ag₂, Ag₃, and Ag₅ in a previous study by Diez *et al.*¹⁵

3.11 Atomic force microscopy (AFM)

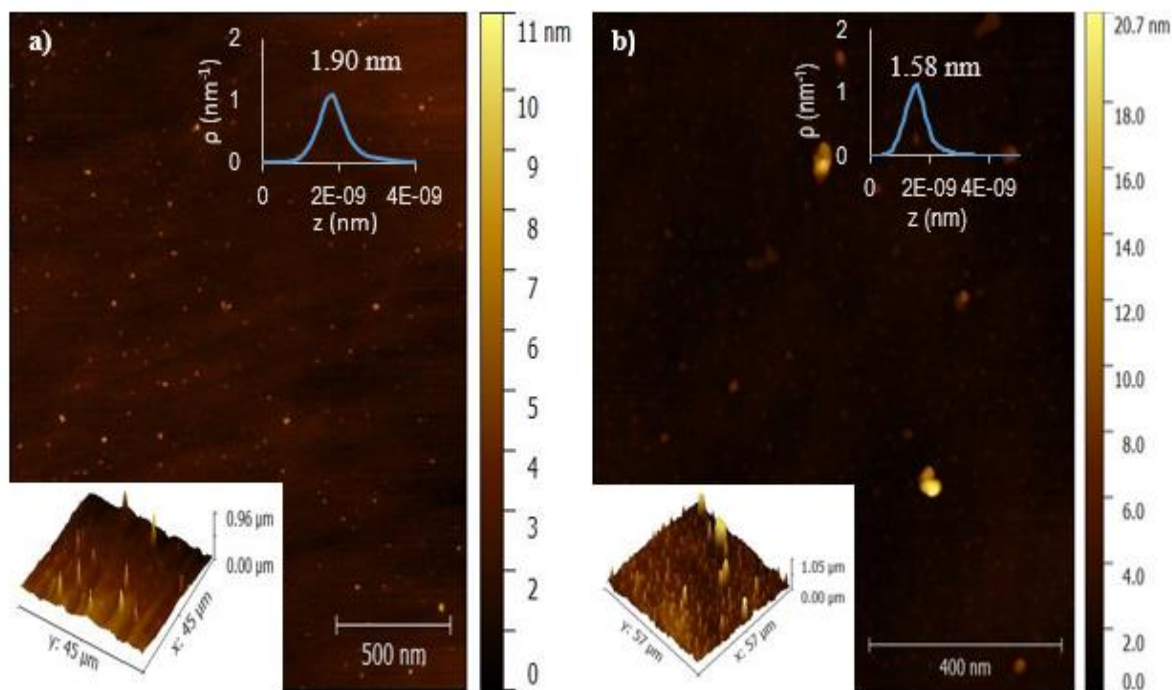


Figure 3.14: AFM images (a) $90 \mu\text{M}$ (b) 1 mM Ag NPs drop-casted on clean silicon wafers. Inset: Probability chart of particles sizes.

Figure 3.14, show results of Atomic Force Microscopy (AFM) analyses of the Ag NCs samples. These 3D images further confirm the synthesis of silver nanoparticles as well as verifying the particles sizes. The charts inset of both images represent a probability function which predicts the size of the particles under the Gaussian curve. Thus, the peak of the area represented by the Gaussian curve represents the mean particle size. The coordinate of this point on the y-axis represents the probability value. Therefore, the probability of finding particles of 1.90 and 1.58

nm (figures 3.14a&b) respectively is ~ 1 . The particle sizes obtained from the AFM measurements corroborates those earlier obtained from the TEM.

3.12 Electrospray ionization mass spectroscopy

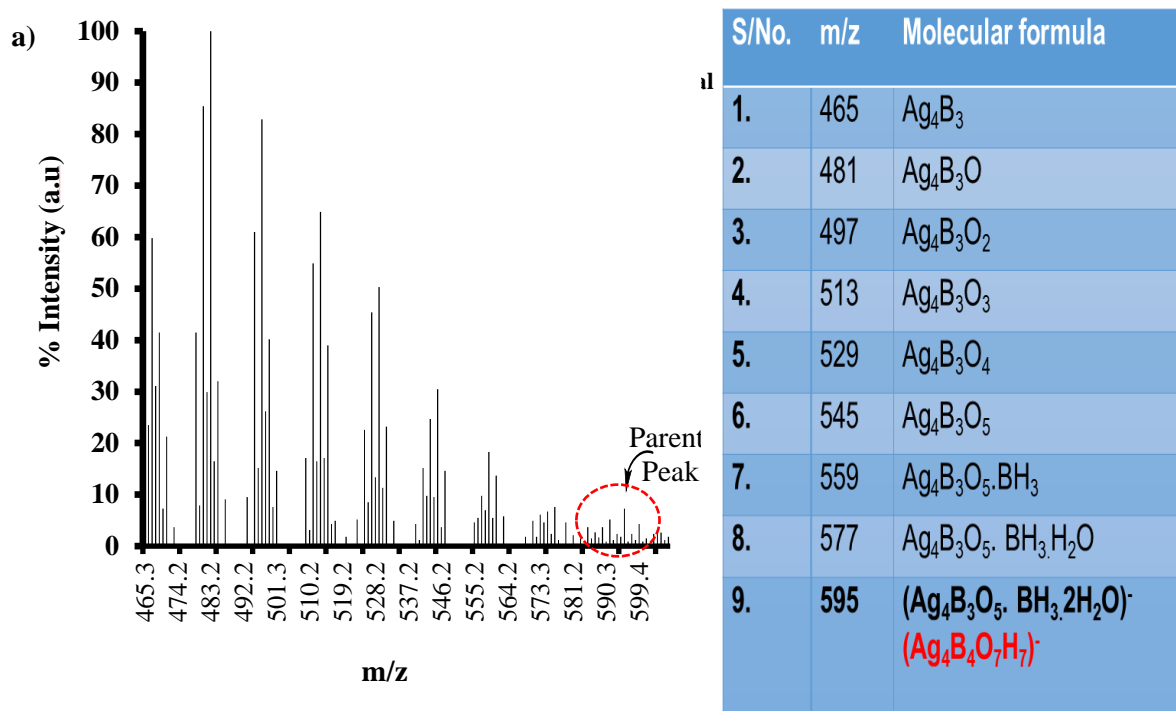


Figure 3.15: ESI-MS spectrum of both 90 μ M and 1 mM Ag NCs corresponding to $[\text{Ag}_4\text{B}_3\text{O}_5.\text{BH}_3.2\text{H}_2\text{O}]^-$ i.e. $[\text{Ag}_4\text{B}_4\text{O}_7\text{H}_7]^-$.

Electrospray ionization mass spectrometry (ESI-MS) result is presented in figure 3.15 (above) showing a series of nine peaks within the m/z range of 465 to 595 of immediate analytical significance. The peaks at m/z 465, seem to correspond to Ag₄B₃. While the next sets of five peaks (m/z 465 to 545) are consecutively different from each other by an m/z factor of 16 (15.9998) corresponding to one oxygen atom, therefore giving a total of five atoms of oxygen. This is followed by another set of peaks different from the former by a mass increment of 14 (13.999) at m/z 559 representing to the (BH₃) group. Finally, there are two consecutive m/z gains of 18 (17.9988) which translates to two molecules of H₂O (from m/z 577 to 595). No clusters of silver was detected in the lower m/z below 465 to 595 m/z range. Beyond this (m/z 595) also, no Ag peaks were observed in the higher m/z 600 – 1400 range, a likely indication of the absence of larger cluster sizes. Hence the peak at m/z 595 is referred to as the *parent peaks*.

Also deduceable from the spectrum is the separation between successive Ag peaks of the same isotopic abundance, which gave a value of $\Delta = 2$ units. This corresponds to a charge of -1 ; the scan having been done in the negative ion mode. The positive mode did not reveal any discernible information.

In conclusion therefore, the parent peaks at m/z 595 in the spectrum corresponds to $[\text{Ag}_4\text{B}_3\text{O}_5\cdot\text{BH}_3\cdot 2\text{H}_2\text{O}]^-$ i.e $[\text{Ag}_4\text{B}_4\text{O}_7\text{H}_7]^-$. This experimental result matched well with the simulated (calculated) version presented inset in figure 3.15b. The simulated results were obtained using the University of Manchester Fluorine-chemistry software, as well as the Water's ESI instrument software (see Appendix fig. 8.8). The as-synthesized Ag NCs were comprised of four atoms of silver all in the oxidation state of zero, with borate, borane, and two water molecules as ligands with the compound having a net charge of -1 .

3.13 Calibration curve for concentration vs number of silver atoms

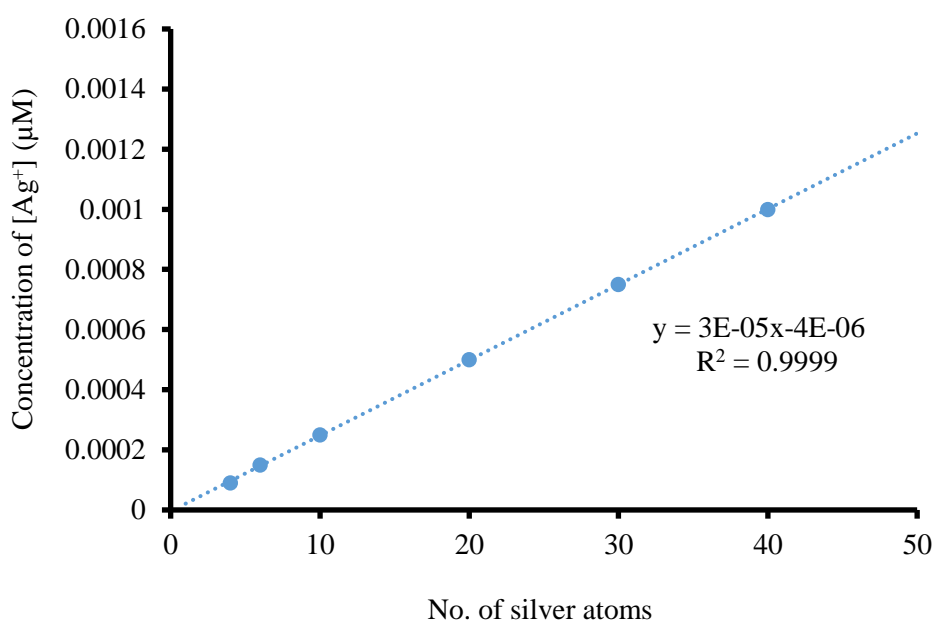


Figure 3.16: Calibration curve of number of atoms of silver per droplet (using the 50 nm droplets size obtained from Rayleigh curve fitting) against increasing $[\text{Ag}^+]$ concentration.

Fitting the UV-Vis data with the Rayleigh theory gave a droplet diameter of 48.3 nm for the samples (see Appendix fig. 8.3); having already concluded that there were no silver atoms in the 5 nm particle size which has already been assigned to reverse micelles in the DLS results. Taking an average droplet diameter of 50 nm for the $90 \mu\text{M}$ and 1mM samples therefore, the

number of silver atoms per sample was calculated from the concentrations of the silver ions. In this way, the total number of silver atoms contained in the concentration ranges of 90, 150, 250, 500, 750, and 1000 μM were determined per droplet and plotted out in figure 3.16 to obtain a straight line curve. From this, the 90 μM sample would have a 4-atom cluster of silver (Ag_4), or two 2-atom Ag clusters per droplet, and the 1 mM, approximately 40 Ag atoms comprising ten 4-atom clusters. The concentration-dependent decreases in the fluorescence emission (max) intensities of the 90, 150, 250, 500, 750, and 1000 μM samples were shown in Fig. 3.5 above, this tallies with the increasing number of Ag atoms (concentration) in the calibration curve above and points at inner filter effect.

Notwithstanding the number of Ag atoms produced, it appears that certain “magic number” cluster sizes (in this case, Ag_2 and Ag_4) were favoured as indicated by the similarities in emission spectra for both the 90 μM and 1 mM Ag NCs samples presented in Fig. 3.4 above. Invariably therefore, these reactions followed the mechanism presented below:



This then complexes with another Ag^{+} ion in solution



Ag_2^{+} dimerises



Lastly, reduction of Ag_4^{2+}



Notice that this mechanism favours the formation of Ag_4 from Ag_2 , preferring instead to dimerise rather than forming the intermediate Ag_3 . A similar mechanism has been reported by Antoku, and Hilpert *et al.*^{64,65} This would suggest that Ag_4 is energetically more stable than Ag_3 . More so, if it is considered that the structure of Ag_3 may likely entail a higher degree of “ring” strain (bond length and angle) than that of Ag_4 as a result of a tighter acute angles, assuming a triangular planar structure for Ag_3 , and a rhombus for Ag_4 as already supported by density function theory (DFT). This hypothesis was confirmed by Linnert and co-workers,⁶⁴ and Antoku in 2007⁶⁵ using silver electrode as a function of the agglomeration number of silver,⁶⁴ the standard potentials of silver atom, silver dimers and silver trimers were calculated

by Linnert *et al.*,⁶⁴ from the thermodynamic properties of the gas phase clusters and the free enthalpy of silver using data obtained from previous works by Hilpert *et al.*, and Henglein.^{66,67} Besides, evidence already exists of the formation of Ag_4^{2+} following the reduction with borohydride in the UV-Vis spectra,⁴⁵ all of which support the formation of Ag_4 clusters.

The conclusion drawn from these therefore is that there are basically two cluster types of Ag_2 and Ag_4 in all the six samples synthesized. This is considered to be thermodynamically favourable. The $90 \mu\text{M}$ sample contained approximately four atoms per the 50 nm droplet. But as the concentration of the Ag^+ ions increased, the proportions of these Ag atoms increased as well from 4 to 6, 10, 20, 30, and 40 atoms per droplet for the 150, 250, 500, 750, and 1000 μM concentration, corresponding to 1.5, 2.5, 5.0, 7.5, and 10.0 increment factors of Ag atom respectively. According to the observed intensities of the 305 and 430 nm emissions for the Ag_2 and Ag_4 clusters in figure 3.4a&b, there are seemingly twice the Ag_2 clusters than there are of the Ag_4 in the $90 \mu\text{M}$ sample, and approximately four times Ag_2 clusters than there are of the Ag_4 in the 1 mM Ag nanoclusters sample. All of these point at an evolution of Ag_4 from Ag_2 clusters, the former being the equilibrium cluster size.

3.14 Fourier transform infrared spectroscopy

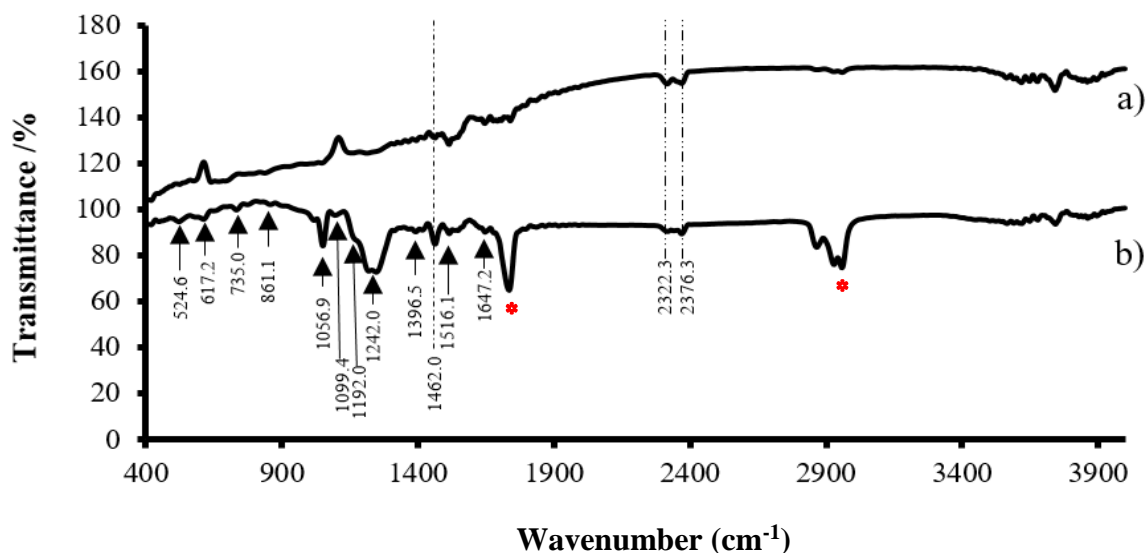
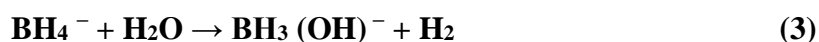


Figure 3.17: Fourier transform infrared spectra of (a) $90 \mu\text{M}$ (b) 1 mM dried samples of Ag NCs on clean silicon wafer. The red asterisks represent some peaks assigned to the surfactant.

Fourier transform infrared (FTIR) analyses of the samples were performed to determine the nature of the capping ligands on the Ag nanoclusters by the appearances of signature vibrational

bonds in figure 3.17 above. The peak at 2322.3 and 2376.3 cm^{-1} are assigned to the terminal B-H stretching modes of the BH_3 group. This is consistent with those observed by Golub *et al.* in a study of the borohydride ligand.⁶⁸ The conspicuous absence of any peak at $\sim 2268 \text{ cm}^{-1}$ (singlet) which is a signature for the BH_4^- group^{69,70} is a clear indication of the hydrolysis and oxidation of the BH_4^- ion in the system. Also, both bands at 1099.4 and 1192.0 cm^{-1} are associated with the BH_3 symmetric and asymmetric bend modes. These two bands are particularly synonymous with complex molecules containing the BH_3 group.^{71,72} The presence of the 1099.4 and 1192.0 cm^{-1} bands demonstrate that BH_3 is associated with OH^- group, thereby forming the BH_3OH^- moiety. This was formed from the oxidative hydrolysis of the BH_4^- ion in aqueous solution as expressed in the mechanism below:^{69,73}



Another band whose frequency of vibration appeared at 1516.1 cm^{-1} was also identified. This has been ascribed to the B-O bond stretch vibration of the borate (BO_3) group^{74,75} which expectedly should appear at a lower frequency relative to the borane ligand above arising from its higher reduced mass. Also, a series of peaks can be observed within 400 – 1100 cm^{-1} in the 1 mM spectrum. The bands at 500 – 750 and 750 – 1100 cm^{-1} are typical of different BO_3 bending vibrations, and the B-O and B-O-B stretching vibrations respectively.⁷⁵

Furthermore, there is the in-plane B-O-H bending mode at 1242.0 cm^{-1} , and the B-O stretch at 1396.5 cm^{-1} of the BO_2 group, and the stretching vibrational band of the B-O-B mode.⁶⁹ The peak at 1647.2 cm^{-1} has been assigned to H_2O bending vibration as well as the weak peak (not well resolved due the dry sample used) in the 3380 – 3500 cm^{-1} region for H_2O stretching vibration.⁷⁵

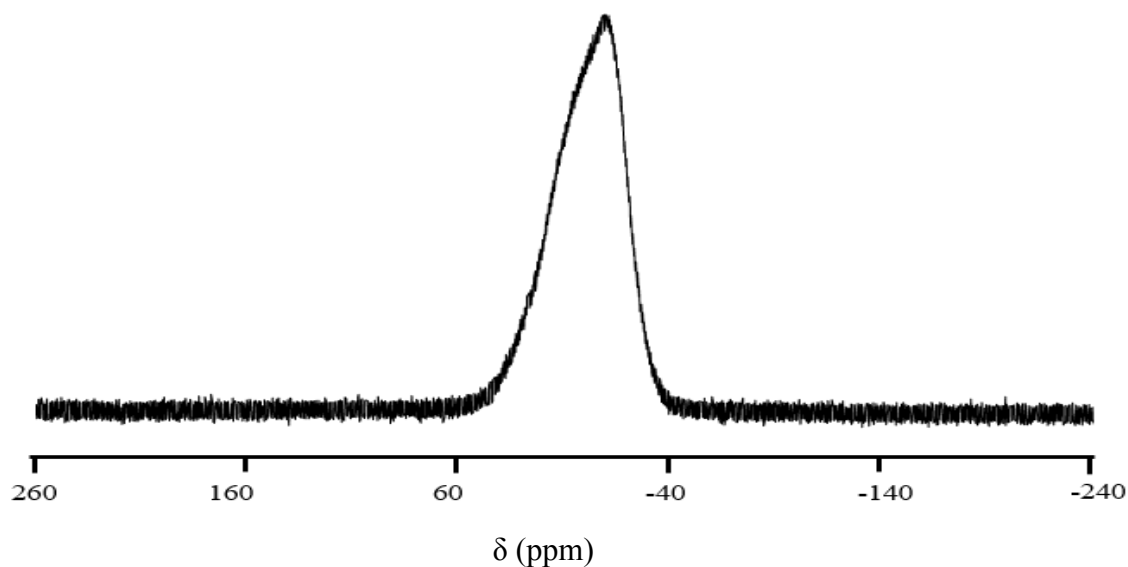
3.15 ^{11}B NMR

Figure 3.18: ^{11}B NMR spectrum of $[\text{Ag}_4\text{B}_3\text{O}_5\cdot\text{BH}_3\cdot 2\text{H}_2\text{O}]^-$ aqueous solution at 298 K, with boron trifluoride diethyl etherate, $\text{BF}_3\cdot\text{O}(\text{C}_2\text{H}_5)_2$ as a reference.

^{11}B NMR analysis of the 1 mM sample was undertaken to establish the presence of boron as a constituent of the ligand. The higher (1 mM) rather than the 90 μM sample was used for this analysis in order to obtain better spectrum resolution. A broad ^{11}B peak was observed from this measurement as can be seen in the spectrum of figure 3.18 above. Peak broadening about this chemical shift position for ^{11}B is typical of three-fold coordinated boron atoms.⁷⁵

3.16 X-ray photoelectron spectroscopy (XPS)

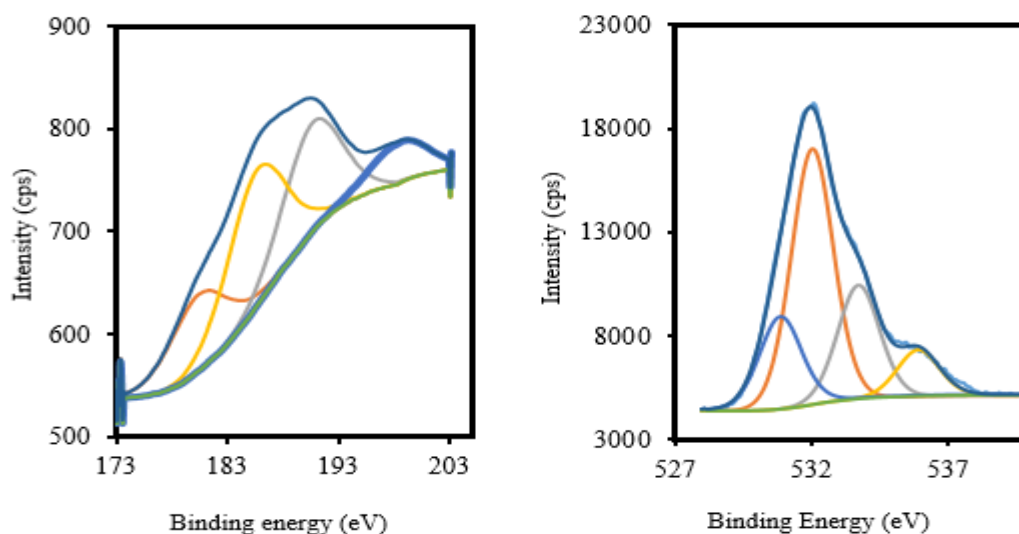


Figure 3.19: XPS charts of $[\text{Ag}_4\text{B}_3\text{O}_5\cdot\text{BH}_3\cdot 2\text{H}_2\text{O}]^-$ (a) Boron. See (inset) survey spectrum in Appendix section) (b) Oxygen.

Furthermore, X-ray photoelectron spectroscopy (XPS) of the $90\ \mu\text{M}$ and $1\ \text{mM}$ samples were analyzed on cleaned silicon wafer. Results obtained are presented above in figures 3.19 (a), (b), for boron, and oxygen. Signals were too weak to determine the presence of silver because of the high noise background. However, the information obtained was also critical to confirming the chemical composition and environment of the capping ligand on the cluster metalcore.

Figure 3.18a has boron peaks at 182.02, 187.33, 192.73, and 199.83 eV binding energies respectively. These four boron peaks seem to imply that there are four boron chemical environments in the molecule according to the molecular formula of the clusters $[\text{Ag}_4\text{B}_3\text{O}_5\cdot\text{BH}_3\cdot 2\text{H}_2\text{O}]^-$.

The bands at 187.33 and 192.73 eV can readily be assigned to the B – H (BH_3)⁷⁶ and the B_2O_3 (borate) group;^{77,78} but the other bands at 182.02 and 199.83 eV could not be immediately assigned. However it is thought that these bands may be associated with the BO_2/BO (boron oxide) and possibly an Ag-B bond.

Figure 3.15b shows the binding energies of the oxygen signals from the Ag NCs samples. Four signals can be seen at 531.30; 532.40; 534.1; and 536.1 eV corresponding to O1s peaks for metal oxides (M_nO_m) or metal hydroxides ($\text{M}(\text{OH})_x$);⁷⁹ organic (ether-oxygen) $-(\text{CH}_3-\text{CH}(\text{OCH}_2)-$,^{80,81} oxygen of the ketone, sulphonyl group,⁸² or carbonyl sulphur/silver;⁸³ or

oxygen from (hydrated) water (H_2O),^{39,84,85} and the M_2O or oxide of nitrogen (NO)⁸⁶ accordingly. The absence of an O1s signal at 530.4 eV correlates with the ESI data and precludes the possibility of Ag(I) in the form of a silver oxide (Ag_2O) in the synthesized Ag NCs.⁸⁷ This further underscores the position that the clusters have all four Ag atoms in the oxidation state of zero (Ag^0). All peaks were assigned with the help of the National Institute of Standards and Technology (NIST) XPS database and XPS-Photoelectron Spectroscopy Reference pages (www.xpsfitting.com).

3.17 Conclusion

Ag NCs of ~1.4 nm size have been made from silver nitrate salt and reduced with sodium borohydride in a 1:1 ratio at room temperature in microemulsion solution with iso-octane (2, 2, 4-trimethylpentane) and sodium bis-(2-ethyl hexyl) sulfosuccinate (AOT) as oil phase and surfactant respectively. These NCs were not passivated with the usually ubiquitous organic-based ligands (nucleic acids, sulphur-based, and phosphorus-containing), many of which are expensive, toxic and environmentally hazardous. These Ag NCs offer rather inexpensive, less toxic and environmentally safer alternatives.

The NCs are fluorescent with emissions in the blue region of the visible spectrum. They have large bandgaps characteristic of molecular semiconductor nanoclusters. These clusters have been observed to be very stable in the microemulsion system over six months post-synthesis and yet retain their fluorescence.

Furthermore, it has also been demonstrated that we can achieve size control of NCs by careful control of experimental conditions as well as the concentrations of reactants. Meanwhile, this is believed to be the first reported case of the synthesis of Ag_4 nanoclusters with inorganic passivating borate and borane ligand by microemulsion synthesis.

3.18 Reference

- 1 L. Mulfinger, S. D. Solomon, M. Bahadory, A. V. Jeyarajasingam, S. a. Rutkowsky and C. Boritz, *J. Chem. Educ.*, 2007, **84**, 322–325.
- 2 H. Xu and K. S. Suslick, *Adv. Mater.*, 2010, **22**, 1078–1082.
- 3 T. M. D. Dang, T. T. T. Le, E. Fribourg-Blanc and M. C. Dang, *Adv. Nat. Sci. Nanosci. Nanotechnol.*, 2011, **2**, 15009.
- 4 C. Vázquez-Vázquez, M. Bañobre-López, A. Mitra, M. A. López-Quintela and J. Rivas, *Langmuir*, 2009, **25**, 8208–8216.
- 5 A. Pietrini, 2003, PhD Thesis, Swiss Federal Institute of Technology, Zurich.
- 6 D. Philip, *Spectrochim. Acta - Part A Mol. Biomol. Spectrosc.*, 2008, **71**, 80–85.
- 7 M. Abdulla-Al-Mamun, Y. Kusumoto and M. Muruganandham, *Mater. Lett.*, 2009, **63**, 2007–2009.
- 8 L. Li, Q. Guo, J. Li, W. Yan, C. Leng, H. Tang, Q. Lu and B. Tan, *J. Mater. Chem. B*, 2013, **1**, 3999.
- 9 A. Ledo-Suárez, J. Rivas, C. F. Rodríguez-Abreu, M. J. Rodríguez, E. Pastor, A. Hernández-Creus, S. B. Oseroff and M. A. López-Quintela, *Angew. Chemie - Int. Ed.*, 2007, **46**, 8823–8827.
- 10 T. Udaya Bhaskara Rao and T. Pradeep, *Angew. Chemie - Int. Ed.*, 2010, **49**, 3925–3929.

- 11 T. Baksi, A. Bootharaju, M. S. Chen, Xi. Häkkinen, H. Pradeep, *J. Phys. Chem. C*, 2014, **118**, 21722–21729.
- 12 D. Buceta, N. Busto, G. Barone, J. M. Leal, F. Domínguez, L. J. Giovanetti, F. G. Requejo, B. García and M. A. López-Quintela, *Angew. Chemie Int. Ed.*, 2015, **54**, 7612–7616.
- 13 J. T. Petty, J. Zheng, N. V. Hud and R. M. Dickson, *J. Am. Chem. Soc.*, 2004, **126**, 5207–5212.
- 14 J. Li, J. J. Zhu and K. Xu, *TrAC - Trends Anal. Chem.*, 2014, **58**, 90–98.
- 15 I. Díez, M. Pusa, S. Kulmala, H. Jiang, A. Walther, A. S. Goldmann, A. H. E. Müller, O. Ikkala and R. H. A. Ras, *Angew. Chemie - Int. Ed.*, 2009, **48**, 2122–2125.
- 16 R. P. Haynes, Christy L. Van Duyne, *J. Phys. Chem. B*, 2001, **105**, 5599–5611.
- 17 S. Link and M. A. El-Sayed, *J. Phys. Chem. B*, 1999, **103**, 4212.
- 18 I. Shipway, Andrew N. Willner, *Chem. Commun.*, 2001, **0**, 2035–2045.
- 19 M. Crooks, Richard M. Lemon III, Buford I. Sun, Li. Yeung, Lee K. Zhao, in *Dendrimers III*, ed. V. F. (eds) D. III, Springer, Berlin, Heidelberg, Berlin, 2001, vol. 212, pp. 81–135.
- 20 Y. Takagi, Daisuke. Homma, Yoshikazu. Hibino, Hiroki. Suzuki, Satoru. Kobayashi, *Nano Lett.*, 2006, **6**, 2642–2645.
- 21 C. A. Fedlheim, Daniel L. Foss, *Metal Nanoparticles: Synthesis, Characterization, and Applications*, CRC Press, 2001.

- 22 T. Sun and K. Seff, *Chem. Rev.*, 1994, **94**, 857–870.
- 23 J. Ramírez, M. Sanaú and E. Fernández, *Angew. Chemie - Int. Ed.*, 2008, **47**, 5194–5197.
- 24 J. Kong, Hyeyoung. Jang, *Langmuir*, 2008, **24**, 2051–2056.
- 25 J. N. Anker, W. P. Hall, O. Lyandres, N. C. Shah, J. Zhao and R. P. Van Duyne, *Nat. Mater.*, 2008, **7**, 442–453.
- 26 H. D. Hill and C. A. Mirkin, *Nat. Protoc.*, 2006, **1**, 324–336.
- 27 C. S. Thaxton, D. G. Georganopoulou and C. A. Mirkin, *Clin. Chim. Acta*, 2006, 363, 120–126.
- 28 C. A. Hill, Haley D. Vega, Rafael A. Mirkin, *Anal. Chem.*, 2007, **79**, 9218–9223.
- 29 C. A. Seferos, Dwight S. Giljohann, David A. Hill, Haley D. Prigodich, Andrew E. Mirkin, *J. Am. Chem. Soc.*, 2007, **129**, 15477–15479.
- 30 Y. Shiraishi and N. Toshima, *J. Mol. Catal. A Chem.*, 1999, **141**, 187–192.
- 31 D. Astruc, F. Lu and J. R. Aranzaes, *Angew. Chemie - Int. Ed.*, 2005, 44, 7852–7872.
- 32 J. Y. . Somorjai, Gabor A. Tao, Feng. Park, *Top. Catal.*, 2008, **47**, 1–14.
- 33 G. Schmid and B. Corain, 2003, 3081–3098.
- 34 C. A. Millstone, Jill E. Hurst, Sarah J. Me´traux, Gabriella S. Cutler, Joshua I. Mirkin,

- Small*, 2009, **5**, 646–664.
- 35 R. P. Dick, Lisa A. McFarland, Adam D. Haynes, Christy L. Van Duyne, *J. Phys. Chem. B*, 2002, **106**, 853–860.
- 36 Y. Chen, C. Wang, Z. Ma and Z. Su, *Nanotechnology*, 2007, **18**, 5.
- 37 R. Ramanathan, S. K. Bhargava and V. Bansal, *Biological Synthesis of Copper / Copper Oxide*, 2010.
- 38 N. Durán, R. Cuevas, L. Cordi, O. Rubilar and M. Diez, *Springer*, 2014, **3**, 645.
- 39 J. A. Creighton, C. G. Blatchford and M. G. Albrecht, *J. Chem. Soc. Faraday Trans. 2*, 1979, **75**, 790.
- 40 I. Chakraborty, T. Udayabhaskararao and T. Pradeep, *Chem. Commun.*, 2012, **48**, 6788.
- 41 H. C. Yeh, J. Sharma, I. M. Shih, D. M. Vu, J. S. Martinez and J. H. Werner, *J. Am. Chem. Soc.*, 2012, **134**, 11550–11558.
- 42 J. M. Obliosca, C. Liu, R. A. Batson, M. C. Babin, J. H. Werner and H. C. Yeh, *Biosensors*, 2013, **3**, 185–200.
- 43 J. Zheng, P. R. Nicovich and R. M. Dickson, *Annu. Rev. Phys. Chem.*, 2007, **58**, 409–431.
- 44 R. Denis, W. Nathan, Muhoberac, B. Barry, Newton, C. John, Kumbar, A., Sardar, *Plasmonics*, 2014, **9**, 111–120.

- 45 C. Petit, P. Lixonf and M.-P. Pileni, *J. Phys. Chem*, 1993, **97**, 12974–12983.
- 46 H. J. Yeh, Hsin-Chih, Sharma, Jaswinder, Han, J. Jason, Martinez, S. Jennifer, and Werner, *IEEE Nanotechnol. Mag.*, 2011, 28–33.
- 47 M. B. Teunis, S. Dolai and R. Sardar, *Langmuir*, 2014, **30**, 7851–7858.
- 48 D. Schmid, G., and Fenske, *Phil. Trans. R. Soc.*, 2010, **368**, 1207–1210.
- 49 S. Dolai, A. Dass and R. Sardar, *Langmuir*, 2013, **29**, 6187–6193.
- 50 B. Zeiger, *Superatoms*, Lect. Semnr Abst. 2008, 1-3.
- 51 J. R. Lakowicz, *Instrumentation for Fluorescence Spectroscopy*, 2006, 1-954.
- 52 B. Valeur, *Atomic Spectrometry with Flames and Plasmas Handbook of Analytical Techniques Single-Molecule Detection in Solution . Methods and Applications, Related Titles from WILEY-VCH Analytical* 2001, vol. 8.
- 53 G. G. Guilbault, *Practical Fluorescence*, Marcel Dekker, New York, Second Edi., 1990.
- 54 Perkin Elmer, *Microchem. J.*, 2000, **65**, 353.
- 55 H. Wang and T. Nann, *Springer Series on Fluorescence*, 2011, vol. 7.
- 56 J. S. Bowers, J. Michael, McBride, R. James, Rosenthal, *J. Am. Chem. Soc*, 2005, **127**, 15378–15379.

- 57 R. J. Rostron, Y. Chao, G. Roberts and B. R. Horrocks, *J. Phys. Condens. Matter*, 2009, **21**, 235301.
- 58 A. Kumar and V. Kumar, *Chem. Rev.*, 2014, **114**, 7044–7078.
- 59 H. F. Zulauf, Martin. Eicke, *J. Phys. Chem.*, 1979, **83**, 480–486.
- 60 J. Eastoe, *Surfactant Chemistry*, 2003, 1-134.
- 61 M.-P. Pileni, *Nature*, 2003, **2**, 145–150.
- 62 T. Frederick, M Weiss, *ACS Nano*, 2010, **4**, 3195–3200.
- 63 S. Dolai, P. R. Nimmala, M. Mandal, B. B. Muhoberac, K. Dria, A. Dass and R. Sardar, *Chem. Mater.*, 2014, **26**, 1278–1285.
- 64 H. Linnert, T., Mulvaney, P., Henglein, A., & Weller, *J. Am. Chem. Soc.*, 1990, **112**, 4657–4664.
- 65 Y. Antoku, Georgia Institute of Technology, 2007.
- 66 K. A. Hilpert, K. & Gingerich, *Berichte Der Bunsen-Gesellschaft-Physical Chem. Chem. Phys.*, 1980, **84**, 739–745.
- 67 A. Henglein, *Berichte Der Bunsen-Gesellschaft-Physical Chem. Chem. Phys.*, 1990, **94**, 600–603.
- 68 S. E. Golub, E. Igor; Filippov, A. Oleg; Gutsul, I. Evgenii; Belkova, V. Natalia; Epstein, M. Lina; Rossin, Andrea; Peruzzini, Maurizio; and Shubina, *Inorg. Chem.*, 2011, **51**, 6486–6497.

- 69 B. M. Concha, M. Chatenet, F. Maillard, E. A. Ticianelli, F. H. B. Lima and R. B. de Lima, *Phys. Chem. Chem. Phys.*, 2010, **12**, 11507.
- 70 K. Nakamoto, *Infrared and Raman Spectra of Inorganic and Coordination Compounds: Part A: Theory and Applications in Inorganic Chemistry*, Sixth Edit., 2008.
- 71 T. Shimanouchi, *J. Phys. Chem. Ref. Data.*, 1977, **6**, 993–1102.
- 72 W. D. Smith, J., Seshadri, K. S., *J. Mol. Spectrosc.*, 1973, **45**, 327–337.
- 73 P. Krishnan, T. H. Yang, S. G. Advani and A. K. Prasad, *J. Power Sources*, 2008, **182**, 106–111.
- 74 R. Cong, J. Sun, T. Yang, M. Li, F. Liao, Y. Wang and J. Lin, *Inorg. Chem.*, 2011, **50**, 5098–5104.
- 75 Sun Hua-Yu. Zhou Yan Huang Ya-Xi Sun Wei MI Jin-Xiao, *Chinese J. Struct. Chem.*, 2010, **29**, 1387–1393.
- 76 W. L. Hendrickson, D.N. Hollander, J.N. Jolly, *Inorg. Chem.*, 1970, **9**, 2642.
- 77 D. M. Stranick, M. A. Houalla, M. Hercules, *J. Catal.*, 1987, **104**, 396.
- 78 Z. Rong, B.V.R. Chowdari, *Solid State Ionics*, 1995, **78**, 133–142.
- 79 M. C. Biesinger, L. W. M. Lau, A. R. Gerson and R. S. C. Smart, *Appl. Surf. Sci.*, 2010, **257**, 887–898.
- 80 Acker, M. and B. Ratner, *J. Surf. Sci. Spectra.*, 1992, **1**, 96.

- 81 D. Beamson, G. and Briggs, *Adv. Mater.*, 1992, **5**, 778.
- 82 M. M. Chehimi and M. Delamar, *J. Electron Spectrosc. Relat. Phenom.*, 1989, **49**, 213.
- 83 J. M. Zhou, X.-L. White, *Surf. Sci.*, 1990, **235**, 259–268.
- 84 D. Wang B. Liu J. Yang, S. Jin, *Polyhedron*, 1995, **14**, 895.
- 85 F. S. Key and G. Maass, *Silver Colloids*, 2001, 1–6.
- 86 A. Pashutski and M. Folman, *Surf. Sci.*, 1989, **216**, 395–408.
- 87 J. Pate, F. Zamora, S. M. D. Watson, N. G. Wright, B. R. Horrocks and A. Houlton, *J. Mater. Chem. C*, 2014, **2**, 9265–9273.

4 CHAPTER FOUR

4.1 RESULTS AND DISCUSSION II

4.2 Synthesis and Characterization of Silver Nanoclusters in Microemulsion by Photochemical Reduction

4.3 Introduction

A quasi-green synthetic method of making silver nanoclusters (Ag NCs) in microemulsion without the use of sodium borohydride (NaBH_4) or any chemical reducing agent is considered in this chapter. More importantly, by avoiding the use of a chemical reducing agent we hope to generate a cleaner preparation of Ag NCs that would be simpler to analyse because of the lack of additional reagents. Silver ions are readily reduced to Ag^0 from Ag^+ ions by solvated electrons when exposed to light.

Using the method of pulse radiolysis, Mulvaney¹ synthesized Ag NCs in aerated aqueous solution of AgClO_4 containing methanol using high energy γ -rays pulse to effect the reduction of Ag^+ ions by hydrated electrons. This produced short-lived Ag NCs which readily agglomerated into large Ag NPs in the absence of a stabilizer. Polymer groups are often employed as stabilizers of the nanoclusters during photoreduction of metal ion precursors as demonstrated by Henglein,² with polyphosphates in the production of known concentration of metal atoms (Ag, Pt) by pulse radiolysis, the development of the metal absorption spectrum is recorded against time as the clusters coalesced into larger particles which act as catalysts in photochemical and radiation chemical reactions.² Harada and Einaga,³ using poly(N-vinyl-2-pyrrolidone) (PVP) for the photoreduction of Pt^{4+} to metallic Pt^0 NPs in a study of the mechanism of the formation of Pt^0 NPs in aqueous ethanol solution. Petty *et al.*,⁴ and Copp *et*

al.,⁵ and several other researchers with DNA in aqueous solution for the production of Ag NCs by reduction with NaBH₄; and Zhang *et al.*,⁶ reported the synthesis of fluorescent Ag NCs in polymer microgels (poly(N-isopropylacrylamide-acrylic acid-2-hydroxyethyl acrylate)) as stabilizers during photoirradiation in aqueous reactions. Others like Shang⁷ have used inexpensive polyelectrolytes like polymethyl acrylic acids (PMAA) and polyacrylic acids (PAA) to synthesize Ag NCs by photoreduction of the Ag⁺ ions as highlighted by Xu *et al.*, in their Research News Article in 2010.⁸

Although, the application of light energy in the production of Ag NCs in solution is not new, the photosynthesis of silver nanoparticles in microemulsion system has been rarely studied. The adoption of the advantages of microemulsion systems in controlling reactions in well-defined nano-reactors^{9,10} (water-droplets) for the synthesis of fluorescent metal nanoclusters makes this study a compelling one.

The synthesis of Ag NCs in microemulsion by photoreduction under similar conditions of the NaBH₄ reduction is undertaken in this chapter. The idea is to reproduce the synthesis of Ag NCs in microemulsion system using photons of light to effect reduction of Ag⁺ ions.

4.4 Aim

The aim of this study is to synthesize ultra-small, fluorescent Ag NCs by the photoreduction method in microemulsion using water molecules as ligands to passivate the Ag NCs in the absence of the complex boron oxyhydroxide oxidation products of the reducing agent in the preceding chapter; and to compare the efficiencies of the photoreduction method to the borohydride reduction.

4.5 Reaction scheme

90 μ M and 1 mM aqueous AgNO₃ solutions were added to two separate 5 and 18 mL isooctane solutions containing 0.0005 and 0.0025 M AOT respectively to form microemulsion samples. These were transferred into large 20 mL quartz cuvettes and placed in the photoreactor and were irradiated with UV-light of 250 nm wavelength for an average of five hours to produce Ag NCs.

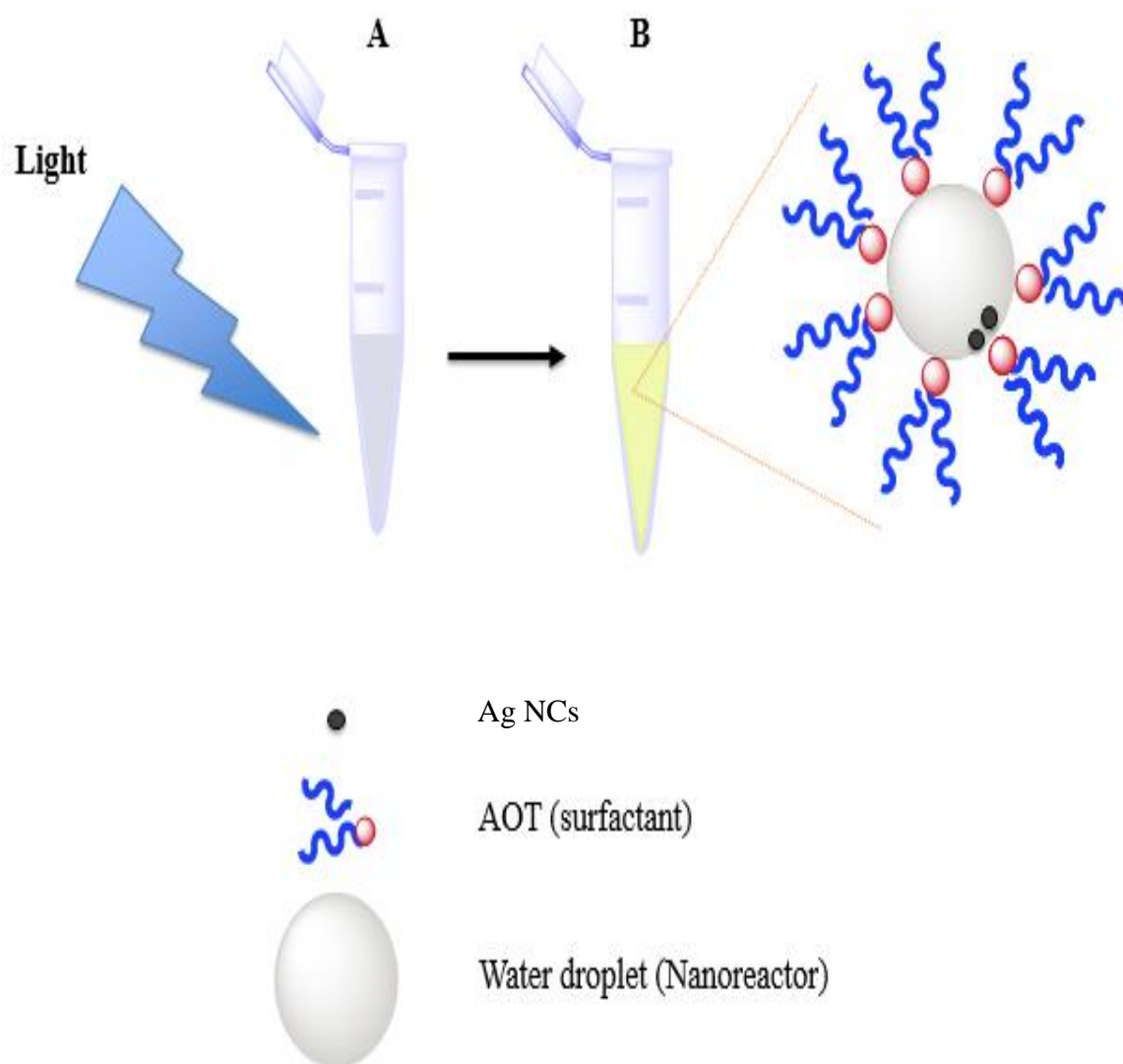


Figure 4.1: Photoreduction reaction scheme; (A) is AgNO_3 in microemulsion, (B) is Ag NCs formed in microemulsion at room temperature in a photochemical reactor with a light source of 254 nm wavelength.

4.4 Absorbance

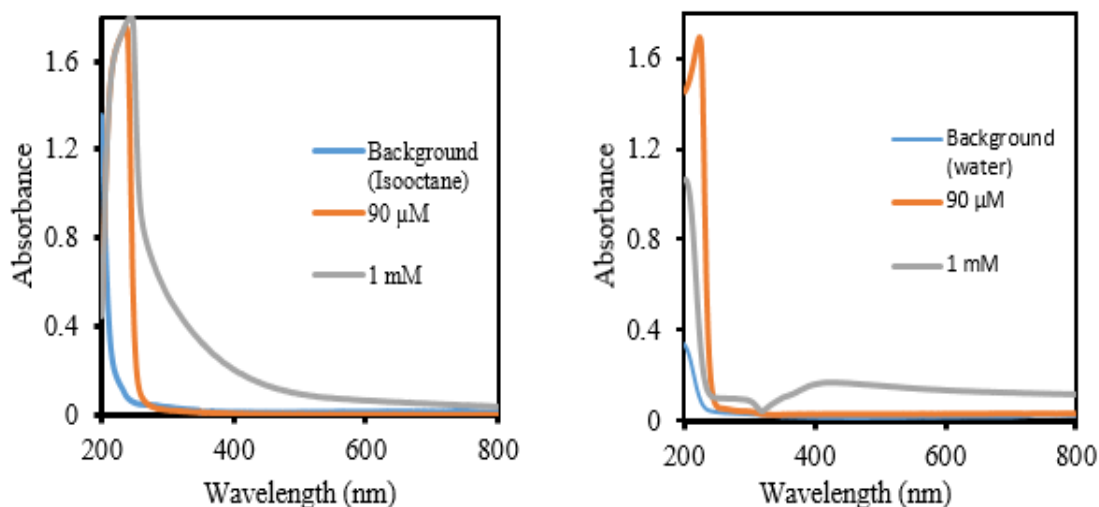


Figure 4.2: Absorbance of (a) $90\ \mu\text{M}$ and $1\ \text{mM}$ Ag NCs in microemulsion, (b) $90\ \mu\text{M}$ and $1\ \text{mM}$ Ag NPs in aqueous solution (control) synthesized by photoreduction of Ag^+ ions.

Figures 4.2 (a&b) are absorbance spectra of $90\ \mu\text{M}$ and $1\ \text{mM}$ Ag NCs in microemulsion and aqueous (control) samples respectively. The photoreduced microemulsion samples show no surface plasmon resonance peaks of silver around the 420 nm wavelength.^{4,10,11,12} However, the appearance of a pale yellow coloration especially in the $1\ \text{mM}$ sample (see Appendix fig. 8.1) is often an indication of the formation of Ag NPs,^{13,14,15} whose colour intensities are linked to their sizes^{15,16} and produce surface plasmon resonance at 420 nm.^{10,14,17}

In the spectra of figure 4.2b, the $1\ \text{mM}$ (control) aqueous samples show the presence of resonance plasmon peak at 429 nm. This is not available for the lower $90\ \mu\text{M}$ sample which is interpreted not to have formed aggregated Ag nanoparticles, since plasmonic resonance peaks of silver are attributes of large non-luminescent Ag NPs.^{14,18-21}

The use of nanoreactors ensured that controlled synthesis of small Ag nanoclusters (Ag NCs) was achieved with the conspicuous absence of the SPR peaks. These results give an impression of the effectiveness of the microemulsion system in controlling the reactions and restricting the spontaneous aggregation of the particles of silver as they are formed, which is a common feature of the aqueous reaction. The stabilization of water droplets by molecules of surfactant provides a convenient environment for the synthesis of ultrafine nanoclusters.²²

The peak ~280 nm peak attributed to Ag_4^{2+} which is usually formed immediately after adding NaBH_4 to a solution of AgNO_3 according to Petit *et al*¹¹ is absent in the UV-Vis spectra of all the photoreduced Ag samples.

4.6 Fluorescence

Fluorescence results of the samples are presented in figures 4.3, 4.4, and 4.5. The photosynthesized microemulsion samples show fluorescence centred at 439 and 453 nm for the 90 μM and 1 mM at an excitation wavelength of 340 nm. These indicate that small NCs of Ag have been produced, since only small NCs with the characteristic HOMO-LUMO bandgap²³ would show fluorescence.¹⁸

The 1 mM sample appeared to have the highest peak intensity of the two samples (figure 4.3). This was attributed to a larger concentration of fluorescent Ag NCs in the 1 mM concentration sample, and so recorded more counts per second in the emission scan. Chen *et al.*,²⁴ had observed that increases in AgNO_3 concentration resulted in the formation of more nuclei of silver. Emission peak intensities of 50000 cps at 439 nm and 100000 cps at 453 nm were recorded for the 90 μM and 1 mM Ag NCs. The shift to the higher wavelength (red shift) in the 1 mM Ag NCs sample also suggest the presence of larger Ag nanoclusters.

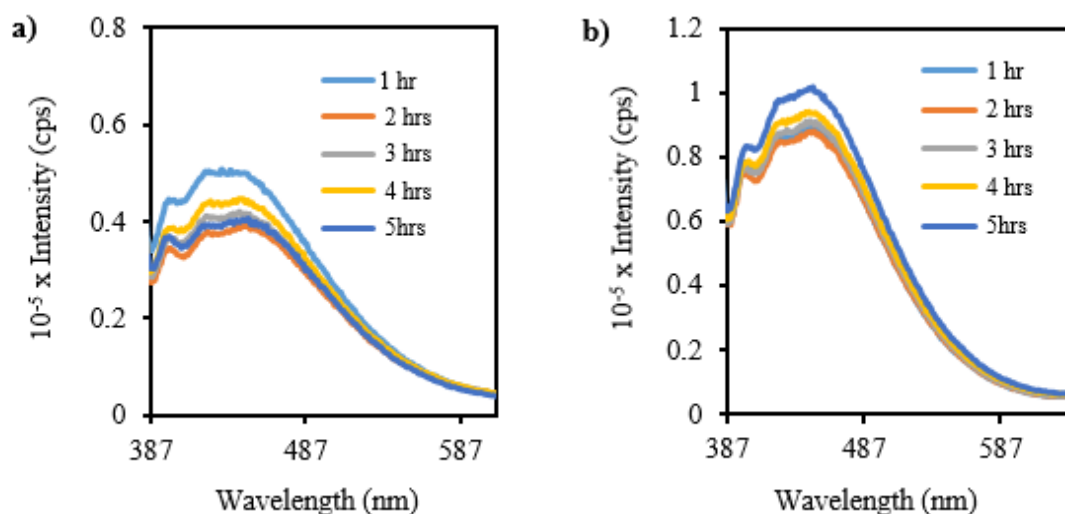


Figure 4.3: Emission intensity of (a) $90 \mu\text{M}$ Ag NCs excited at $\lambda_{\text{exc}} = 340 \text{ nm}$ (Highest peak intensity at 439 nm). (b) Emission intensity for 1 mM Ag NCs at $\lambda_{\text{exc}} = 340 \text{ nm}$ by photoreduction of Ag^+ for five hours (highest peak intensity at 453 nm).

Other emission bands were observed at 305 and 610 nm for both samples which corresponds to Ag_2 NCs and aggregating Ag NCs respectively (Appendix). The observed fluorescence of the Ag NCs is ascribed to interband transition.¹² The emission bands of both samples show broad peaks respectively of approximately 200 nm spread attributed to deep trapped states.²⁵

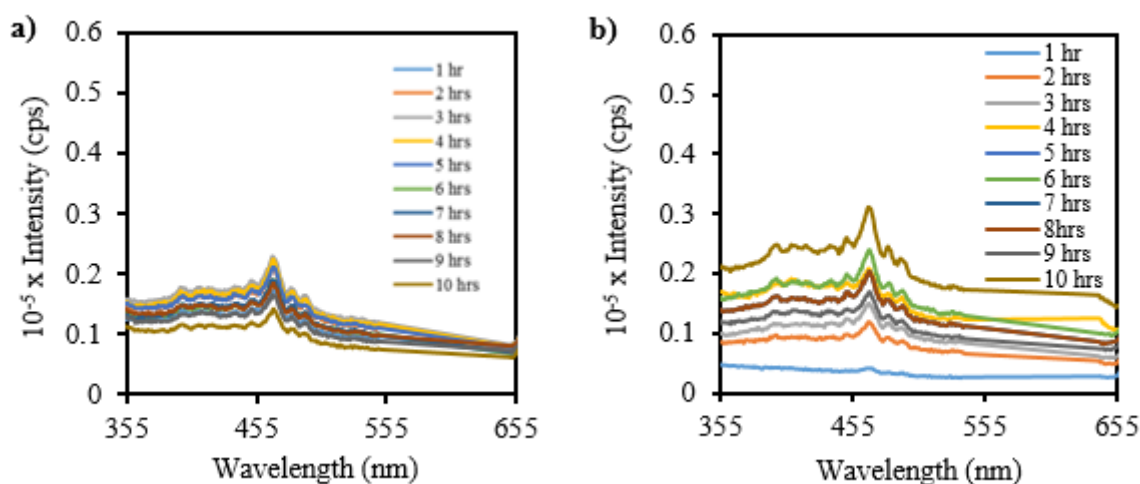


Figure 4.4: Emission intensity at 301 nm excitation of photoreduced aqueous solutions (control samples) of Ag NPs (a) $90 \mu\text{M}$ (peak max at 468 nm) (b) 1 mM Ag NPs (peak max at 470 nm).

A similar fluorescence study of the $90 \mu\text{M}$ and 1 mM control samples basically showed no fluorescence (figure 4.4a&b) except for a little spike at 470 nm. By comparing the emissions

of the control samples with the microemulsion samples, the near absence of fluorescence activity in the control experiments can be noticed. This indicates the production of large non-fluorescent Ag NPs without the requisite bandgap.^{14,18} Large non-fluorescent Ag NPs are usually prepared in aqueous solution in the absence stabilizers which prevent aggregation^{26,27,28} The weak fluorescence peaks at 470 nm observed in the control samples infers that a weak proportion of Ag NCs may exist in these control samples. However, the near general plateau nature of these emission spectra is an indication of the preponderance of Ag NPs in the control samples.

A plot of intensity at the 453 nm emission peak maximum against photoreduction time for each of the microemulsion samples (figure 4.5a&b) and their controls (figure 4.6a&b) was made to investigate the trend in the emission intensities of these samples with time during the photosynthesis of the Ag NCs. The observation of emission is an indication of the production of clusters of silver. The highest emission intensity was associated with the optimum concentration of Ag NCs in the system.

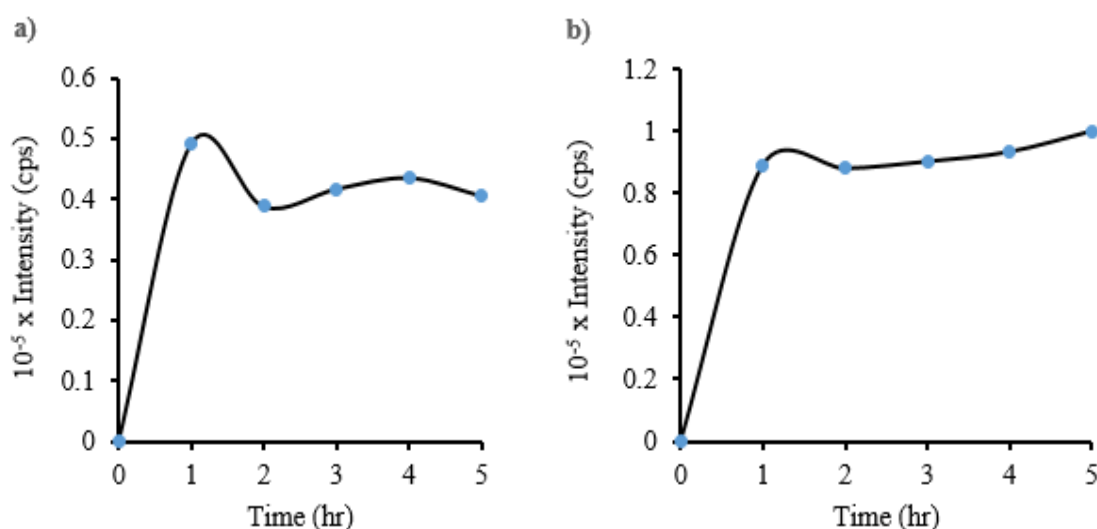


Figure 4.5: A plot of emission intensity against time for Ag NCs in microemulsion at peak max of 453 nm (a) $90 \mu\text{M}$ (b) 1 mM samples.

For the microemulsion samples, the time-dependent emission-intensity study of both samples showed that for the $90 \mu\text{M}$ sample, the highest intensity (I_{max}) was attained after one hour of

light irradiation, before dropping to what may be described as a steady state with no significant change in intensity four hours later (figure 4.6). The intensity of emission similarly rose steadily in the first hour of photoreduction of the 1 mM sample and remained steady for another hour (second hour). The intensity then rose gradually, signifying an increase in the nucleation process spanning the next three hours before reaching a maximum at the fifth hour of exposure to light. The difference in the emission-time dependent study of both samples has been attributed to the difference in the concentration of Ag^+ ions. In both case cases, the maintenance of a plateau (steady state) is considered a measure of the stability of the emulsion Ag NCs against aggregation.

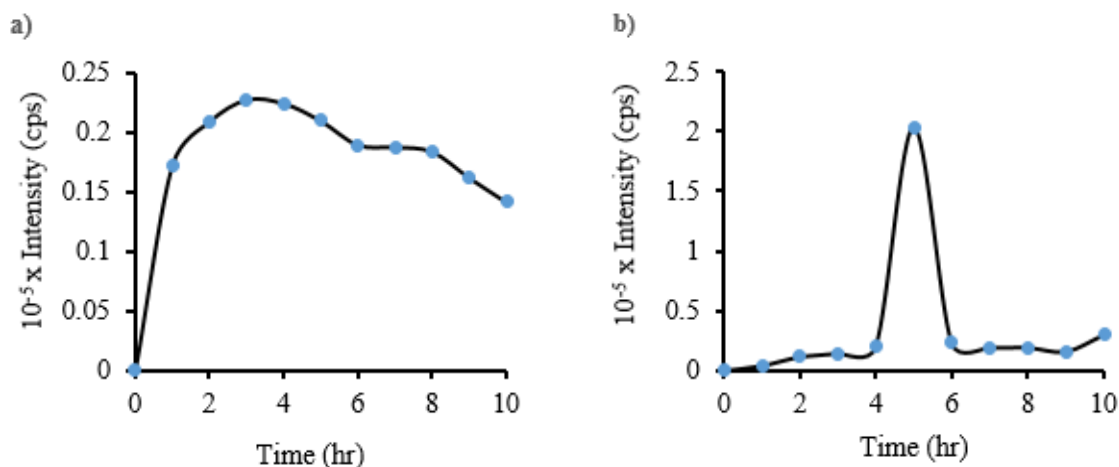


Figure 4.6: A plot of emission intensity against time for the Ag NCs samples in aqueous solution (control samples) (a) $90\ \mu\text{M}$ (peak max of 468 nm) (b) $1\ \text{mM}$ (peak max of 470 nm).

Slightly similar observations were noted for the control samples in figure 4.6 as well, but for a little variation in the time it took the $90\ \mu\text{M}$ Ag^+ ions control sample to reach the highest peak intensity. The highest peak intensity was recorded after the third-hour of a steady rise in emission intensity. In comparison with the microemulsion sample, this translates to a two-hour time lag. There was a slow rise in emission intensity of the $1\ \text{mM}$ control sample with marginal increases in intensity in the first four-hours of light irradiation. However, there was a sudden rise in intensity after the fourth-hour, peaking in the fifth hour before dropping drastically back to almost its initial value and remaining relatively constant afterwards.

In summary, it took within 1-hour for the $90\ \mu\text{M}$ Ag^+ ion emulsion reaction to reach its peak emission intensity while it required three hours for the $90\ \mu\text{M}$ Ag^+ ion control samples to attain

maximum intensity. This may be attributed to the dispersal of the Ag^+ ions in to water droplets in emulsion which allowed easier access to the incident light, as against the bulk $90 \mu\text{M}$ Ag^+ ion of the control sample. For the 1 mM sample emulsion and control samples, an average of 5 hours was required for the 1 mM sample to attain its maximum emission peak intensity. The 1 mM emulsion-synthesized sample displayed a more significant rise in intensity than the 1 mM (control) aqueous sample. This again has been attributed to the dispersal of the Ag^+ ions in water droplets in the emulsion, therefore affording easier accessibility to light illumination. The bulk nature of the control sample was again thought to be responsible for the slow response to irradiation by these sample.

Although more data is required, however indications are that the concentration of the samples played a role in the time it took the samples to reach the maximum emission intensity (I_{max}) as earlier suggested. The emission intensity of a sample is related to the concentration of the fluorophores.²⁹ The dip in the intensity of the control samples (especially the $90 \mu\text{M}$ sample, and the 1 mM sample after the fifth hour), are footprints of a rapid aggregation process of the Ag clusters.

4.7 Fluorescence kinetic study

To compare the rate of formation of these Ag NCs with those synthesized by reduction with borohydride, a fluorescence kinetic study of the Ag^+ ion reduction with borohydride was undertaken, and results presented in figure 4.7(a&b) below.

The samples were monitored by fluorescence emission intensity for over one-hour period immediately following the addition of the equivalent amounts of borohydride solution according to the reaction stoichiometry (1:1). A plot of the highest peak intensities at 340 nm excitation wavelength (which resulted in the maximum emission) against time is presented in figure 4.7(a&b). These show broad emission bands of Ag NCs centred at 440 and 423 nm for the $90 \mu\text{M}$ and 1 mM Ag NCs samples. An average emission intensity of 60 000 cps for both samples was obtained. However, the 1 mM Ag NCs sample had a slightly higher emission intensity than the $90 \mu\text{M}$ which again translates to a higher concentration of Ag NCs fluorophores.

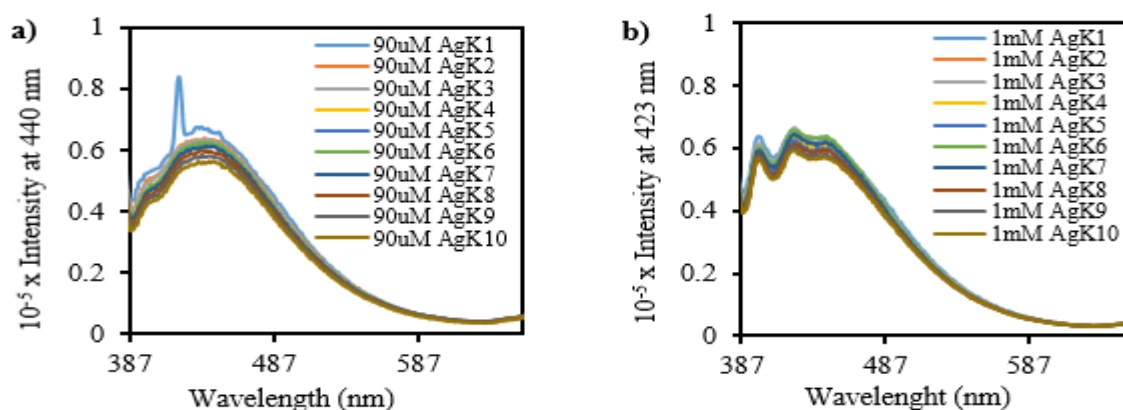


Figure 4.7: Emission intensity at 340 nm excitation for (a) $90 \mu\text{M}$ AgK. (b) 1 mM AgK of photoreduced microemulsion sample. 440 nm at 423 nm respectively. The label AgK denotes “silver kinetic study”, and the numbers 1, 2,..10 are the number of scans at $\lambda_{\text{exc}}=340 \text{ nm}$.

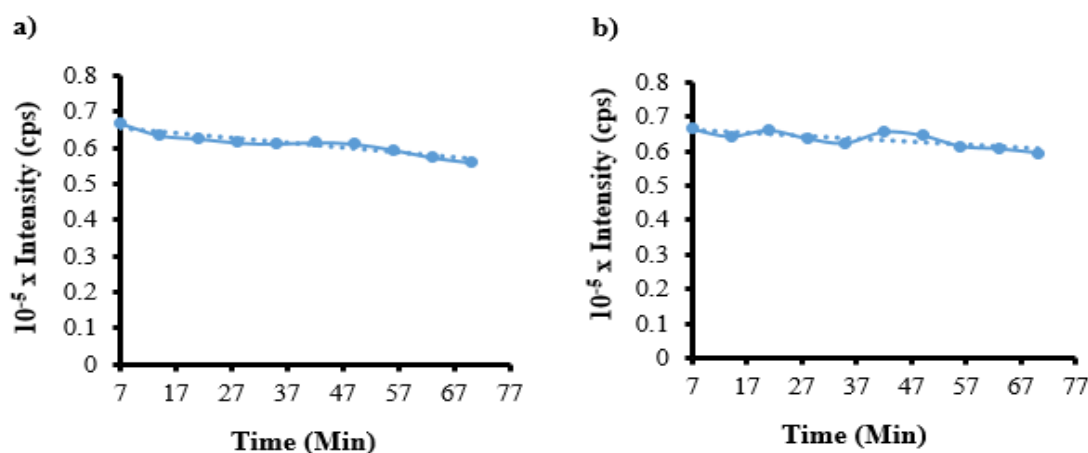
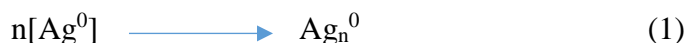


Figure 4.8: Emission at highest peak intensity (a) at emission wavelength of 440 nm for $90 \mu\text{M}$ (b) at emission wavelength of 423 nm for 1 mM Ag NCs. Fluorescence intensity was negligible before addition of NaBH_4 . Both samples were excited at 340 nm.

A similar time-dependent study of the emission peak maximum at 440 and 423 nm wavelengths for the $90 \mu\text{M}$ and 1 mM samples was done also to investigate the trend in emission intensity with time after reduction as presented in figure 4.8 a&b above. These show that the highest peak intensity of 70 000 cps was attained about 7 minutes from an initial fluorescence intensity value of zero at time zero for both the $90 \mu\text{M}$ and 1 mM samples, suggesting that the reaction had reached completion within the seventh minute of the start of the reaction, after which the intensity dropped briefly over the course of time. In both samples, the first spectrum was acquired about 7 min after addition of NaBH_4 , the sample was non-fluorescent initially and so the rise in fluorescence intensity occurring during the first 7 minutes represents the rates of

nucleation and formation of small fluorescence clusters. The slight drop in intensity at the conclusion of the nucleation process spanning a wide range of time corresponds to the growth phase (where the clusters gradually begin to grow into bigger cluster sizes) represented by the horizontal part of the curve in the spectra. This was similarly observed by Solanki *et al.*¹⁰ However, there were some fluctuations in this growth phase especially for the 1 mM sample which has been attributed to the growth transitions from Ag₂ to Ag₄ as the latter was formed over time as more Ag₂ NCs became available. Furthermore, the near constancy of the growth phase (especially of the 90 μM sample) represents the rapid formation of Ag₄ NCs and the stability offered by the microemulsion system. Meanwhile, the growth mechanism is synonymous with coalescence rather than aggregation if the horizontal curve is considered.

At time zero, the concentration of Ag⁰ was also zero, but at the peak of the reaction (time = 7 minutes, and assuming the reaction has reached completion at this point), the concentration of Ag⁰ should be at its maximum, after which is the growth phase. Since fluorescence intensity is a function of the concentration of the fluorophores, then the rate of growth in terms of intensity change (the rate at which the emission intensity diminishes with time), for the reaction:



will be:

$$\text{Rate} = -\frac{\delta[\text{Ag}^0]}{\delta t} = -k[\text{Ag}^0] \quad (2)$$

Figure 4.8 (a&b) can be represented schematically below:

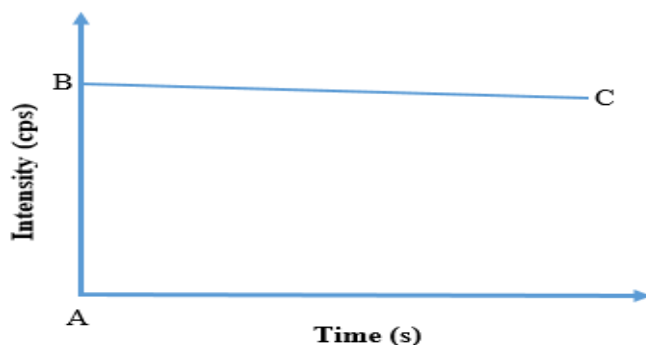


Figure 4.9: Schematic representation of figure 4.8 a&b.

The rate (speed) of the growth process can be deduced from the change in the emission intensity from the 7th to the 70th minutes (Fig. 4.9 a&b). This translates to a fluorescent decay rate of

approximately 3.0 cps² for the 90 μM and 2.0 cps² for the 1 mM Ag NCs samples, both representing a slow growth (decay) rate with an average of 2.5 cps² for both samples.

4.8 Dynamic light scattering (DLS)

Figure 4.10 is a DLS result for 90 μM and 1 mM Ag NCs synthesized by the photoreduction of Ag^+ ions in micro-(nano-) emulsion. These results show “droplet sizes” for both samples of 2.696 and 4.849 nm respectively at the lower size distribution. These diameter values are comparatively, lower than the borohydride reduced analogues, and maybe adduced to the absence of the coalescence of droplets and the consequent exchange of contents that takes place between droplets containing Ag^+ ions and BH_4^- ions in the chemical reduction process. In this case however, light was used rather than borohydride for the reduction of the Ag^+ ions. Thus, instead of having coalesced droplet dimer³⁰ as was with the chemical reduction, there were monomer of droplets by inference in the photoreduction process.

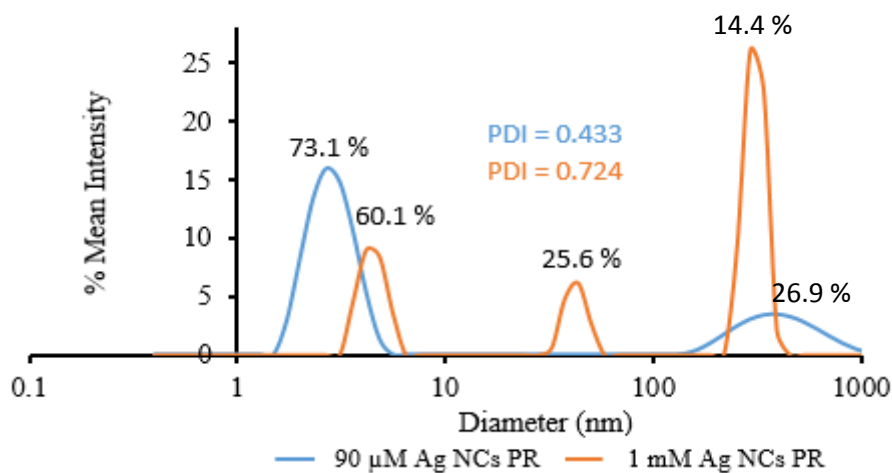


Figure 4.10: Hydrodynamic diameter of 90 μM and 1 mM Ag NCs photoreduced samples in microemulsion with Ag NCs dispersed and water the dispersant phase.

Two major particles size distributions: 5 and the >100 nm range were again observed as was the case in the previous chapter.³⁰ A notable exception being the 1 mM sample which has a third peak just before the 1000 nm mark which is often present immediately following synthesis.^{31,32,33} The ~3 and 5 nm particle sizes are again thought to be small reverse micelles, while the second peak at 43.8 nm for the 1 mM sample are assigned to droplets; the latter at 300

nm attributed to aggregates of coalesced droplets.³⁰ The polydispersity index (PDI) would expectedly be high as was actually recorded (Figure 4.10), especially for the 1 mM sample.

These size distribution pattern also show that large reverse micelle populations were obtained with the higher reaction concentration.^{9,34,35} By fitting the UV-Vis data for these samples with the Rayleigh theory, we have obtained a value of 40.0 nm for the water droplet size (see Appendix fig. 8.4) which supports the earlier conclusion that the <10 nm particles were reverse micelles.

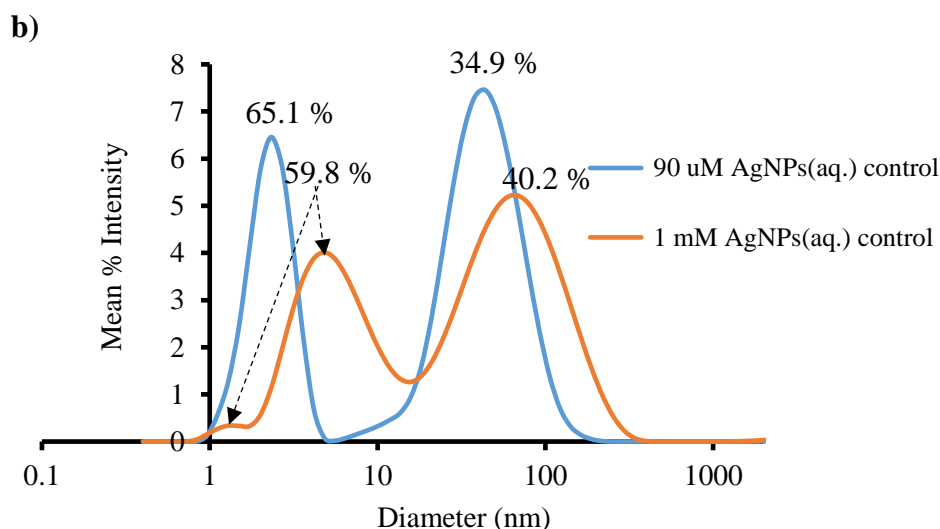


Figure 4.11: 90 μM and 1 mM Ag NPs photoreduced from AgNO₃ aqueous solution obtained 24 hours after synthesis.

Results of a similarly photoreduced 90 μM and 1 mM samples studied in aqueous solution (without the microemulsion) are provided in figure 4.11, which show striking differences with the photoreduced emulsion samples. Particles sizes close to those of the reverse micelles of the microemulsion samples were obtained at 2.3 and 5.6 nm for both aqueous samples. In the higher diameter range, 43.9 and 68.1 nm were recorded for the 90 μM and 1 mM samples. These are much lower than the reported 255 nm average size of the light-reduced microemulsion samples, giving credence to the earlier assertion that the >100 nm “particles” were very possibly coalesced water droplets of approximately 40 – 50 nm in the emulsion system. Meanwhile, the 43.9 and 68.1 nm sizes for the aqueous samples in the absence of a stabilizer suggest that these particles are large aggregated Ag NPs.

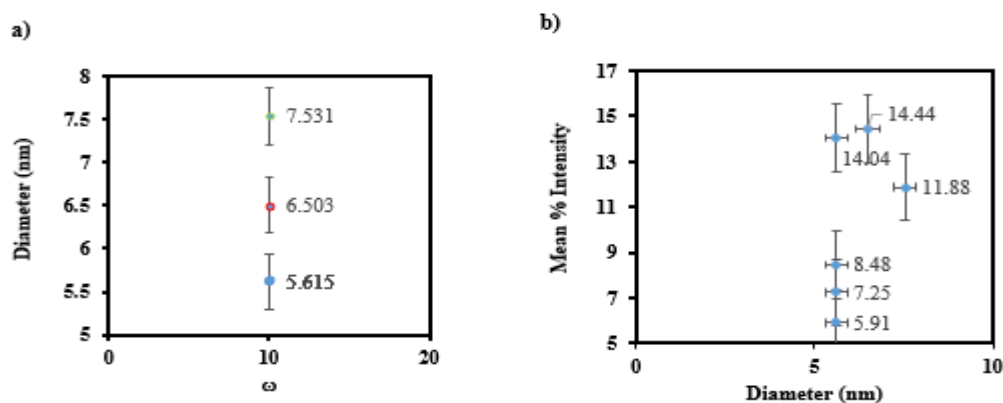


Figure 4.12: (a) Chart of size (diameter) nm with varying Ag NCs ($90 - 1000\mu M$) concentrations at fixed ω . (b) The intensity of scattered at increasing ω .

To understand the effects of increasing Ag and AOT concentrations at a fixed ω -value of the microemulsion system, a plot of the droplets diameter against ω was done for the borohydride-reduced microemulsion samples at a fixed ω -value of 10 (figure 4.12a), and another for intensity against observed droplet diameters in figure 4.12b.

Figure 4.12a shows that an average reverse micelle diameter of 5.61 nm ($\sim 70\%$ of the time) was obtained when the ω -value was fixed at 10 (same AOT and water volume all through but with increasing [Ag]), with slightly higher values of 6.50 and 7.53 nm respectively. These results also imply that the concentration of silver in the droplets did not significantly affect the resulting reverse micelles size.

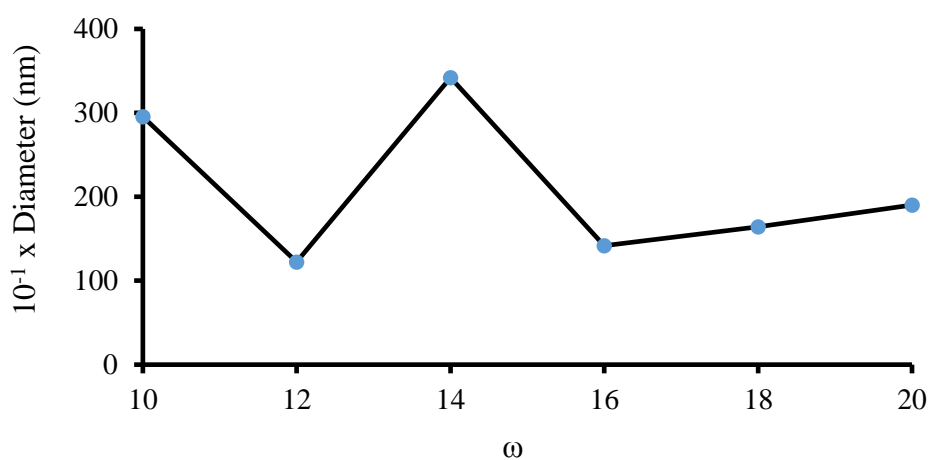


Figure 4.13: Droplet diameter of (>100 nm) vs varying ω .

For the higher particle diameter of above 40 nm (fig. 4.10) which represents the water droplet size of the microemulsion, we would expect an increase in droplet diameter as the ω -values increased, with corresponding increases in the intensities of the scattered light as demonstrated in fig. 4.12b. This is in agreement with the theory that large particles scattered light more than the smaller.³⁶ This was achieved at a varying AOT concentration,³⁰ as was observed in fig. 4.12b. That being the case, the observation of a random distribution of droplet sizes was observed in figure 4.13 with increasing ω -values, alongside the water contents for the six (90, 150, 250, 500, 750, 1000 μM) concentrations studied. It seems to indicate that at lower ω -values of 10 – 14, random variations of droplet diameters were obtained but this assumed a more definite increasing pattern with further increases in water content from ω -value of 16 – 20. The physical properties of bound water are expected to increasingly approach those of pure bulk water as the volumes/concentration proportions of the bound water increases.³⁷ The physical properties of both reverse micelle-bound water and free bulk water have been established to be different on the basis of size (volume) according to Pietrini,³⁰ and Higuchi *et al.*³⁷

4.9 Transmission electron microscopy

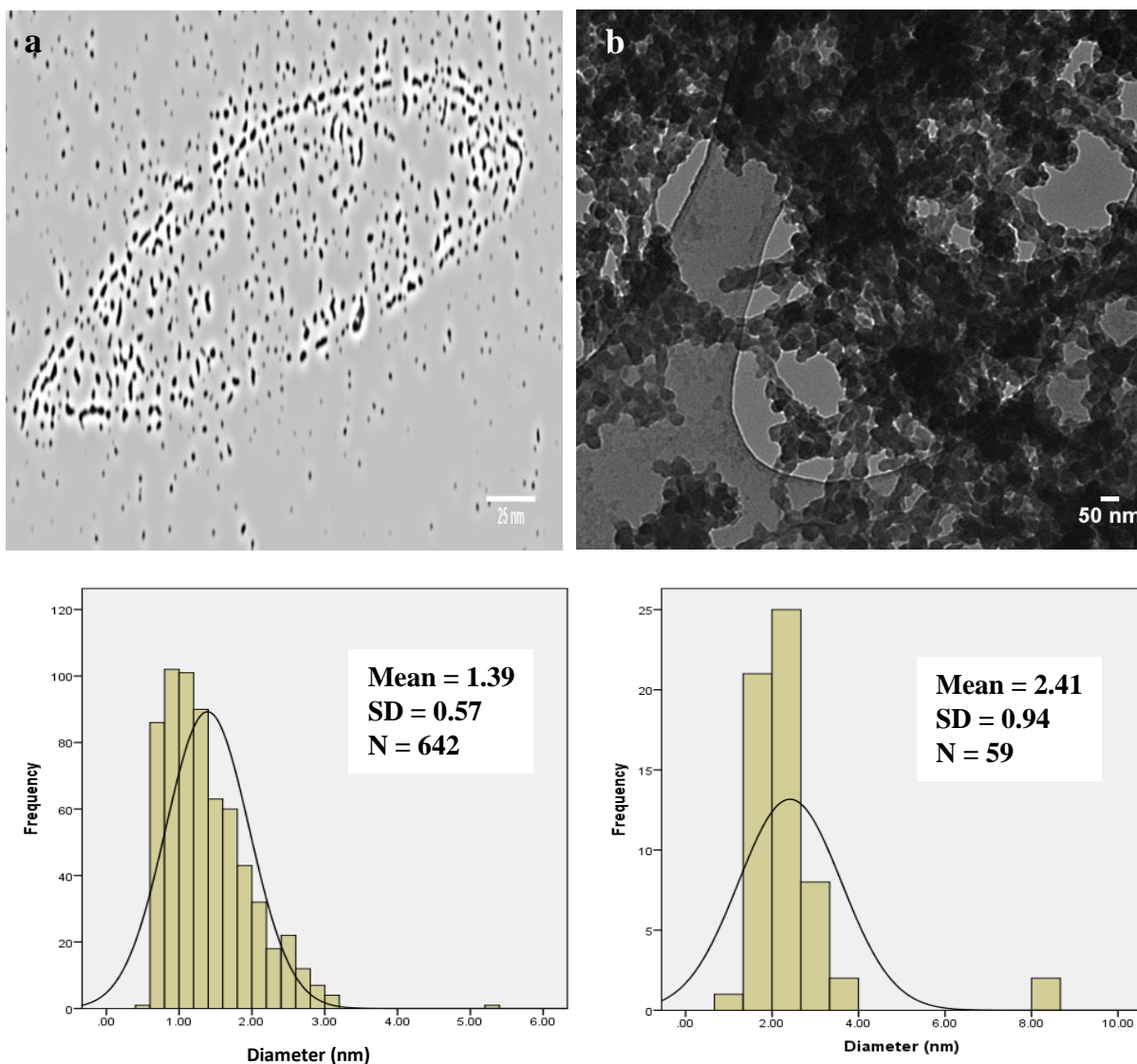


Figure 4.14: TEM images of photosynthesized Ag NCs in microemulsion (a) $90 \mu\text{M}$ and (b) 1 mM Ag NCs; particles size analysis histogram is placed below each sample.

TEM images of both samples show small, monodispersed, nanoparticles of silver. These nanoparticles can be seen enmeshed in surfactant molecules in figure 4.14b, with a higher concentration of samples. Both of these images display what looks like spherical Ag NPs dispersed on holey carbon-coated copper grids. Particles size analysis indicate an average size of 1.40 ± 0.57 and 2.40 ± 0.94 nm for the $90 \mu\text{M}$ and 1 mM samples respectively. These values are slightly different from the values obtained for the particle sizes in the preceding chapter. There is a larger average particles size in the 1 mM sample, which can be associated to its higher sample concentration and the droplet size as can be seen in the DLS data, and hence a better

chance of forming bigger particles by aggregation. Liu and Anderson *et als.*,^{38,39} reported that by increasing the ω -values (droplet size), the average MNCs size increased as well, resulting in larger size distribution and aggregates.¹⁰ Furthermore, Sharma *et al.*,⁴⁰ noted that there is a linear relationship between droplet size and the resultant particles size.

4.10 Cyclic Voltammetry

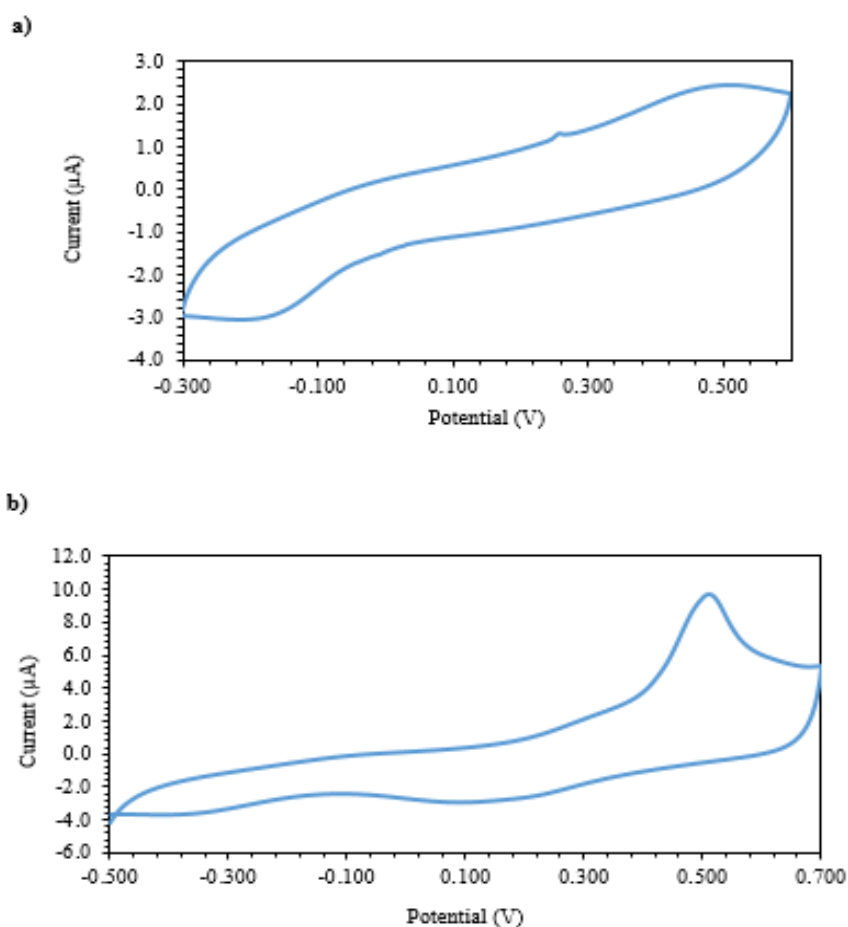


Figure 4.15: Cyclic voltammograms of (a) 90 μM and (b) 1 mM Ag NCs in microemulsion with 100 mM NaNO_3 with Ag/AgCl reference electrode and scan rate of 0.05 V/s at room temperature.

Electrochemistry measurements of the samples were done to establish that we have produced particles of Ag^0 and to determine particles size, oxidation state and bandgap of these particles electrochemically. The cyclic voltammograms of both samples in microemulsion were obtained in the presence of 100 mM NaNO_3 to enhance the electrical conductivity of the solution. In the absence of Ag^+ ions in solution, only the oxidation peak of $\text{Ag}^0 \rightarrow \text{Ag}^+ + \text{e}^-$ should be obtained,

but we still see weak reduction peaks in the voltammograms in figures 4.15a & b. These show that there were still unreacted Ag^+ ions in the system which hindered further analyses.

4.11 Electrospray ionization mass spectrometry

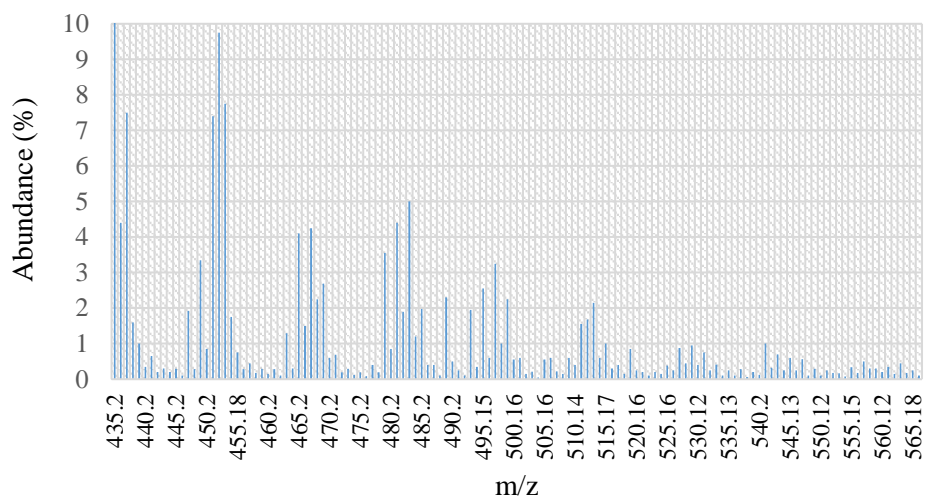


Figure 4.16: Electrospray ionization mass spectrometry spectrum of photosynthesized $90 \mu\text{M}$ and 1 mM Ag NCs samples.

ESI-MS analyses of both samples showed a high silver abundance in the m/z region of 435 to 565 (figure 4.16). A peak difference ($\Delta m/z = 2$) was observed between peaks of the same isotopic abundance which indicated a net charge of -1 for both samples obtained in the instrument's negative ionization mode. No discernible data was obtained from data in the positive mode.

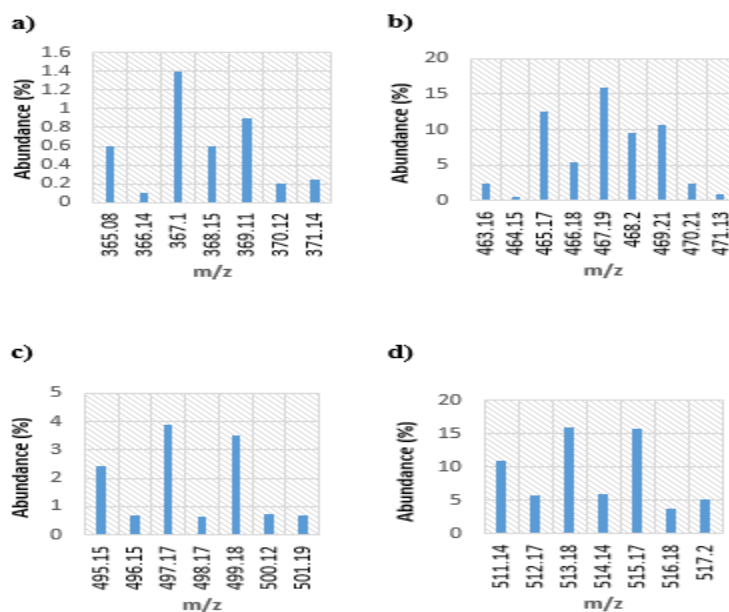


Figure 4.17: ESI-MS spectra of (a) $\text{Ag}_3(\text{H}_2\text{O})\cdot\text{H}_7^-$ (b) $\text{Ag}_4(\text{H}_2\text{O})\text{OH}^-$ (c) $\text{Ag}_3(\text{H}_2\text{O})_9\cdot\text{H}_{11}^-$ and (d) $\text{Ag}_3(\text{H}_2\text{O})_{10}\cdot\text{H}_9^-$. (e) $\text{Ag}_4(\text{H}_2\text{O})\cdot\text{H}_9^-$ (not included).

A parent peak was assigned to Ag_4 cluster in the m/z position of 557. Using the margin of separation between each set of successive peaks in the 435 - 565 m/z range, it was deduced that this *parent* molecular ion was composed of six water molecules and an hydroxyl ion as capping ligands. It therefore follows that the samples consisted of $[\text{Ag}_4(\text{H}_2\text{O})_6(\text{OH})]^-$ as the largest silver cluster, with many variants of $[\text{Ag}_3(\text{H}_2\text{O})_n(\text{OH})]^-$ smaller cluster groups (figure 4.17) having several hydrogen atoms replacing the OH^- group in some instances. After the poorly resolved 565 m/z peak, there were no Ag signals in the higher m/z region in the ESI-MS spectra.

Meanwhile, the sets of peaks in the m/z of 220 – 280, and 365 – 371 which represent peaks of Ag_2 clusters at m/z of 233 for $\text{Ag}_2(\text{OH})^-$, and m/z of 348 for $\text{Ag}_3(\text{H}_2\text{O})\cdot\text{H}_7^-$ were also observed. It is apparent that both the 90 μM and 1 mM samples have a mix of Ag_2 , Ag_3 and Ag_4 clusters (figure 4.17 b-e). Although, it is not certain if these Ag_2 and Ag_3 clusters are fragments of the parent clusters. However, it has already been established in the preceding chapter that Ag_4 clusters were formed from the dimerization of Ag_2 . The assignment of molecular weights and formulae to the Ag NCs were done using the University of Manchester Fluorine-chemistry (Mass spec) software, as well as the Waters ESI instrument's software, which showed good match with the experimental results (see figure 4.17 and Appendix section).

The negative charge on the clusters are indications of the loss of a proton during ionization, which implies yet again that similar to the borohydride-reduced microemulsion Ag NCs samples, these photosynthesized Ag NCs have all silver atoms in the oxidation state of zero

(Ag⁰)₂, (Ag⁰)₃ and (Ag⁰)₄, with both metal core and capping ligands held together by coordinate bonds.

4.12 Conclusion

We have demonstrated to the best of our knowledge the first time the syntheses of Ag NCs by photoreduction of Ag⁺ ions in microemulsion system. These Ag nanocrystals are monodispersed, and fluorescent. The size of the water droplets (nanoreactors) in the case are smaller than those obtained from the borohydride-reduced samples; which is understandable considering that the complementary droplets containing borohydride were absent.

Mass spectrometry data of these nanocrystals indicated three diversities of clusters – the (Ag⁰)₂, Ag₃ and Ag₄ with average diameters of 1.4 and 2.4 nm for the 90 μM and 1 mM samples. All the Ag NCs were capped by a number of water molecules and a hydroxyl group in one case, as ligands, or they may have only water molecule(s) with a number of hydrogen atoms replacing the hydroxyl group. The latter seeming to have been formed as a product of the ionization of water molecule arising from the loss of a proton. Hence, the Ag NCs come as anions with a net charge of -1, having the general formula: Ag_n(H₂O)_m(OH)⁻ or [Ag_n(H₂O)_mH_o]⁻, where n = 2, 3 or 4, m ranging from 1 – 9, and o = 1 – 7 as the case maybe, with metal core and ligands in a coordinate bonding.

These clusters have been observed to be stable and remained fluorescent for about six months in the emulsion, and can be used as precursors for various applications especially with labile passivating ligands. In terms of the production of three groups of clusters, the photoreduction in microemulsion systems are similar to those formed via borohydride chemical reduction, however the duration of the process is a little drawback. Although, UV-Vis analysis showed that the highest absorbance was usually obtained in the first one-hour of photoirradiation. But if the reaction requires the elimination of the borate group, then this method can be considered as efficient as the chemical reduction in producing monodispersed, fluorescent Ag NCs.

4.13 Reference

- 1 P. Mulvaney and A. Henglein, 1990, **168**, 391–394.
- 2 A. Henglein, *J. Phys. Chem.*, 1993, **97**, 5457–5471.
- 3 H. Harada, Masafumi Einaga, *Langmuir*, 2006, **22**, 2371–2377.
- 4 J. T. Petty, J. Zheng, N. V. Hud and R. M. Dickson, *J. Am. Chem. Soc.*, 2004, **126**, 5207–5212.
- 5 S. M. Copp, P. Bogdanov, M. Debord, A. Singh and E. Gwinn, *Adv. Mater.*, 2014, **26**, 5839–5845.
- 6 J. Zhang, S. Xu and E. Kumacheva, *Adv. Mater.*, 2005, **17**, 2336–2340.
- 7 S. J. Shang, L Dong, *Chem. Commun.*, 2008, **0**, 1088–1090.
- 8 H. Xu and K. S. Suslick, *Adv. Mater.*, 2010, **22**, 1078–1082.
- 9 W. Zhang, X. Qiao and J. Chen, *Mater. Sci. Eng. B Solid-State Mater. Adv. Technol.*, 2007, **142**, 1–15.
- 10 J. N. Solanki and Z. V. P. Murthy, *Ind. Eng. Chem. Res.*, 2011, **50**, 12311–12323.
- 11 C. Petit, P. Lixonf and M.-P. Pileni, *J. Phys. Chem*, 1993, **97**, 12974–12983.
- 12 G. Smitha, S. L., Nissamudeen, K. M., Philip, Daizy, *Spectrochim. Acta - Part A*, 2008, **71**, 186–190.
- 13 E. G. Gwinn, P. O’Neill, A. J. Guerrero, D. Bouwmeester and D. K. Fyngenson, *Adv. Mater.*, 2008, **20**, 279–283.
- 14 R. Denis, W. N. Athan, Muhoberac, B. Barry, Newton, C. John, Kumbar, A., Sardar, *Plasmonics*, 2014, **9**, 111–120.
- 15 R. P. Bagwe and K. C. Khilar, *Langmuir*, 1997, **13**, 6432–6438.
- 16 H. R. Khodashenas, B. Ghorbani, *Arab. J. Chem.*, 2015.
- 17 P. Qiu, C. Jensen, N. Charity, R. Towner and C. Mao, *J. Am. Chem. Soc.*, 2010, **132**, 17724–17732.
- 18 H. J. Yeh, Hsin-Chih, Sharma, Jaswinder, Han, J. Jason, Martinez, S. Jennifer, and Werner, *IEEE Nanotechnol. Mag.*, 2011, 28–33.
- 19 N. Durán, R. Cuevas, L. Cordi, O. Rubilar and M. Diez, *Springer*, 2014, **3**, 645.
- 20 J. A. Creighton, C. G. Blatchford and M. G. Albrecht, *J. Chem. Soc. Faraday Trans. 2*,

- 1979, **75**, 790.
- 21 I. Chakraborty, T. Udayabhaskararao and T. Pradeep, *Chem. Commun.*, 2012, **48**, 6788.
- 22 H. J. Bae, Dong-Sik., Kim, Eun-Jung., Bang, Jae-Hee., Kim, Sang-Woo., Han, Kyong-Sop., Lee, Jong-Kyu., Kim, Byung-Ik., and Adair, *Met. Mater. Int.*, 2005, **11**, 291–294.
- 23 B. Zeiger, *Superatoms, Lect. Sem. Abstr.*, 2008, 1-3.
- 24 D.-H. Chen, J.-H. Chen and T.-C. Hang, *J. Chinese Inst Chem Eng.*, 2000, **31**, 203–210.
- 25 G. M. Nocera, K. Ben M'Barek, D. G. Bazzoli, G. Fraux, M. Bontems-Van Heijenoort, J. Chokki, S. Georgeault, Y. Chen and J. Fattaccioli, *RSC Adv.*, 2014, **4**, 11564–11568.
- 26 A. Kumar and V. Kumar, *Chem. Rev.*, 2014, **114**, 7044–7078.
- 27 S. H. Lee, H. J., Yeo, S. Y., Jeong, *J. Mater. Sci.*, 2003, **38**, 2199–2204.
- 28 T. A. C. Kennedy, J. L. MacLean and J. Liu, *Chem. Commun.*, 2012, **48**, 6845.
- 29 J. R. Lakowicz, *Instrumentation for Fluorescence Spectroscopy*, 2006, 1-954.
- 30 A. Pietrini, PhD Thesis, 2003, Swiss Federal Institute of Technology, Zurich.
- 31 R. Sarkar, and Pal, K. S., *Biopolymers*, 2006, **83**, 675–686.
- 32 V. G. Budker, P. M. Slattum, S. D. Monahan and J. A. Wolff, *Biophys. J.*, 2002, **82**, 1570–1579.
- 33 A. V. Pietrini and P. L. Luisi, *Biochim. Biophys. Acta - Biomembr.*, 2002, **1562**, 57–62.
- 34 S. Bucak, and D. Rende, *Colloid and Surface Chemistry: A laboratory guide for exploration of the nano world*, CRC Press, Taylor & Francis Group, Boca Raton, 1st edn., 2014.
- 35 I. Capek, *Adv. Colloid Interface Sci.*, 2004, **110**, 49–74.
- 36 M. Instruments, *Malvern Guid.*, 2011, 1–6.
- 37 R. Higuchi, G. Dollinger, P. S. Walsh and R. Griffith, *Biotechnology*, 1992, 10, 413–417.
- 38 C. Pileni, M. P., Taleb, A., Petit, *J. Dispers. Sci. Technol.*, 1998, **19**, 185–206.
- 39 J. H. Liu, H. Y. Wang and C. H. Ho, *J. Polym. Res.*, 2003, **10**, 13–20.
- 40 M. Andersson, J. S. Pedersen, and A. E. C. Palmqvist, *Langmuir*, 2005, **21**, 11387–11396.

5 CHAPTER FIVE

5.1 RESULTS AND DISCUSSION III

5.2 Synthesis and Characterisation of Cu₇ NCs in Microemulsion

5.3 Introduction

In a study of Cu NPs, Vasquez *et al.*,¹ noted that copper clusters of 2 – 13 atoms were fluorescent, while those above Cu₁₃ (Cu_n with $n \geq 13$) were not, being already too big (≥ 3 nm).¹ In that and several other similar studies, there was no mention of the synthesis of any particular Cu NCs for detailed study. Fewer papers on Cu NCs have been documented in the literature and these are typical by their lack of detailed study and characterization of specific number of Cu NCs isolates in contrast to those of gold and silver which have been more intensively investigated.²⁻²⁴ While a number of these studies consisted essentially of data from a range of Cu NC sizes,^{25,26,27} many others^{1,28-38} fell short in detailed molecular characterization of Cu NCs with n number of atoms per cluster, where n is an integer value ($n = 2, 3, 4, \dots$).

In 2009, Vazquez *et al.*, reported what they observed was the first microemulsion synthesis of Cu NCs by the reduction of Cu²⁺ ions using very low, non-stoichiometric proportions of aqueous sodium borohydride (NaBH₄) solutions, using a non-ionic sodium dodecyl sulphate (SDS) as surfactant. This is the only notable report of the synthesis of Cu NCs by the microemulsion method as supported by YiZhong *et al.*, in their review paper in 2012.²⁷ In a more recent review paper by Siraj *et al.*, in 2016,³⁹ on the synthesis of Cu NPs, Chen and co-workers were reported to have synthesized Cu₆(GSH)₃ using hydrazine as a reducing agent under alkaline condition, and glutathione (GSH) as the capping agent.⁴⁰ Using bovine serum albumin (BSA), Qing *et al.*, 2013 (in Siraj *et al.*, 2016) prepared Cu NCs templated on 30-mer poly(thymine) with fluorescence emission centred at 615 nm. Wang *et al.*, 2014 (in Siraj *et al.*, 2016) reported the synthesis of stable, but weakly fluorescence Cu NCs using hydrazine hydrate as reducing agent under alkaline conditions.³⁹ Zhang and his group (in Siraj *et al.*, 2016),

announced the sonochemical synthesis of Cu NCs stabilized by glutathione (GSH) with paramagnetic properties.³⁹ Ghosh *et al.*, 2015 (in Siraj *et al.*, 2016), reported the synthesis of blue emitting Cu NCs (emitting at 414 nm) passivated by human serum albumin (HSA). Apart from the Cu₆(GSH)₃ reported by Chen *et al.*, all others were not characterized to the molecular details.

Copper like gold and silver is a coinage noble metal. Unlike silver and gold, it is relatively more abundant in the Earth crust,⁴¹ hence cheaper and more available.⁴² Nonetheless, its nanoclusters are less studied probably because of their susceptibility to oxidation and the problem of synthesizing small clusters of metals.²⁷ However, they have a number of important industrial applications in catalysis, where cheap, ultra-small, monodispersed, metallic particles with high conductivity are essential.^{28,29,39} Therefore, the need to synthesized stable, precise-sized, fluorescent Cu NCs of known molecular composition for application in catalysis and biomedical research is crucial for these industries.

5.4 Aim

The aim of this study is to synthesize and fully characterize ultra-small, monodispersed, precise-sized, fluorescent copper nanoclusters (of fewer than 13-atoms) passivated by inorganic ligands using the water-in-oil microemulsion system with AOT as a stabilizer.

5.5 Method

Cu NCs were synthesized in two separate reactions comprising 90 μM and 1 mM aqueous solutions of Cu(NO₃)₂ and NaBH₄ microemulsion systems. Each emulsion solution of 90 μM and 1 mM metal precursor was reacted with its equivalent portion of NaBH₄ microemulsion solution in a 1:1 ratio as shown in figure 5.1 below. A magnetic stir bar was inserted into the sample solutions and placed on a magnetic stirrer set at 500 rpm for five minutes. The 90 μM and 1 mM emulsion samples contained 0.0005 and 0.0025 M AOT surfactant respectively, previously dissolved in 5 and 18 mL isooctane (oil phase) and divided into two equal portions.

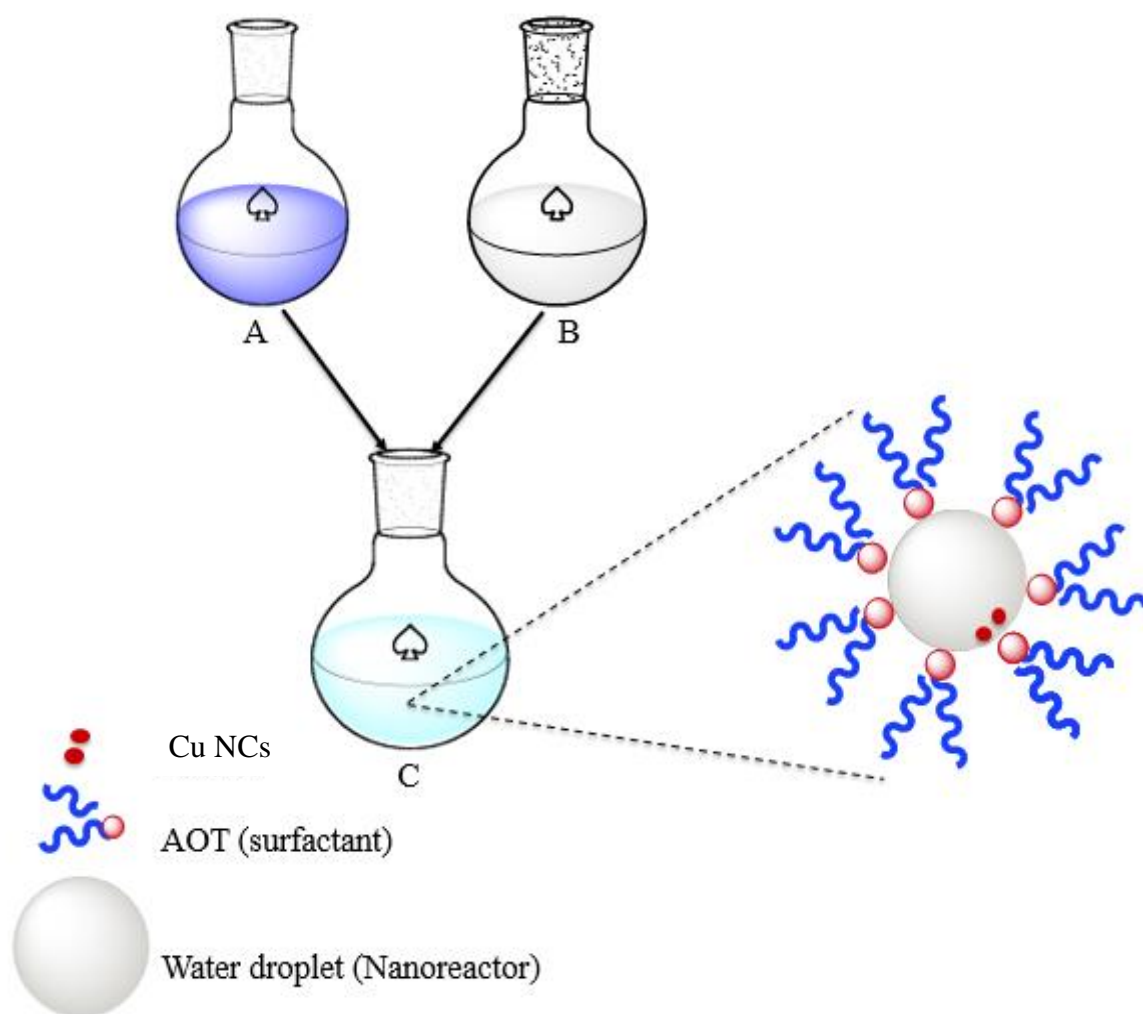


Figure 5.1: Reaction scheme for the synthesis of Cu NCs in microemulsion at ambient temperature (A) copper nitrate (B) sodium borohydride (C) Copper nanoclusters.

Equation of the reaction:



5.6 Absorbance

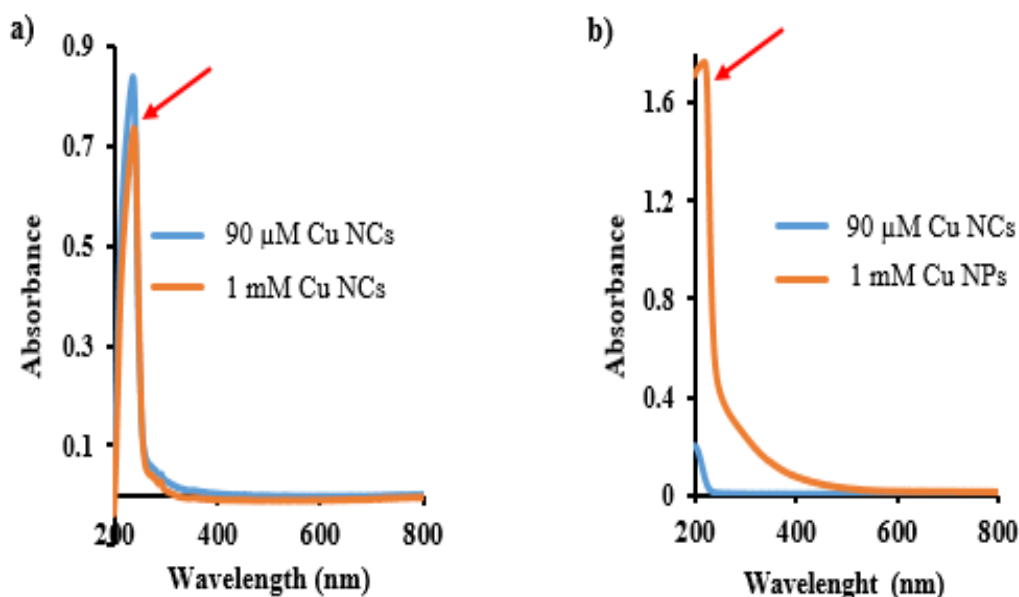


Figure 5.2: Absorbance spectra of $90\ \mu\text{M}$ and $1\ \text{mM}$ Cu NCs (a) in microemulsion (b) aqueous solution. Red arrows indicate the ligand-to-metal charge transfer transition for $[\text{Cu}(\text{H}_2\text{O})_6]^{2+}$ cations.

Figure 5.2 is the UV-Vis spectra of the emulsion samples and the aqueous-synthesized (control) samples both of which did not show plasmon resonance peaks. These are pointers of the formation of small clusters of copper and not copper nanoparticles Cu NPs. Lisiecki and Pileni,^{28,29} had observed that strong absorption bands due to plasmon resonance excitation or interband transitions in the ultraviolet and visible region of light are typical of colloidal metal nanoparticles (above 3 nm). Resonance plasmon bands of Cu NPs are usually positioned around 560 – 570 nm wavelength,^{1,28,29} with a characteristic secondary peak due to CuO layer usually observed at 800 nm.^{1,43} Similarly, the peak associated with Cu_2O NPs usually found between 400 – 700 nm centred at 510 nm was not observed in the UV-Vis spectra^{1,44} in figures 5.2 a & b respectively. The absence of Cu_2O peak has been ascribed to the effect of the strong NaBH_4 reducing agent.¹ The band at 560 nm progressively evolves as the copper cluster size increases,^{28,29} that is, as the clusters aggregate and grow in size over time.

Meanwhile in figure 5.2, a sharp band is observed at 240 nm, this according to Zhao *et al.*,⁴⁵ is associated with hydrated $[\text{Cu}(\text{H}_2\text{O})_6]^{2+}$ ions in aqueous solution. The ligand-to-metal core charge transfer transition is responsible for this 240 nm band.⁴⁵ Vazquez *et al.*,¹ reported difficulty in observing bands of small, planar clusters in the UV-Vis spectra of Cu NCs because

of the screening effect of the strong 240 nm band of $[\text{Cu}(\text{H}_2\text{O})_6]^{2+}$ cations still remaining in solution.

5.7 Fluorescence

Fluorescence measurements of the $90 \mu\text{M}$ and 1 mM Cu NCs samples show similar photoluminescence spectra (Figure 5.3 a&b). Peaks corresponding to different wavelengths of excitations were observed in the emission spectra. A broad but weak emission band occurred at 350 nm for both Cu NCs emulsion samples. Weak fluorescence of Cu NCs have previously been reported by Chen, and Wang *et als.*, in water^{40,46} as have been observed in this study. For both the $90 \mu\text{M}$ emulsion and control samples, two bands of emission were observed at 350 and 430 nm. The 430 nm band is covered by a collection of sharp peaks immediately following the 350 nm band in the spectra of the emulsion samples. These band of sharp peaks are thought to be associated with the surfactant (AOT). The presence of the 430 nm band suggests the evolution of thermodynamically more stable clusters, more so, as the energy of emission is inversely related to the cluster size.^{47,48} Meanwhile, no fluorescence was observed for the 1 mM control samples, which is an indication of the formation of large nonfluorescent Cu NPs.

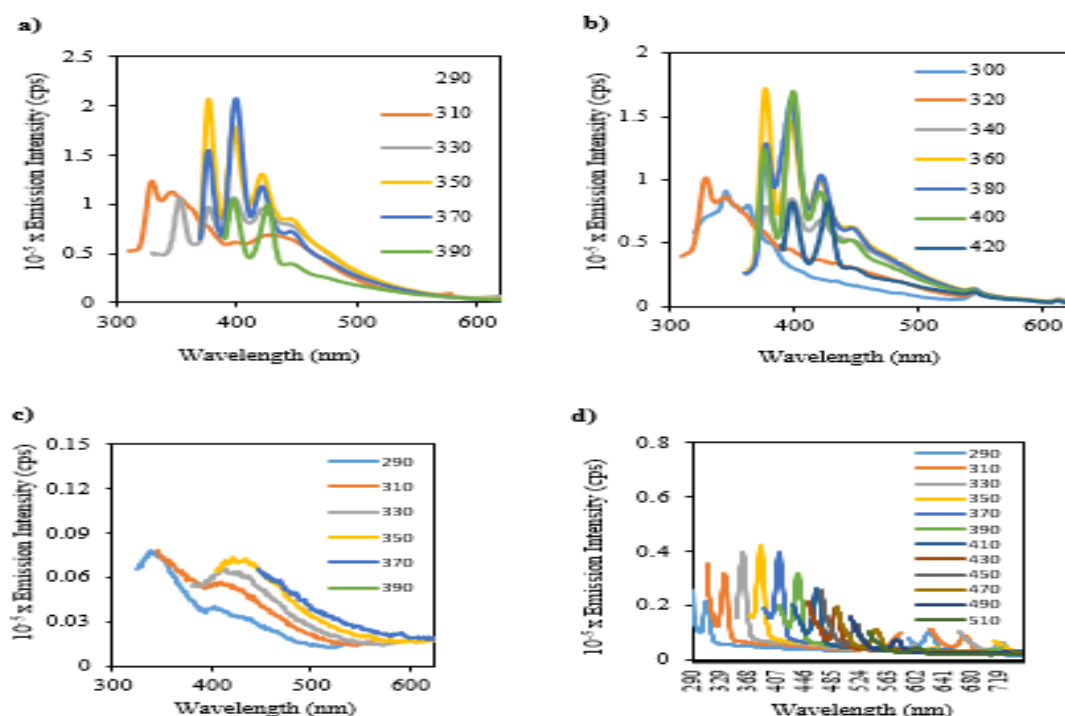


Figure 5.3: Fluorescence emission spectra of (a) $90 \mu\text{M}$ Cu NCs in microemulsion (b) 1 mM Cu NCs in microemulsion. (Encircled are peaks indicating aggregated particles) (c) $90 \mu\text{M}$ Cu NCs in aqueous solution (Raman peaks removed), and (d) 1 mM Cu NPs in aqueous solution (spectrum only contains unremoved Raman peaks for water). Excitation wavelengths are shown in the legends.

Two excitation wavelengths of 290 and 310 nm are responsible for the emissions with peak maxima at $\lambda_{\text{emi}} = 350$ and 430 nm. These excitation wavelengths are consistent for small clusters with large bandgaps⁴⁹ and show blue emissions.²⁷ Vazquez and co-workers reported the fluorescence of Cu NCs at 333 nm upon excitation at $\lambda_{\text{exc}} = 290$ nm in a similar study. The 90 μM samples produced the higher emission intensity ($>1.1 \times 10^5$ cps) of the two emulsion samples, signifying a higher concentration of the clusters with emission centred at 350 nm. There appear to be weak bands at the 550 and 618 nm wavelengths in the 1 mM Cu NCs sample that has been assigned to larger aggregating Cu NCs. These were not present in the 90 μM emulsion sample. However the low intensities of these 550 and 618 nm bands is a pointer to the preponderance of the smaller Cu NCs observed at shorter wavelengths.

The absence of the formation of oxides of copper is again ruled out by the absence of a strong emission band at the 493 nm position and a broadband in the 400 – 700 nm region centred at 510 nm.⁴⁴ Besides, the formation of copper (I) oxides is unlikely according to Vázquez *et al.*, because sodium borohydride is a strong reducing agent.¹

The onset of absorption (of excitation energy) at 326 and 394 nm in both emission spectra indicates bandgaps of 3.80 and 3.15 eV respectively. These are yet again, in agreement with values obtained for ultra-small blue emitting nanoclusters in a previous study.⁵⁰

As has already been discussed, analysis of the aqueous solution (control) samples (figure 5.3 c&d) show fluorescence emission bands only in the 90 μM spectrum, although with rather weak intensities (~ 7750 and 7000 cps respectively), which are much less intense when compared with the emulsion analogues.

5.8 Dynamic light scattering

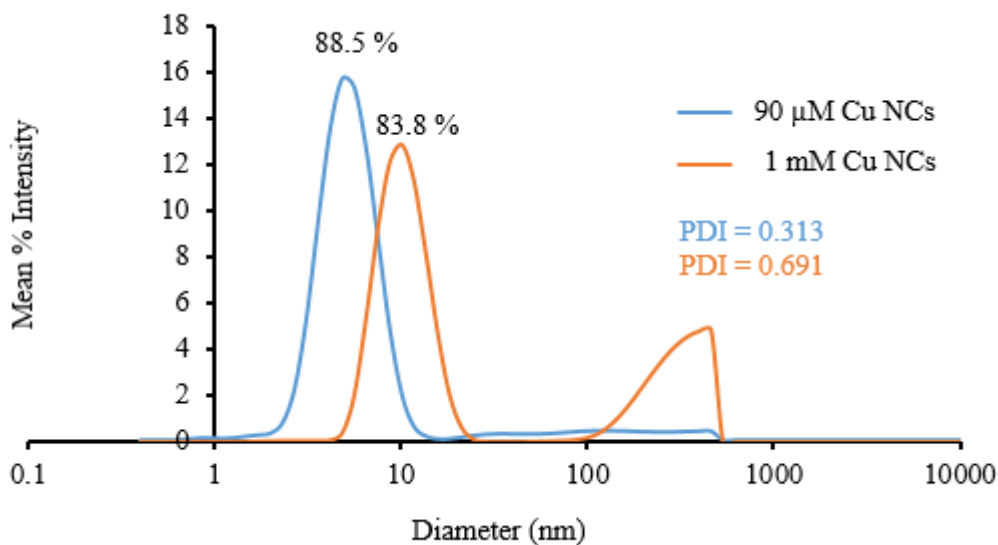


Figure 5.4: DLS charts of 90 μM and 1 mM Cu NCs in microemulsion

Two diameter sizes were basically observed for both the 90 μM and 1 mM Cu NCs samples in microemulsion (Figure 5.4). These consisted of a pair of peaks at 5.6 and 10.0 nm, and one above 100 nm. While the lower diameter values have been ascribed to reverse micelles, the higher diameter size (~100 nm) are considered to be water droplets.^{51,52,53} However, the percentage proportions of these larger “particles” are relatively lower in relation to the 5/10 nm sizes.

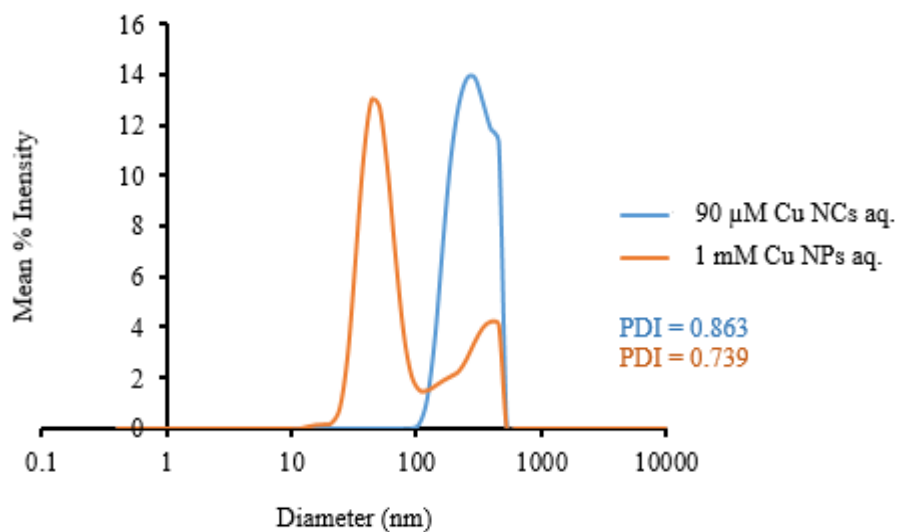


Figure 5.5: DLS chart of $90 \mu\text{M}$ and 1 mM Cu NPs (control) samples in aqueous solution.

The control samples recorded diameters between 50 – 300 nm (figure 5.5). These are in actual sense the diameters of colloidal Cu NPs in the aqueous solutions which are already too big to fluoresce¹ (see the 1 mM sample (control) spectrum). Nonetheless, the $90 \mu\text{M}$ sample contained a small population of fluorescent Cu clusters which were observed in figure 5.3c above.

Both control samples recorded high polydispersity indexes which are a measure of the variability in particle sizes; therefore, implying that the control samples were generally inhomogeneous in sizes. Lisiecki and Pileni²⁹ had similarly reported a high polydispersity index with colloidal nanoparticles in aqueous solution.

5.9 Transmission electron microscopy (TEM)

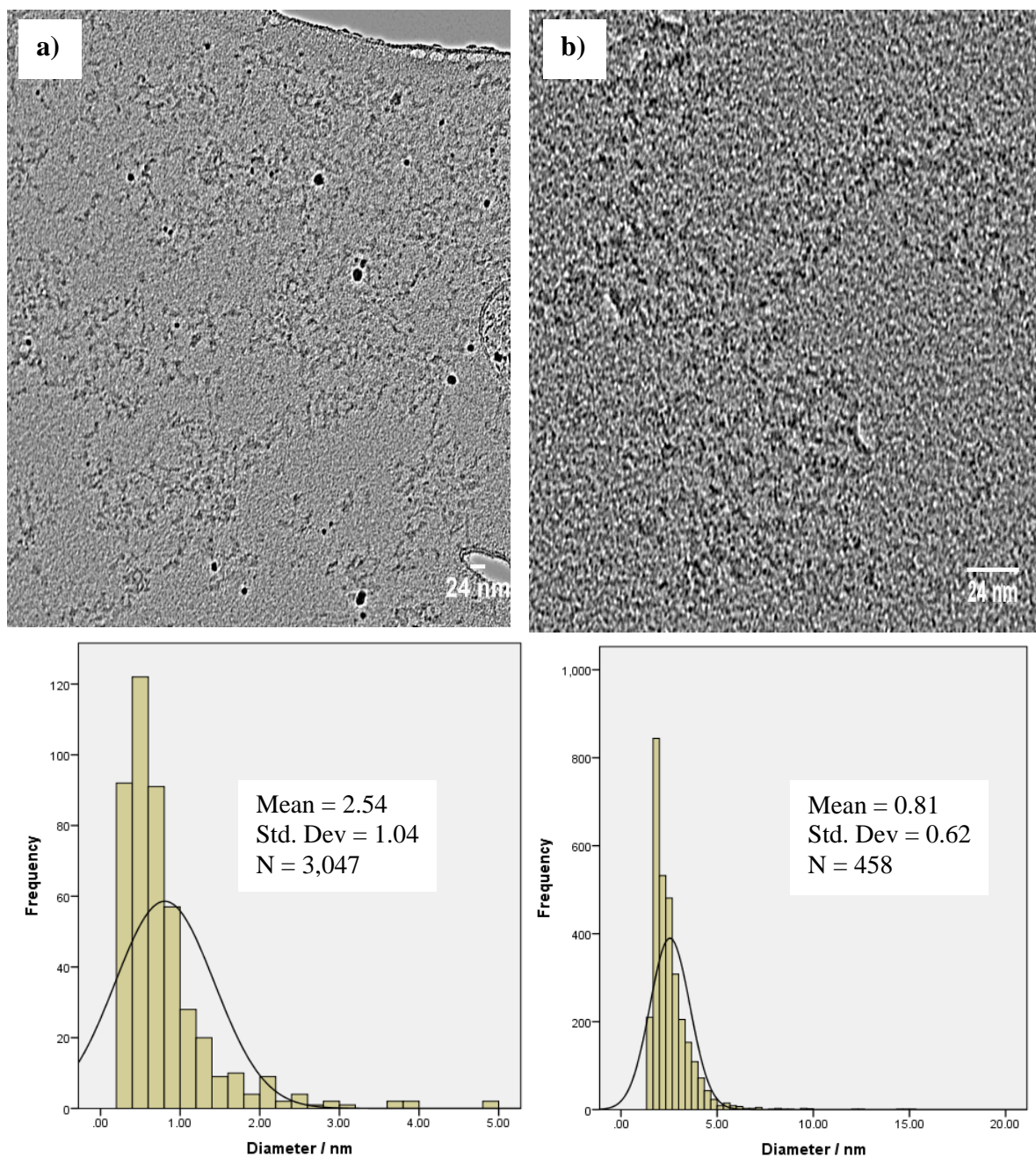


Figure 5.6: TEM images of (a) $90 \mu\text{M}$ and (b) 1 mM Cu samples in microemulsion obtained by drop casting the samples on holey carbon copper grids and drying overnight before TEM imaging.

TEM images of the $90 \mu\text{M}$ and 1 mM samples obtained on holey carbon copper grids show Cu NPs dispersed on the surface of the grid (Figure 5.6 a&b). An average particle size of 2.54 and 1.00 nm were measured for each of these samples accordingly. It should be noted however, that these TEM images (especially the $90 \mu\text{M}$) represent aggregated/coalesced particles since by the values of their diameters, they would already be composed of hundreds of atoms of Cu, too

much to be fluorescent. The limitation of the TEM instrument for analysing ultra-small metal cluster has previously been emphasized by various researchers.^{54,55} Although, copper is notorious for forming oxide layer due to oxidation,⁴³ it is not immediately clear if this affected the particles sizes obtained from the TEM imaging.

The smaller average particle size of 1 nm for the 1 mM Cu emulsion sample is thought to be connected with the increase in AOT concentrations used in the synthesis which has been shown to produce smaller droplets, lower amounts of metal cation precursors.²⁹ Lisiecki and Pileni²⁹ had observed that increases in the AOT concentration resulted in a decrease in droplets sizes as well as an increase in the number of droplets. This would also translate to a decrease in the number (concentration) of copper ions per droplet generally. Consequently therefore, the decrease in the concentration of copper ions per droplet would invariably translate to smaller copper clusters per droplet as was observed from the 1 mM TEM sample measurements.

5.10 Atomic force microscopy (AFM)

The AFM images of the samples in figure 5.8 also show aggregated Cu particles. These are shown more clearly in the 3D images (figures 5.7 c&f). Further particle size analyses of the 90 μM and 1 mM samples using the probability function of the Gwyddion software, the mean value of the particle sizes and their probability values were determined from a plot of probability function against diameter (see figure 5. 7 e&f) next to the main AFM images in figure 5.7 (a&b) respectively for the samples. A probability value of 0.6 that the 90 μM sample had an average particle size of 2.50 nm, and a value of 0.9 for the 1 mM sample having an average particle size of ~1.00 nm was obtained. Such low Cu NCs size have also been reported by Lisiecki and Pileni²⁹ with a high AOT concentration. Meanwhile, there is also a good agreement between the AFM and the TEM values for the 90 μM and 1 mM Cu samples.

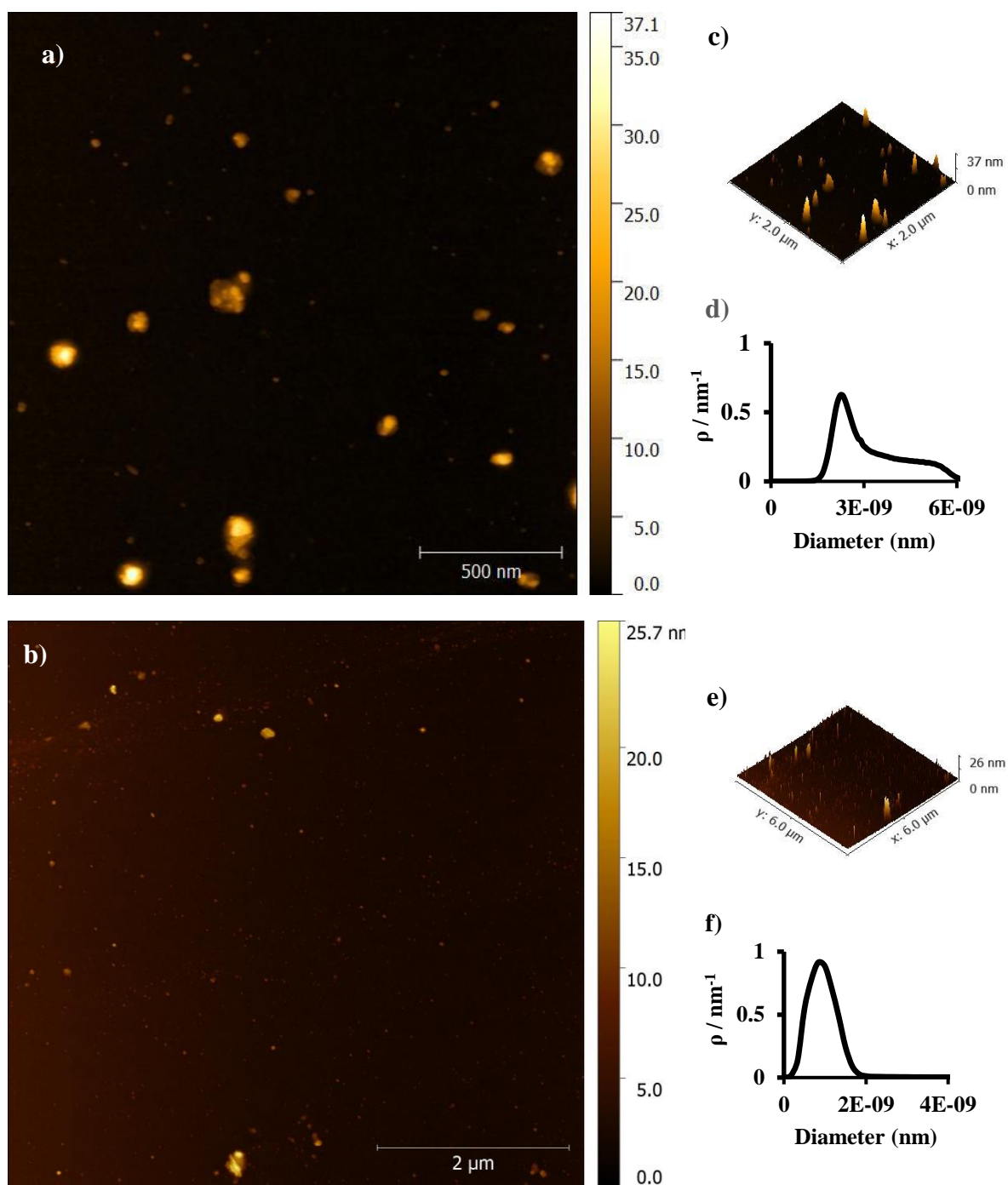


Figure 5.7: AFM images of (a) $90 \mu\text{M}$ and (b) 1 mM Cu NPs in microemulsion. (c) 3D image of $90 \mu\text{M}$ Cu NPs (d) Probability factor chart of particle diameter ($90 \mu\text{M}$ Cu NPs); (e) 3D image of 1 mM Cu NPs (f) Probability factor chart of particle diameter (1 mM Cu NPs).

5.11 Electrospray ionisation mass spectroscopy

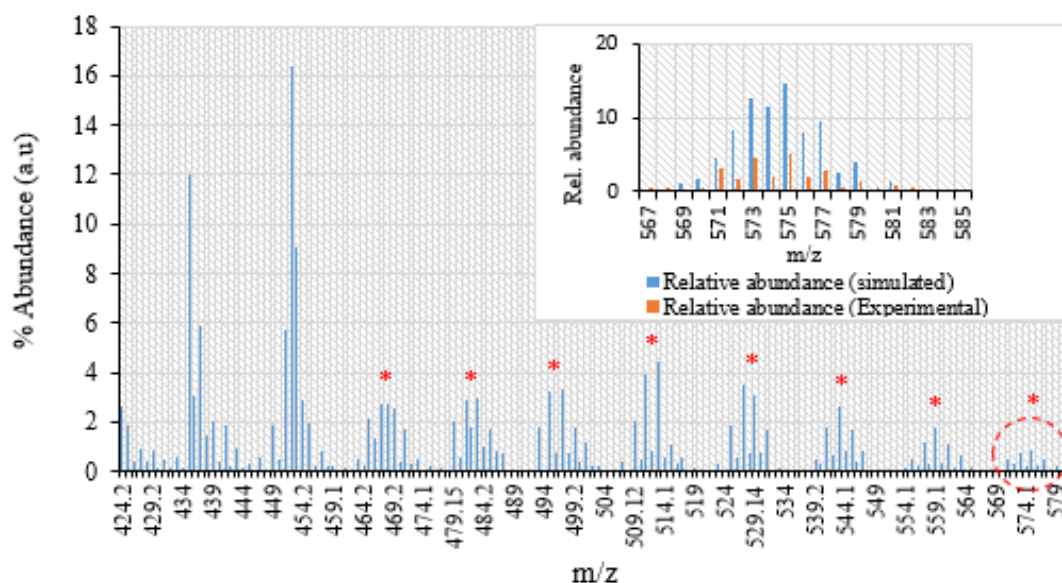


Figure 5.8: ESI-MS spectrum of dilute oil-separated 90 μM and 1 mM Cu NCs in microemulsion solutions; inset is the peak at 575 (experimental and simulated). The red asterisk are peaks ascribed to species of Cu₇ clusters.

Figure 5.8 shows a set of consecutive peaks in the m/z range of 424 - 603 which contains information of relevant analytical importance relating to the size of the Cu clusters. The differences in values between each successive set of peaks in this region provide information on the number and group(s) of atoms of elements comprising the ligand and metal core. A group of peaks at m/z 575.8 was resolved as $[\text{Cu}_7\text{B}_3\text{O}_5\cdot\text{H}_2\text{O}]^-$. The individual peaks in these bands, have a separation difference with a value of two (2) between them corresponding to a charge of one (1). Since the spectra scans were obtained in the negative mode arising from the deprotonation of the compound, a net minus charge is therefore attached to the molecular formulae. Furthermore, the peak pattern for this group of peaks matched almost perfectly with the simulated version (see Appendix fig. 8.12 & 8.13) obtained with the aid of the Fluorine Chemistry mass spec software provided by the University of Manchester website. The peaks at m/z 575.8 have tentatively been considered the “parent peaks”, instead of the two peaks above it at 589.8 and 603.1 respectively which are not well resolved. Even though, their m/z values of 589.8 and 603.1 appear to correspond to the molecular formulae of $[\text{Cu}_7\text{B}_3\text{O}_5\cdot\text{BH}_3\cdot\text{H}_2\text{O}]^-$ and $[\text{Cu}_7\text{B}_3\text{O}_5\cdot\text{BH}_3\cdot 2\text{H}_2\text{O}]^-$, their peak distribution did not match very well with the simulated versions, probably due to the poor resolution of these peaks in the spectra of the experimental

samples. These two peaks have values corresponding to 14 and 18 m/z units consecutively from the m/z 575 peaks. Meanwhile below the m/z 424, no clusters of copper were observed. Similar ESI-MS results were obtained for the spectra of both the 90 μM and the 1 mM Cu NCs samples having produced similar isotopic distributions.

Finally, indications from the ESI results seems to support a Cu NCs model with an empirical formula of $\text{Cu}_n\text{B}_m\text{O}_o\text{H}_p$, where $n=7$, m , o , and p are integer values.

5.12 X-ray photoelectron spectroscopy

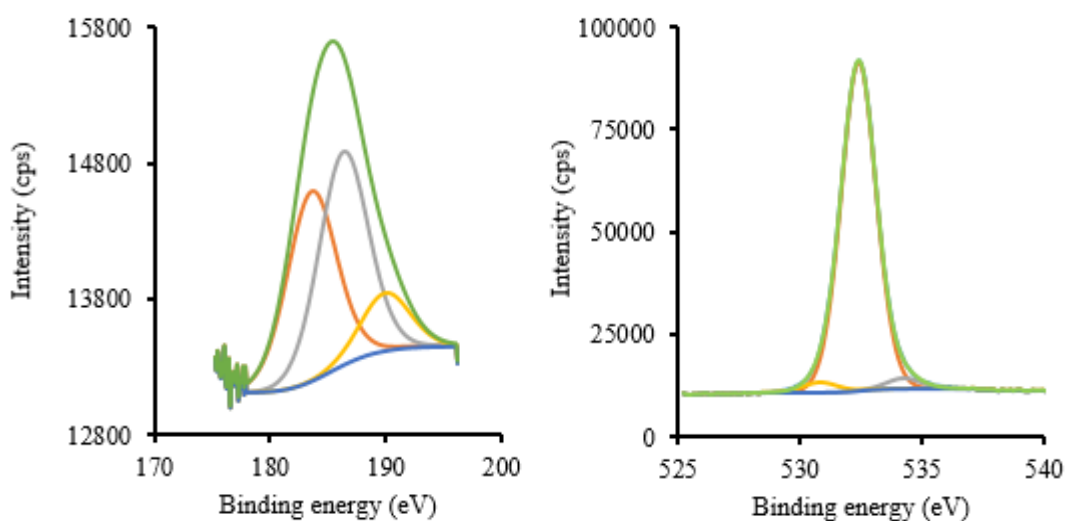


Figure 5.9: XPS chart of (a) Boron 1s and (b) oxygen 1s of Cu NPs samples on silicon wafer.

X-ray photoelectron spectroscopy studies of the as-synthesized Cu NCs samples were investigated in order to establish their elemental compositions and oxidation states, although the results were rather disappointing in terms of the absence of clear signals of the metal-core because of the high noise background (see Appendix fig. 8.7). Nonetheless, data recorded for the other elements were helpful in confirming the elemental nature of the passivating ligands.

In the absence of the usual organic ligands in this study, the Cu NCs are believed to be capped by the borate (B_3O_5) and the borane (BH_3) ligands with at least, one or two water molecules (H_2O). The first two of these ligands are believed to be products of the oxidation and hydrolysis of sodium borohydride (NaBH_4) in aqueous solution.^{56,57}

The XPS results confirmed the presence of the expected elemental components of these ligands (fig. 5.9 a&b). Figure 5.9a did not only indicate that there was boron in the samples but also

indicated that there were three boron chemical environments. Similarly, oxygen was also detected in three chemical environments in figure 5.9b. The following peak values were recorded for boron and oxygen respectively: 183.85, 186.75, and 191.70 eV, and 530.45, 532.35, and 534.65 eV in that order.

Although the signal at 183.85 eV could not be assigned in the literature, but the peak at 186.75 eV have been ascribed to the BH_3 (borane) group of $[(\text{C}_{10}\text{H}_{24}\text{N}_4)\text{Cu}](\text{BH}_4)_2$,⁵⁸ and $[\text{n-C}_4\text{H}_9)_4\text{N}]_3[\text{Cu}(\text{B}_{11}\text{H}_{11})_2]$,⁵⁹ while the 191.70 eV signal is thought to belong to the oxide of boron (B_2O_3)⁶⁰ or some copper- boron oxides $[\text{MCuB}_x\text{O}_y]$.⁶¹

The oxygen peaks at 530.45 and 532.35, were assigned to metal dioxide (MO_2) or metal trioxide (M_2O_3),^{62,63} and the 534.65 eV peak is associated with the aliphatic organic oxygen (from ester, organic acid),⁶² or the oxide of water (H_2O) respectively.^{33,35,64}

Scrutinizing the XPS results further, the percentage elemental compositions for boron and oxygen were given as 16.93 and 26.15 % (see the survey spectrum data in Appendix section). The ratio of these values for (oxygen: boron) is 1.54. This ratio is replicated approximately with a similar value of 1.50 obtained from the electrospray ionisation mass spectrometry (ESI) result for oxygen and boron in the proposed molecular formula of $[\text{Cu}_7\text{B}_3\text{O}_5.\text{BH}_3.\text{H}_2\text{O}]^-$. That is, if you consider that there are 6 oxygen to 4 of boron atoms per molecule. Therefore, the XPS results seem to support the molecular formula of $[\text{Cu}_7.\text{B}_3\text{O}_5.\text{BH}_3.\text{H}_2\text{O}]^-$ with a m/z of 589.8 (refer to section 5.11 above).

5.13 Fourier transform infrared spectroscopy

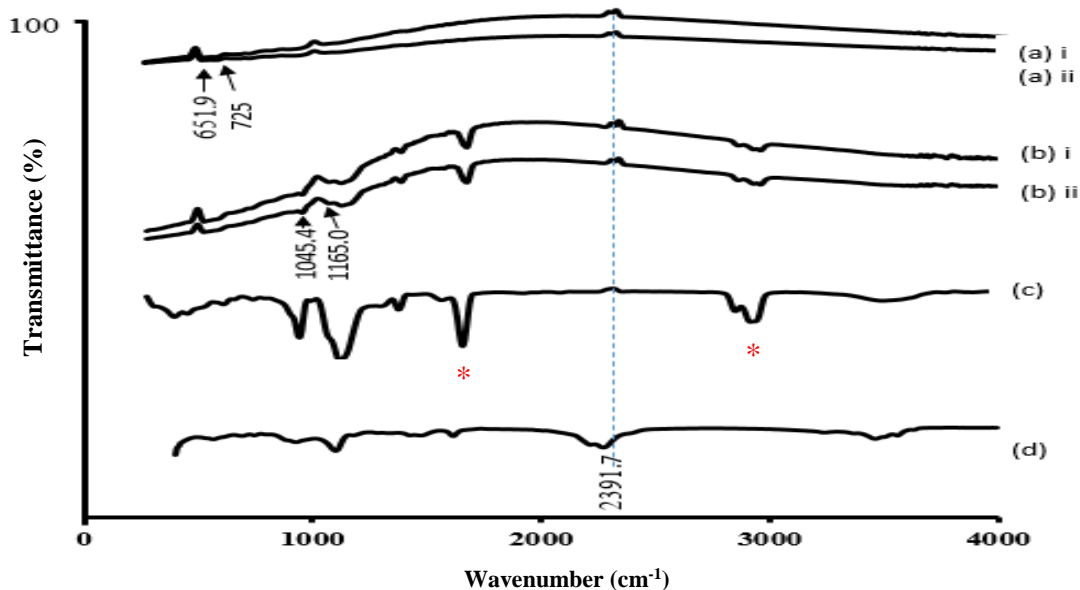


Figure 5.10: Fourier transform infrared spectra (a) 90 μM & 1 mM Cu NPs cartridge oil separated samples (b) 90 μM & 1 mM Cu NPs in emulsion (c) AOT- containing emulsion only (d) NaBH_4 , all dried samples on silicon chips.

Fourier transformed infrared (FTIR) spectra generally provide some valuable information as to the nature of the chemical bonds in a compound. The particular vibrational frequencies of these bonds are an indication of their presence in the compound. The rather weak concentration of the samples, made the FTIR measurement a challenging exercise, however several invaluable information were obtained from this analytical tool.

The Infra-red (IR) bands at 2385 and 2353 cm^{-1} were attributed to the terminal B-H stretching modes.⁵⁷ These were observed at 2391.7 cm^{-1} in the spectra of Cu NCs for both the cartridge cleaned and the crude emulsion (dried) samples; and in the NaBH_4 (control) as well, although, the latter, at a little lower frequency (2291 cm^{-1}) (Figure 5.10). The presence of this B-H stretch vibrational frequency mode, as well as the bending vibrations at 1045.4 and 1165.0 cm^{-1} ,⁶⁵ provides evidence of the presence of the BH_3 group. The slight difference in the vibrational frequencies of the BH_3 group in the Cu samples and the NaBH_4 can be attributed to the structure of the NaBH_4 with its full complement of four hydrogen atoms in the sodium tetrahydridoborane compound, in contrast to the fewer hydrogen atoms (three H- atoms) in the trihydridoborane group of the BH_3 ligand. The borane (BH_3) group vibrating at higher frequency than the BH_4 group, signifying stronger bonds even though their atoms are the same. The frequencies of the stretching vibrations depend on the mass of the atoms, and the strength/stiffness of the bond.⁶⁶

Similarly, it should also be expected to see in the IR spectra of the samples, bands corresponding to the borate group (B_3O_5) in the form of B-O bonds in the spectra of the samples. A weak band can be seen at 725 cm^{-1} which may be assigned to the B-O asymmetric stretch vibration of the BO_3 units.⁶⁷ Another weak band was also observed at 1024 cm^{-1} (especially in the emulsion sample in Figure 5.1b) and has been assigned to BO_4 unit.^{68,69,70}

The near complete absence of the organic portion in the spectra of cartridge oil-separated Cu NPs samples ($90\text{ }\mu\text{M}$ and 1 mM) is an indication of the effectiveness of the cartridge-separation process, as most of the bands (the C=O and CH_{3str} especially) present in the blank (AOT-emulsion only) and the Cu NCs in emulsion samples are essentially gone.

5.14 Conclusion

Cu_7 NCs have been synthesized and characterized from copper nitrate precursor by reduction with sodium borohydride in microemulsion. Sodium bis (2-ethyl hexyl) sulfosuccinate (AOT) was the surfactant, and isooctane was the oil phase. The syntheses were done at room temperature with a 1:1 molar ratio of the metal precursor to the reducing agent.

Cu NCs exhibited blue fluorescence and have a characteristic large bandgap of 3.80 eV typical of ultra-small nanoclusters of the strong zone of confinement. Thus, they displayed molecule-like spectroscopic properties. TEM and AFM measurements gave a diameter in the region of 1.0 – 2.5 nm for the samples in unanimity. Obviously, this showed that the clusters had aggregated during the drying process before measurement was taken, besides, the possibility of these ultra-small clusters melting and mixing up under the impact of the strong electron beam of the TEM instrument also existed.

Indications are that the Cu NCs did not form oxide of copper according to the XPS, UV-Vis (absence of the peak at 800 nm), and the ESI data. The ESI results confirmed the molecular formula of $[Cu_7.B_3O_5.BH_3.H_2O]^-$ for the Cu clusters with a m/z of 575.8. Although, evidence exists of the molecular formula of $[Cu_7.B_3O_5.BH_3.2H_2O]^-$ at a m/z of 603.1, however, the spectra peaks at this m/z region were poorly resolved and did not match with the simulated spectrum. The clusters also have a net charge of -1 which signifies that the compound was in the anionic form and thought to have been formed by the loss of a proton during ionization. This would infer that the seven atoms of Cu in the molecule were all in the oxidation state of zero.

5.15 Reference

- 1 C. Vázquez-Vázquez, M. Bañobre-López, A. Mitra, M. A. López-Quintela and J. Rivas, *Langmuir*, 2009, **25**, 8208–8216.
- 2 J. Doak, R. K. Gupta, K. Manivannan, K. Ghosh and P. K. Kahol, *Phys. E Low-Dimensional Syst. Nanostructures*, 2010, **42**, 1605–1609.
- 3 P. Georgiev, A. Bojinova, B. Kostova, D. Momekova, T. Bjornholm and K. Balashev, *Colloids Surfaces A Physicochem. Eng. Asp.*, 2013, **434**, 154–163.
- 4 K. D. Bhatt, D. J. Vyas, B. A. Makwana, S. M. Darjee and V. K. Jain, *Spectrochim. Acta - Part A Mol. Biomol. Spectrosc.*, 2014, **121**, 94–100.
- 5 Z. Khan, T. Singh, J. I. Hussain and A. A. Hashmi, *Colloids Surfaces B Biointerfaces*, 2013, **104**, 11–17.
- 6 H. Wu, X. Ji, L. Zhao, S. Yang, R. Xie and W. Yang, *Colloids Surfaces A Physicochem. Eng. Asp.*, 2012, **415**, 174–179.
- 7 S. F. Lai, C. C. Chien, W. C. Chen, H. H. Chen, Y. Y. Chen, C. L. Wang, Y. Hwu, C. S. Yang, C. Y. Chen, K. S. Liang, C. Petibois, H. R. Tan, E. S. Tok and G. Margaritondo, *Biotechnol. Adv.*, 2013, **31**, 362–368.
- 8 L. Yu, *Biochem. Physiol. Open Access*, 2012, **1**, 111–112.
- 9 R. K. DeLong, C. M. Reynolds, Y. Malcolm, A. Schaeffer, T. Severs and A. Wanekaya, *Nanotechnol. Sci. Appl.*, 2010, **3**, 53–63.
- 10 A. G. Rad, H. Abbasi and M. H. Afzali, *Phys. Procedia*, 2011, **22**, 203–208.
- 11 L.-N. Ma, D.-J. Liu and Z.-X. Wang, *Chinese J. Anal. Chem.*, 2010, **38**, 1–7.
- 12 C. Li, D. Li, G. Wan, J. Xu and W. Hou, *Nanoscale Res. Lett.*, 2011, **6**, 440.
- 13 G. Upert, F. Bouillère and H. Wennemers, *Angew. Chemie - Int. Ed.*, 2012, **51**, 4231–4234.
- 14 J. M. Gorham, R. I. MacCuspie, K. L. Klein, D. H. Fairbrother and D. Holbrook, *J. Nanoparticle Res.*, 2012, **14**, 1–16.
- 15 Y. Lv, Z. Long, C. Song, L. Dai, H. He and P. Wang, *BioResources*, 2013, **8**, 6161–6172.

- 16 E. J. E. Stuart, Y.-G. Zhou, N. V. Rees and R. G. Compton, *RSC Adv.*, 2012, **2**, 6879.
- 17 P. Prieto, V. Nistor, K. Nouneh, M. Oyama, M. Abd-Lefdil and R. Díaz, *Appl. Surf. Sci.*, 2012, **258**, 8807–8813.
- 18 A. M. Ferraria, S. Boufi, N. Battaglini, A. M. B. Do Rego and M. Reivilar, *Langmuir*, 2010, **26**, 1996–2001.
- 19 Ratyakshi and R. P. Chauhan, *Asian J. Chem.*, 2009, **21**, 113–116.
- 20 N. Cathcart, P. Mistry, C. Makra, B. Pietrobon, N. Coombs, M. Jelokhani-Niaraki and V. Kitaev, *Langmuir*, 2009, **25**, 5840–5846.
- 21 A. Šileikaitė, I. Prosyčėvas, J. Puišo, A. Juraitis and A. Guobienė, *Mater. Sci.*, 2006, **12**, 1392–1320.
- 22 G. Zhou and W. Wang, *Orient. J. Chem.*, 2012, **28**, 651–655.
- 23 I. S. Vijayashree, S. Yallappa, P. Niranjana and J. Manjanna, 2014, **4**, 598–603.
- 24 F. Porcaro, L. Carlini, A. Ugolini, D. Visaggio, P. Visca, I. Fratoddi, I. Venditti, C. Meneghini, L. Simonelli, C. Marini, W. Olszewski, N. Ramanan, I. Luisetto and C. Battocchio, *Materials (Basel)*, 2016, **9**, 1–15.
- 25 J. Tanori, N. Duxin, C. Petit, I. Lisiecki, P. Veillet and M. P. Pileni, *Colloid Polym. Sci.*, 1995, **273**, 886–892.
- 26 B. L. Cushing, V. L. Kolesnichenko and C. J. O'Connor, *Chem. Rev.*, 2004, **104**, 3893–3946.
- 27 Y. Z. Lu, W. T. Wei and W. Chen, *Chinese Sci. Bull.*, 2012, **57**, 41–47.
- 28 M. P. Lisiecki, I and Pileni, *J. Am. Chem. Soc.*, 1993, **115**, 3837–3896.
- 29 M. P. Lisiecki, I and Pileni, *J. Phys. Chem.*, 1995, 5077–5082.
- 30 J. N. Solanki and Z. V. P. Murthy, *Ind. Eng. Chem. Res.*, 2011, **50**, 12311–12323.
- 31 Sun Hua-Yu. Zhou Yan Huang Ya-Xi Sun Wei MI Jin-Xiao, *Chinese J. Struct. Chem.*, 2010, **29**, 1387–1393.
- 32 M. A. Malik, M. Y. Wani and M. A. Hashim, *Arab. J. Chem.*, 2012, **5**, 397–417.
- 33 J. Pawlonka, G. Słowik and W. Gac, *Annul. UMCS, Chem.* 2014, **68**, 1–2, 107–120.

- 34 H. Ohde, F. Hunt and C. M. Wai, *Chem. Mater.*, 2001, **13**, 4130–4135.
- 35 B. K. Park, S. Jeong, D. Kim, J. Moon, S. Lim and J. S. Kim, *J. Colloid Interface Sci.*, 2007, **311**, 417–424.
- 36 A. Umer, S. Naveed, N. Ramzan and M. S. Rafique, *Nano*, 2012, **7**, 1230005.
- 37 R. M. Sierra-Ávila, Rubén. Pérez-Alvarez, Marissa. Cadenas-Pliego, Gregorio. Padilla, Víctor Comparán. Ávila-Orta, Carlos. Pérez Camacho, Odilia. Jiménez-Regalado, Enrique. Hernández-Hernández, Ernesto. Jiménez-Barrera, *J. Nanomater.*, 2015, **2015**.
- 38 A. Musa, M. B. Ahmad, M. Z. Hussein, M. I. Saiman and H. A. Sani, *Nanoscale Res. Lett.*, 2016, **11**, 438.
- 39 N. Siraj, B. El-Zahab, S. Hamdan, T. E. Karam, L. H. Haber, M. Li, S. O. Fakayode, S. Das, B. Valle, R. M. Strongin, G. Patonay, H. O. Sintim, G. A. Baker, A. Powe, M. Lowry, J. O. Karolin, C. D. Geddes and I. M. Warner, *Anal. Chem.*, 2016, **88**, 170–202.
- 40 W. Gao, Xiaohui Lu, Yizhong Liu, Minmin Heab, Shuijian Chen, *J. Mater. Chem. C*, 2015, **3**, 4050–4056.
- 41 PeriodicTable.com
- 42 H. R. Khodashenas, B., and Ghorbani, *Arab. J. Chem.*, 2015.
- 43 A. Yanase and H. Komiyama, *Surf. Sci.*, 1991, **248**, 20–26.
- 44 H. S. Sharma, and P. Bhatti, *Mater. Chem. Phys.*, 2009, **114**, 889.
- 45 M. Zhao, L. Sun and R. M. Crooks, *J. Am. Chem. Soc.*, 1998, **120**, 4877–4878.
- 46 E. Jia, Xiaofang Yang, Xuan Li, Jing Li, Dongyue Wang, *Chem. Commun.*, 2014, **50**, 237–239.
- 47 J. Zheng, C. Zhang and R. M. Dickson, *Phys. Rev. Lett.*, 2004, **93**, 5–8.
- 48 Z. Wu and R. Jin, *Nano Lett.*, 2010, **10**, 2568–2573.
- 49 A. Ledo-Suárez, J. Rivas, C. F. Rodríguez-Abreu, M. J. Rodríguez, E. Pastor, A. Hernández-Creus, S. B. Oseroff and M. A. López-Quintela, *Angew. Chemie - Int. Ed.*, 2007, **46**, 8823–8827.
- 50 D. Schmid, G., and Fenske, *Phil. Trans. R. Soc.*, 2010, **368**, 1207–1210.
- 51 J. Eastoe, *Surfactant Chemistry*, 2003, 1-134.

- 52 M.-P. Pileni, *Nature*, 2003, **2**, 145–150.
- 53 P. L. Walde, P. Giuliani, A. M. Boicelli, C. A. Luisi, *Chem. Phys. of Lipids*, 1990, **53**, 265–288.
- 54 T. Frederick, M Weiss, *ACS Nano*, 2010, **4**, 3195–3200.
- 55 S. Dolai, P. R. Nimmala, M. Mandal, B. B. Muhoberac, K. Dria, A. Dass and R. Sardar, *Chem. Mater.*, 2014, **26**, 1278–1285.
- 56 P. Krishnan, T. H. Yang, S. G. Advani and A. K. Prasad, *J. Power Sources*, 2008, **182**, 106–111.
- 57 B. M. Concha, M. Chatenet, F. Maillard, E. A. Ticianelli, F. H. B. Lima and R. B. de Lima, *Phys. Chem. Chem. Phys.*, 2010, **12**, 11507.
- 58 Y.M. Shul’ga and V.D. Makhaev, *Koord. Khim.*, 1993, **19**, 809.
- 59 J. G. Kester, D. Keller, J. C. Huffman, M. A. Benefiel, W. E. Geiger, C. Atwood, A. R. Siedle, G. A. Korba and L. J. Todd, *Inorg. Chem.*, 1994, **33**, 5438–5442.
- 60 D. R. Brainard, W.A. and Wheeler, *J. Vac. Sci. Technol.*, 1998, **15**, 1801.
- 61 M. Kurmaev, E.Z., Fedorenko, V.V., Galakhov, V.R., Bartkowski, S., Uhlenbrock, S., Neumann, *J. Supercond.*, 1996, **9**, 97.
- 62 D. Beamson, G. and Briggs, *Adv. Mater.*, 1992, **5**, 778.
- 63 M. C. Biesinger, L. W. M. Lau, A. R. Gerson and R. S. C. Smart, *Appl. Surf. Sci.*, 2010, **257**, 887–898.
- 64 J. Russat, *Surf. Interface Anal.*, 1988, **11**, 414–420.
- 65 J. D. Wang B., J. Liu, S. Yang, *Polyhedron*, 1995, **895**.
- 66 B. H. Stuart, *Infrared Spectroscopy: Fundamentals and Applications*, 2004, vol. 8.
- 67 W. D. Smith, J., Seshadri, K. S., *J. Mol. Spectrosc.*, 1973, **45**, 327–337.
- 68 R. Debnath, Radhaballabh, and Sahoo, *Curr. Sci.*, 2004, **87**, 975–981.
- 69 D. Peak, G. W. Luther and D. L. Sparks, *Geochim. Cosmochim. Acta*, 2003, **67**, 2551–2560.
- 70 S. D. Ross, *Mineral. Soc.*, 1974, **4**, 205–226.

6 CHAPTER SIX

6.1 RESULTS AND DISCUSSION IV

6.2 Syntheses and Characterisation of Ag NCs Templated on ssDNA in Microemulsion

6.3 Introduction

The work in this chapter is a development of the previous chapter (Chapter 3) with the same reaction conditions, only here there are the introduction of single-stranded deoxyribonucleic acids (ssDNA) molecules into the water droplets of the microemulsion system. The DNA is added to the reaction medium at a molar ratio of 1 ssDNA molecule: 6 Ag⁺ ions before reducing the Ag⁺ ions with equivalent molar portions of NaBH₄ solution after incubating at room temperature for 30 minutes in the dark.

Three different ssDNA strands were used, these were:

1. 22-mer (5'- TGACTAAAAACCCTTAATCCCC-3' (**T₅C₈A₈G₁**)),
2. 29-mer (5'-AGTCACCCCAACCTGCCCTACCACGGACT-3' (**T₄C₁₄A₇G₄**)), and
3. 34-mer (5'-GGCAGGTTGGGGTGACTAAAAACCCTTAATCCCC-3' (**T₇C₉A₉G₉**))

oligonucleotide sequences. This would give a ratio of 1:4, 1:5, and 1:6 Ag: DNA bases respectively. Two sets of reactions were done comprising either 90 μM or 1 mM AgNO₃ and NaBH₄ solutions in a 1:1 mole ratio, with each of the three ssDNA types. In all, there were six reactions - 90 μM AgNO₃ and NaBH₄ with DNA1, 2, & 3; and 1 mM AgNO₃ and NaBH₄ with DNA1, 2, & 3 (see Chapter two- Experimental chapter for more details).

Dickson and co-workers demonstrated that DNA can be used as a template to stabilize fluorescent Ag NCs in aqueous solution in a pioneering work published in 2004 using NaBH₄ as a reducing agent to reduce Ag⁺ ions bound to a 12-base oligonucleotide.¹ They followed this up with another paper in a similar study in 2007 this time using a 12-base cytosine (dC₁₂)

oligonucleotide (a homopolymer) as a stabilizing ligand for Ag NCs by reducing Ag (I) dC₁₂ complex with NaBH₄ in aqueous solution.² Antoku also studied polycytosine-encapsulated Ag NCs using 8-, 12- and 24-base polycytosine DNA oligonucleotide at different pH-values in a PhD dissertation presented to the Georgia Institute of Technology in 2007.³ In 2009, Chang *et al.* reported the synthesis of metal (Au and Ag) nanoclusters stabilized by DNA for biomedical application as biomarkers.⁴ Sharma *et al.* in 2010 similarly documented the synthesis of Ag NCs using three strands of varying base lengths of 22, 29, 34, 46, and Cy5-DNA (the first three of these are being used in this study) in aqueous solution studying the effect of the DNA base lengths on the emission characteristics of the resulting DNA-Ag NCs.⁵ Yeh *et al.* in 2011 also reported the synthesis of guanine-rich oligonucleotide-templated Ag NCs as a molecular probe which lights up upon binding with target nucleic acids.⁶ Nithyaja *et al.* also synthesized DNA stabilized Ag NPs in aqueous solution at room temperature for optical applications in optoelectronics in 2012.⁷ Between 2013 and now, several other researchers have similarly published papers on DNA-templated Ag NCs in aqueous solution.^{8,9,10,11,12,13} However in all of these studies, one of the concerns are raised is the containment non-fluorescent nanoparticles during synthesis in aqueous solution.^{4,14,15}

Putting DNA at high dilution in small water droplets (nanoreactors),¹⁶ creates a situation where it is likely to have one molecule of ssDNA per water droplet. By carefully controlling the amount of Ag⁺ ions in the droplets there would be little possibility of making large (i.e. >10 nm) non-fluorescent Ag nanoparticles (Ag NPs) since there are not enough Ag⁺ ions in the droplets in the first place. Meanwhile, Ag⁺ ions and ssDNA are both entrapped in the nanoreactors hence not likely to escape into the oil phase since DNA can only be solubilized in the aqueous phase of the emulsion system.¹⁷

DNA is present in the chromatin of eukaryotic cells in the condensed form.¹⁷ Similar observation of DNA existing in the condensed form in the water droplets of microemulsion systems have been reported by researchers.^{18,19,20} Therefore, incorporating DNA into water droplets in microemulsion systems also offers the opportunity of replicating *in vitro*, such similar *in vivo* cellular physiology. Although the incorporation of DNA into microemulsion systems has been studied and reported by some researchers in recent times, such studies were however very few and limited only to DNA-containing water-in-oil microemulsion.¹⁷⁻²⁰

6.4 Aims

The aims of the work in this chapter are to produce small, fluorescent, Ag-nanoclusters bound to ssDNA in microemulsion systems without, making large Ag NPs, thereby obtaining a cleaner synthesis of DNA-templated Ag NCs; and to further investigate the interaction of the DNA containing AgNO₃ water-in-oil droplets with NaBH₄ containing water-in-oil emulsion as a means of producing Ag⁰ clusters of well-defined sizes.

6.5 Reaction Scheme

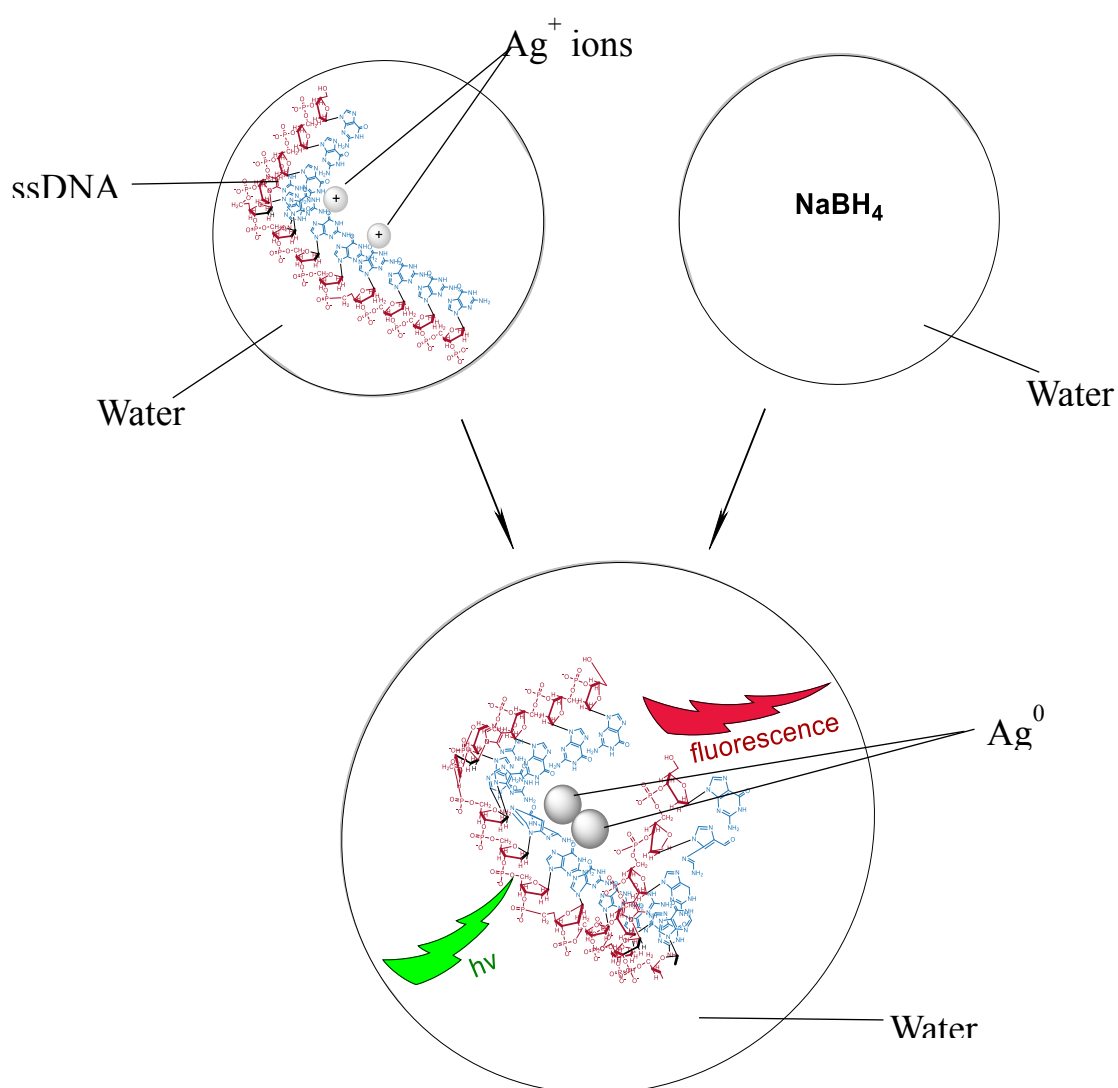


Figure 6.1: Reaction scheme for the reduction of Ag⁺-ssDNA with sodium borohydride in microemulsion droplets. Droplets containing aqueous solution of DNA oligomer (red portion representing the sugar and phosphate groups, and the blue portion is the nucleobases), previously treated with Ag (I) ions were reacted with NaBH₄ from another droplet to effect reduction and formation of ssDNA-templated Ag NCs in a larger droplet.

Ag NCs were prepared by reacting Ag^+ ions with ssDNA in a 1:6 ratio in microemulsion and incubating in the dark for 30-45 minutes before reducing the Ag^+ ions with equimolar portions of aqueous sodium borohydride in another microemulsion solution (Figure 6.1) and then stirred for 5 minutes with a clean magnetic stirrer at 450 revolutions per seconds (rps).

6.6 Absorbance

Ultraviolet-visible absorption spectroscopy is helpful in determining cluster size and binding between metals and ligands.^{21,22} Figures 6.2, 6.3, & 6.4, show absorbance spectra of DNA-templated Ag NCs samples (Ag-DNA) in microemulsion (Figure 6.2a, 6.3a, 6.4a) and in aqueous media as controls (Figure 6.2b, 6.3b, 6.4b). The concentrations of silver ions, DNA, and borohydride, were the same in all cases these sets of reactions. However, there were three different DNA sequences, and hence, three oligomer base lengths corresponding to the label: DNA1, 2, and 3. These three ssDNAs comprise 22, 29, and 34 bases per molecule respectively. In all, the 1:4, 1:5, and 1:6 ratios of silver to DNA bases (Ag: bases) were obtained for each of the ssDNAs. There was a pair of experiments for each of these ssDNAs with the $90\ \mu\text{M}$ the $1\ \text{mM}$ Ag^+ ions in aqueous solution (without the microemulsion). The aqueous solution experiments served as the control. Altogether, there were six emulsion samples and another six control samples.

There were no plasmon resonance bands in the UV-Vis spectrum of the $90\ \mu\text{M}$ the $1\ \text{mM}$ microemulsion samples. But the presence of the plasmon resonance peak due to metallic silver nanoparticles can be observed in the aqueous-reaction samples, particularly with the $1\ \text{mM}$ sample due to its higher silver concentration. Generally, there was a decrease in absorption intensity of the DNA peak with the addition of Ag^+ ions, which is in agreement with similar observation by Mello and coworkers.²³ In the control samples however, this decrease is more pronounced with higher silver concentration even as the silver plasmon band increases. Another peak present at 240 nm in all the microemulsion emission spectra have been attributed to the ligand to metal transition.²⁴

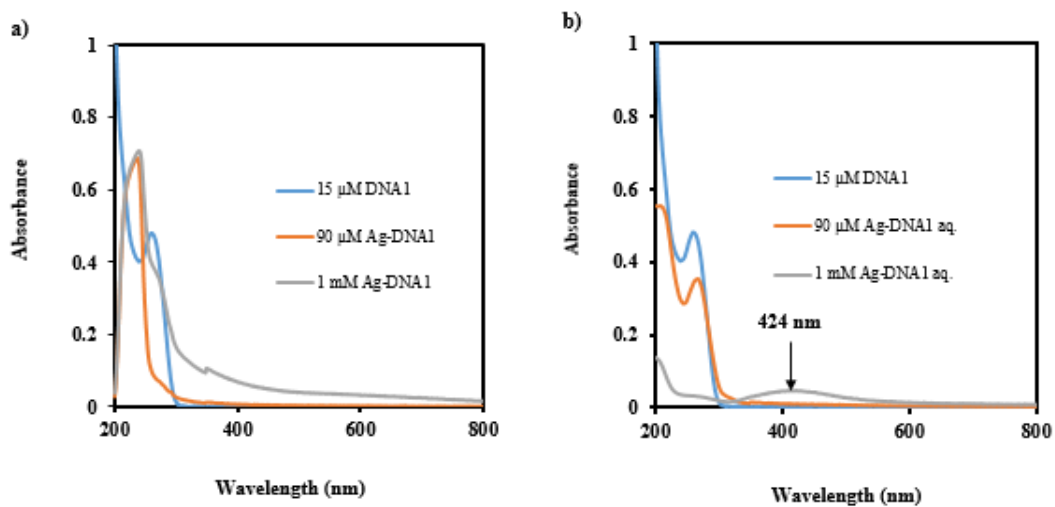


Figure 6.2: Absorbance spectra of DNA1 templated 90 μM and 1 mM Ag in (a) microemulsion (b) aqueous solution.

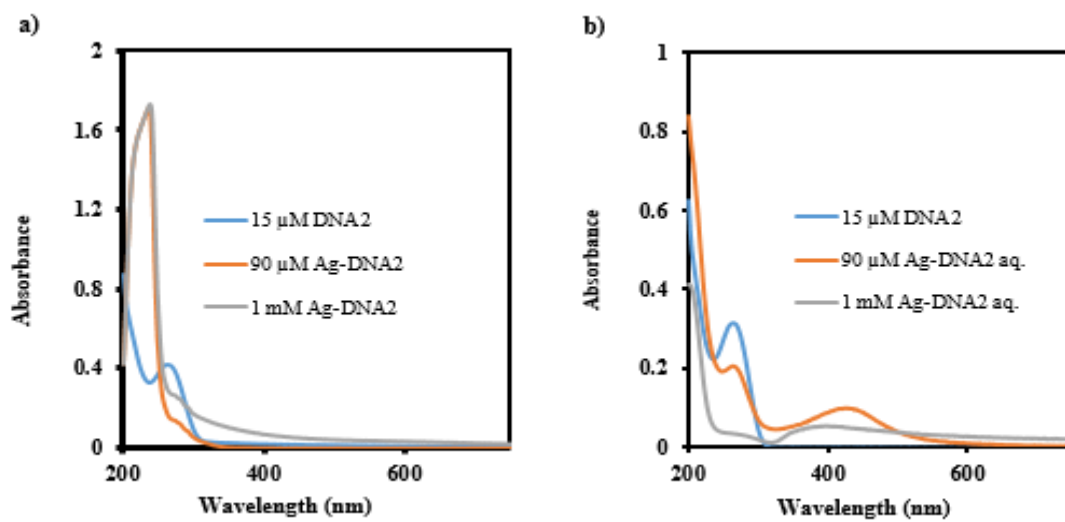


Figure 6.3: Absorbance spectra of DNA2 templated 90 μM and 1 mM Ag⁰ in (a) microemulsion (b) aqueous solution.

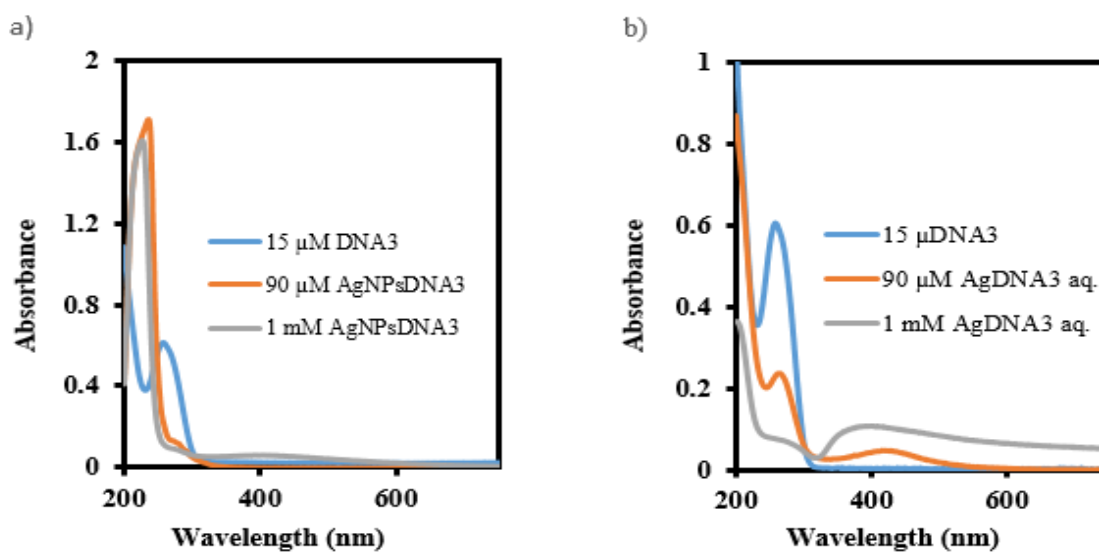


Figure 6.4: Absorbance spectra of DNA3 templated $90\ \mu\text{M}$ and $1\ \text{mM}$ Ag^0 in microemulsion (a) microemulsion (b) aqueous solution.

The appearance of prominent plasmon band became more intense with increasing DNA type (length) for the samples in the control samples. However, only the faintest hint of this band can be noticed in the $1\ \text{mM}$ Ag-DNA3 microemulsion samples (figure 6.4a).

Similar patterns were replicated in the other $90\ \mu\text{M}$ and $1\ \text{mM}$ Ag-DNA2 and $90\ \mu\text{M}$ and $1\ \text{mM}$ Ag-DNA3 for both microemulsion and aqueous systems. Although, few variations were observed with the $1\ \text{mM}$ Ag-DNA2 & 3 aqueous (control) samples where the absorbance seemed to trail off into the near infra-red (IR) region, an indication of light scattering.

The DNA absorption band of the microemulsion samples are comparatively less intense and slightly blue-shifted as similarly observed by Pietrini and Luisi²⁰ than was the case with aqueous (control) samples. Similar changes in the wavelength of the DNA absorption peak maximum upon addition of Ag^+ ions have been highlighted by Ritchie *et al.*² Meanwhile, there was no noticeable light scattering in the UV absorption spectra of all the microemulsion samples, indicating that the solutions were transparent to light.²⁰ This implies that DNA molecules were solubilized in the aqueous phase of the emulsion as was expected.

6.7 Fluorescence

Figure 6.5, 6.6, and 6.7 are emission spectra for each of the three ssDNAs used in this study, these show that all three DNAs are fluorescent. They all have emissions centred at 375 nm, and display similar bandwidth of approximately 150 nm, spreading between 320 – 470 nm. Their excitation energies are also similar and range between 290 – 330 nm in wavelength. Above this excitation energy ranges, no emission was observed subsequently. In all the three ssDNAs, the excitation energy at 310/315 nm produced the most fluorescence intensity. The observed fluorescence of these ssDNA samples is believed to be associated with contaminants from the protecting groups during DNA synthesis.

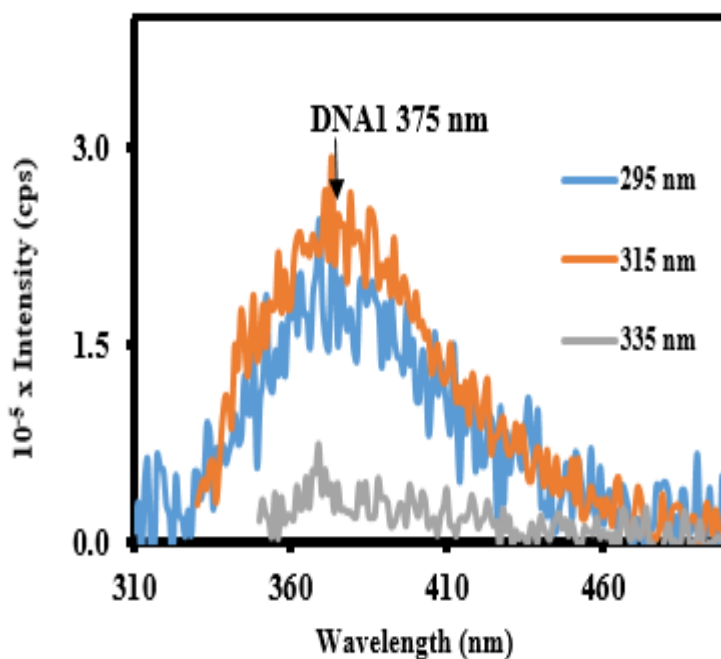


Figure 6.5: Emission spectra of aqueous solutions of DNA1 only (without Ag). Excitation wavelengths are shown in the figure legend.

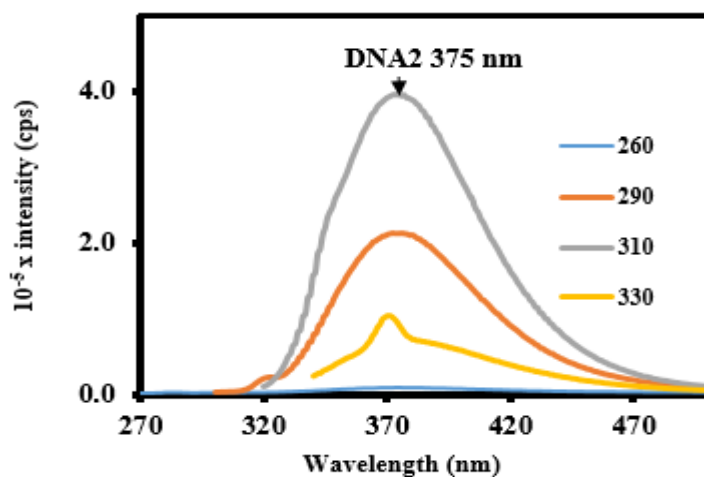


Figure 6.6: Emission spectra of aqueous solutions of DNA2 only (without Ag). Excitation wavelengths are shown in the figure legend.

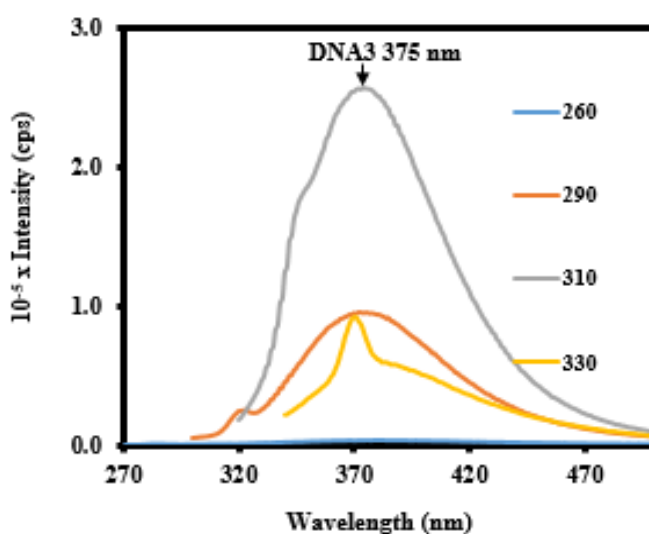


Figure 6.7: Emission spectra of aqueous solutions of DNA3 only (without Ag). Excitation wavelengths are shown in the figure legend.

Emission by DNA has similarly been reported by Liu and co-workers²⁵ working with 15-mer poly-nucleotides. Again, Vaya *et al.*, also observed fluorescence with Calf thymus DNA in aqueous solution.²⁶

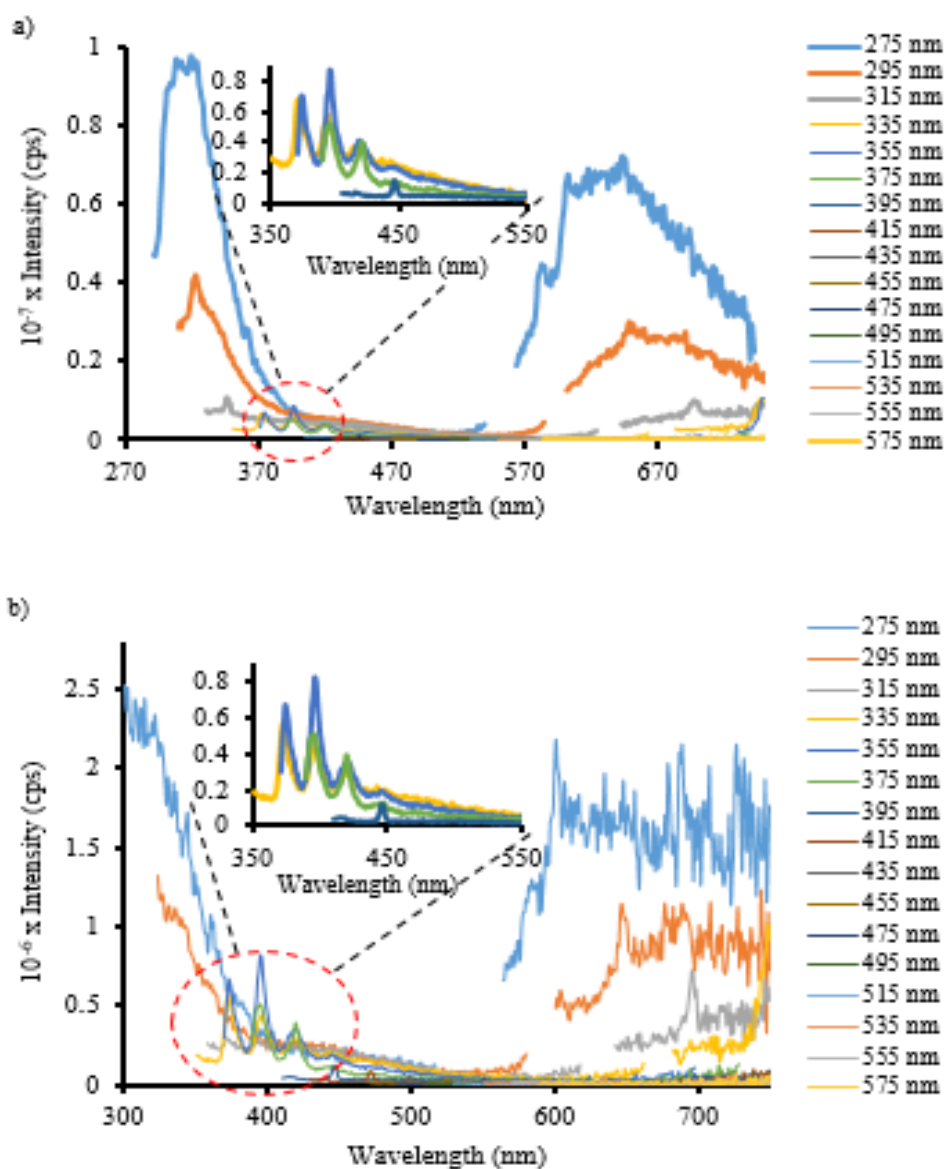


Figure 6.8: Fluorescence emission spectra of (a) $90 \mu\text{M}$ Ag-DNA1 and (b) 1 mM Ag-DNA1 in the microemulsion. The encircled set of peaks are thought to be contaminants from the AOT. Spectra (b) & (c) were acquired at emission and excitation slits each set at 2 nm in order to improve the signal to noise quality.

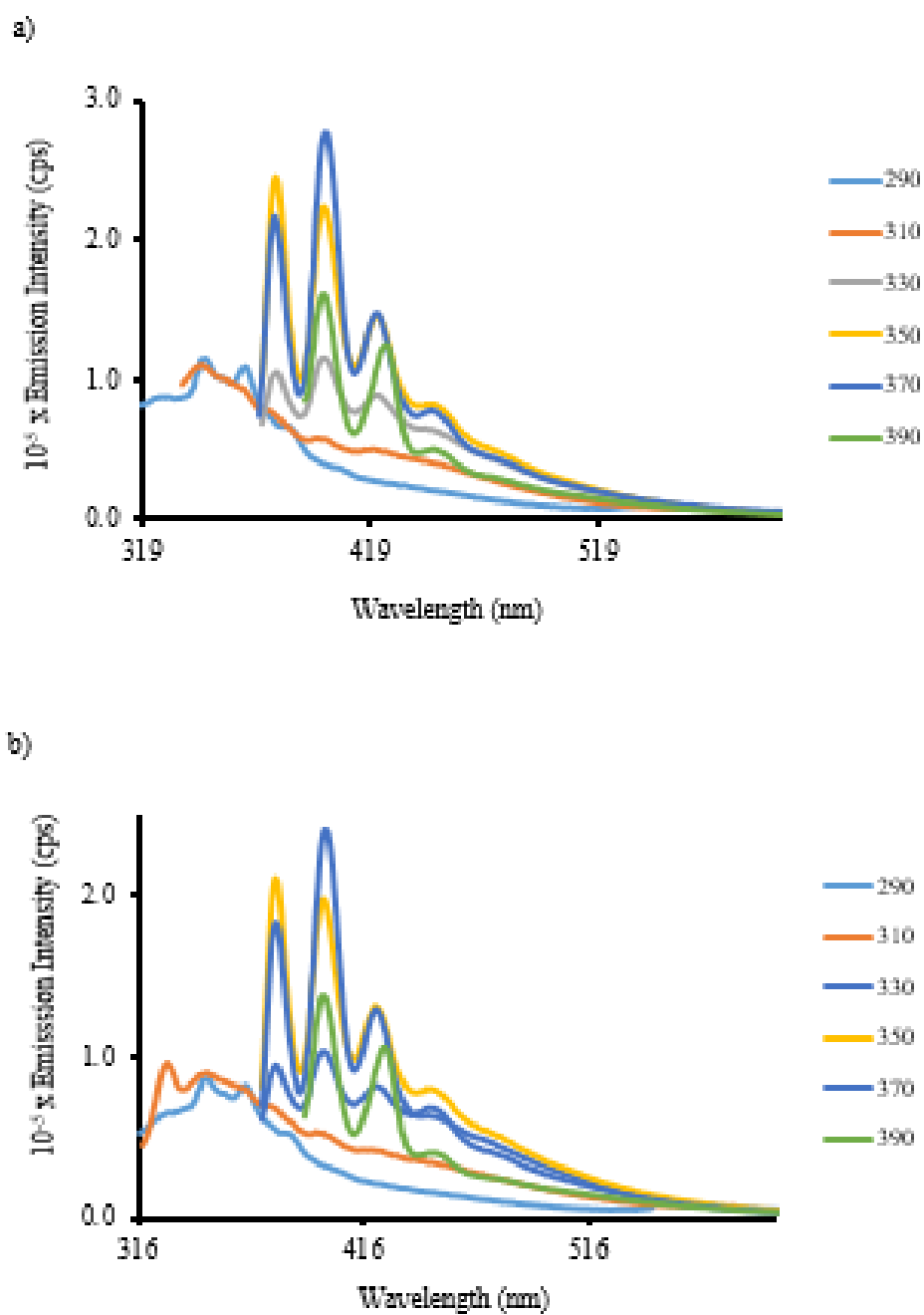


Figure 6.9: Fluorescence emission spectra of (a) $90 \mu\text{M}$ Ag-DNA2 and (b) 1 mM Ag-DNA2 in the microemulsion.

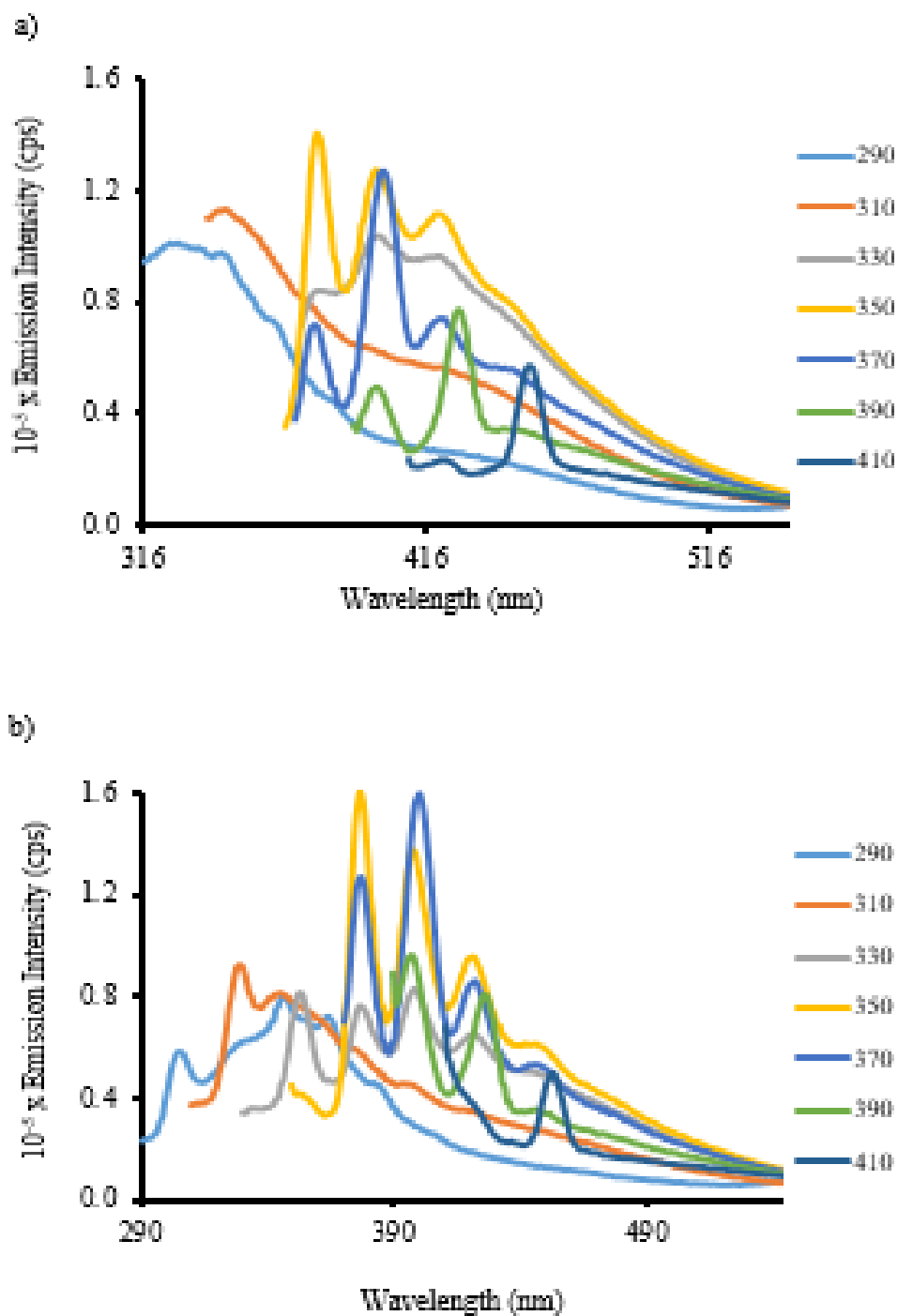


Figure 6.10: Fluorescence emission spectra of (a) $90 \mu\text{M Ag-DNA3}$ and (b) 1 mM Ag-DNA3 in the microemulsion.

Figure 6.8 a&b are emission spectra of $90 \mu\text{M Ag-DNA1}$ and 1 mM Ag-DNA1 microemulsion-synthesized samples. These show a sharp emission band between $\sim 320\text{-}325 \text{ nm}$ centred at 315 nm with high intensity, and another at 645 nm which is broad and less intense. Between these

two emission bands, is a set of complex bands with peak maximum centred at 401 nm which are thought to be contaminants from the AOT. This was confirmed by determining the differences in wavenumber between each successive peaks and were found to correspond to $1313.2 - 1517.4 \text{ cm}^{-1}$ with an average of 1393.5 cm^{-1} . This tallies with the stretch vibrational frequency of a C–C bond or a C–H bend vibration of an organic compound.^{27,28}

These spectra further indicate that two clusters of Ag^0 were produced according to their wavelengths of emission. While the bands at 315 nm are attributed to small clusters, probably of Ag_2 or Ag_3 ²⁹, the 650/680 nm is ascribed to larger aggregated Ag NCs.¹

Figures 6.9 and 6.10 (a&b) are very similar, they are emission spectra of $90 \mu\text{M}$ Ag-DNA2 and 1 mM Ag-DNA2 and $90 \mu\text{M}$ Ag-DNA3 and 1 mM Ag-DNA3 samples respectively in microemulsion. They all have a single emission band at $\sim 350 \text{ nm}$ which is broad and low in intensity with a shoulder at $\sim 422 \text{ nm}$ for the $90 \mu\text{M}$ Ag-DNA3 sample. These 350 nm emission bands have excitation energies at 290 and 310 nm. Again, the similar sets of complex emission bands were observed within 365 – 465 nm centred at 401 nm in these spectra which has been assigned to contaminants from the AOT. No other luminescence bands were observed for these samples.

Thus, there was only one emission band at 315 nm besides the complex set of peaks at 401 nm for Ag-ssDNA2 and 3 microemulsion samples, and this was observed at relatively higher wavelengths when compared with those of the Ag-ssDNA1. The intensities of the $90 \mu\text{M}$ Ag-DNA2 and 3 were slightly higher than the 1 mM Ag-DNA2 and 3 samples. Theoretically, the large intensities of the signals at 320 and 680 nm are often indicative of a high concentration of fluorophores,^{2,30,31} the wavelength of fluorescence emission is dependent on the electronic density of state and hence, the size of the metal cluster.³²⁻³³

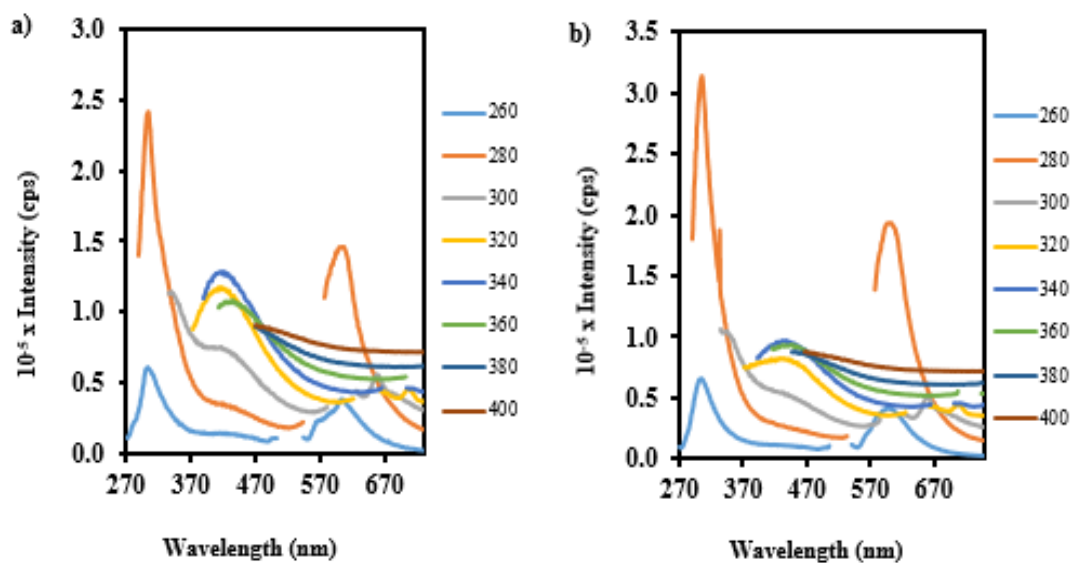


Figure 6.11: Fluorescence emission spectra of (a) $90 \mu\text{M}$ and (b) 1 mM Ag NCs in the microemulsion.

Meanwhile, figure 6.11 (a&b) are emission spectra for the $90 \mu\text{M}$ and 1 mM Ag NCs in chapter three synthesized by the emulsion reaction, these did not contain any of the three ssDNAs. The spectra show three emission bands at 305, 423/447, and 610 nm. The emission at 305 nm represents the smallest Ag NCs which appear to be more in the solutions. As these clusters grow in size, a new band appeared at 423/447 nm for both the $90 \mu\text{M}$ and 1 mM samples respectively, followed by a third band at 610 nm attributed to larger aggregating Ag NCs.

Compared with the ssDNA-containing samples, these emission bands (figure 6.11) are inherently different, with the exception perhaps of the Ag-DNA1 samples which look closest to these, the peak positions of the ssDNA-containing samples are obviously different from those in figure 6.11. On the basis of the observed differences in both set of spectra (figures 6.8, 6.9, 6.10, and 6.11) therefore, we can infer at this point, that the addition of the ssDNAs to the emulsion samples changed the emission spectra, and thereby assume that Ag_n^0 were bound to the ssDNAs in the microemulsion droplets.

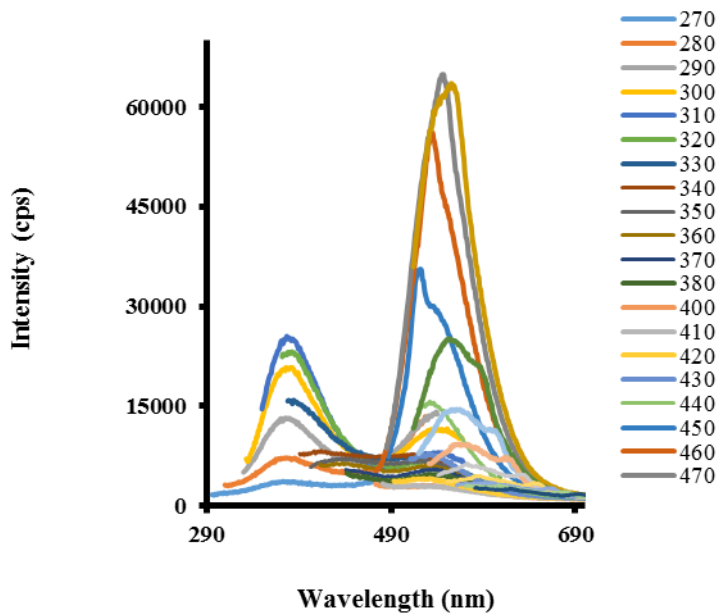


Figure 6.12: Emission spectrum of $90 \mu\text{M}$ Ag-DNA1 at an Ag: base ratio of 1:4. Excitation wavelengths are shown in the figure legend.

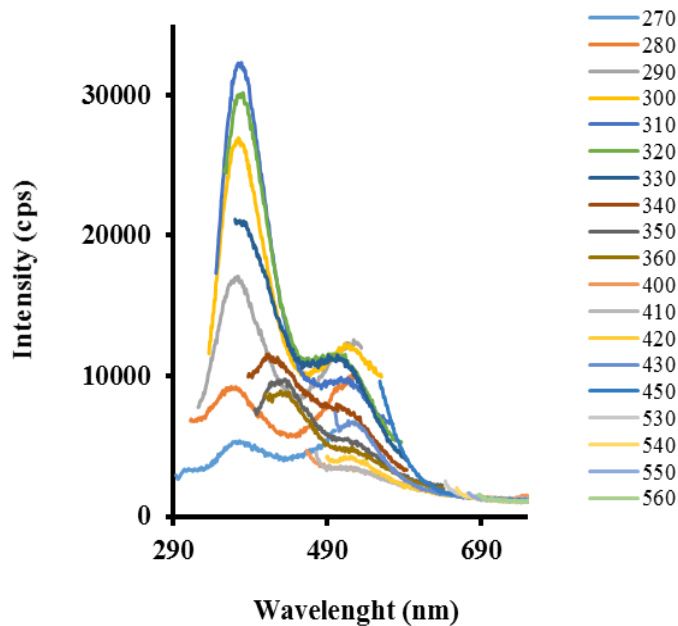


Figure 6.13: Emission spectra of $90 \mu\text{M}$ Ag-DNA2 at an Ag: base ratio of 1:5. Excitation wavelengths are shown in the figure legend.

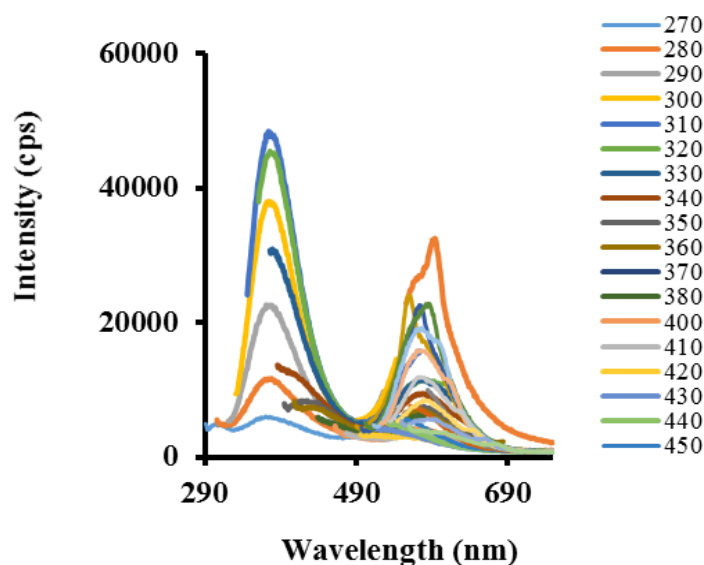


Figure 6.14: Emission spectra of $90 \mu\text{M}$ Ag-DNA3 at an Ag: base ratio of 1:6. Excitation wavelengths are shown in the figure legend.

Figure 6.12, 6.13, and 6.14 are emission spectra for the $90 \mu\text{M}$ Ag-DNA1, 2, & 3 in aqueous solution without the emulsion; they are the control samples obtained under the same reaction conditions as the microemulsion samples above. These samples were prepared by reacting aqueous solutions of $90 \mu\text{M}$ of Ag^+ ions with $15 \mu\text{M}$ portions of either of the ssDNA1, 2, or 3 to maintain the molar ratio of 1:6 ssDNA molecule: 6 Ag^+ ions. These were shaken and then similarly incubated for 30 minutes in the dark and were finally reduced with equimolar solutions of aqueous $90 \mu\text{M}$ NaBH_4 .

The spectra of these samples show two bands of emission at 380 nm which is consistent for all the ssDNAs, and a second emission band at 560, 510, and 590 for the Ag-DNA1, 2, & 3 respectively. The second emission band at 560 nm is very intense for Ag-DNA1 relative to the Ag-DNA2, and 3 samples. However, for Ag-DNA2, and 3, the band at 380 nm was more intense than the >500 nm, meaning that the 380 nm band was more preponderant in both sample solutions, while the Ag NCs concentration was low. The emission band above 500 nm emission is generally ascribed to Ag_n -DNA clusters as supported by the reports of Sharma *et al.*,⁵ and Neidig *et al.*,²⁹ in similar studies. The intensity of the 560 nm band for the Ag-DNA1 sample was highest compared with the other two samples, implying that the Ag-DNA1 sample contained the most proportion of Ag_n NCs.

Put together, the emission properties of the three Ag-DNAs samples synthesized in microemulsion and aqueous reactions show wavelength characteristics of Ag-ssDNA NCs

comprising 2 to 8 atoms of Ag,^{34,35,36} and show red fluorescence in the ~ 500 – 700 nm region of the visible light spectrum. According to the equation ($N = (E_F/E_g)^3$) correlating fluorescence emission peak maximum with cluster size proposed by Buceta *et al.*,³⁷ where E_F and E_g are the Fermi level (5.4 eV for bulk Ag) and the HOMO–LUMO energy bandgap, all three emulsion-synthesized Ag NCs DNA-bound emissions in the 316 - 395 nm region were resolved to correspond to 2 or 3 atoms of Ag.

Meanwhile, like previous researchers who had worked with these same ssDNAs, we have so far observed some notable “anomalies” in the fluorescence properties of the Ag-DNA1 sample which appears to be different from the other two: Ag-DNA2 and 3 with respect their base lengths. Optical properties of the Ag-DNA2 and 3 samples seem to tally in a progressing manner comparatively with each other according to their base lengths than did the Ag-DNA1 sample. Sharma *et al.*,⁵ and Neidig *et al.*,²⁹ observed notable dissimilarities in the optical properties of Ag NCs-templated with DNA1 and those of DNA2 and 3 as well. These they attributed to the DNA1 having formed a much larger number (~30) of Ag atoms per molecule,^{1,34} and also that the differences in the sequences also affected the binding sites of the Ag NCs on the DNA1,²⁹ hence optical properties of the resulting Ag-DNA complex.

The band at 380 nm in figure 6.12, 6.13, and 6.14, are assigned to emissions due to the individual ssDNAs; that is DNA1, 2, and 3 respectively. This band is consistent in all of these samples and has similar characteristics with those of the separate ssDNAs earlier highlighted in figure 6.5, 6.6, and 6.7. Their excitation energies are very much the same and the excitation energy range similar. In addition, apart from having the same excitation energy maximum of 310/315 nm, their band width of 150 nm is also congruent, spanning between 290 – 490 nm.

To further confirm that the 380 nm emission was related to the individual ssDNAs, another set of experiments were done with a higher Ag: ssDNA-base ratio of 1:2 using a higher amount of 180, 217, and 255 μM Ag^+ ions per samples while keeping the concentrations of the ssDNAs constant at 15 μM , before reducing the Ag^+ -ssDNA complexes with equimolar aqueous solutions of NaBH_4 . These would translate to a general ratio of 1:2 (Ag: DNA bases) for all three oligonucleotides. The spectra obtained are presented in figure 6.15, 6.16, and 6.17 for the three samples. While we observed only the 380 nm emission band in all three Ag^0 -ssDNA1, 2, and 3 samples, the bands above 500 nm totally disappeared.

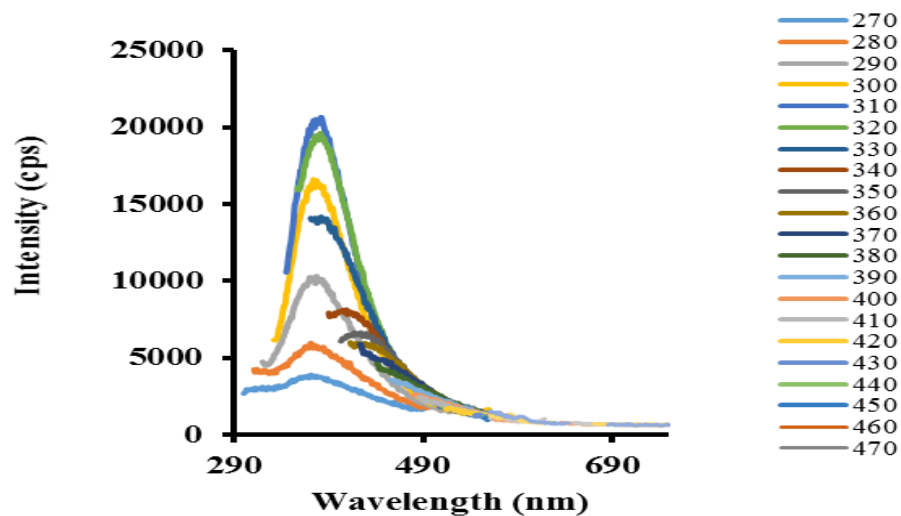


Figure 6.15: Emission spectra of $180 \mu\text{M}$ Ag-DNA1 at an Ag: base ratio of 1:2. Excitation wavelengths are shown in the figure legend.

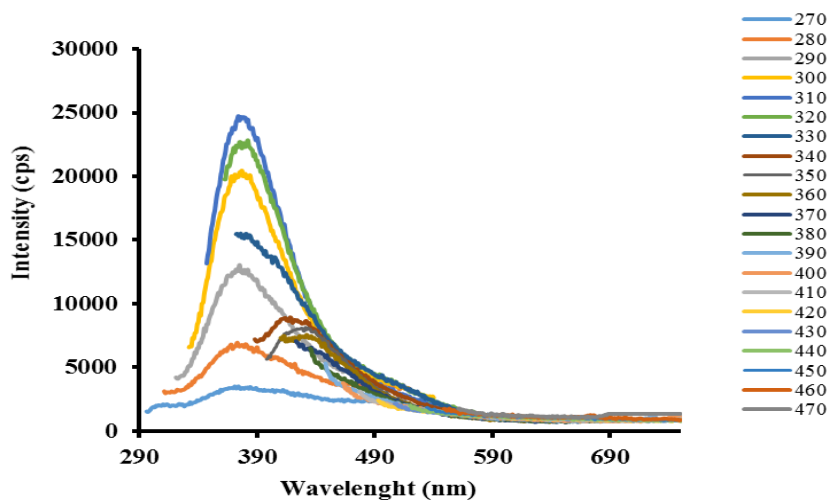


Figure 6.16: Emission spectra of $217 \mu\text{M}$ Ag-DNA2 at an Ag: base ratio of 1:2. Excitation wavelengths are shown in the figure legend.

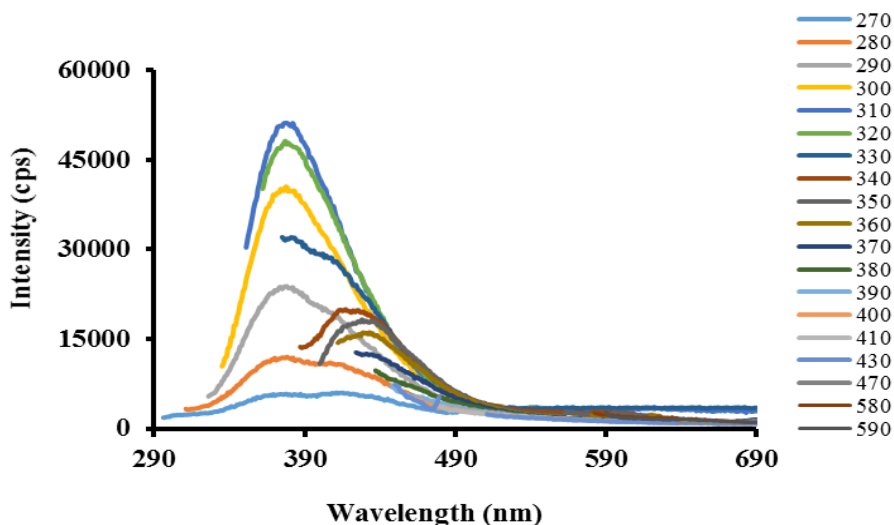


Figure 6.17: Emission spectra of $255 \mu\text{M}$ Ag-DNA3 at an Ag: base ratio of 1:2. Excitation wavelengths are shown in the figure legend.

These results imply that Ag-ssDNA clusters were not present in the 1:2 samples thus, indicating that there were too many Ag^+ ions in the solutions which resulted in the formation of nonfluorescent Ag NPs instead. More importantly however, is that the results further support the initial assumption that the 380 nm emission was associated with the individual ssDNAs and not attributed to DNA templated Ag NCs which are generally known to have emissions between $\sim 500 - 700 \text{ nm}$ as earlier stated.⁹

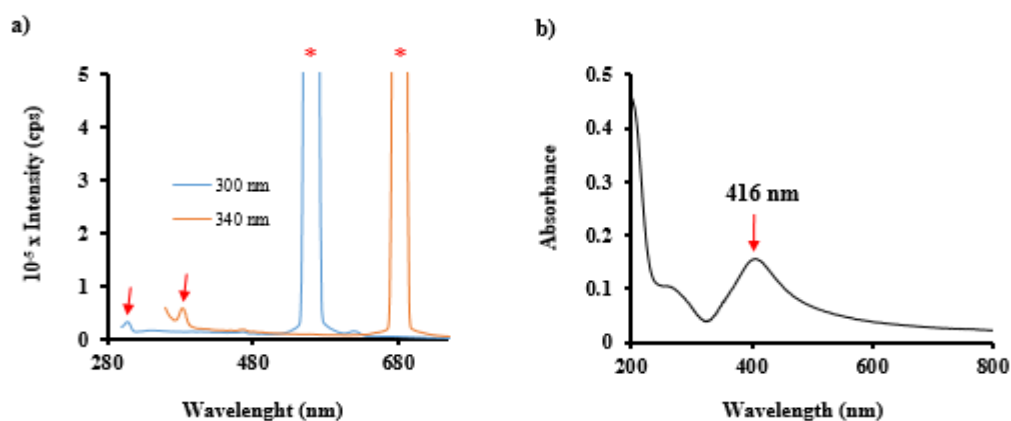


Figure 6.18: Emission spectra of (a) $90 \mu\text{M}$ Ag NPs in aqueous solution in the absence of DNA (b) absorbance spectrum of the same $90 \mu\text{M}$ Ag NP aqueous solution sample. The peaks indicated by red arrows and asterisks (fig. 6.18a) are assigned to Raman peaks of water, and the second-order scattering respectively.

When the ssDNAs were removed from the reactions, leaving the $90 \mu\text{M}$ Ag^+ ions, and then reducing this with equimolar aqueous BH_4^- solution, no fluorescence was observed (figure 6.18a). The absence of the ssDNAs is confirmed by the absence of the 380 nm band in the spectrum. Also, the absence of any emission band similarly infers the absence of fluorescence activity ascribed to Ag NCs more so, as any Ag NCs formed would be expected to rapidly aggregate in the solution in the absence of a stabilizer. Furthermore, the absence of emissions of Ag NCs in the spectrum in figure 6.18a, is confirmed by the appearance of a plasmon resonance peak at 416 nm in the UV-Vis spectrum in figure 6.9b which is the signature of Ag NPs.

6.8 Dynamic light scattering

Evidence are available from previous studies that DNA is encapsulated in water compartments in water-in-oil microemulsions.^{17–20} These have been possible because DNA is known to be very soluble in aqueous solutions.^{17–20} Literature report is unanimous in observing a condensed form of DNA in water droplets.^{17–20} The condensation being driven by a combination of factors which include compartment effect and strong coulombic interactions¹⁹ in the droplet environment.

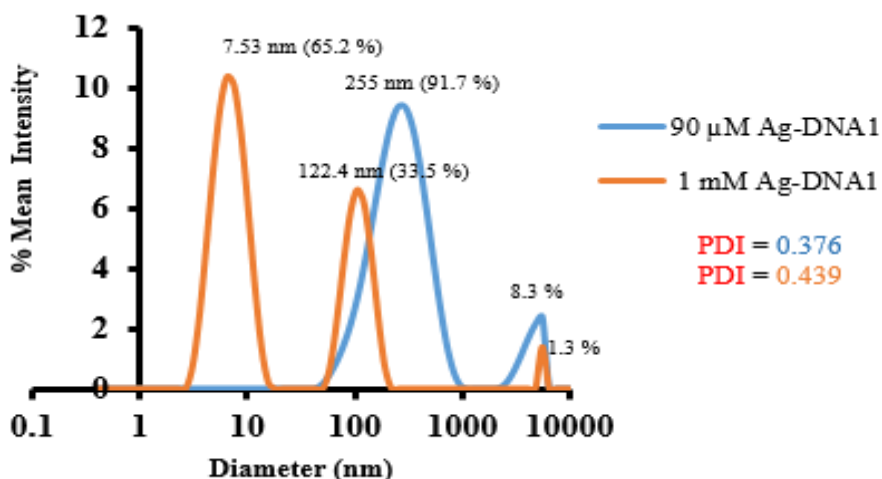


Figure 6.19: DLS spectra of $90 \mu\text{M}$ and 1 mM Ag-DNA1 microemulsion samples.

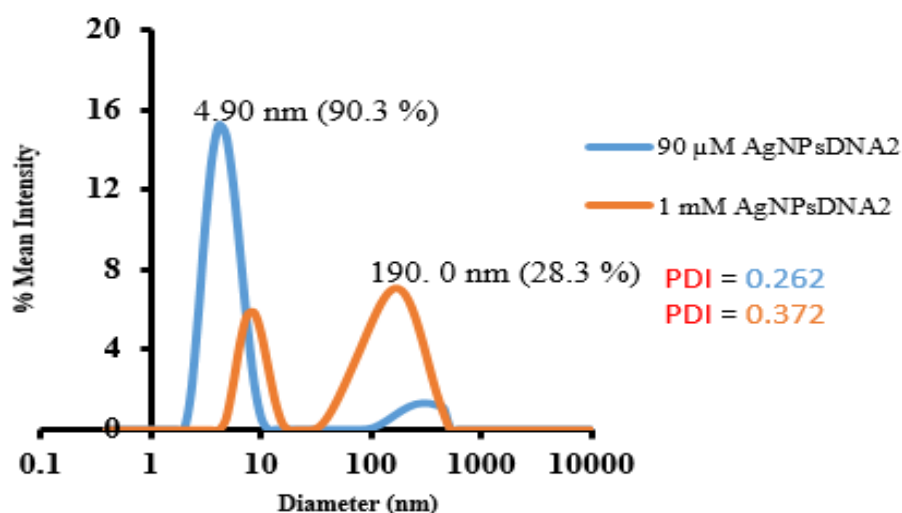


Figure 6.20: DLS spectra of 90 μ M and 1 mM Ag-DNA2 microemulsion samples.

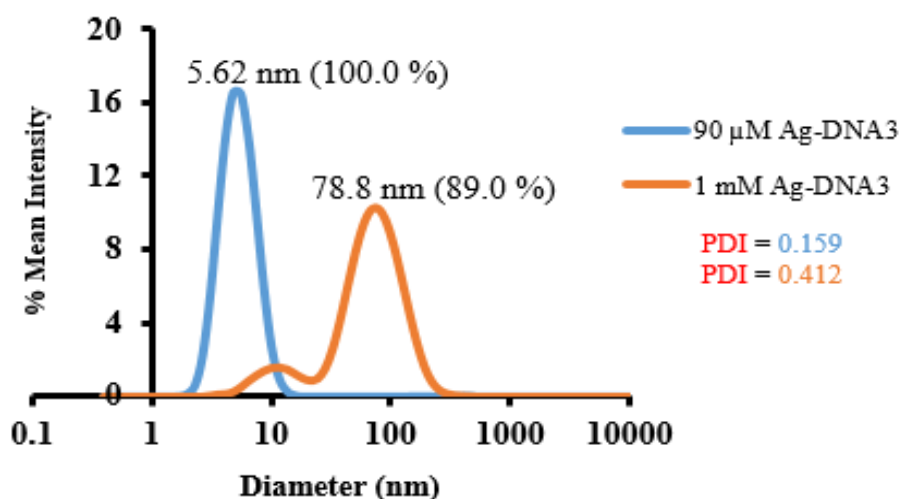


Figure 6.21: DLS spectra of 90 μ M and 1 mM Ag-DNA3 solutions in the microemulsion.

All samples were analysed by dynamic light scattering (DLS) method and the results presented in figures 6.19, 6.20, and 6.21 representing each pair of 90 μ M and 1 mM Ag-ssDNA1, 2, and 3 samples. Generally, the three DNA-templated silver nanocluster samples show small (particles) sizes of \sim 5.00/ \sim 10 nm and \sim 150 nm. However, a much larger “particle” size of \sim 1000 nm scale can be observed especially if DLS measurement was obtained immediately after synthesis as was the case for the samples in figure 6.19. These have been described as temporarily coalesced droplets which have been reported to disappear much later (usually after 24 hours) post-synthesis, thereby, leaving the predominant 5 and 100 nm sizes seen in figures 6.20 and 6.21.³⁸ The 1 mM samples essentially formed large droplets of above 100 nm with only a very small

proportion of the less than 10 nm reverse micelles. The observed size distributions are quite similar with those reported by Sarkar and Pal,¹⁷ Swami *et al.*,¹⁸ Budker *et al.*,¹⁹ and Pietrini and Luisi.²⁰ It has been documented that for DNA-containing microemulsion droplets, two size populations at the 5 and >100 nm sizes were obtained several hours post-synthesis.^{17,19,20} A third “particle” size at ~1000 nm is not unusual (as was observed in figure 6.19 for 90 μ M and 1 mM Ag-DNA1 samples).^{17,19,20}

However, previous studies on DNA encapsulation in water droplets of microemulsion with AOT as a surfactant unanimously reported that DNA is usually contained in the second droplet size of >100 nm.^{17,19,20} This was confirmed by observing subsequent increases in droplet diameter with corresponding increases in the concentrations of solubilized DNA,¹⁷⁻²⁰ reaching a maximum size at 50 - 60 nm after which there was no further concentration-size increase effect.¹⁹ The conclusion was that the smaller 5/10 nm reverse micelles were “empty” and do not contain solubilized DNA^{17 - 20} even though it is rather difficult to distinguish reverse micelles with DNA from those without DNA in these (5/10 nm) sizes.^{17 - 20} DNA is reported to be easily encased in water droplets sizes much smaller than its radius of gyration (~200 nm) for calf thymus, lambda, and 5865-kb plasmid DNAs.^{18,19}

Data from this study show basically two droplet populations, with the exception of the Ag-DNA1 samples whose DLS data were obtained less than 24 hours after synthesis. This apparently explains the appearance of the third peak at 1000 nm in line with observations mentioned previously in similar studies.^{17,19,20} There were no changes in droplets sizes as a function of DNA base lengths judging by the DLS measurements. According to reports by previous researchers^{17 - 20} therefore, we may infer that DNA in the microemulsion samples would be expected to reside in the 100 nm droplets and not the ~5 nm ‘droplet’. Although, the 90 μ M Ag-DNA samples had a higher percentage of droplets in this 5 nm size category (65 - 100 %) and the reverse the case for the 1 mM Ag-DNA samples. A droplet diameter of ~50 nm as supported by Rayleigh curve fitting of the emulsion data have already been reported in chapter three. This would suggest that the emulsion reactions for the DNA templated Ag NCs occurred essentially in the larger ~100 nm droplets.

6.9 Transmission electron microscopy

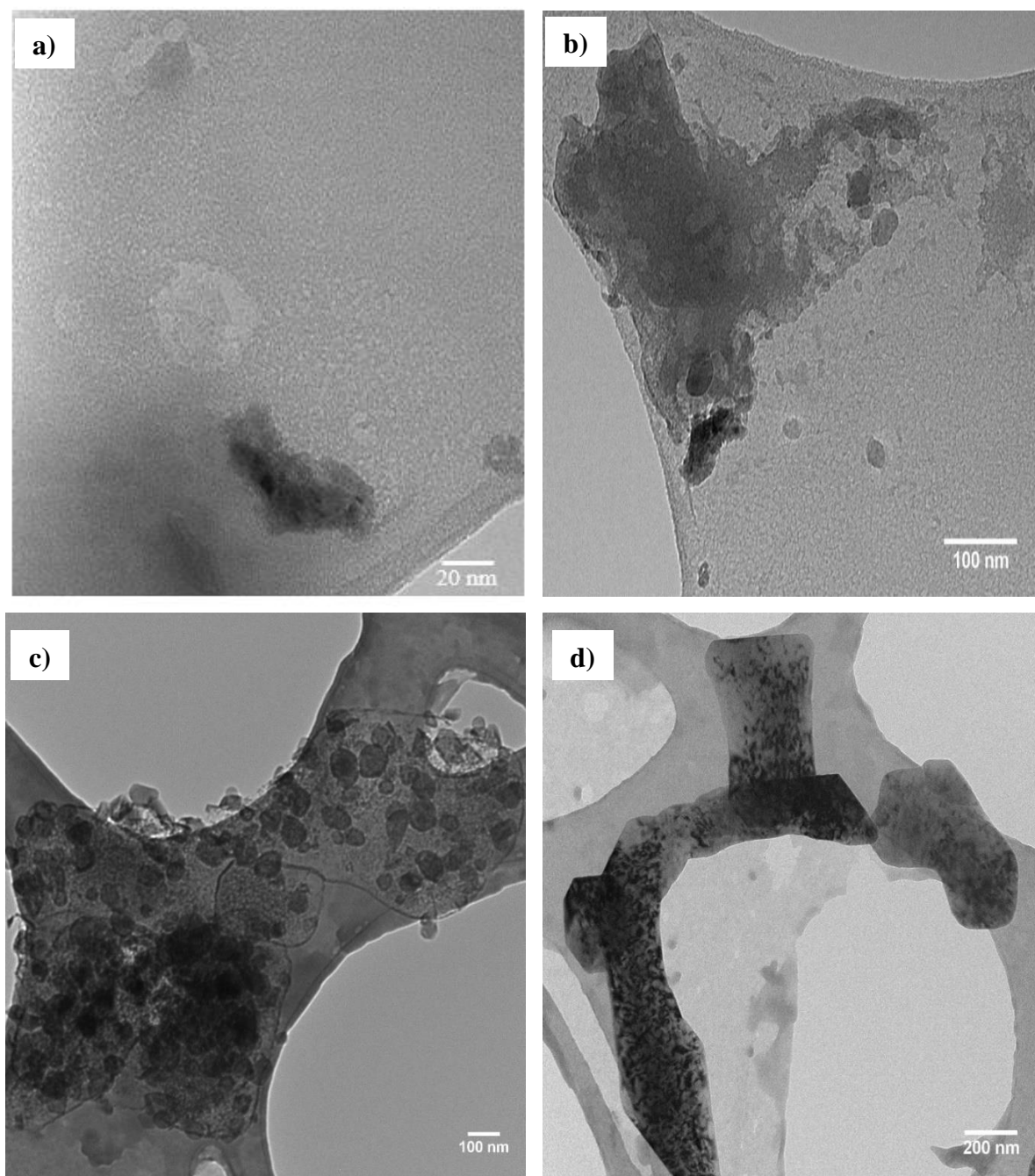


Figure 6.22: Transmission electron microscopy images of (a&b): $90 \mu\text{M}$ Ag-DNA1 (c&d) 1 mM Ag-DNA1.

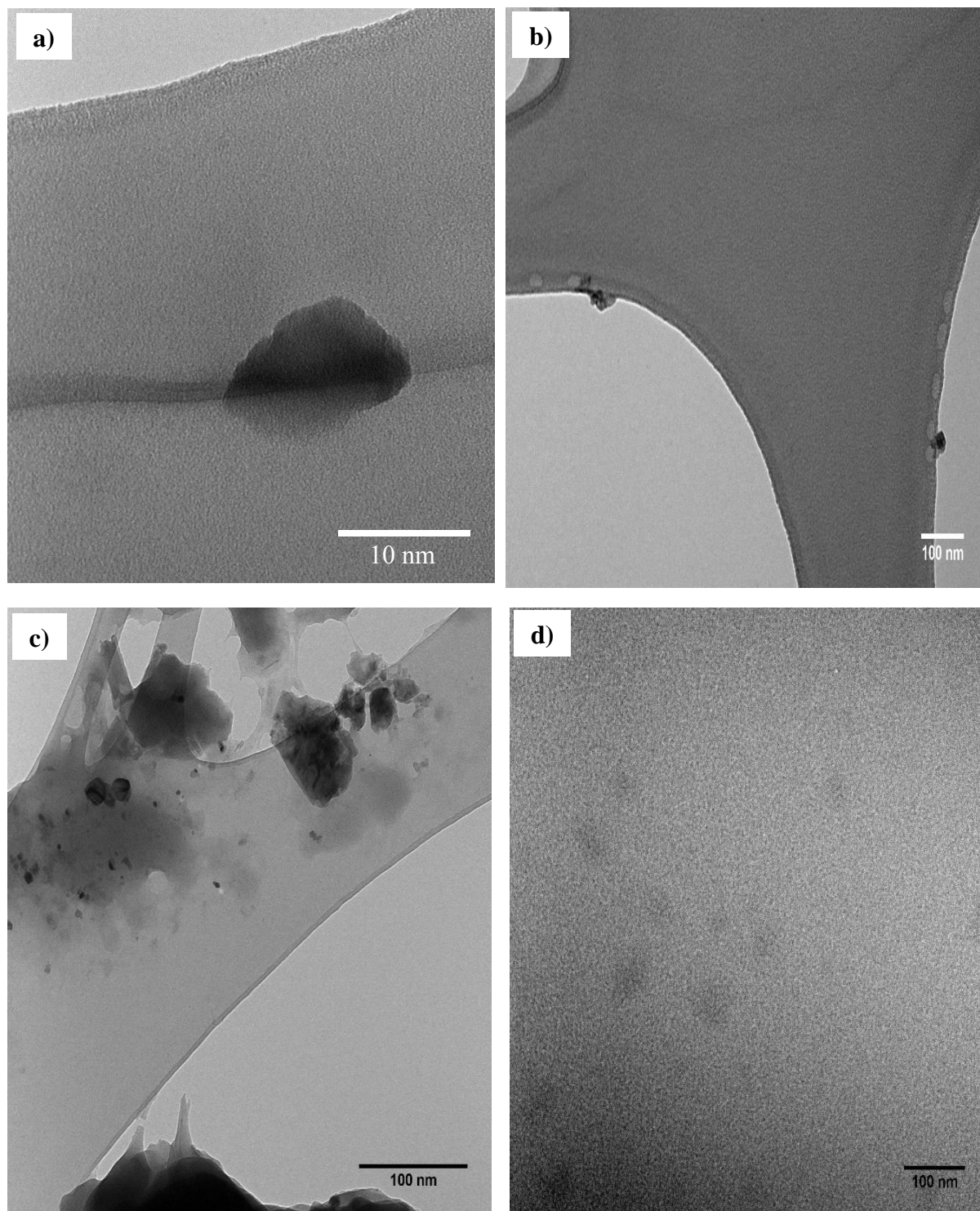


Figure 6.23: Transmission electron microscopy images of (a&b): $90 \mu\text{M}$ Ag-DNA2 (c&d) 1 mM Ag-DNA2.

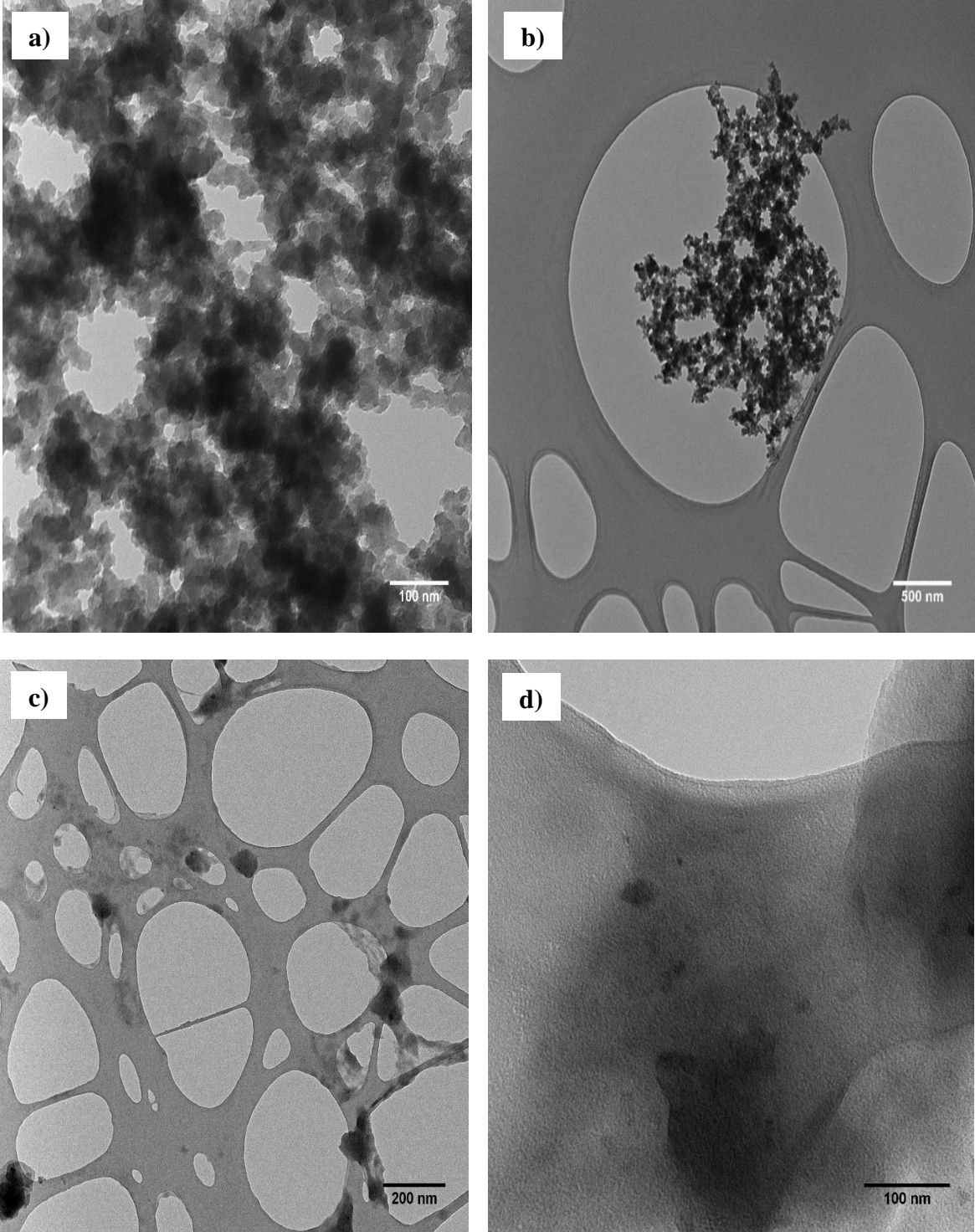


Figure 6.24: Transmission electron microscopy images of (a&b): $90 \mu\text{M}$ Ag-DNA3 (c&d) 1 mM Ag-DNA3.

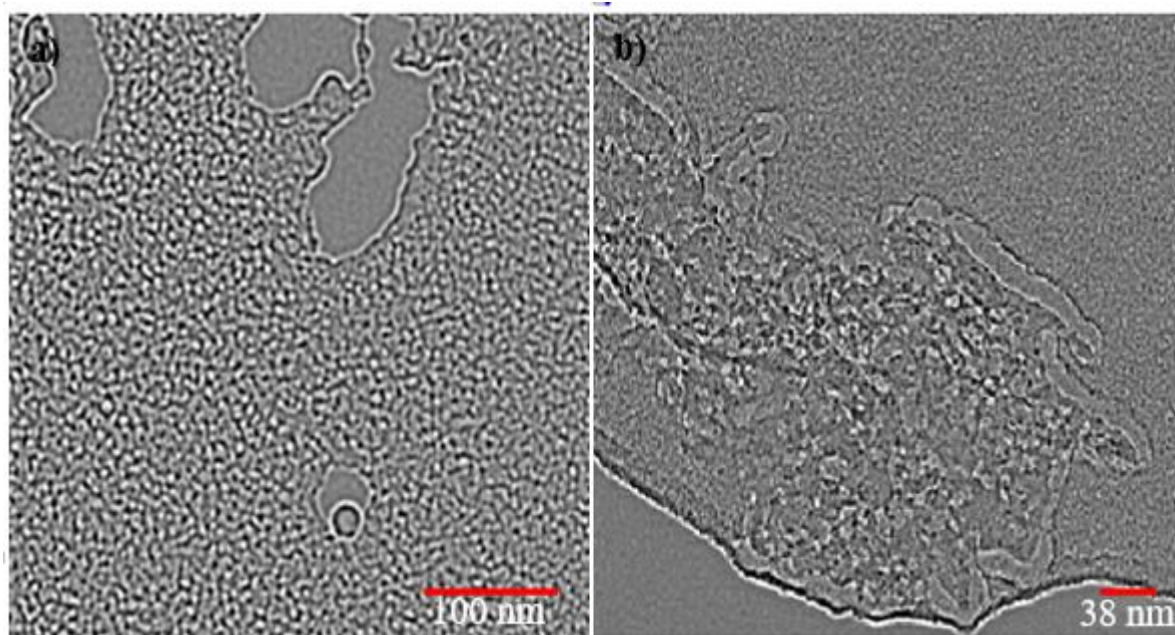


Figure 6.25: Transmission electron microscopy images of (a): $90 \mu\text{M Ag}^0$ (b) 1 mM Ag^0 without the ssDNAs.

Transmission electron microscopy images were obtained from the emulsion samples by taking aliquots of the microemulsion samples and adding an equal volume of deionised water to it in a separating flask to achieve phase separation of the water and oil components, and then allowed stand for 5 minutes. The denser aqueous phase at the base of the flask was carefully extracted into a clean glass vial and portions of it further dissolved in another portion of water to minimise and further dilute the solution against the encumbrant effect of the AOT. Finally, portions of the resulting solution were drop-casted on TEM grids and allowed to dry before measurements were taken.

TEM images obtained for all three ssDNAs with $90 \mu\text{M}$ and 1 mM Ag NPs are presented in figures 6.22, 6.23, and 6.24, reveal a tendency to form packs of “colonies”. This is thought to be connected with the Coulombic repulsion between the polyanionic DNA molecule and the surrounding negative (anionic) polar head groups of the AOT molecules from the droplet monolayer.¹⁶ Thus, forming a condensed structure of DNA in the emulsion as has been similarly documented by previous researchers.^{17–20} The Ag NPs appear bound within the mesh of the condensed DNA and could be seen as small dark masses of Ag enclosed in DNA “colonies”. The electronic interaction between the solubilized DNA molecules and the enveloping AOT polar head group causes DNA to fold up into a lump, and in doing so, similarly encases Ag NPs as was observed in the TEM images presented. This may have the disadvantage of bringing the Ag NCs closer together, thereby causing them to coalesce/aggregate and form large Ag NPs.

These “colonies” of DNA encased Ag particles were not observed in the TEM images in figure 6.25 for Ag NPs of the emulsion samples that did not contain the DNAs. Instead, these were characterized by randomly dispersed (homogeneous) array of Ag NPs, some of which can be seen also lining the edge of the TEM grid. This was not the case with the DNA-containing samples which generally agglomerated into what appears to be packs of Ag NPs-encased DNAs lumps, without the regular homogeneity observed for the control samples in figure 6.25. The entrapment of clusters of Ag⁰ within the condensed mass of DNA in all the DNA-containing samples may promote the tendency of Ag⁰ to aggregate especially in some cases, like in the images of the 90 μ M and 1 mM Ag- DNA3 samples (figure 6.24). Whereas, in the samples of 90 μ M and 1 mM Ag-DNA1 we can observe basically small isolated Ag⁰ NPs within the mesh of DNA.

Apparently, the sizes of the particles in figure 6.25 as indicated by the scale bars, are indeed smaller than the DNA-containing samples in figure 6.22 – 6.24. These evidence put together, demonstrate the presence of DNA in the emulsion samples in figure 6.22 – 6.24. Generally, the sizes of the DNA-containing samples range from ~50 – 200 nm, and appeared to match with similar values obtained from the DLS measurements. The absence of particle sizes of ~ 1000 nm from the TEM measurements is a confirmation that these 1000 nm values obtained in the 90 μ M and 1 mM Ag-DNA1 DLS measurement are temporary coalesced droplets which disappeared (broke off) hours later as earlier explained.

6.10 Electrophoresis

Further analysis of the as-synthesized Ag-ssDNA samples by agarose gel electrophoresis (AGE) was made considering that DNA was highly negatively charged. Therefore, the idea was to observe the migration of Ag-bound DNA species stained with ethidium bromide across the medium according to their sizes in response to the applied electric potential. However, this was not successful. Ethidium bromide (EtBr) usually has an intense fluorescence with DNA. It is believed that the hydrophobic environment between DNA-base pairs where ethidium cation intercalates is responsible for this strong EtBr luminescence in double-stranded DNAs.³⁹ By moving into this hydrophobic centres in double-stranded DNAs, ethidium cation loses its associated water molecules, thereby, becoming highly fluorescent since water is an efficient fluorescent quencher.⁴⁰ Reports indicate that single-stranded DNAs can also show fluorescence with EtBr if there is a fold up of the strand thereby providing a local base-pairing (intrastrand duplexes) for intercalation with EtBr.^{41,42} It is thought that ethidium cation did not intercalate

with the ssDNA molecules in the samples under analysis. Although, the instrument's transilluminator is of a fixed 314 nm excitation wavelength, thereby limiting the possibility of varying the excitation energy. Nonetheless, we should have observed luminescence of the Ag NCs even at this excitation wavelength. The failure to observe luminescence therefore, suggests that the Ag NCs may have aggregated or been oxidised. This would seem possible in the presence of oxidising agents like the Br⁻ ion from the EtBr molecule in the solution as well as dissolved oxygen. The sensitivity of metal particles towards oxidation has been documented by Mulvaney *et al.*⁴³ Furthermore, such unique redox properties and reactivity of small metal particles towards nucleophiles have similarly been expounded by Henglein.⁴⁴

6.11 Electrospray ionization mass spectroscopy

Electrospray ionization mass spectroscopy (ESI-MS) results are shown in figures 6.26 – 6.30 for the 90 μ M and 1 mM Ag-DNA samples. These reveal two regions of m/z distributions between 200 – 600 m/z for the Ag-containing DNA samples (figures 6.26b&c - 6.29b&c), and 700 – 1300 m/z (figures 6.26a - 6.29a) for the DNA samples only. Further analyses of these spectra, indicates that there are two observed chemical groups according to the m/z regions. At the lower m/z range of 465 to 600, this corresponds to silver nanoclusters similar to those obtained in the emulsion experiments in the previous chapter (Chapter three). This was confirmed when matched with the theoretical peaks (see inset figure 6.30). The other signals at the higher m/z range of 700 to 1300 corresponding to free ssDNA molecules are evident by the lack of Ag isotopes (figure 6.26a - 6.29a). This can be seen much more clearly in figures 6.27a especially, and in figure 6.29a. When DNA was added to the Ag⁺ ion-containing 90 μ M and 1 mM microemulsion droplets and then reduced with emulsion droplets containing NaBH₄, we still observed essentially the DNA signals at the same m/z as was initially recorded for the individual DNA samples without Ag. These led to the conclusion that Ag did not form a stable complex with DNA in the microemulsion.

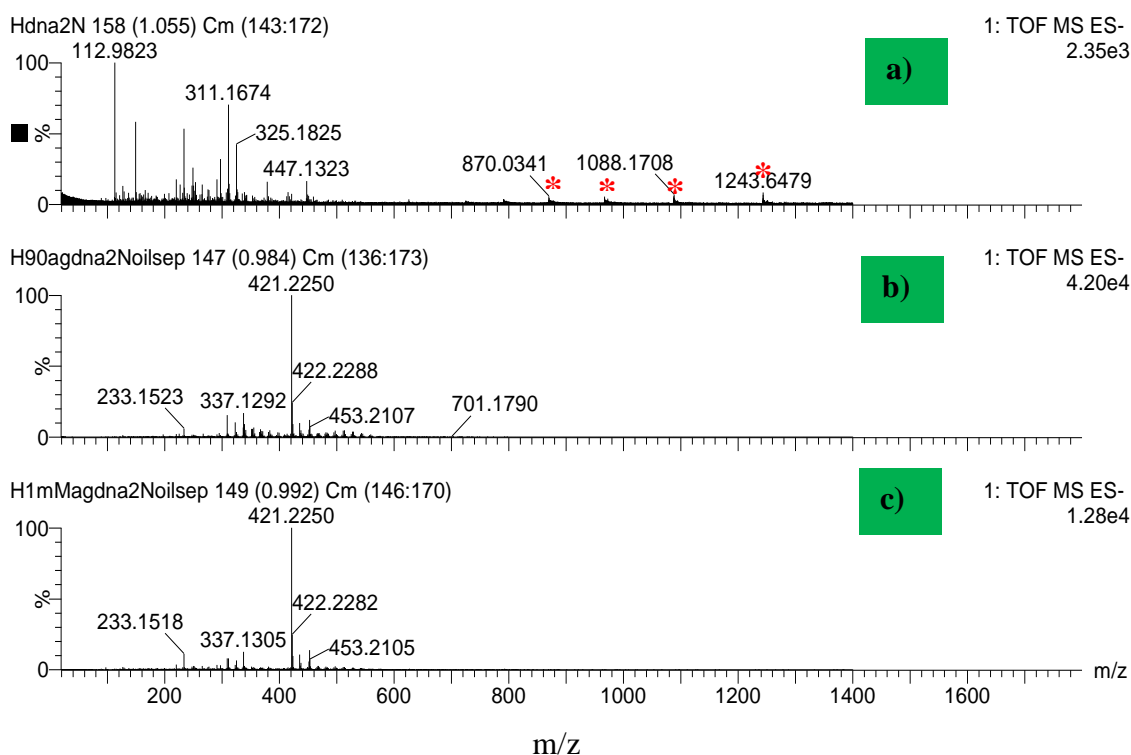


Figure 6.26: Full ESI-MS spectra of (a) Free ssDNA2 (b) $90 \mu\text{M}$ Ag-DNA2 conjugate (c) 1 mM Ag-DNA2 in microemulsion. Red asterisks represent DNA signals.

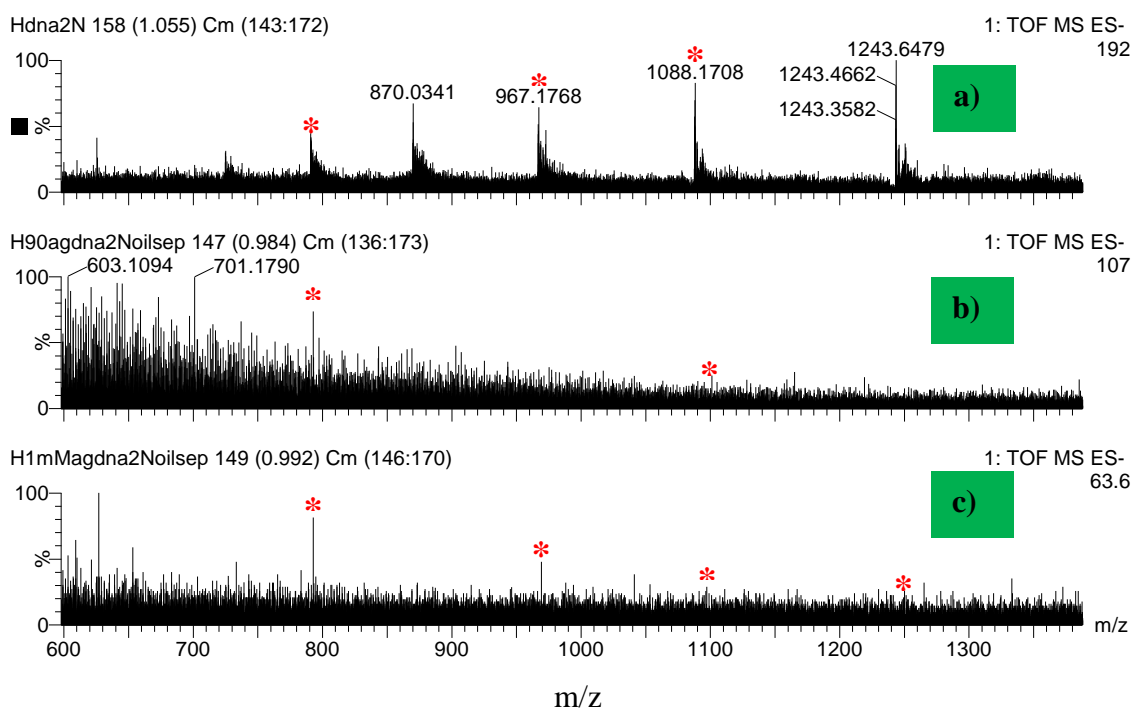


Figure 6.27: Full ESI-MS spectra of (a) Free ssDNA2 (b) $90 \mu\text{M}$ Ag-DNA2 conjugate (c) 1 mM Ag-DNA2 in microemulsion. Red asterisks represent DNA signals.

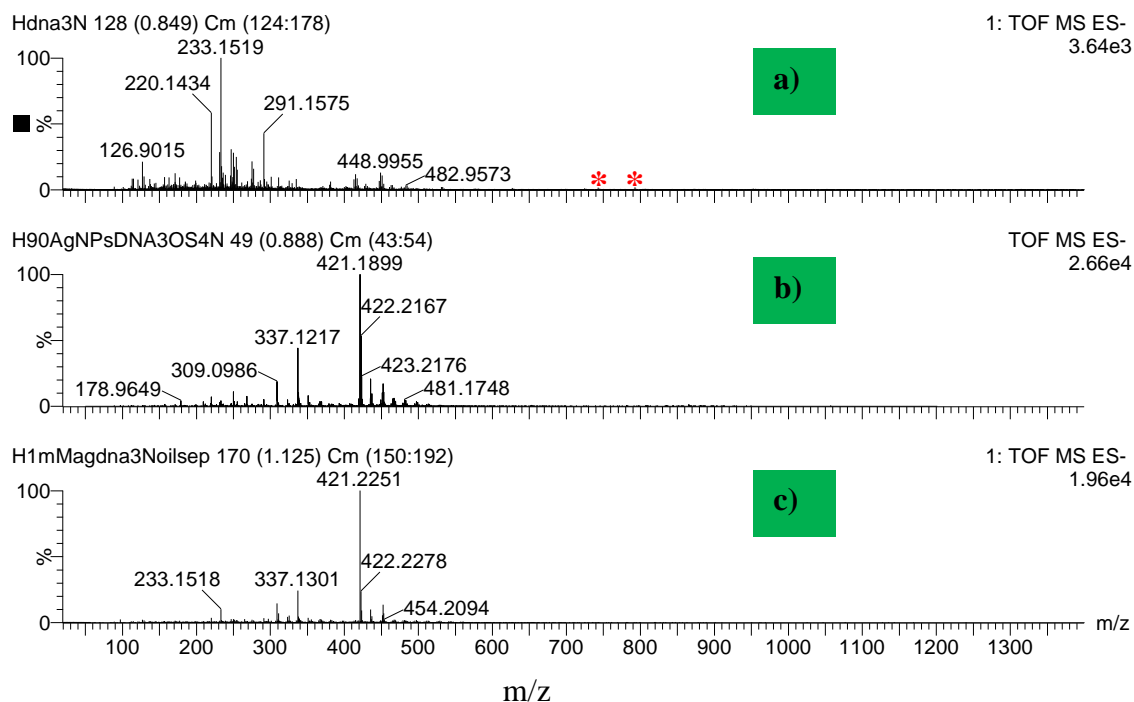


Figure 6.28: Zoomed in ESI-MS spectra at higher m/z (600 – 1300) of (a) Free ssDNA3 (b) $90 \mu\text{M}$ Ag-DNA3 conjugate (c) 1 mM Ag-DNA3 in the microemulsion. Red asterisks represent DNA signals.

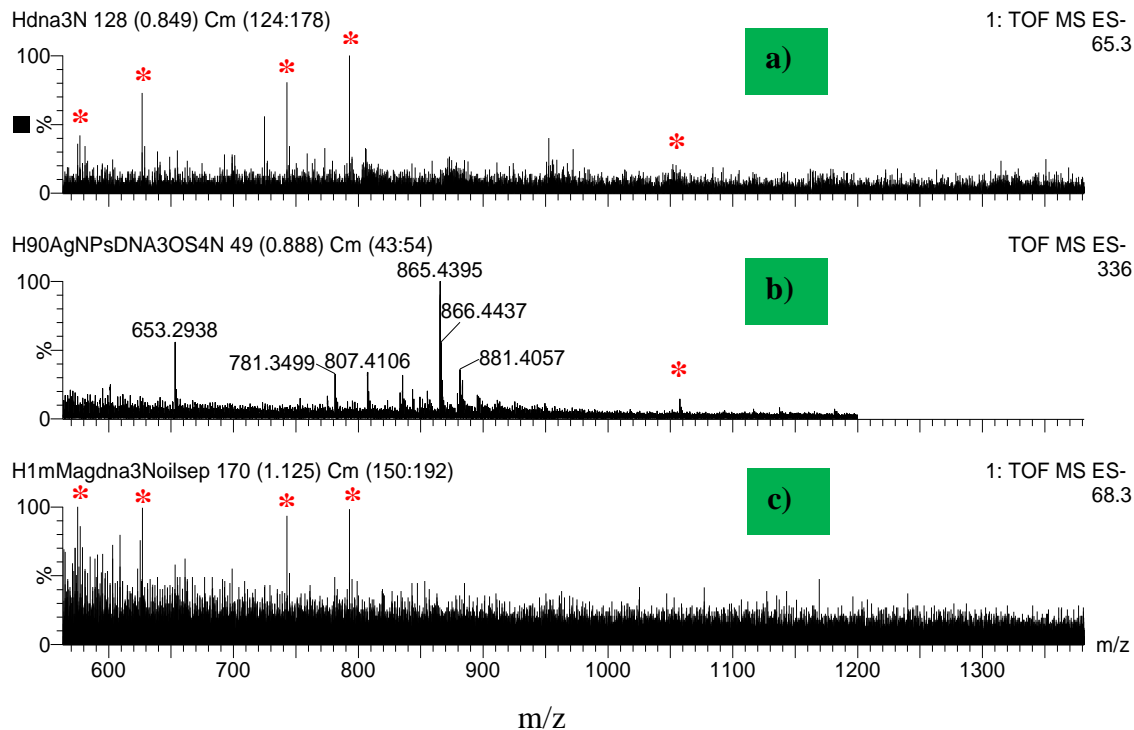


Figure 6.29: Zoomed in ESI-MS spectra at higher m/z (600 – 1300) of (a) Free ssDNA3 (b) $90 \mu\text{M}$ Ag-DNA3 conjugate (c) 1 mM Ag-DNA3 in the microemulsion. Red asterisks represent DNA signals.

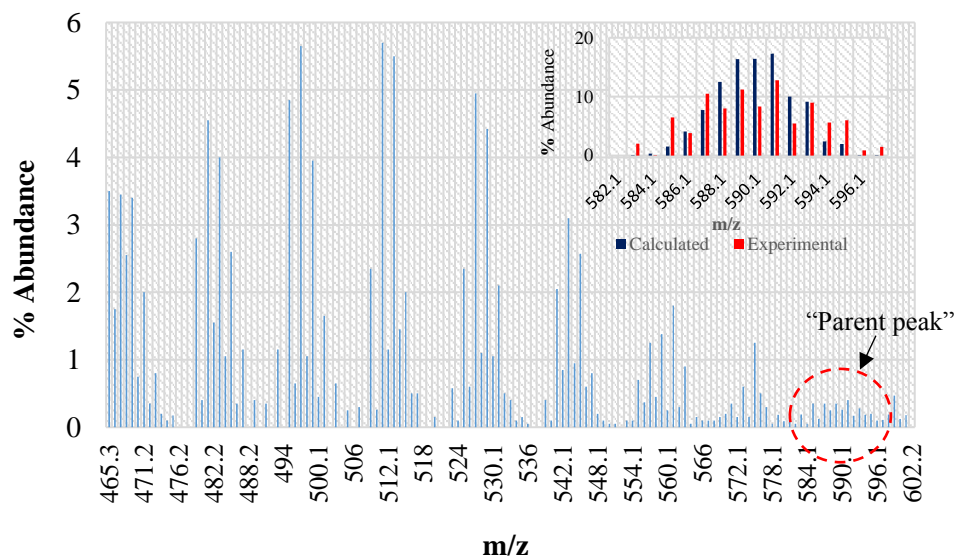


Figure 6.30: Zoomed in ESI-MS spectra for $90 \mu\text{M}$ Ag-DNA2 and 3 showing peaks in the region of 465 – 600 m/z $[\text{Ag}_4\text{B}_3\text{O}_5(\text{BH}_3)_2 \cdot \text{H}_2\text{O}]^-$ with a m/z value of 591.1. Inset is the matching of the experimental and calculated spectra of the peaks centred at 591.1.

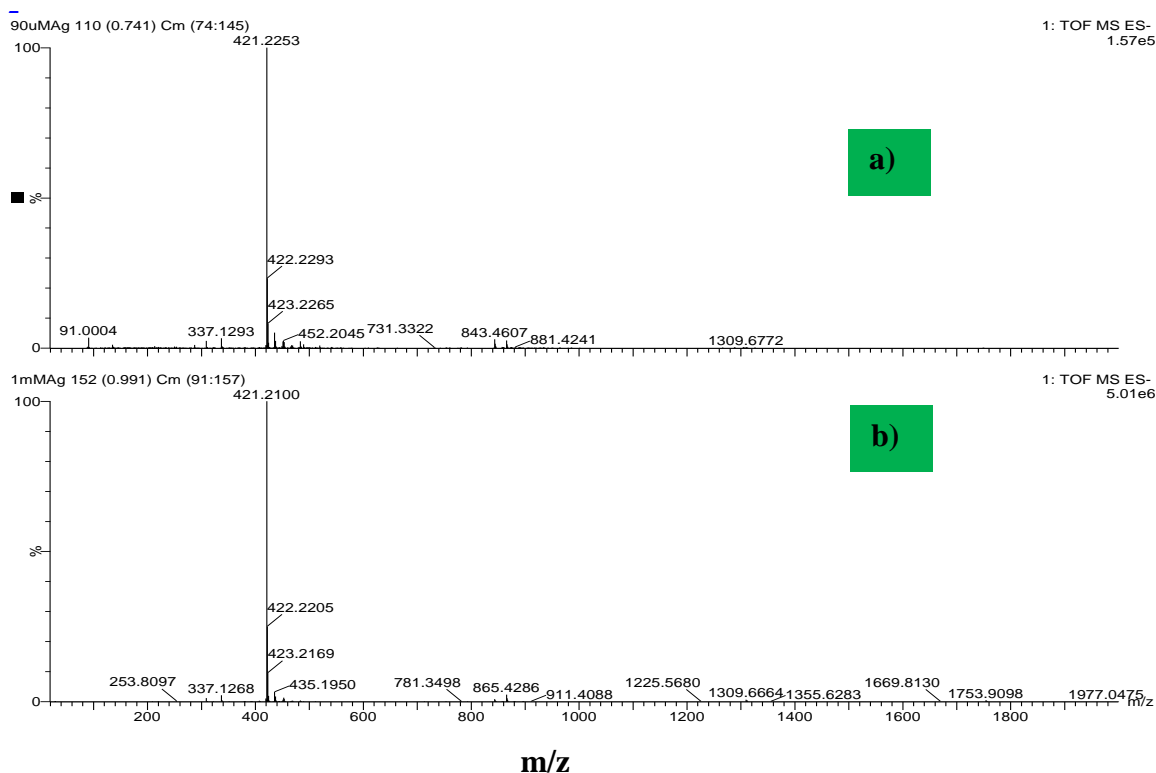


Figure 6.31: ESI-MS spectra of (a) $90 \mu\text{M}$ and (b) 1 mM Ag⁺ ions in microemulsion.

Figure 6.26 – 6.29 containing ESI-MS spectra of all the samples were acquired after phase separating the oil and water phases and subsequently running the predominantly aqueous portion through the Restek cartridge to further eliminate remnants of the organic components of the emulsion, and then diluting further before running them through the ESI-MS instrument to obtain the m/z ratios and isotopic abundance of the samples.

Figure 6.26a is the spectrum of DNA2 only, (b) and (c) are the spectra of $90\ \mu\text{M}$ and $1\ \text{mM}$ Ag-DNA2 respectively, these are the full spectra of the individual samples. What is immediately observed is the difference in the spectrum of DNA2 sample from those of Ag⁰-containing $90\ \mu\text{M}$ and $1\ \text{mM}$ Ag-DNA2 samples. This difference is highlighted by the obvious differences in the peak distributions of the samples. The DNA2 samples show DNA signals at higher m/z ratio region of $\sim 550 - 1300\ m/z$, whereas the Ag⁰-containing samples have Ag isotope signals between $200 - 700\ m/z$ approximately. Beyond this range, no signals were subsequently observed for both the $90\ \mu\text{M}$ and $1\ \text{mM}$ Ag-DNA2 samples. Invariably therefore, two distinct m/z ratio regions were obtained for the DNA2 and the samples with Ag⁰.

Analysis of the peak distribution obtained from the $90\ \mu\text{M}$ and $1\ \text{mM}$ Ag-DNA2 samples, reveal similar isotopic patterns similar with those observed in the spectra of the $90\ \mu\text{M}$ and $1\ \text{mM}$ Ag⁰ without the DNAs (figure 6.30). Yet again, like the spectra of the DNA-free samples in chapter three, both spectra of the $90\ \mu\text{M}$ and $1\ \text{mM}$ Ag-DNA2 are quite similar. These contain signals of Ag isotopic distributions which can be observed between $200 - 700\ m/z$ region in fig. 6.26 and 6.28. Although, one or two peaks assigned to Ag₂ and Ag₃ was recorded at 220 and 368 m/z just like the samples in the previous chapter three, a set of peaks between $465 - 600\ m/z$ are a collection of various species of Ag₄ clusters was similarly observed. These latter group of peaks, analogous with the DNA-free Ag⁰ samples were analysed and found to correspond to $[\text{Ag}_4\text{B}_3\text{O}_5(\text{BH}_3)_2\cdot\text{H}_2\text{O}]^-$ with a m/z value of 591.1 which contains one BH₃ group more than the previously studied DNA-free sample which was not well resolved as these present samples.

Zooming closely into the $600 - 1300\ m/z$ region (figure 6.27) for the DNA2 only, and the $90\ \mu\text{M}$ and $1\ \text{mM}$ Ag-DNA2 samples, we observed the DNA signals at the same positions in the DNA2 (control) samples and the $90\ \mu\text{M}$ and $1\ \text{mM}$ Ag-DNA2 samples. We also observe signals between 650 and $1000\ m/z$ which could not be assigned to Ag species because the peaks did not match with species of Ag⁰ when further investigated.

Analyses of the ESI-MS samples for DNA3 only (without Ag), the $90\ \mu\text{M}$ and $1\ \text{mM}$ Ag-DNA3 samples in figure 6.28 and 6.29 show a similar pattern of results with the DNA2 samples above.

Again, the Ag-containing DNA3 samples are different from the sample of DNA3 (only) as would be expected. Similarly, rather than observe an amalgamation of groups of signals related to a Ag-DNA3 conjugate with successive peaks different from each other by a number of Ag- n atoms, where n are integer values representing the number of Ag-atoms added to the DNA molecule, rather the same split in to two groups of materials: one at the lower m/z ratio of 100 – 600/700 m/z for Ag NCs, and another set of signals at 600 – 1300 m/z assigned to were observed yet again. The region between 100 – 400 m/z in the spectra of the individual DNAs represents signals from the solvent (water); while the most prominent signal at 421 m/z in all the Ag⁰-containing samples has been assigned to the AOT surfactant.

Peaks of Ag₂ and Ag₃ species have also been identified in the spectra of the 90 μM and 1 mM Ag-DNA3 samples as well. These were observed at 220 and 367 m/z ratio in the lower region of the spectra. The region between 465 – 600 m/z again, produced the group of peaks attributed to species of Ag₄ identified by their isotopic peak patterns, and by analysing the differences between each succession of peaks and then resolving the respective m/z values to obtain the component chemical groups associated with the Ag₄⁰ clusters. These were again, resolved to [Ag₄B₃O₅.H₂O(BH₃)₂]⁻ with a m/z value of 591. Note that the molecular formula of these species has been written in order of the m/z values of the successive peak differences between these groups of peaks in the 465 – 600 m/z region.

After this 591 m/z peak, no other peaks of Ag⁰ species were identified in the higher m/z regions. This implied that no other bigger clusters of Ag were available, and further indicate that these Ag₄⁰ clusters are the largest clusters in the distribution, hence we have referred to them as the “parent clusters”. The presence of this parent clusters, indicate their evolution from the small Ag₂ and Ag₃ species earlier identified in the spectra.

In the zoomed in spectra of the 90 μM and 1 mM Ag-DNA3 samples in figure 6.29, we can also observe DNA signals in all three spectra including the Ag⁰-containing 90 μM and 1 mM samples in the higher 600 – 1300 m/z region of the spectra. These portend that Ag-DNA conjugates were not formed or was rather unstable.

Meanwhile, analyses of 90 μM and 1 mM Ag⁺ ions in microemulsion (without reducing the Ag⁺ ions), and running these through the ESI-MS instrument after similar separation process observed for the previous samples was done as a control experiment. The results showed no peaks that could be assigned to Ag in the spectra of both the 90 μM and 1 mM Ag⁺ ions control samples (see figure 6.31a&b) as were observed for the 90 μM and 1 mM Ag-DNA2 & 3 samples

earlier analysed. These confirm that we have made Ag NCs in the reduction reactions as expected.

6.12 Nuclear magnetic resonance (NMR) spectroscopy



Figure 6.32: Fluorescence images of Ag-DNA1 (Black-green), Ag-DNA2 (Yellow), and Ag-DNA3 (Orange) in 99 % D₂O solution (in NMR tubes) under UV light.

To further understand the interaction between ssDNA and Ag, with the three oligonucleotides (DNA1: 22-mer (5'- TGACTAAAAACCCTTAATCCCC-3' (T₅C₈A₈G₁)), DNA2: 29-mer (5'- AGTCACCCCAACCTGCCCTACCACGGACT-3' (T₄C₁₄A₇G₄)), & DNA3: 34-mer (5'- GGCAGGTTGGGGTGACTAAAAACCCTTAATCCCC-3' (T₇C₉A₉G₉)) used for the emulsion experiments with the ratios of Ag⁺: DNA-base maintained as was with the microemulsion experiments above, but this time, the Ag-ssDNA clusters were made in D₂O solution at room temperature. The NMR measurements being sensitive to analyte concentration (the ssDNAs), the proportions of the reactants concentrations were therefore increased to 0.48, 0.34, and 0.18 mM corresponding to 10.6, 9.88, and 6.02 mM DNA-base concentrations so as to obtain good spectra resolution.

Each of the ssDNAs was dissolved in 400 μL D₂O and then 100 μL appropriate portions of the AgNO₃ solution was added to obtain an Ag⁺: ssDNA base ratio of 1:4, 1:5, and 1:6 for ssDNA1, 2 & 3 respectively, and then allowed to stand in the dark for 30 minutes before being reduced

with appropriate equimolar portions of 100 μL D_2O solutions of NaBH_4 . All reactions were done at room temperature, under a nitrogen atmosphere. The resulting Ag-DNA2 and 3 samples (yellow and orange colours respectively) were seen to be brightly luminescent when observed under UV light (figure 6.32).

Figure 6.33 is a ^1H NMR spectra of the three ssDNA oligonucleotides used in this study. All three spectra show signals consistent with the various components of DNA molecule: the nucleobase, and ribose sugar. Special attention is focussed on the four different nitrogen-containing nucleobases and the hydrogen atoms of the purine and pyrimidine aromatic ring^{2,9} appearing between 7.0 and 8.5 ppm⁴⁵⁻⁴⁶ which make up the individual nucleobases.

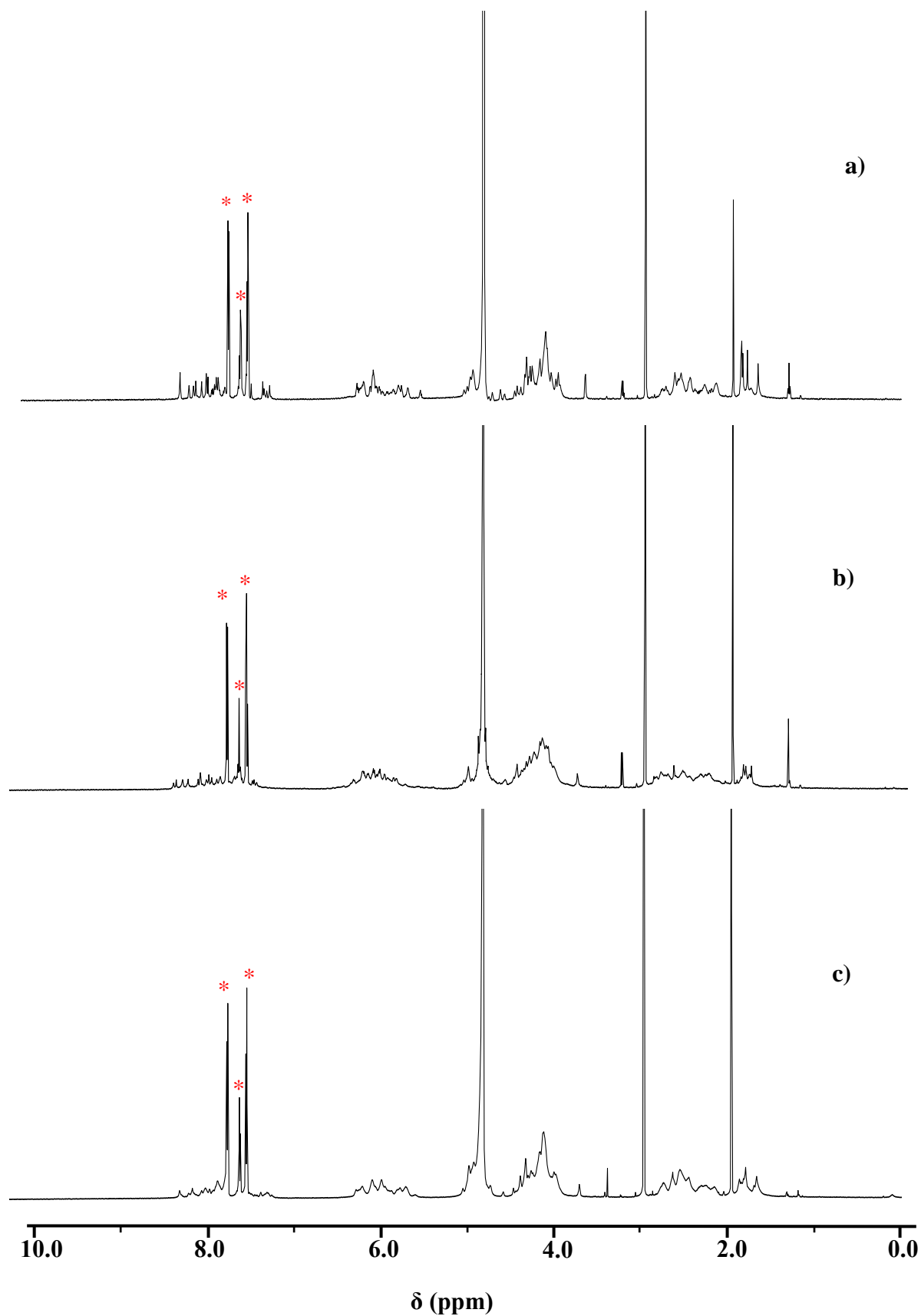


Figure 6.33: ^1H NMR spectra of oligonucleotides a) DNA1 (22-mer) b) DNA2 (29-mer); and c) DNA3 (34-mer) dissolved in 99 % D_2O . All spectra acquired at 298 K in D_2O with tetramethylsilane (TMS) as a reference. Asterisks are signals from the DNA protecting groups used during the DNA synthesis.

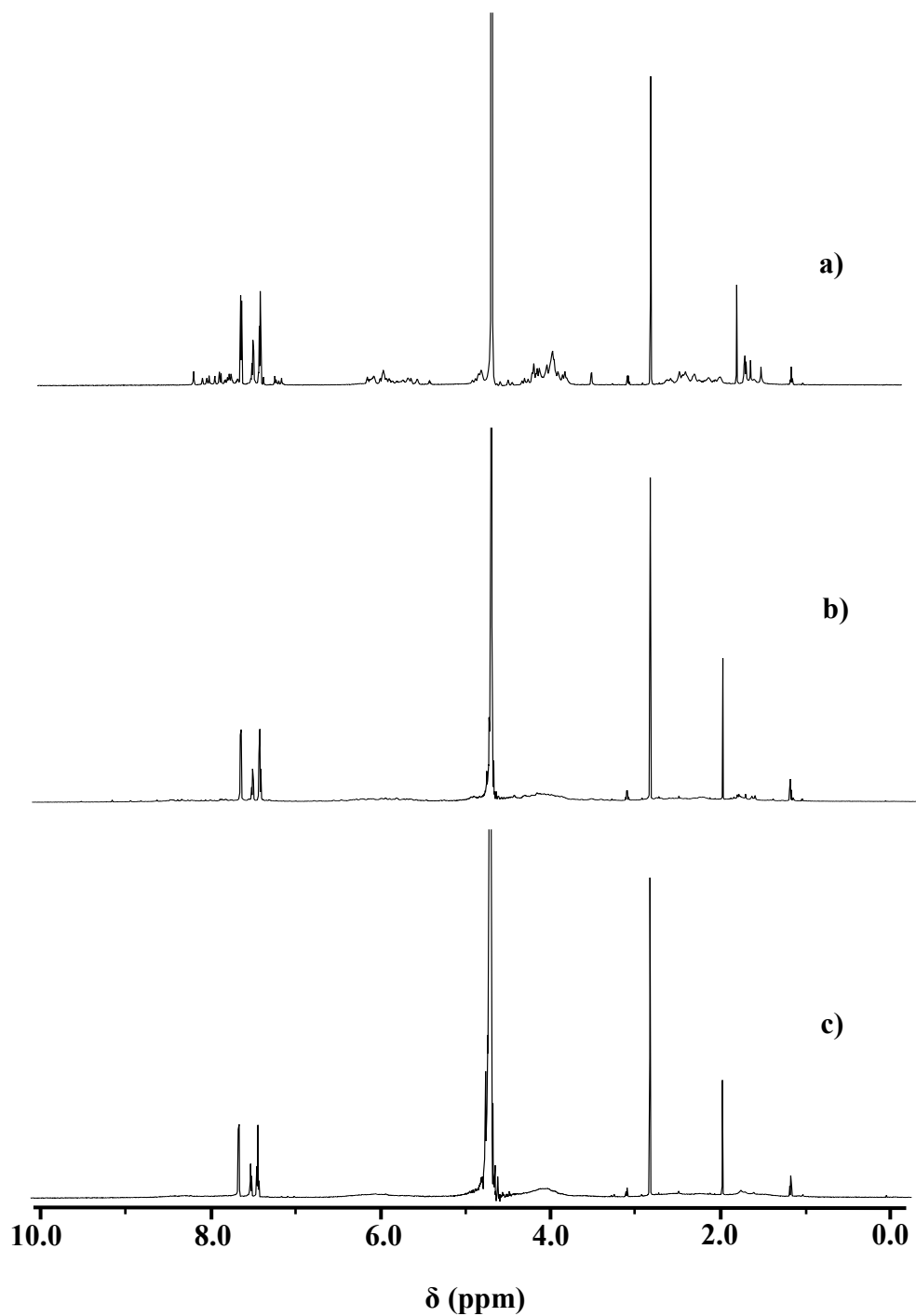
6.12.1 ^1H NMR study of Ag-DNA1

Figure 6.34: ^1H NMR spectra of oligonucleotides (a) DNA1 (22-mer) (b) Ag^+ -DNA1; and (c) Ag-DNA1. All spectra acquired at 298 K in D_2O with tetramethylsilane (TMS) as a reference.

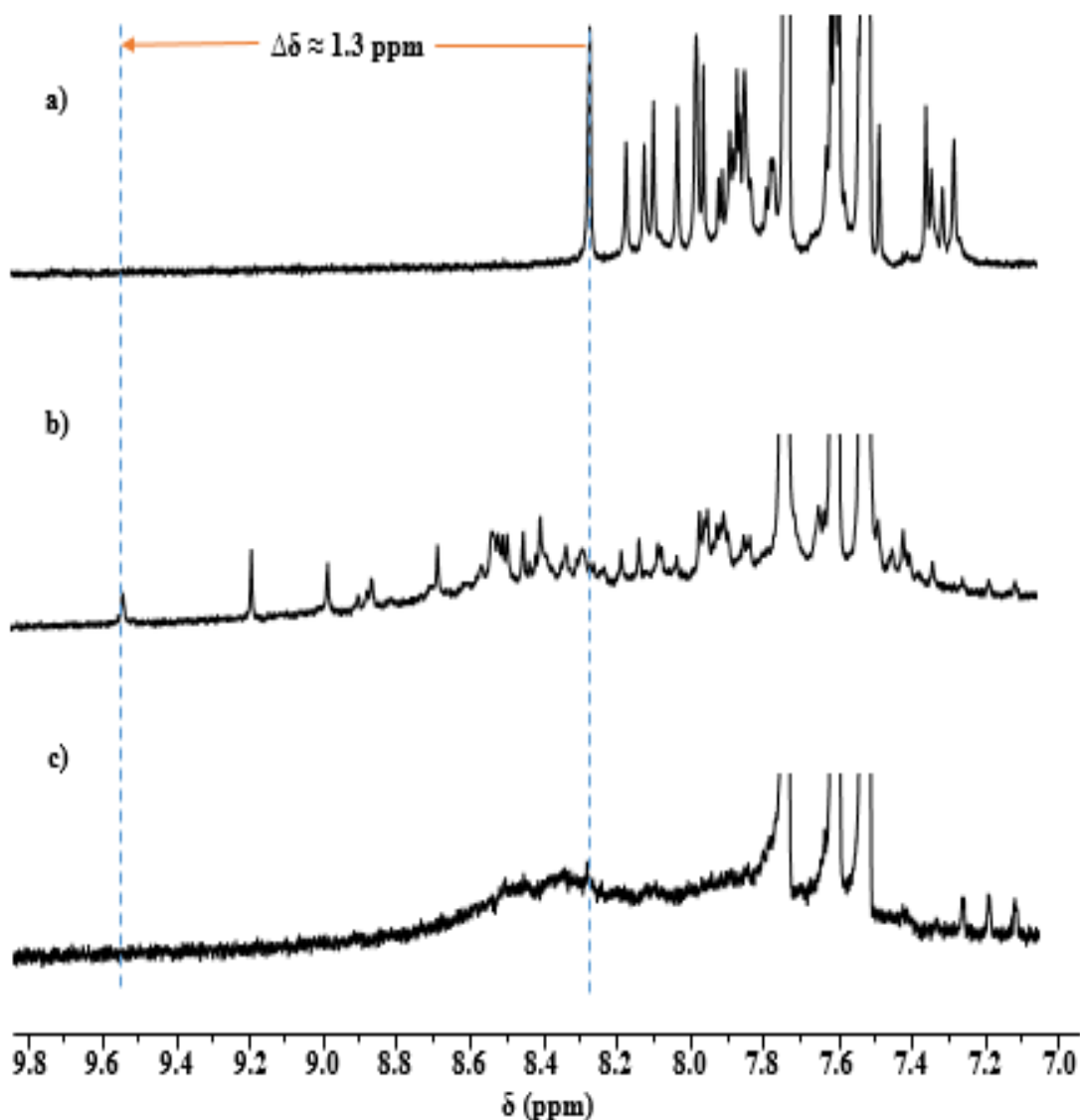


Figure 6.35: ^1H NMR spectra of oligonucleotides (a) DNA1 (22-mer); (b) Ag^+ -DNA1; and (c) Ag^0 -DNA1. All spectra acquired at 298 K in D_2O with tetramethylsilane (TMS) as a reference.

Figure 6.34 is a stacked ^1H NMR spectrum of (a) DNA1, (b) Ag^+ -DNA1 and (c) Ag^0 -DNA1 respectively, this shows the effect of adding Ag^+ ions to the ssDNA1 and then reducing it with NaBH_4 D_2O solution. For the purpose of this study, emphasis is placed on the aromatic resonance signals already assigned between 7.0 – 8.5 ppm, which is considered the binding sites for Ag^+ ions.¹ This region has been further expanded to highlight these signals in figure 6.35 above.

The peaks between 1.5 – 1.9 in figure 6.34 have been assigned to the methyl protons (CH₃) of the thymine nucleobase. Following these are a group of peaks at 2.0 – 3.0 ppm representing the H2' and H2'' of the ribose sugar. A combination of peaks at 3.9 – 4.7 ppm are resonance signals of H5'/H5'' and H4' in that order also belonging to the sugar group of DNA. These are immediately accompanied by the strong signal of the deuterium solvent (HOD) at 4.7 ppm, which is closely coupled with the H3' signal at 4.8 – 5.2 ppm also belonging to protons of the sugar group. The cytosine H5 (CH5) breaks the order for the protons of the ribose sugar, appearing next at 5.5 – 5.9 ppm, accompanied closely by the H1' sugar proton which appeared at 6.0 – 6.7 ppm. Then is the turn of the aromatic proton signals already assigned again to the 7.0 – 8.5 ppm region and collectively represent protons of the four nucleobases (A, C, G, and T) with the exception of the amino and imino protons.^{47,46,48}

A general loss of intensity of the signals of the aromatic protons between 7.65 – 8.25 ppm on the addition of Ag⁺ ions to DNA1 (figure 6.35b), are attributed to bonding occurring at multiple sites of the ssDNA1 molecule. The loss of signal intensity is ordinarily associated with exchange interactions between magnetic nuclei⁵⁰ from the different chemical environment. This results in the broadening and sometimes the flattening out of the resonance signals to baseline in the NMR spectrum. Exchanges occur when nuclei change magnetic environment either as a result of conformational change caused by the rotation of the molecule about a bond, or by a chemical reaction involving the breaking or formation of bond(s).⁵¹⁻⁵²

The signals in the 7.65 – 8.25 ppm region were also observed to be displaced downfield of their initial positions up to 9.47 ppm (figure 6.35b). A chemical shift value of $\Delta\delta \approx 1.3$ ppm was obtained for the AH8 signal from its initial position of 8.20 ppm prior to the addition of Ag⁺ ions, to 9.47 ppm after the addition of Ag⁺ ions to the ssDNA1 molecule (figure 6.35b). The displacement of the resonance signals relative to their initial positions, as well as the broadening of the proton signals are considered here as indications of binding of Ag⁺ ions to the nucleobases. The magnitude of the displacement of the AH8 signals in terms of the $\Delta\delta$ value of 1.3 ppm, was considered as a measure of the deshielding /electron cloud displacement effect on the protons. The decrease in the electron cloud around nuclei can result from the introduction of an electrophile such as Ag⁺ ion in this case, on electron rich sites on the DNA molecule. The addition of the Ag⁺ ions to the ssDNAs is thought to have caused an enhanced mesomeric effect in the aromatic rings, with the electron cloud around the magnetic (proton) nuclei being pulled more towards the now electron-deficient site of the electrophilic attack considered to be the nitrogen (N) sites of the nucleobase. Thereby, leaving the proton nuclei more exposed to the

effect of incident magnetic field, causing it to resonate at a higher frequency and therefore resulting in a shift downfield from its previous δ -position.

Although, binding may have occurred on multiple sites of the oligonucleotide according to the observed loss of intensity and displacement of the **TH6 CH6**, **GH8** and **AH8** resonances of the ssDNA1 molecule, **CH6** signals generally, and the **AH8** at and 8.21 ppm (shifted to ~ 9.60 ppm in figure 6.35b) were the most affected. This is because their signals were significantly diminished in intensity after binding with Ag^+ ion (figure 6.35b), they were together the most significantly shifted downfield of TMS. These observations enable the conclusion that binding took place on the adenine **AN7** site and cytosine **CN3** to a greater extent than the **GN7** and **TN3** positions in general.

However, the intensity of the broadened aromatic signals was not restored after reduction of the Ag^+ -DNA1 complex. Instead, further broadening of the signals which lead to a complete loss of intensity was noticed, an indication of strong conformational changes on the ssDNA1 molecule after the reduction of Ag^+ -DNA1 to Ag-DNA1.

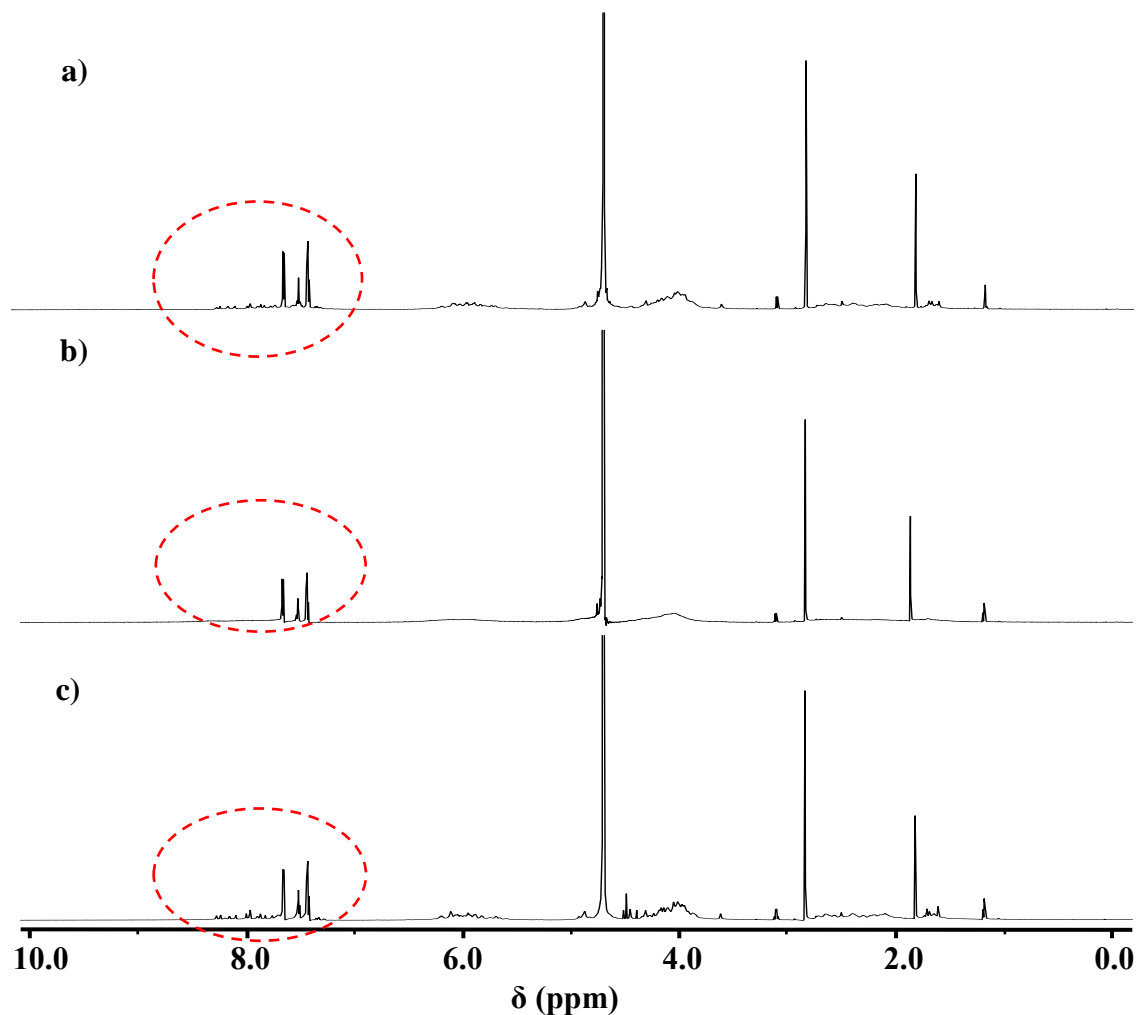
6.12.2 ^1H NMR of Ag: DNA2

Figure 6.36: ^1H NMR spectra of (a) DNA2 (29-mer) oligonucleotide (b) Ag^+ -DNA2 and (c) Ag-DNA2. All spectra acquired at 298 K in D_2O with tetramethylsilane (TMS) as a reference. Encircled peaks represent the aromatic region of the ssDNA molecule and the binding site for Ag^+ ions.

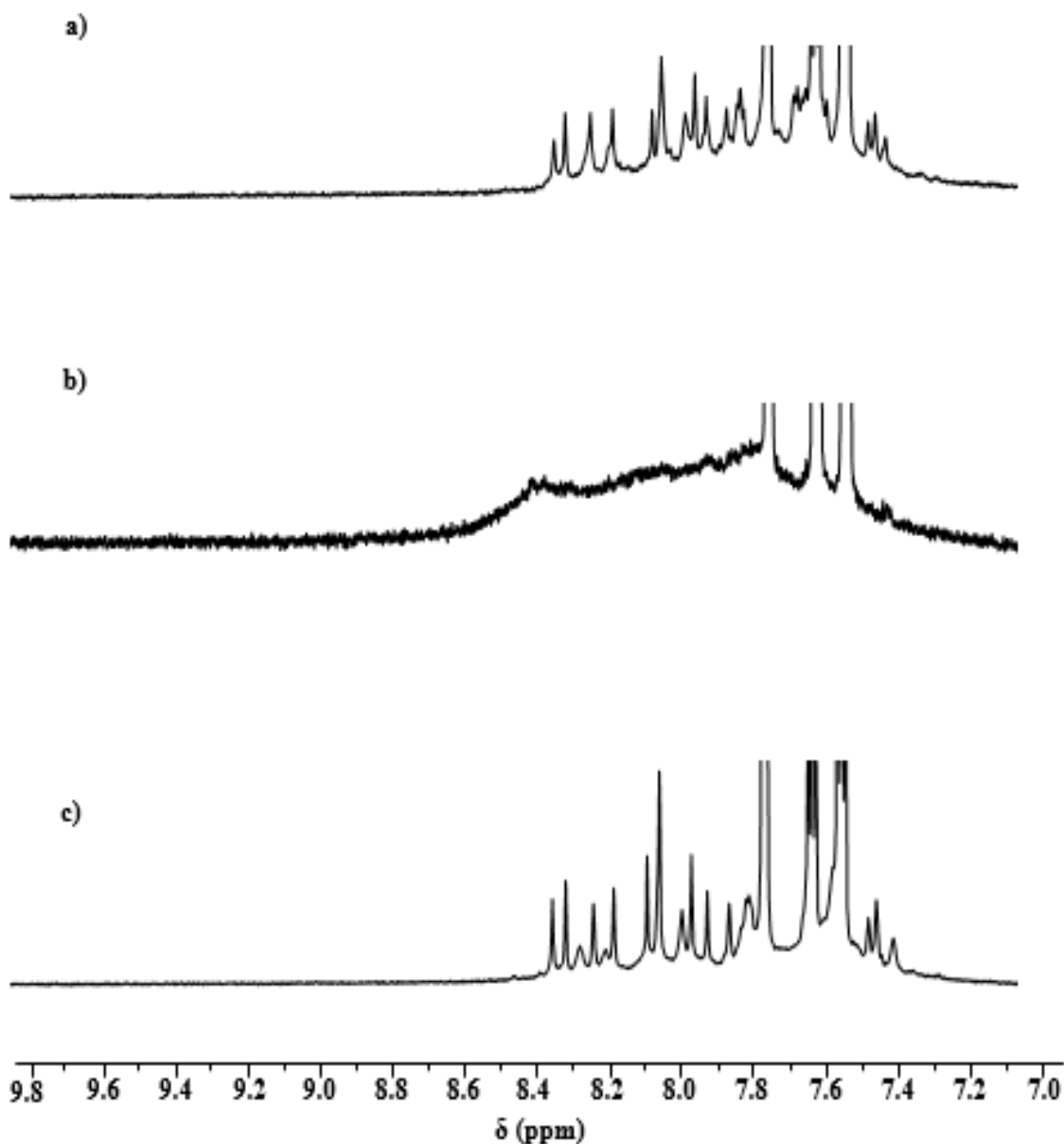


Figure 6.37: ^1H NMR spectra of (a) DNA2 (29-mer) oligonucleotide (b) Ag^+ -DNA2 and (c) Ag-DNA2. All spectra acquired at 298 K in D_2O with tetramethylsilane (TMS) as a reference.

Figure 6.36 shows the differences in the ^1H NMR spectra of (a) DNA2 only, from those of the same ssDNA2 molecule after reacting with Ag^+ ions (Figure 6.36b), and after the reduction of the resulting Ag^+ -DNA2 complex (Figure 6.36c). These again are expanded in Figure 6.37a, b, and c for better resolution and analysis of the aromatic region of the spectra.

Upon the addition of Ag^+ ions to DNA2 in D_2O , again the aromatic signals broadened out to baseline as the signal intensities were lost due to exchange interactions of the nuclei. Apart from

the three prominent bands in the 7.40 – 7.75 ppm, we could not see any other signals in the aromatic region in figure 6.37b.

However, on reducing of the Ag⁺-DNA2 cation, unlike the DNA1 (figure 6.37c), we observed the reappearance of the aromatic signals which became even more resolved and slightly more shifted upfield of TMS, appearing at lower frequencies from their initial positions prior to the addition of Ag⁺ ions to the DNA2 molecule. This was not the case with the DNA1, and was thus considered a significant observation, as it would be seen in the subsequent section that the Ag-DNA1 sample was the only one (of the three ssDNAs) which did not produce fluorescent Ag NCs in the NMR experiments.

Meanwhile, the spectra of the Ag-DNA2 sample after reduction revealed further important information: the region between 8.10 – 8.20 ppm of the ssDNA2 sample (figure 6.37a) initially showed two broad peaks assigned to the coupling of the AH2 and AH8 signals. The AH2 signals at 8.10 and 8.16 ppm became better resolved and sharper upon reduction of the Ag⁺-DNA2 complex and slightly shifted upfield. However, interesting to note is the appearance of two new broad but weak signals at 8.14 and 8.19 ppm, each coming just after their preceding stronger AH2 signals, these weak signals belong to the AH8 resonance initially coupled with AH2 resonances. These two “new” AH8 signals together with the CH6 doublets at 7.70 and 7.58 ppm (which broadened, the latter almost completely) were the most significant changes to the aromatic signals of the Ag-DNA2 compound after reduction. Therefore, we infer that the Ag NCs were possibly bonded to the cytosine N3 and adenine N7 sites of the DNA2 oligonucleotide.

The observed sensitivity of the ribose sugar protons of DNA was ascribed to conformational changes in the DNA molecule following bonding of the nucleobase with metal ions.^{53,54,55,56} The bonding of Ag⁺ ions to the nucleobases should induce some concomitant conformational change on the DNA molecule as demonstrated in figures 6.34b and 6.36b. The aromatic region displayed a more prominent chemical shift changes (7.0 - 9.5 ppm) downfield of the reference TMS.¹ These have been interpreted as indications of binding of Ag⁺ ions to the DNA leading the formation of Ag⁺-DNA complex.^{57,58,59} Petty *et al.*,¹ and Chakraborty *et al.*,⁵⁰ both reported similar binding occurrence between Ag⁺ ions and oligonucleotides in related studies in D₂O.

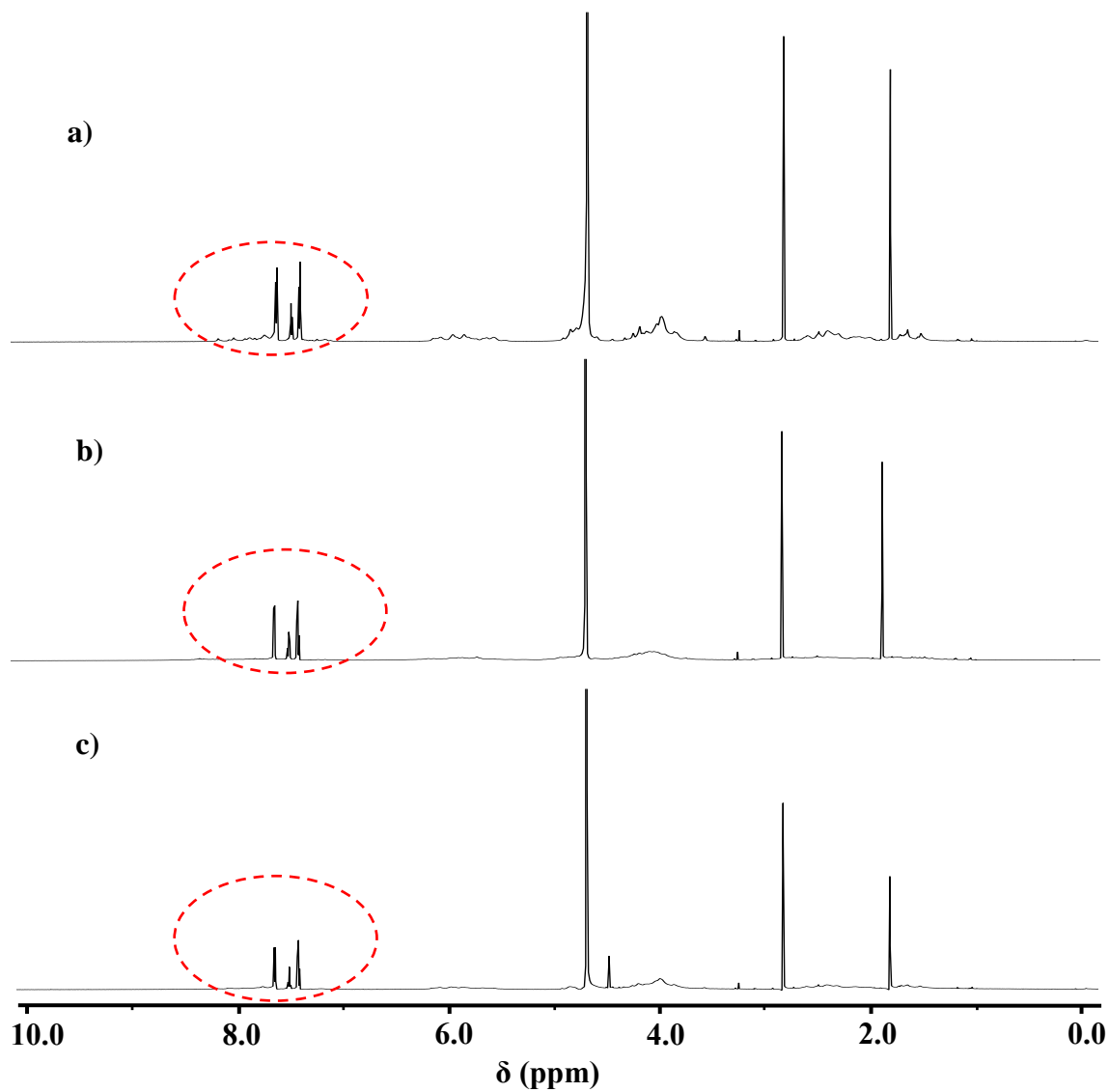
6.12.3 ^1H NMR of Ag: DNA3

Figure 6.38: ^1H NMR spectra of (a) DNA3 (34-mer) oligonucleotide (b) Ag^+ -DNA3 and (c) Ag-DNA3. All spectra acquired at 298 K in D_2O with tetramethylsilane (TMS) as a reference. Encircled peaks represent the aromatic region of the ssDNA molecule and the binding site for Ag^+ ions.

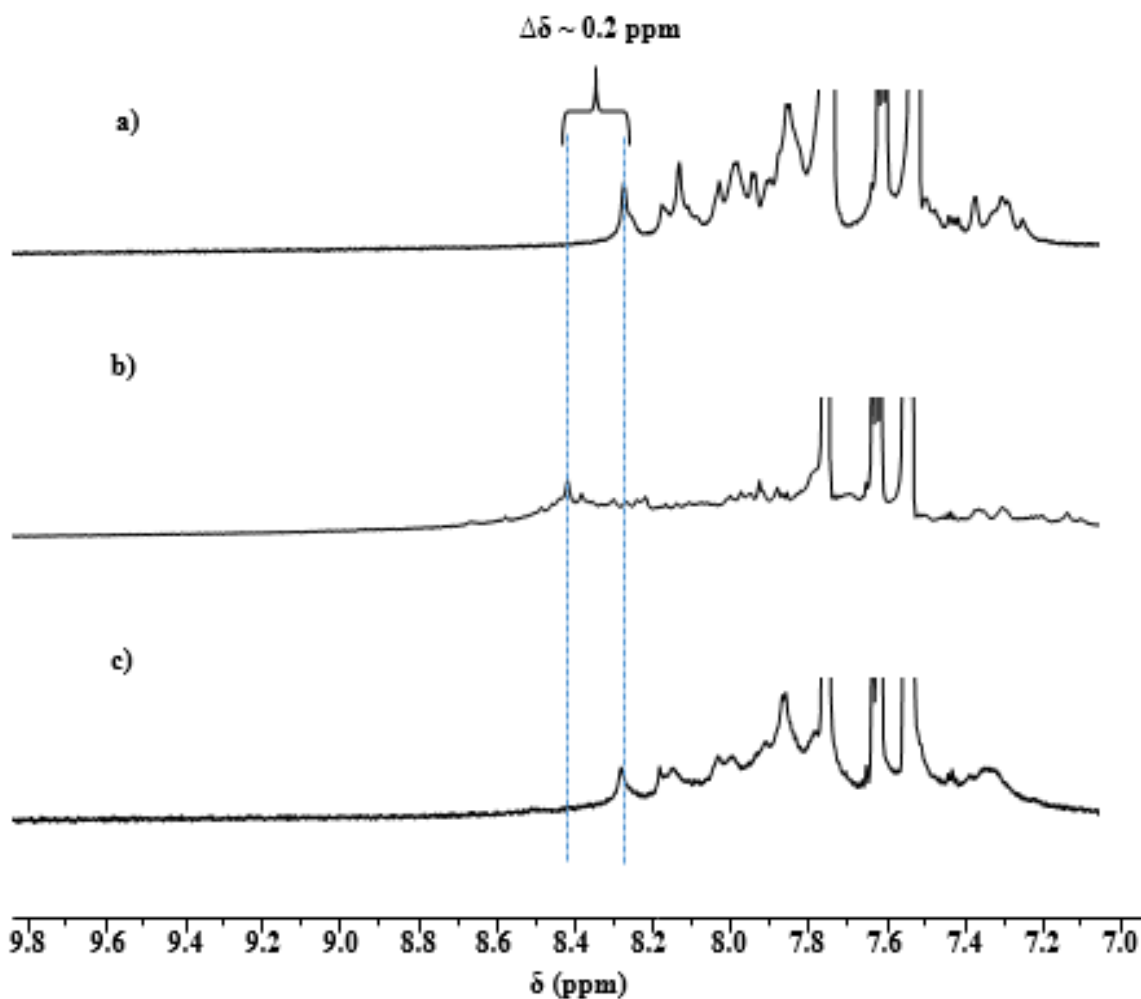


Figure 6.39: ¹H NMR spectra of (a) DNA3 (34-mer) oligonucleotide (b) Ag⁺-DNA3 and (c) Ag-DNA3. All spectra acquired at 298 K in D₂O with tetramethylsilane (TMS) as a reference.

Figures 6.38a, b, and c, are ¹H NMR spectra of DNA3, Ag⁺-DNA3 and Ag-DNA3 respectively, and similarly expanded in figure 6.38a, b, and c for the purposes of studying the aromatic resonances. The assignments of signals in this region, follows similarly with those of the previous two ssDNA1 and 2 using the ¹H, ¹³C, homonuclear correlation spectroscopy (COSY), and the heteronuclear single quantum coherence (HSQC) NMR data for the samples, in combination with similar DNA assignments in the literature.^{47,60,61}

CH5 signal appeared between 5.62 – 6.10 ppm, while the CH6 were recorded at 7.40 – 7.80 ppm where they can be distinguished by their doublet structure. TH6 resonances were observed between 7.35 – 7.45 ppm, within the same region of 7.40 – 7.75 ppm are signals of AH2 which appear coupled with other AH2 resonances. GH8 signals appeared at 7.85 – 7.93 ppm, followed by resonance signals of the AH8 groups at 8.15 – 8.25 ppm.

The addition of Ag^+ ions to ssDNA3 also followed similar trends of loss of signal intensities in the aromatic region, but unlike the Ag^+ -ssDNA2, these did not flatten out completely. Like with the previous Ag^+ -ssDNA1 sample, there was an apparent shift in the resonances downfield from their initial positions after adding Ag^+ ions to the ssDNA3 solution. Although, this downfield shift was smaller, covering a range of $\Delta\delta \sim 0.20$ ppm compared with the $\Delta\delta = 1.30$ ppm shift of the Ag^+ -ssDNA1 sample. The CH6 signals at 7.20, 7.28, 7.34, 7.92 ppm in figure 6.39a broadened, while a few became sharper after adding Ag^+ ions (figure 6.39b). The GH8 signal at 7.96 ppm also lost its initial intensity, however, the pair of AH2 and AH8 signals which often appeared coupled, become uncoupled after addition of Ag^+ ions. The appearance of these AH8 signals and the ensuing chemical shift from their previous positions where they were coupled with the AH2 resonances are indications of binding to the AN7 site of the DNA3 molecule. Further evidence of Ag^+ ion binding to AN7 was confirmed by the chemical shift and significant loss of intensity of the terminal AH8 at 8.29 ppm (figure 6.39a), appearing at 8.42 ppm after the reaction with Ag^+ ion in figure 6.39b. In conclusion therefore, although Ag^+ ion seems also to have bonded on the GN7, results indicate that binding occurred more preferentially on the CN3, AN7 sites.

The reduction of the Ag^+ -ssDNA3 complex saw the re-emergence of the aromatic signals back to their original positions prior to the addition of Ag^+ ions to the ssDNA3 solution. The aromatic signals also became better resolved as their intensities were apparently improved. The reappearance of the proton signals after reduction was interpreted as an indication of less conformation change to the DNA2 and 3 molecules after forming Ag -ssDNA2 and 3 compounds.

The binding positions of Ag^+ ions to DNA1, 2, and 3 were influenced by the concentration ratios of Ag^+ ions: DNA-bases going by the results obtained in these experiments.¹ Petty *et al.*,²¹ noted two modes of binding between Ag^+ ion and the oligonucleotides. At low Ag^+ : DNA-base concentration of 1:5 ratio or less, strong binding took place at the N7 position of the purine ring in adenine and guanine. However, weaker coordination occurred when binding took place simultaneously at both the N1 and N7 positions of the pyrimidine and purine rings of adenine and guanine nucleobases for higher Ag^+ : DNA-base concentration ratios in the order of 1:2. In our experiments, the concentration ratio of the Ag -DNA1 sample was above the 1:5 threshold for the formation of stable Ag -DNA complexes according to Petty *et al.*²¹ As was demonstrated in figure 6.35b, the shifts of the AH2 and AH8 signals are demonstrations of simultaneous binding at the adenine (AN1 and AN7) sites of ssDNA1. Meanwhile, Kumar and Kumar reported that a higher Ag : ssDNA-base ratio favoured a red-fluorescence of the resulting Ag -DNA complex, just as was observed with the DNA2 and 3 in our study.⁹

6.13 ^{31}P NMR study of DNA1, 2, and 3 in D_2O solution

^{31}P NMR analyses of the samples were similarly undertaken in D_2O solution to further scrutinize the interaction of Ag^+ ions with the DNA molecules before and after reduction, and results are displayed below.

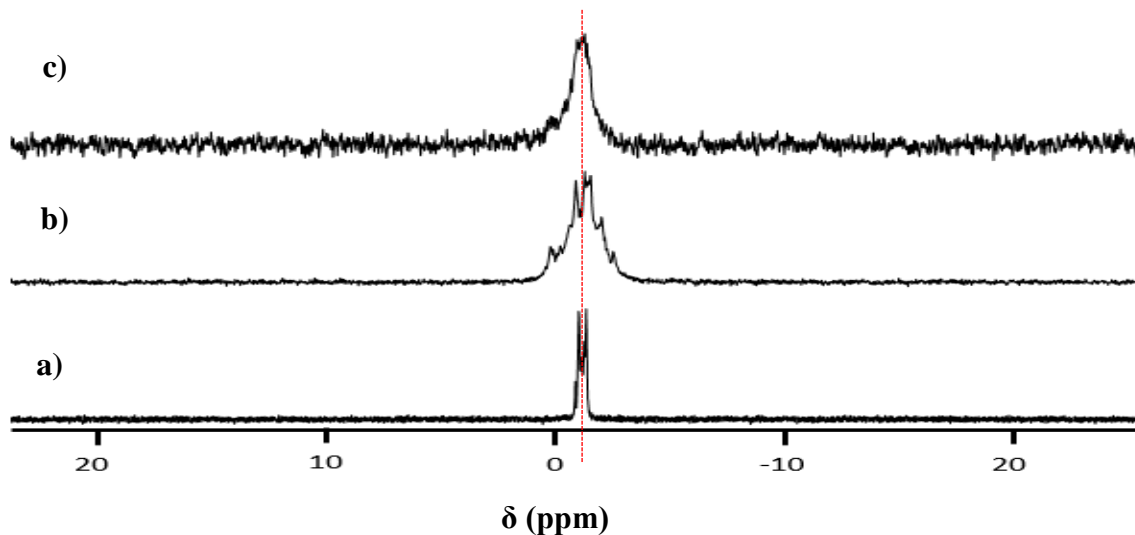


Figure 6.40: ^{31}P NMR of DNA1 (a) DNA1 only (22-mer) oligonucleotide (b) Ag^+ -DNA1 (c) Ag -DNA1 in D_2O at 298 K in D_2O with 85 % phosphoric acid as a reference.

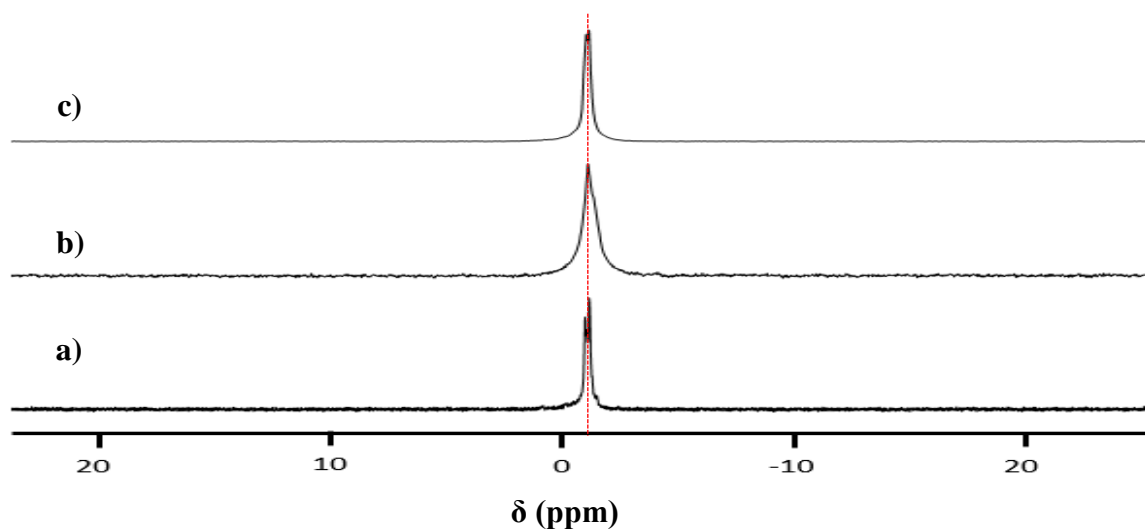


Figure 6.41: ^{31}P NMR of DNA2 (a) DNA2 only (29-mer) oligonucleotide (b) Ag^+ -DNA2 (c) Ag -DNA2 in D_2O at 298 K in D_2O with 85 % phosphoric acid as a reference.

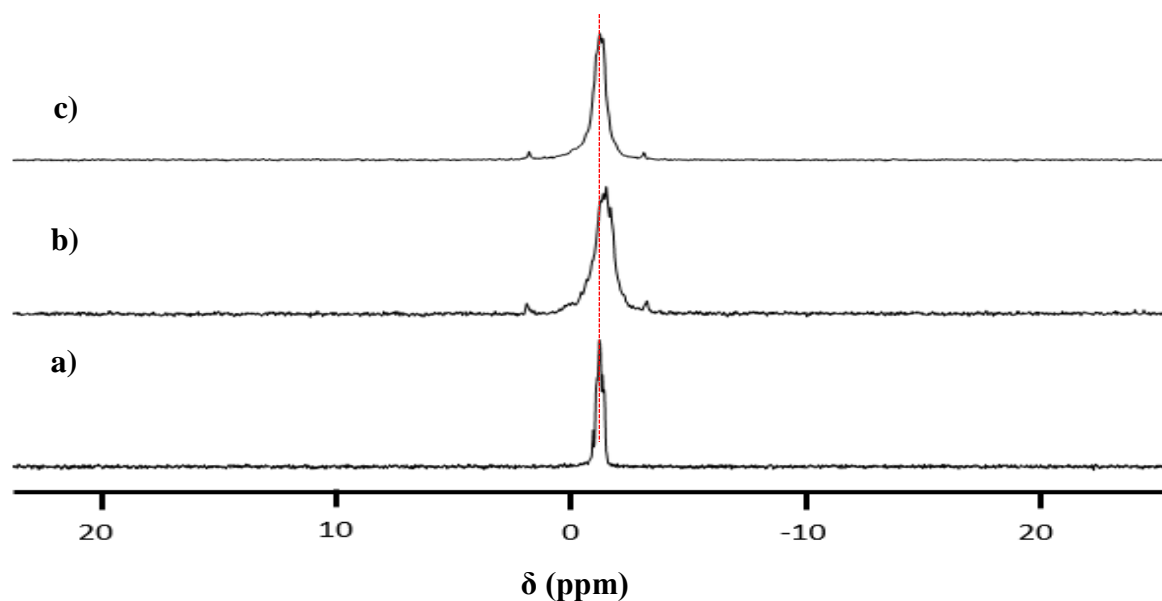


Figure 6.42: ^{31}P NMR of (a) DNA3 only (34-mer) oligonucleotide (b) Ag^+ -DNA3 (c) Ag -DNA3 in D_2O at 298 K in D_2O with 85 % phosphoric acid as a reference.

There were no shifts in the phosphorus peak positions in any of the ^{31}P NMR spectra collected for the three DNA oligonucleotides after addition and reduction of Ag^+ ions (figure 6.40, 6.41, and 6.42). However, a significant broadening and splitting of the ^{31}P NMR peak of the Ag^+ -DNA1 sample was observed after adding Ag^+ ions to the DNA1, whereas, we could barely notice any significant broadening in the ^{31}P NMR spectra of the other two Ag^+ -DNA2 and 3 samples. This was considered important because the Ag^+ -DNA1 sample was the only one of the three whose aromatic signals were not resolved after reduction of the Ag^+ -DNA1 complex.

The significant broadening of the ^{31}P NMR signal of the Ag -DNA1 sample is thought to indicate that binding may have also occurred on the ssDNA phosphate backbone. This was considered to account for the remarkable ^{31}P NMR signal broadening of the Ag -DNA1 sample. The binding of Ag^+ ion to the phosphate oxygen, could apparently result in such significant enlargement of the ^{31}P NMR signal as was observed with this sample. This makes a strong case that binding probably occurred on the phosphate side of the molecule. This proposition is given credence on the basis of the higher concentration of Ag^+ ions in this sample relative to the other two (ssDNA2 and 3). This high Ag^+ ion concentration may have caused binding to occur at N1, N7, and PO_4^{3-} (multiple) sites on ssDNA1. Conformational changes to DNA structure are often monitored by observing the changes in the signals of the phosphate group in the ^{31}P NMR spectra.⁴⁸

There were no signs of phosphorus-31 NMR peak broadening in the ssDNA2 and ssDNA3 samples after adding Ag^+ ions to the individual ssDNAs. However, no apparent broadening of the ^{31}P NMR signals of the DNA2 and 3 samples were noticed when Ag^+ ions were added to these two DNA solutions. The effect of adding Ag^+ ions to the DNA1 solution of the ^{31}P NMR samples was significant, with the ^{31}P signal broadening more remarkably. The splitting of the ^{31}P NMR signals following the addition of Ag^+ ions to the ssDNA1 was also observed. This phenomenon is associated with spin-spin relaxation and interaction between pairs of magnetic nuclei.⁶² Such peak-broadening are strong indications of conformational changes in DNA backbone⁶³ as previously stated. These effect put together were more prominent in the Ag^+ -DNA1 ^{31}P NMR samples. Therefore, demonstrating that the DNA1 molecule may have undergone a major conformational change following the addition of Ag^+ ions to it.

6.14 ^1H NMR of DNA Mononucleotides

In an effort to gain further insight into the binding of Ag^+ ions with the nucleobase on DNA, a series of experiments was conducted with the mononucleotides and Ag^+ ions at a 1:2 (Ag: DNA base) ratio. The 1:2 ratio was used instead of a 1:4, because of the 1:4 ratio produces weak NMR spectra resolution and therefore the 1:2 ratio was maintained.

^1H NMR spectra obtained for each of the four A, T, G, and C, DNA mononucleotides with Ag^+ ion, and after reduction with NaBH_4 all in D_2O solution under argon gas atmosphere at room temperature are presented below.

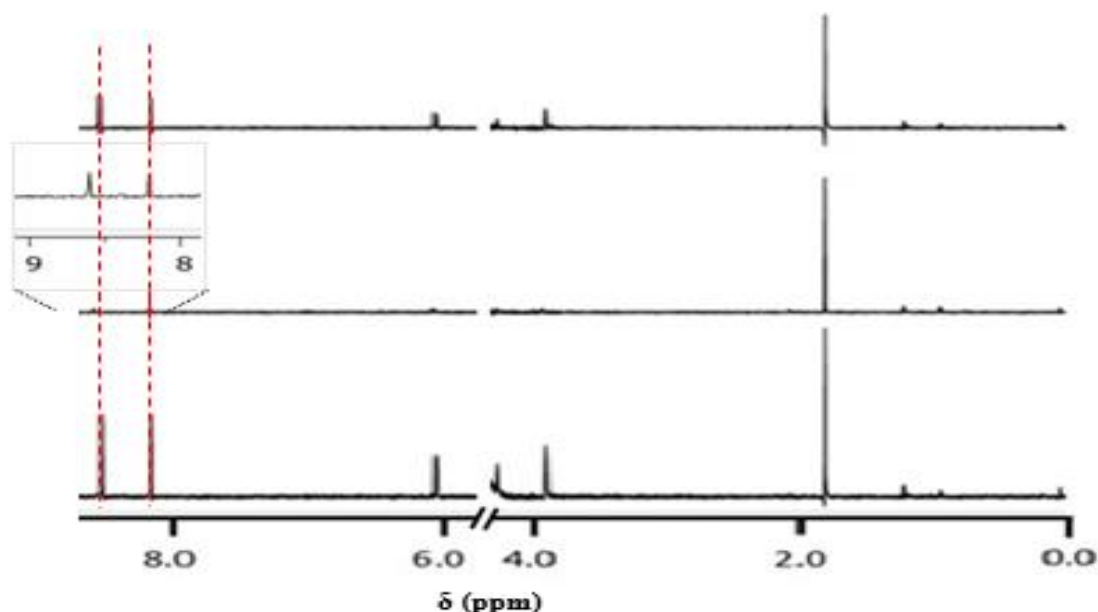
6.14.1 Adenosine ^1H NMR

Figure 6.43: ^1H NMR spectra of a) adenosine b) adenosine_ Ag^+ complex and c) adenosine_ Ag . All spectra acquired at 298 K in D_2O with tetramethylsilane (TMS) as a reference.

Results of the reaction of Ag^+ ions with adenosine in D_2O solution, display similar loss of intensity as was observed with the oligonucleotides (figure 6.43). The peaks at ~ 6.20 ppm represent $\text{H1}'$ resonance of the sugar component of the nucleotide and those in the aromatic region at 8.20 and 8.70 ppm are assigned to adenine AH2 and AH8 signals respectively. After incubating with Ag^+ ions for 30 minutes (figure 6.43b) with exception of the methyl (CH_3) peak at ~ 1.9 ppm, these signals almost broadened out completely as their intensities were lost. A more significant shift in peak position of the AH8 signal with respect to the AH2 after adding Ag^+ ions was only observed at the aromatic region as was previously indicated by Ritchie *et al.*, Petty *et al.*, Sharma *et al.*, and Gwinn *et al.*,^{2,1,5,34} this demonstrate a preference for the AN7 binding site of the adenosine molecule. Since Ag^+ ion is not paramagnetic, the loss of intensity and broadening of the aromatic signals indicates some exchange interactions of the magnetic proton nuclei. This loss of intensity and displacement of the resonance signals were interpreted as evidence of binding between Ag^+ ions and adenosine mononucleotide.

However, on reducing the Ag^+ ions with an equivalent portion of the NaBH_4 solution, the peaks reappeared and became slightly more intense than previously observed in figure 6.43b, but also a little shifted upfield of TMS (figure 6.43c). Drawing inferences from the reduced Ag -DNA2 and 3 samples therefore, the restoration of the signal intensities of the AH2 and AH8

accompanied by their upfield shift, were considered as indications of stable binding between adenosine 5'-mononucleotide and Ag to form adenosine _Ag complex. Since the AH8 signal was the more upfield-shifted of the two nucleobase protons after reduction, we consider that the preferred binding site of Ag on the adenosine 5'-mononucleotide.

6.14.2 Cytidine ^1H NMR

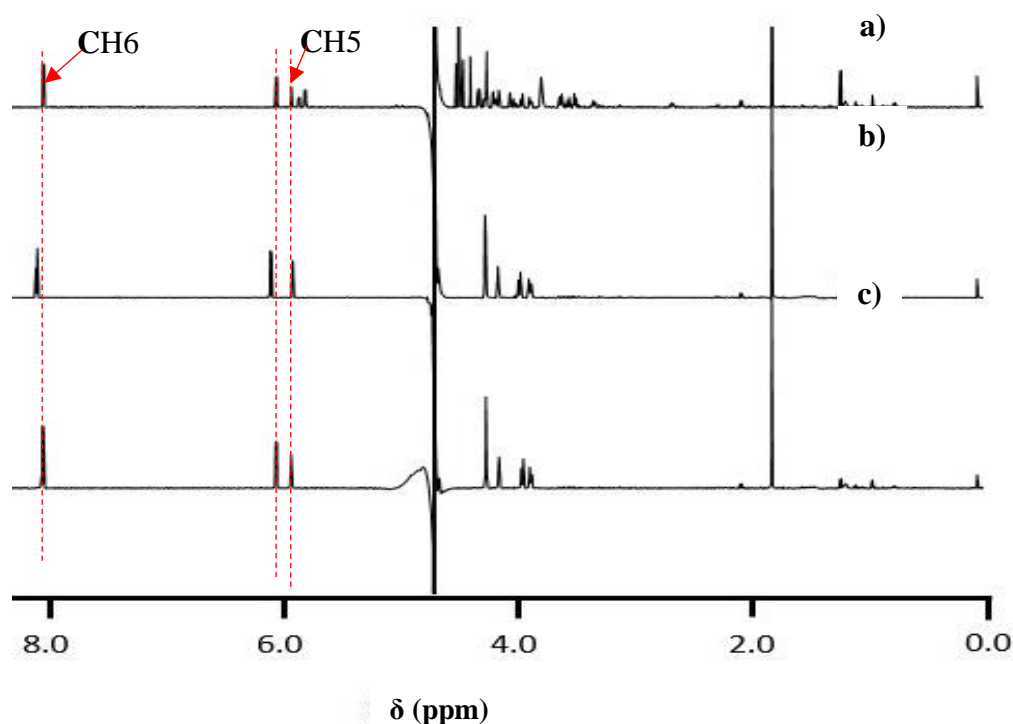


Figure 6.43: ^1H NMR spectra of (a) cytidine (b) cytidine_ Ag^+ complex and (c) cytidine_ Ag . All spectra acquired at 298 K in D_2O with tetramethylsilane (TMS) as a reference.

Apart from the slight shift of both the $\text{H1}'$ of the sugar group, and the cytosine CH6 resonance, cytidine ^1H NMR spectra (figure 6.44b) showed no loss of peak intensity or broadening after incubating with Ag^+ ions. The marginal chemical shift of approximately 0.2 ppm downfield from the initial $\text{H1}'$ and the CH6 peak positions, generally implied that Ag^+ ions were bonded to cytidine at the N3 position.^{2,64} A chemical shift of peak position downfield was noted as a sign of deshielding of NMR protons, which would be expected upon the introduction of an electrophile to an electron-rich site. This proposition is further strengthened by the fact that after reduction, these initially displaced peaks returned to their former positions pre- Ag^+ ion addition. Thus, signifying an upfield shift (shielding effect) of the protons following reduction of the Ag^+ ions.

However, because these signals returned to their initial position pre- Ag^+ ion addition and not further upfield, we may conclude that the cytidine- Ag complex may not have been stable. The return of the signal to their original position after reduction was interpreted as a reversible effect. This notwithstanding, the experiment showed that Ag^+ ions bonded to cytosine nucleobase at the nitrogen (N3) site and the resulting mesomeric effect caused a slight deshielding of the CH6 proton, bearing in mind its distance from the reaction centre.

6.14.3 Guanosine ^1H NMR

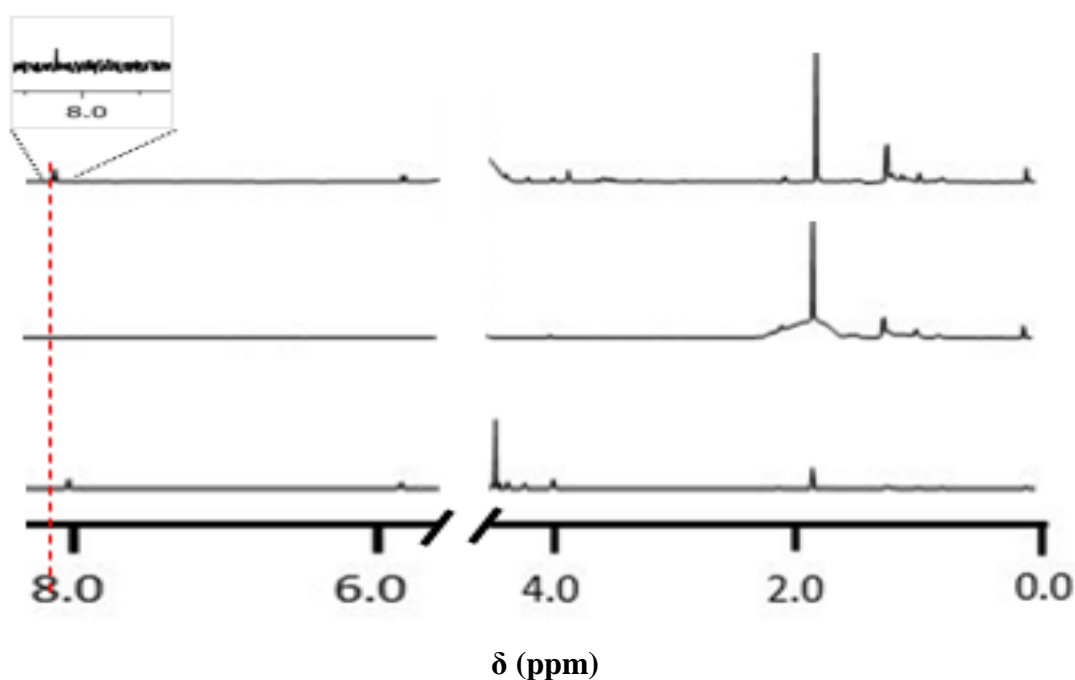


Figure 6.44: ^1H NMR spectra of (a) guanosine (b) guanosine- Ag^+ complex and (c) guanosine- Ag . All spectra acquired at 298 K in D_2O with tetramethylsilane (TMS) as a reference.

Guanosine mononucleotides, showed pronounced loss of resonance signal intensities on treating with Ag^+ ions. This implied that exchange interactions occurred when Ag^+ ions were added to the guanosine 5'-mononucleotide in D_2O solution. The intensity of the GH8 signal at 8.10 ppm (figure 6.45b) was totally lost. Thus, demonstrating that binding occurred between Ag^+ ion and guanosine nucleobase. Again, just like the case with adenosine and cytidine, there was an upfield shift of the 8.10 ppm peak upon reduction of the guanosine- Ag^+ complex. The peaks reappeared, although with poor intensity after reduction of the guanosine- Ag^+ complex but were significantly shifted upfield of TMS from their original position pre-addition of Ag^+ ion due to the proximity of the GH8 proton to the GN7 reaction site. In line with previous

conclusions, this indicates that Ag^+ ion was bonded with guanosine at the N7 site drawing conclusion from the loss of signal intensity and chemical shift downfield of the **GH8** signal as well as its reappearance and pronounced shift more upfield from its original position after reduction.

6.14.4 Thymidine ^1H NMR

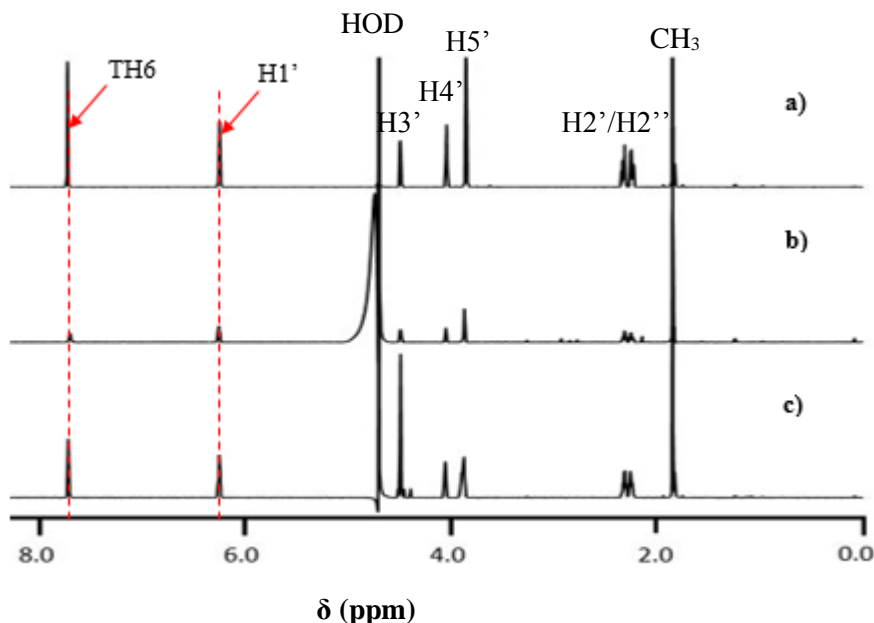


Figure 6.45: ^1H NMR spectra of a) thymidine b) thymidine -Ag^+ complex and c) thymidine -Ag . All spectra acquired at 298 K in D_2O with tetramethylsilane (TMS) as a reference.

The reaction between thymidine mononucleotide and Ag^+ ions produced a similar loss of peak intensity especially of the aromatic signal at ~ 7.90 ppm for the thymidine proton (**TH6**). Although, we did not observe a change in the frequency positions of the **H1'** and **TH6** signals when the mononucleotide was reacted with Ag^+ ions (figure 6.46b), the decrease in the intensities of these signals however, especially of the **TH6** signal is, interpreted to be connected with the binding of Ag^+ ions to thymine nucleobase. This also means that exchange of nuclei similarly occurred when thymidine reacted with Ag^+ ions. Reduction of the resulting thymidine -Ag^+ complex also produced no chemical shift either (figure 6.46c), but the intensities of the signals were improved.

By these observations therefore, we conclude that Ag^+ ions were temporarily bonded to thymidine, whose signal intensity was significantly affected by the reaction with Ag^+ ions as demonstrated in figure 6.46b. The **TH6** resonance was not shifted after the addition of Ag^+ ion

to thymidine and its (Ag^+) subsequent reduction, the TH6 proton may have been shielded by the effect of the electron donating methyl (CH_3) group attached to the C5 position of the pyrimidine ring of the thymine molecule.

6.15 ^{31}P NMR of DNA Mononucleotides

Results of the ^{31}P NMR study of the four mononucleotides are presented in figures 6.47, 6.48, 6.49, and 6.50 for cytidine, thymidine, adenosine and guanosine 5'- mononucleotides respectively. Cytidine 5'- monophosphate sample did not show any broadening or shifts in its ^{31}P peak position when Ag^+ ions were added, and even after reduction (Figure 6.47b and c), neither was there any loss of signal intensity. This leads us to confirm that binding between Ag^+ ion and the cytidine molecule took place at the cytidine N3 site as the ^{31}P remained unchanged.

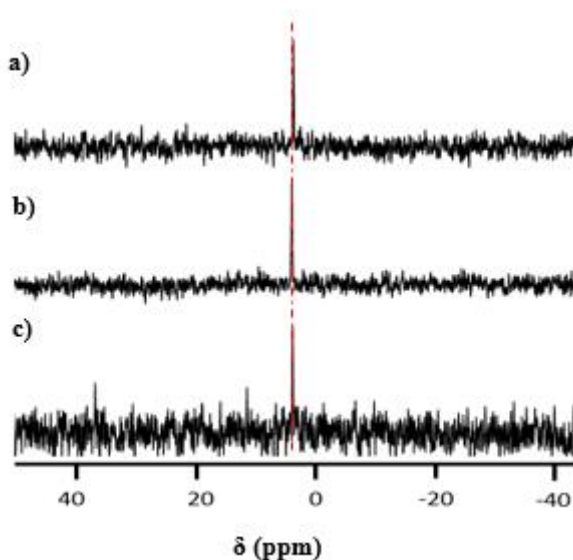


Figure 6.46: ^{31}P NMR spectra of a) cytidine b) cytidine_ Ag^+ complex and c) cytidine_ Ag in D_2O at 298 K with 85 % phosphoric acid as a reference.

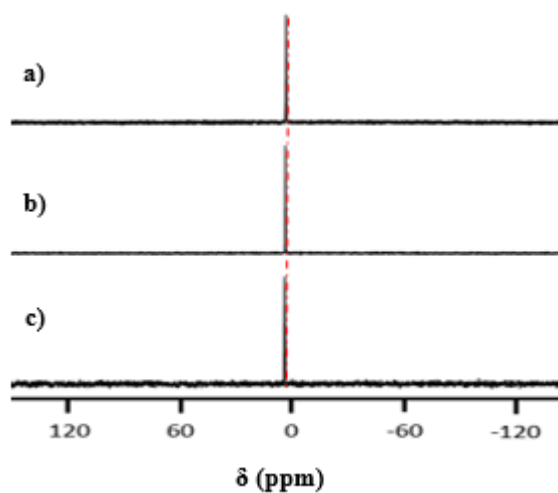


Figure 6.47: ^{31}P NMR spectra of a) thymidine b) thymidine Ag^+ complex and c) thymidine Ag in D_2O at 298 K with 85 % phosphoric acid as a reference.

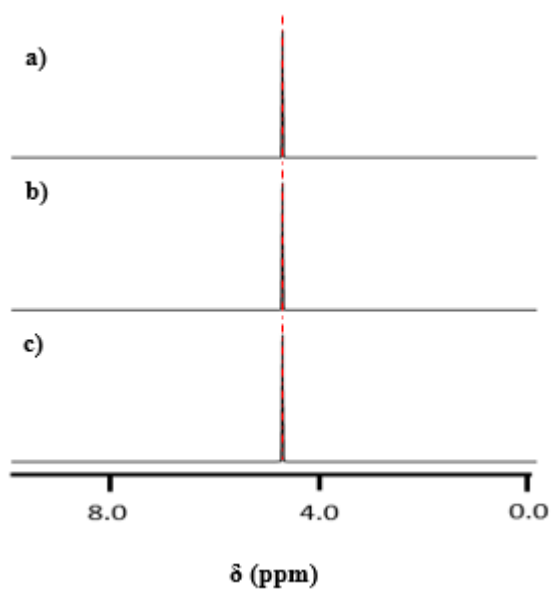


Figure 6.48: ^{31}P NMR spectra of a) adenosine b) adenosine Ag^+ complex and c) adenosine Ag in D_2O at 298 K with 85 % phosphoric acid as a reference.

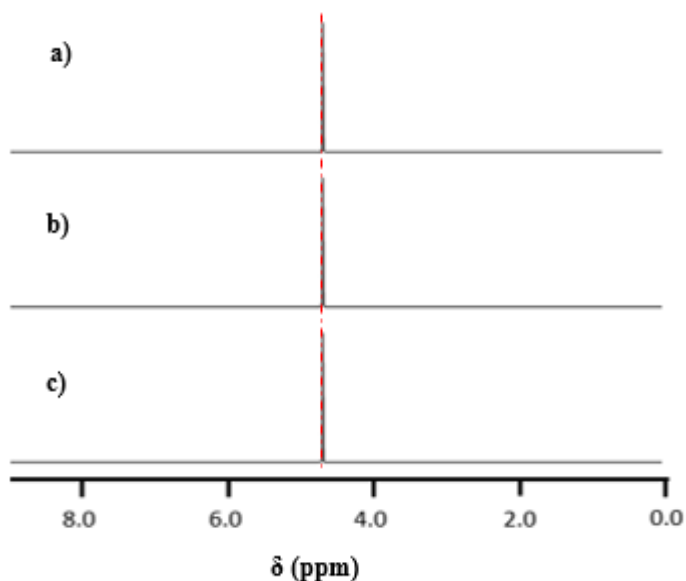


Figure 6.49: ^{31}P NMR spectra of a) guanosine b) guanosine $_{\text{Ag}^+}$ complex and c) guanosine $_{\text{Ag}}$ in D_2O at 298 K with 85 % phosphoric acid as a reference.

Similarly, thymidine, adenosine, and guanosine 5'- monophosphates ^{31}P NMR spectra, all showed no shift of ^{31}P signals, neither were the signals broadened nor their intensities changed after reacting with portions of Ag^+ ions in D_2O solutions and subsequently reducing them with equivalent molar solutions of NaBH_4 in D_2O solutions (Figures 6.47 - 6.50). Therefore, these implied that Ag^+ ion binding site(s) on the mononucleotides was not the phosphate group, but on the nitrogen-containing aromatic nucleobases as indicated by the ^1H NMR spectra. Consistent with these findings is their alignment with those of previous researchers for Ag -bound DNA nanoclusters.^{2,32,5,65}

In summary therefore, there were no changes to the ^{31}P NMR signals for the four individual monomer nucleotides, neither were the peaks broadened or were they split in the ^{31}P spectra. These confirm that Ag^+ ions did not bind to the phosphate end of the nucleotides.

6.16 Fluorescence analyses of the ssDNA1, 2, and 3 D₂O samples

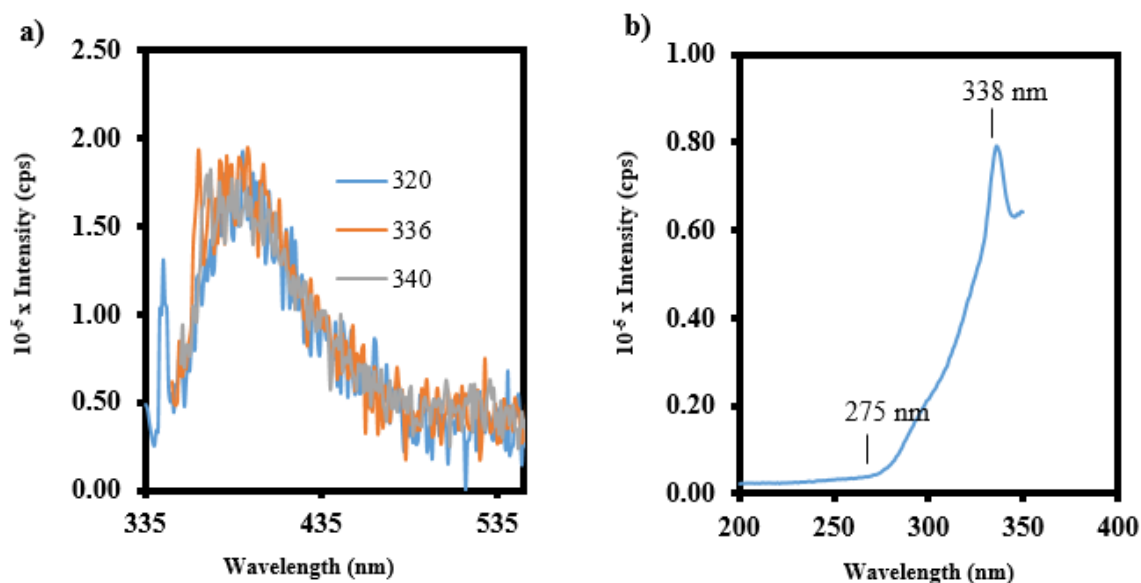


Figure 6.50: Fluorescence spectra of (a) emission spectrum of Ag-DNA1 and (b) excitation spectrum of the emission at 390 nm in 99 % D₂O solution.

The Ag-DNA1 D₂O sample produced a single fluorescence band at 388 nm, which has been assigned to the DNA1 molecule, in line with the earlier conclusion that there was no stable binding between Ag⁺ ion and this oligonucleotide in the D₂O NMR experiment. This similarly indicates that the Ag-DNA1 sample consisted of non-fluorescent Ag NPs. Neidig *et al.*,²⁹ had previously noted a remarkable difference in the photoluminescent properties of this same oligonucleotide in comparison with the other two DNAs in their study. They reported that much large Ag NPs were produced with ssDNA1 than were the case with the other two ssDNA2 and 3. For effective binding to occur between Ag NCs and DNA, Victor *et al.*,³² observed that planar geometries and appropriate molecular orientations (steric factor) of both the Ag NCs and the DNA were important in the binding process. Furthermore, that clusters of Ag₁ to Ag₆ having planar geometries are considered favourable for successful binding with DNA bases.^{32,66,67} Therefore, large, non-fluorescent Ag NPs already, because of their increased density of state would no longer be expected to be planar in geometry. The only peak in the fluorescence spectrum of the Ag-DNA1 sample was seen at ~388 nm wavelength, would signify a large blue shift of approximately 170 nm with reference to the bands above 500 nm for the other two ssDNA in D₂O solution. The 388 nm signal therefore, (Figure 6.51a) has been ascribed to the fluorescence emission of the DNA1 molecule rather than to Ag NCs, thus ruling out the later.

This peak is slightly red-shifted from the 375 nm position obtained in fig.6.5 above for the emission of DNA1 (Ag-free) aqueous solution.

Excitation fluorescence study of this same sample proves that the signal at ~388 nm resulted from the absorption of energy within the 275 – 340 nm range (figure 6.50b). A range obviously within the excitation wavelengths for the DNA1 (Ag-free) sample in aqueous solution (figure 6.5).

On the contrary, fluorescence analysis of DNA2-Ag NCs in D₂O showed a strong emission band at 573 nm with a peak-max intensity just over 1.0 x 10⁶ cps (figure. 6.51 below). Two emission bands were observed in the spectrum at 388 and 581 nm wavelengths. The former at 388 nm (same with the DNA1 emission above in figure 6.5) has also been ascribed to DNA2 emission (see emission of DNA2 Ag-free sample) spectrum in figure 6.6 for comparison.

Excitation spectrum of the Ag-ssDNA2 sample (figure 6.51b) revealed that it absorbed radiant energy at 299 nm (for the emission at 388 nm which is thought to be DNA2), and at 537 nm (the maxima), with shoulders at 474, 485, and 494 nm for the Ag-DNA2 broad peak.

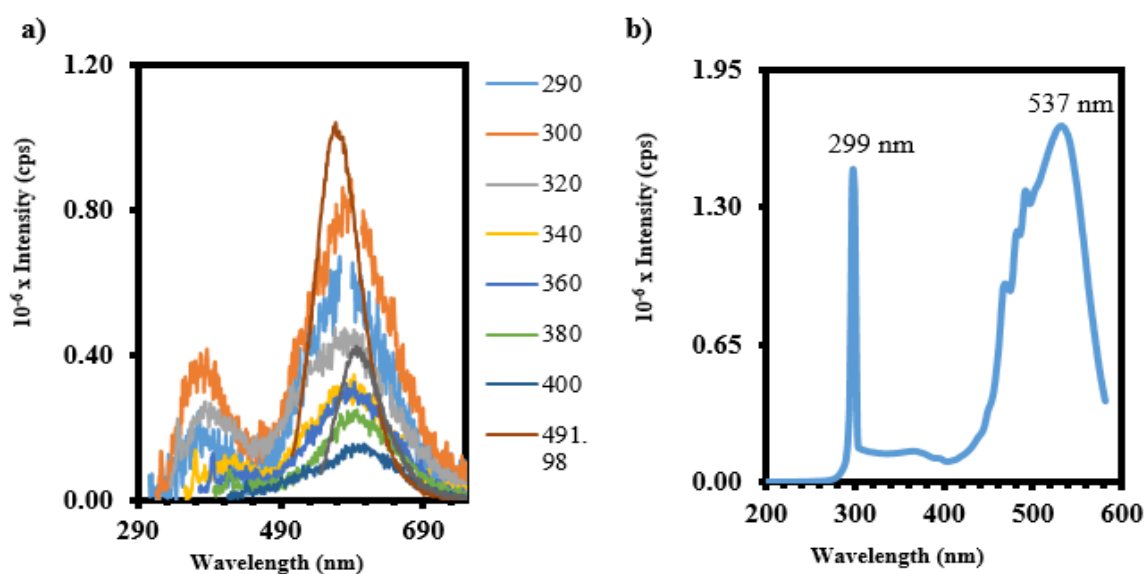


Figure 6.51: Fluorescence spectra of (a) emission spectrum Ag-DNA2 and (b) excitation spectrum of the emission at 591 nm in 99 % D₂O solution.

The 581 nm peak (figure 6.52a), doubles the former both in intensity and full width at half maximum, FWHM. The almost 300 nm FWHM peak broadness (480 – 750 nm) is an indication of large, deep trapped state internal energy conversion process.^{13,9,68} This peak was ascribed to Ag NCs templated on the DNA2 molecule with an emission peak-maximum at 577/590 nm.

This is a red shift by comparison with the emission-max of the microemulsion sample observed at 350 nm.

The broad peak and red shift in emission spectra are characteristics of DNA-templated nanoclusters.⁹ As already mentioned, the broad peak is connected with the non-radiative deep (energy) trapped state, decay process accompanied by the loss of some excitation energy. This can happen when there is a lack of electronic orbital symmetry between the delocalized wave function of the metal-core and those of the passivating ligand.^{9,68} Resulting in the excited electron (exciton) undergoing more stages of non-radiative (dark stage) decay, before eventually returning to the ground state energy level at a significantly longer wavelength.⁹

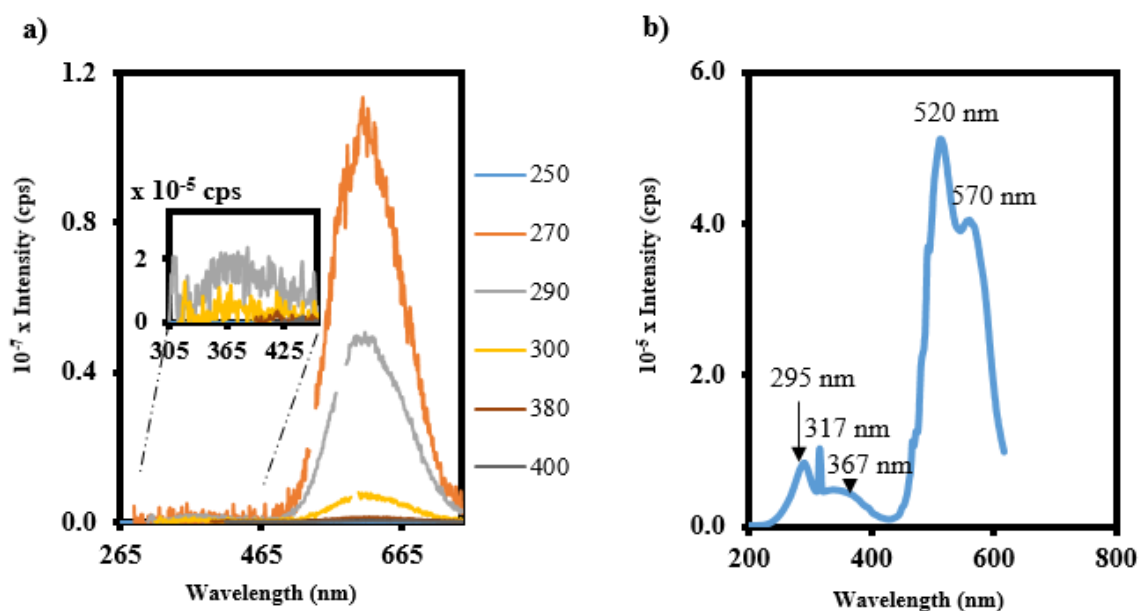


Figure 6.52: Fluorescence spectra of (a) emission spectrum of Ag-DNA3 and (b) excitation spectrum of the emission at 632 nm in 99 % D₂O solution.

In the same vein, a much stronger fluorescence was recorded for the Ag-DNA3 NCs in D₂O (figure 6.53a). The intensity of this sample's fluorescence far exceeded that of the previous Ag-DNA2 NCs, with an intensity count of $\sim 1.2 \times 10^{-7}$ cps despite the measurement having been done with a reduced aliquot sample volume of 2 μ L solution as against 10 μ L in the 500 μ L cuvette for the other samples (DNA1 and 2) due to its intense fluorescence.

Two emission peaks were obtained, the first at ~ 388 nm is again ascribed to the DNA3, but the other peak at ~ 630 nm wavelength has been assigned to the Ag-DNA3. Due to the intense fluorescence of the emission of the band at 630 nm as already mentioned, the emission at ~ 380 nm was significantly suppressed and almost flattening out, making it look as if there was no

emission there in the first place. The characteristic strong fluorescence at 630 nm is consistent with those reported for Ag bound to a 12-mer ssDNA nanoclusters by Petty *et al.*,¹ and Li *et al.*⁶⁹

Fluorescent properties of Ag bound DNA clusters have been linked to clusters of two to four atoms of silver.^{34,35} Neidig *et al.*,²⁹ noted that Ag NCs bonded to this same DNA3 oligomer in aqueous solution, consisted of the smallest number of Ag NCs (possibly, Ag₂) compared with the other two oligomers.

A similar large, broad peak was also observed with the Ag-DNA2 sample in D₂O. This translated to a ~200 nm shift in emission to longer wavelengths when compared with the 430 nm peak maximum position obtained for the Ag clusters without the DNAs in Chapter three.

Excitation fluorescence scan of the 388 nm peak (figure 6.53b) showed that the sample was excited at 297 and 317 nm for the DNA3 emission band, which tallies with the wavelength of absorption for the DNA3 sample in figure 6.5a above. More importantly however, the excitation wavelength at 520 nm with shoulders at 471, 482, 492 and 570 nm have been ascribed for the emission at 630 nm for ssDNA3 bound Ag NCs.

According to these findings, fluorescence emission intensity, as well as the wavelength of emission (red shifted), seemed to increase with ssDNA base length from DNA2 to DNA3 as the ratio Ag: ssDNA-bases increased from 1:5 to 1:6 in the deuterated solvent, even though, no emission bands could be assigned to Ag NCs with DNA1. It would then imply that the oligonucleotide sequences may have contributed to the extent of electron delocalization and fluorescence energy transfer between metal-core and capping ligands.¹ Such red-shifts in emission for the Ag-ssDNA bound clusters, have similarly been highlighted by Kumar and Kumar⁹, and O'Neill *et al.*⁷⁰ Although, Copp *et al.*,⁷¹ contend that both the variation in ssDNA-base sequence and indeed the base length did not affect the position of the fluorescence emission wavelength. However, their study was based on a 10-mer mixed-base oligonucleotide which translates to about 1/2, 1/3, and almost 1/4 of the lengths of the three oligonucleotides in this present study. In their views, Yeh,⁷² Jia, Obliosca *et als.*, all maintained that the base sequences of the DNA ligand, is the major determinant of the resulting fluorescence emission colour of the resulting Ag: DNA complex formed.^{73,74,10}

6.17 Conclusion

Ag⁺-ssDNA were reduced with sodium borohydride in microemulsion with isooctane and bis-sodium as the oil phase and AOT the surfactant. Two separate concentrations of 90 μ M and 1 mM Ag⁺ were treated with each of three different ssDNAs of 22, 29, and 34 base sequences in water droplets corresponding to an omega (ω) value of 10 and 20 respectively. A molar ratio of 1:6 was maintained for silver to each oligonucleotide molecule to obtain a ratio of 1:4, 1:5 and 1:6 for the three ssDNAs according to the DNA base lengths. All reactions were done at room temperature.

The general conclusion of this study is that the reduction of Ag⁺ ions with sodium borohydride in the presence of single-stranded DNAs in confined water droplets produced fluorescent Ag NCs. The size of the Ag NCs is indicated by the wavelength of the emission which was centred at 350 nm. The difference in the emission spectra of the emulsion samples without the ssDNA (Chapter three) and those with DNA (here studied) was considered an indication of the formation of Ag-bound DNA complexes. Furthermore, a combination of the UV-Vis, fluorescence, and ESI-MS data all indicate the formation of small fluorescent Ag NCs. ESI-MS results of the DNA-containing emulsion samples showed two sets of separate bands, one at higher m/z farther from those of the emulsion-containing Ag NCs without the ssDNA which appeared in the lower m/z region. These higher m/z signals which were distinguished by the absence of Ag isotopes, were resolved and found to be associated with the individual DNAs with the m/z values of the separation between successive peaks in this region corresponding to the phosphate (PO₄³⁻) group. These high m/z signals matched with the signals in the spectrum of the individual Ag-free DNA samples. The observations highlighted from the ESI-MS results, demonstrate that Ag clusters and the ssDNAs did not form strong, stable complexes in the emulsion system.

The NMR results showed that Ag bonded with all three ssDNA1, 2 and 3 types, resulting in a significant conformational change especially of the resulting Ag-DNA1 molecule. Multiple bonding was observed between Ag and DNA1 molecule resulting in a general shift of virtually all of the aromatic signals, although the CH6 and AH8 signals were the most significantly affected by the reaction. ¹H NMR results of the Ag-ssDNA1 sample demonstrate that Ag was bonded to ssDNA1 at the AN1, AN7, and PO₄³⁻ sites. In all, Ag bonded with the ssDNAs on the AN1, AN7, CN3, GN7, and TN3 sites, but more significantly, with the AN7 and CN3 from the results obtained. Although, all the ssDNAs formed a conjugate with Ag, indications are that

large, non-fluorescent Ag NPs were formed in the case of ssDNA1. This is thought to be responsible for the significant conformational change observed especially in the ^{31}P NMR spectra of Ag-DNA1 and the fact that the ^1H aromatic signals remained remarkably flattened even after reduction, all of which indicate a major strain on the DNA1 molecule. Binding may also have occurred on the AN1 as well as the phosphate sites as indicated by the ^{31}P NMR spectra in figure 6.40b of the DNA1 according to the results, these are thought to have an influence on the stability of the resulting Ag-DNA1 complex. The restoration of resonance signal intensity post-reduction of the Ag^+ -DNA complex together with a further chemical shift upfield of TMS, was generally considered a demonstration of the formation of stable bond in Ag-ssDNA compounds.

Studies of the individual DNA mononucleotides showed that binding occurred between Ag^+ ions and the nucleobases. However, in the case of the purine bases, there was a significant loss of intensity and subsequent shift further upfield after reduction of their Ag^+ -nucleobase complexes; which was not the case with the pyrimidine nucleobases of cytosine and thymine. CH6 signal showed a downfield shift after reacting with Ag^+ ions without loss of intensity, thymine did not show any shift of the TH6 signal but recorded a significant intensity loss. However, both pyrimidine nucleobases had their CH6 and TH6 aromatic signal positions restored after reduction, the CH6, the signal was shifted upfield of TMS back to its position prior to the reaction with Ag^+ ions.

Furthermore, the slightly more significant chemical shift of the AH8 signal of the adenosine 5'-mononucleotide following the reaction with Ag^+ ions, infers that binding may have taken place at the adenine nitrogen-7 (AN7) site, while the apparent loss of the GH8 signal after adding Ag^+ ions, together with its significant chemical shift further upfield after reduction, were regarded as signs of binding on the GN7 site of the guanosine mononucleotide. The CN3 was of course, the obvious site for binding with the metal ion in the cytidine 5'- mononucleotide, as was shown by the marginal shift of the CH6 signal after reacting with Ag^+ ions, but returned to its initial chemical shift position after reduction. These conclusions were confirmed by results from the ^{31}P NMR analyses of the mononucleotides, all of which showed no change in the ^{31}P signals when they were reacted with Ag^+ ions, and similarly no changes even after reduction, thus indicating that Ag was not bonded to the phosphate group.

6.18 Reference

- 1 J. T. Petty, J. Zheng, N. V. Hud and R. M. Dickson, *J. Am. Chem. Soc.*, 2004, **126**, 5207–5212.
- 2 C. M. Ritchie, K. R. Johnsen, J. R. Kiser, Y. Antoku, R. M. Dickson and J. T. Petty, 2007, 175–181.
- 3 Y. Antoku, PhD Thesis, Georgia Institute of Technology, 2007.
- 4 C. A. J. Lin, C. H. Lee, J. T. Hsieh, H. H. Wang, J. K. Li, J. L. Shen, W. H. Chan, H. I. Yeh and W. H. Chang, *J. Med. Biol. Eng.*, 2009, **29**, 276–283.
- 5 J. Sharma, H.-C. Yeh, H. Yoo, J. H. Werner and J. S. Martinez, *Chem. Commun. (Camb)*., 2010, **46**, 3280–2.
- 6 H. J. Yeh, Hsin-Chih, Sharma, Jaswinder, Han, J. Jason, Martinez, S. Jennifer, and Werner, *IEEE Nanotechnol. Mag.*, 2011, 28–33.
- 7 B. Nithyaja, H. Misha and V. P. N. Nampoori, *Nanosci. Nanotechnol.*, 2012, **2**, 99–103.
- 8 A. Latorre, R. Lorca, F. Zamora and Á. Somoza, *Chem. Commun. (Camb)*., 2013, **49**, 4950–2.
- 9 A. Kumar and V. Kumar, *Chem. Rev.*, 2014, **114**, 7044–7078.
- 10 S. M. Copp, D. E. Schultz, S. Swasey and E. G. Gwinn, *ACS Nano*, 2015, **9**, 2303–2310.
- 11 N. Santamaría-Díaz, J. M. Méndez-Arriaga, J. M. Salas and M. A. Galindo, *Angew. Chemie - Int. Ed.*, 2016, 6170–6174.
- 12 S. Del Bonis-O'Donnell, Jackson T., Thakrar, Ami., Jeremy, Wain., Hirschberg, Vong, Daniel., Queenan, Bridget N., Fyngenson, Deborah K., and Pennathur, *ACS Chem. Neurosci.*, 2017, **9**, 849–857.
- 13 S. A. Bogh, M. R. Carro-temboury, C. Cerretani, S. M. Swasey, S. M. Copp, E. G. Gwinn and T. Vosch, *Methods Appl. Fluoresc.*, 2018, **6**, 1–7.
- 14 J. Zheng, C. Zhang and R. M. Dickson, *Phys. Rev. Lett.*, 2004, **93**, 5–8.

- 15 S. Duan, Hongwei. and Nie, *J. Am. Chem. Soc.*, 2007, **129**, 2412–2413.
- 16 J. K. Hensel, A. P. Carpenter, R. K. Ciszewski, B. K. Schabes, C. T. Kittredge, F. G. Moore and G. L. Richmond, 2017, 1–6.
- 17 K. S. Sarkar, R. and Pal, *Biopolymers*, 2006, **83**, 675–686.
- 18 A. Swami, G. Espinosa, S. Guillot, E. Raspaud, F. Boué and H. D. Langevin, *Langmuir*, 2008, **24**, 11828–11833.
- 19 V. G. Budker, P. M. Slattum, S. D. Monahan and J. a Wolff, *Biophys. J.*, 2002, **82**, 1570–9.
- 20 A. V. Pietrini and P. L. Luisi, *Biochim. Biophys. Acta - Biomembr.*, 2002, **1562**, 57–62.
- 21 G. L. Eichhorn, *Inorganic Chemistry*, Elsevier, 1973.
- 22 A. Neumeyer, M. Bukowski, M. Veith, C. M. Lehr and N. Daum, *Nanomedicine Nanotechnology, Biol. Med.*, 2011, **7**, 410–419.
- 23 L. D. Mello, R. M. S. Pereira, A. C. H. F. Sawaya, M. N. Eberlin and L. T. Kubota, *J. Pharm. Biomed. Anal.*, 2007, **45**, 706–713.
- 24 C. Petit, P. Lixonf and M.-P. Pileni, *J. Phys. Chem*, 1993, **97**, 12974–12983.
- 25 G. Liu, Y. Shao, F. Wu, S. Xu, J. Peng and L. Liu, *Nanotechnology*, 2013, **24**, 015503.
- 26 I. Vayá, T. Gustavsson, F. A. Miannay, T. Douki and D. Markovitsi, *J. Am. Chem. Soc.*, 2010, **132**, 11834–11835.
- 27 J. Coates, *Encycl. Anal. Chem.*, 2006, 1–23.
- 28 D. Engel, *Nexo Solut. Filtr. Sep. Soc.*, 2016.
- 29 M. L. Neidig, J. Sharma, H. Yeh, J. S. Martinez, S. D. Conradson and A. P. Shreve, *J. Am. Chem. Soc.*, 2011, 11837–11839.
- 30 G. G. Guilbault, *Practical Fluorescence*, Marcel Dekker, New York, Second Edi., 1990.
- 31 R. D. Thompson, *Univ. Maryland, Dep. Biochem. Mol. Biol. Sch. Med.*, 1998.
- 32 V. Soto-Verdugo, H. Metiu and E. Gwinn, *J. Chem. Phys.*, 2010, **132**.
- 33 Z. Shen, H. Duan and H. Frey, *Adv. Mater.*, 2007, **19**, 349–352.

- 34 E. G. Gwinn, P. O'Neill, A. J. Guerrero, D. Bouwmeester and D. K. Fygenson, *Adv. Mater.*, 2008, **20**, 279–283.
- 35 T. Vosch, Y. Antoku, J.-C. Hsiang, C. I. Richards, J. I. Gonzalez and R. M. Dickson, *Proc. Natl. Acad. Sci. U. S. A.*, 2007, **104**, 12616–21.
- 36 B. G. Ershov, *Russ. Chem. Bull.*, 1999, **48**, 1–15.
- 37 D. Buceta, N. Busto, G. Barone, J. M. Leal, F. Domínguez, L. J. Giovanetti, F. G. Requejo, B. García and M. A. López-Quintela, *Angew. Chemie - Int. Ed.*, 2015, **54**, 7612–7616.
- 38 D. Bucak, S. and Rende, *Colloid and Surface Chemistry: A laboratory guide for exploration of the nano world*, CRC Press, Taylor & Francis Group, Boca Raton, 1st edn., 2014.
- 39 J. R. Lakowicz, *Instrumentation for Fluorescence Spectroscopy*, 2006.
- 40 S. S. S. Tobita, K. Ida, *Res. Chem. Intermed.*, 2001, **27**, 205–218.
- 41 J. Sambrook and D. W. Russell, *Cold Spring Harb Protoc.*, 2006.
- 42 R. Higuchi, G. Dollinger, P. S. Walsh and R. Griffith, *Biotechnology*, 1992, **10**, 413–417.
- 43 A. Mulvaney, Paul. Linnert, Thomas. Henglein, *J. Phys. Chem.*, 1991, **95**, 7843–7846.
- 44 A. Henglein, *J. Phys. Chem.*, 1993, **97**, 5457–5471.
- 45 G. M. Clore and A. M. Gronenborn, *J. Magn. Reson.*, 1984, **11**, 95–102.
- 46 J. Feigon, W. A. Denny, W. Leupin and D. R. Kearns, *Biochemistry*, 1983, **22**, 5930–5942.
- 47 R. M. Wadkins, E. A. Jares-Erijman, R. Klement, A. Rüdiger and T. M. Jovin, *J Mol Biol*, 1996, **262**, 53–68.
- 48 D. R. Kearns, *CRC Crit Rev Biochem*, 1984, **15**, 237–290.
- 49 G. Hare, D. R. Wemmer, D. E. Chou, S-H. Drobny, *J. Mol. Biol.*, 1983, **171**, 319–336.
- 50 I. Chakraborty, T. Udayabhaskararao and T. Pradeep, *Chem. Commun.*, 2012, **48**, 6788.
- 51 H. Klages, J. Kessler, *Compr. Med. Chem. II*, 2007, **3**, 901–920.

- 52 P. Dixon, R.M. Styles, in *Encyclopedia of Spectroscopy and Spectrometry*, (Third Edi., 2017, p. 216–221.
- 53 K. Nagayama, A. Kumar, K. Wüthrich and R. . Ernst, *J. Magn. Reson.*, 1980, **40**, 321–334.
- 54 S. Macufla, Y. Huang and D. Suter, *J. Magn. Reson.*, 1981, **281**, 259–281.
- 55 M. J. Hostetler, J. E. Wingate, C.-J. Zhong, J. E. Harris, R. W. Vachet, M. R. Clark, J. D. Londono, S. J. Green, J. J. Stokes, G. D. Wignall, G. L. Glish, M. D. Porter, N. D. Evans and R. W. Murray, *Langmuir*, 1998, **14**, 17–30.
- 56 M. Yoshimasu, H. Aihara, Y. Ito, S. Rajesh, S. Ishibe, T. Mikawa, S. Yokoyama and T. Shibata, *Nucl. Acids Res.*, 2003, **31**, 1735–1743.
- 57 C. R. Murray, C. B. Kagan and M. G. Bawendi, *Annu. Rev. Mater. Sci.*, 2000, **30**, 545–610.
- 58 A. T. Stoltenberg, Randall M. Woolley, *Biomed. Microdevices*, 2004, **6**, 105.
- 59 J. Li, J. J. Zhu and K. Xu, *TrAC - Trends Anal. Chem.*, 2014, **58**, 90–98.
- 60 D. M. Cheng, L. S. Kan, E. E. Leutzinger, K. Jayaraman, P. S. Miller and P. O. P. Ts’o, *Biochemistry*, 1982, **21**, 621–630.
- 61 T. W. Collins, G. J. Sleeman, A. D. Aldrich-Wright, J. R. Greguric, I. Hambley, *Inorg. Chem.*, 1998, **37**, 3133–3141.
- 62 D.R. Kearns and T. L. James, *Crit. Rev. Biochem.*, 1984, **15**, 237–290.
- 63 J. Fischer, *Modern NMR Techniques for Synthetic Chemistry*, CRS Press, Taylor and Francis Group, Boca Raton, Florida, 2015.
- 64 I. Díez and R. H. A. Ras, *Nanoscale*, 2011, **3**, 1963.
- 65 F. A. Aldaye and H. F. Sleiman, *Angew. Chemie - Int. Ed.*, 2006, **45**, 2204–2209.
- 66 H. Xu and K. S. Suslick, *Adv. Mater.*, 2010, **22**, 1078–1082.
- 67 A. A. Zinchenko, N. Chen, D. Baigl, L. I. Lopatina and V. G. Sergeyev, *Biomacromolecules*, 2012, **13**, 1787–1793.
- 68 M. B. Teunis, S. Dolai and R. Sardar, *Langmuir*, 2014, **30**, 7851–7858.
- 69 L. Li, Q. Guo, J. Li, W. Yan, C. Leng, H. Tang, Q. Lu and B. Tan, *J. Mater. Chem. B*, 2013, **1**, 3999.
- 70 P. R. O’Neill, L. R. Velazquez, D. G. Dunn, E. G. Gwinn and D. K. Fygenson, *J. Phys. Chem. C*, 2009, **113**, 4229–4233.

- 71 S. M. Copp, D. Schultz, S. Swasey, J. Pavlovich, M. Debord, A. Chiu, K. Olsson and E. Gwinn, *J. Phys. Chem. Lett.*, 2014, **5**, 959–963.
- 72 H. C. Yeh, J. Sharma, I. M. Shih, D. M. Vu, J. S. Martinez and J. H. Werner, *J. Am. Chem. Soc.*, 2012, **134**, 11550–11558.
- 73 X. Jia, J. Li, L. Han, J. Ren, X. Yang and E. Wang, *ACS Nano*, 2012, 3311–3317.
- 74 J. M. Obliosca, C. Liu, R. A. Batson, M. C. Babin, J. H. Werner and H. C. Yeh, *Biosensors*, 2013, **3**, 185–200.

7 CHAPTER SEVEN

7.1 CONCLUSIONS

7.2 Introduction

Major general findings in all four results chapters are discussed together and summarized here in this concluding chapter.

7.3 General conclusion on findings

7.3.1 Borohydride synthesized Ag NCs

Confinement of the reagents to the dispersed phase of a water-in-oil microemulsion ensures that the reduction of metal ions (Ag^+ , Cu^{2+}) by borohydride results in small metal clusters rather than nanoparticles. The emulsion droplets size determined by DLS, and control of the aqueous concentration of reagents restricts the number of metal ions to each droplet to $90 \mu\text{M}$ and 1 mM . UV-Vis results of the emulsion samples did not show the characteristic surface plasmon resonance (SPR) bands of large, non-fluorescent Ag NPs.

Generally, in both reactions with the $90 \mu\text{M}$ and 1 mM Ag, and within the specified reaction conditions, two particle-size diameters were predominant several hours post-synthesis. These are the $\sim 5 \text{ nm}$ and the $>100 \text{ nm}$ respectively. Observations have shown that the 5 nm size are essentially reverse micelles,¹ the 150 nm second particle size consist of water droplets.² Rayleigh scattering fitting of the UV-Vis results of the samples gave a value of approximately 50.0 nm for the droplets in the emulsion.

Analyses of the fluorescence spectra indicate that a silver cluster of two atoms (Ag_2) was initially formed after nucleation and subsequently grew to a cluster of four atoms (Ag_4) of silver with bandgaps of ~ 4.0 and 2.9 eV respectively. These large bandgap energies make them

chemically very stable.³ Another weak emission band at 610 nm was also observed which is an indication of further growth and presence of larger Ag NCs. In comparison with the transient Ag clusters produced by pulse radiolysis by Henglein⁴, stable, blue emitting Ag NCs have been made without recourse to the typical organic ligands. These Ag NCs were capped by solvated borate ($B_3O_5^-$), borane (BH_3), hydrogen ion (H^+) and water molecules, giving a ligand composition of $[B_3O_5.BH_3.2H_2O]H$ for the neutral compound.

Fluorescence-time-dependent-kinetic studies of the formation of these samples revealed a fast reduction and rapid nucleation processes with the highest emission intensity reached under seven minutes, after which there was a slight fluorescent decay. An average emission decay rate of 2.5 counts per second per second (cps^2) was recorded for both samples after the 7th minute of the nucleation process, reflecting the growth phase.

A calibration curve obtained by calculating the number of silver atoms in the 50 nm droplet according to the concentration of $[Ag^+]$ using a series of six different concentrations values (Chapter three: fig. 3.5) produced a linear plot indicating the increasing number of atoms per droplet. However the eventual cluster sizes formed seemed to favour the evolution of clusters with magic numbers⁵ of atoms in the forms of Ag_2 and Ag_4 , as was confirmed by ESI-MS measurements, rather than forming progressively lumped, large particle sizes according to the total concentration of Ag^+ ions originally in the water droplet.

The following molecular compositions of $[Ag_2(H_2O)H]^-$ and $[Ag_4B_3O_5BH_3.2H_2O]^-$ were obtained from analysis of the ESI-MS results of the samples. These indicate that all silver atoms are in the clusters are in oxidation state zero. Indications are that the silver atoms and the capping ligands interacted by coordinate bonding. Hence, these ligands may be readily exchanged with other ligands if necessary, where they can serve as precursors and employed as sensors.

Fourier Transform Infrared (FTIR) spectroscopy results identified the vibrational bands of the the B-O and BH_3 groups in the fingerprint and functional group regions of the spectra.

Likewise, x-ray photoemission spectroscopy (XPS) analyses of these samples confirmed the presence of elements of boron, oxygen, and carbon. However, it did not successfully detect the Ag, simply because the concentration was below the detection limit.

7.3.2 Photosynthesised Ag NCs

Although the reduction of silver (I) ions by means of light energy is not new, what is novel is undertaking this reduction in a microemulsion system. The comparative study of the chemical reduction and photoreduction methods was undertaken to compare their efficiencies and results. Perhaps, and more importantly, the first advantage offered by the photoreduction method is the absence of sodium borohydride and hence, the elimination of the borate and borane groups. This made it easier to investigate the electrochemical properties of the Ag NCs without the encumbrance of the borates.

Depending on the power rating of the photoreactor, Ag^+ ions can readily be reduced to Ag atoms in the microemulsion. An average of two – five hours respectively, was required for both the $90 \mu\text{M}$ and 1mM samples to reach optimum production of Ag NPs according to the values of the absorbance measurements obtained from the time-dependent study.

DLS measurements were also had two major bands at 5 and 100 nm, representing reverse micelles and water droplets respectively.^{1,2} Rayleigh scattering fitting of the UV-Vis data produced a droplet diameter of 40.0 nm.

Fluorescence emission analysis show that the samples consisted of fluorescing Ag NCs with emission bands at 305 and 439/453 nm, with a third one at 610 nm attributed to larger aggregates, at 280 nm excitation wavelength. These bands were similar to the borohydride reduced samples in emulsion, and indicated Ag NCs of $\text{Ag}_2 - \text{Ag}_4$.

Signals of Ag_2 , Ag_3 and Ag_4 as were observed from the electrospray ionization mass spectrometry (ESI-MS) results. These were capped by solvated water (H_2O) and hydroxides (OH^-) molecules, as well as several numbers of protons (H^+), giving rise to species of $\text{Ag}_n(\text{H}_2\text{O})_m(\text{OH})^-$ or $[\text{Ag}_n(\text{H}_2\text{O})_m\text{H}_o]^+$, where $n = 3$ or 4 , m ranging from $1 - 9$, and $o = 1 - 7$ as the case maybe. Again, these have all their silver atoms in the oxidation state of zero in a coordinate bonding between the silver metal core and the capping ligands as was earlier reported.

Generally, though both reduction methods produced ultra-small clusters according to their emission, and ESI-MS results, their respective transmission electron microscopy (TEM) particles sizes indicated little size variation of 1.4 and 2.4 nm. These are consistent with emission results reported; the second emission band was observed at lower energies with the

borohydride reduced samples, which infer slightly larger clusters. The TEM results are in agreement with the atomic force microscopy (AFM).

7.3.3 Borohydride-synthesized Cu NCs

Under the same reaction conditions of the silver nanoclusters, copper nanoclusters were synthesized in microemulsion for $90\ \mu\text{M}$ and $1\ \text{mM}$ Cu NCs. Again, two droplets sizes of 5 and $\sim 100\ \text{nm}$ were obtained with the former in the higher proportion for the $90\ \mu\text{M}$ sample and the reverse, for the high concentration ($1\ \text{mM}$) sample.

Apart from the strong absorbance at 240 nm for both samples which was attributed to ligand to metal-core transition for $[\text{Cu}(\text{H}_2\text{O})_6]^{2+}$ complex, no plasmon bands were seen in the UV-Vis spectra.

Emission results indicate the presence of fluorescent bands at 350 nm wavelength with excitation wavelengths of 290 and 310 nm. The absorption of excitation energies at these wavelengths is synonymous with small clusters. An optical gap of 3.80 eV was obtained for the Cu NCs. Another emission band was also observed at 430 nm for the $90\ \mu\text{M}$ sample. However, the emission spectra all contained a collection of sharp peaks which are thought to be contaminants of the AOT. Meanwhile, no emissions due to copper oxide nanoparticles were observed at 493 and 510 nm in all the spectra. This together with the ESI-MS results precluded the presence of copper oxide nanoparticles.

ESI-MS measurements confirmed the molecular composition of the copper clusters with a molecular formula of $[\text{Cu}_7\text{B}_3\text{O}_5\cdot\text{BH}_3\cdot 2\text{H}_2\text{O}]^-$ comprising of seven atoms of copper (Cu_7), again with the borate (B_3O_5) and the borane (BH_3) ligands, as well as (two) molecules of water and a proton (H^+) to form a neutral compound $[\text{Cu}_7\text{B}_3\text{O}_5\cdot\text{BH}_3\cdot 2\text{H}_2\text{O}]\text{H}$. Yet again, the molecular formula indicated that all copper atoms existed in the oxidation state of zero. Of course, these copper core and ligands are believed to interact by coordinate bonding.

TEM particles size analyses of both samples gave an average size of $\sim 1.00 - 2.50\ \text{nm}$. The $1\ \text{mM}$ sample had the smaller cluster sizes with an average of $\sim 1.00\ \text{nm}$ and seem to be more monodispersed. These results yet again, are in consonance with the AFM, and both strongly supporting the cluster size recorded.

Further chemical characterisation of the copper clusters of both samples with the aid of the Fourier Transform Infrared (FTIR) spectroscopy demonstrated the presence of the B-O, and B-

H symmetric and asymmetric vibrational bands, thereby further support the chemical composition of the ligands earlier obtained from the ESI-MS.

Although, x-ray photoemission spectroscopy (XPS) analyses of the Cu NCs was similarly unsuccessfully in terms of detecting the chemical properties of the metal-core, it however further supported the composition of the ligands with the detection of boron, oxygen, and carbon 1s signals. Three peaks each for boron and oxygen were detected at 183.85, 186.75, and 191.70 eV, and 530.45, 532.35, and 534.65 eV. The 183.85 eV band is new and previously unreported for Ag-containing compounds, however, this signal was considered to be connected with Ag-B group; the 186.75 and 191.70 eV bands correspond to the BH₃ group of the Cu-containing compound,^{6,7} and the borate (B₃O₅) groups respectively. While the three oxygen signals are associated with the MO₂ or M₂O₃ corresponding to the BO₂ and B₂O₃, the organic carbon-containing oxygen group, and the oxygen of water respectively.

7.3.4 Borohydride-synthesized DNA templated Ag NCs

Absorbance spectra of the single-stranded deoxyribonucleic acids (ssDNA) templated silver nanoclusters (Ag-DNAs NCs) spectra did not display any plasmon peaks of silver nanoparticles (Ag NPs) with bulk-like properties. Evidence of DNA absorption peaks were observed in these absorption spectra, which were slightly shifted to longer wavelengths away from the 260 nm optical density (OD) wavelength for DNA. This shift is considered as an indication of DNA/Ag binding. A peak appearing between 280 – 290 nm was also observed for all samples and corresponds to Ag₄²⁺.⁸

Originally, all three Ag-free ssDNA samples were observed to be fluorescent pre-addition of Ag⁺ ions; with an emission maximum centred at 375 nm. However, after reacting with Ag, different emission properties were observed. Basically, three luminescent bands were detected: a sharp but prominent emission with a maximum at \approx 315 nm, a group of four, weak but sharp bands between 350 – 450 nm, and then finally, a broad but medium-size emission between 550 – 750 nm was for the DNA1 – templated 90 μ M and 1 mM Ag NCs, with the latter emission band thought to be associated with aggregates. The other two ssDNA oligomers (DNA2 and DNA3) on the contrary, exhibited luminescence properties different from the first (DNA1), but were remarkable in being similar with respect to one another. They both have weak, broad emissions at about 348 - 356 nm, before the group of four separate sharp peaks between 365 –

470 nm; just slightly red shifted from those of ssDNA1. There were no other emissions bands observed for these two ssDNA2 and 3 templated with Ag especially at longer wavelengths.

The Ag- containing DNA1 sample showed luminescence properties similar to the emulsion Ag NCs samples (without DNA) in chapter three, but the emission band at 650 nm is synonymous with DNA-templated Ag NCs observed in literature,⁵ thereby indicating that the Ag clusters may have been templated on the DNA1 in the emulsion droplets. However, the introduction of ssDNA2 and 3 in to their respective microemulsion droplets resulted in emissions in the 348 – 356 nm range, with an indication of another band between 365 – 470 nm especially for the 90 μ M Ag-DNA3 sample. These are remarkably different from those of Ag-DNA1 and the DNA-free Ag NCs emulsion samples earlier highlighted, and were considered as indications of Ag clusters not binding with the DNA2 and 3 templates in the emulsion experiments.

DLS results once again pointed at two major size distributions of 5 and ≥ 100 nm as similarly been reported by previous researchers,^{9,10} with the smaller droplets (5 nm) being of the higher population proportion.

TEM images of the ssDNA emulsion samples were significantly different from those of the Ag – containing DNA-free samples in chapter three. The dissimilarity is portrayed by the appearance of colonies of DNA-encased Ag particles in the TEM images of the Ag-DNA emulsion samples as against the randomly dispersed Ag particles TEM images obtained in chapter three.

Although signals of DNA were not prominent in the ESI-MS spectra of the samples, evidence of weak signals very much associated with DNA were detected in the ESI-MS spectra of the samples. These were compared with those obtained from the Ag – free ssDNA spectra and were seen to match at lower m/z signal region. The uniqueness of the ESI-MS results is depicted by the appearance of two regions of different signals in these spectra Ag-templated ssDNA spectra. One, (at lower m/z ratio) corresponding to DNA – free Ag NCs, exactly matching those of the DNA – free samples in the preceding chapter, and another, at higher m/z region which corresponds to spectra of the Ag- free DNA (DNA only) sample.

Put together therefore, it is apparent from the results of the absorption, DLS, TEM images, and ESI-MS, the functionalization of Ag NCs on ssDNA yielded Ag-templated ssDNA complex in the microemulsion, and showed that DNA may have been resident in the water droplets. The fluorescence spectra of these Ag NCs – ssDNA samples were quite different from the previous

DNA – free emission spectra in chapter 3. However, it is presumed that these Ag: ssDNA complexes dissociated during the ionization and desolvation processes in the ESI-MS instrument, probably as a result of some coulombic interaction which may have affected what is now considered a likely unstable conjugate, with a weak metal – DNA ligand binding.

7.3.5 Nuclear magnetic resonance spectroscopy

Nuclear magnetic resonance (NMR) studies of the binding properties of Ag NCs on the ssDNAs in 99 per cent deuterated water (solvent) were obtained to ascertain the binding sites, the ^1H NMR results demonstrated that silver preferentially binds to the DNA bases. Cytosine, guanosine, and adenosine had the most significant changes when treated with Ag^+ ions. These were indicated by the observations of peak broadening and total loss of intensity in some cases; and also by the differences in chemical shift values pre- and post-treatment with Ag^+ ions. However, these peaks generally reappeared, and either returned to their previous positions, or moved to more upfield chemical shift positions relative to their original positions after reduction of the Ag^+ DNA complexes with equivalent portions of the NaBH_4 solution.

In all, binding seems to have occurred at the cytosine N3, adenine N7, guanine N7, and thymine N3 positions of the bases. Further evidence suggested that binding occurred also at the N1-site of adenine, and at the phosphate group of the ssDNA1 molecule according to the concentration of the reactants. At higher Ag^+ : ssDNA concentration (1:4, Ag: ssDNA base), binding occurred at multiple sites (N1, N7, and PO_4^{3-}) of the ssDNA molecule as was the case with DNA1; the N7-site being the most preferred. This multiple site bonding is believed to be responsible for the instability observed in the resulting Ag – ssDNA1 complex due to steric factors associated with the significant conformational changes in the ssDNA1 molecule.

But at lower Ag: ssDNA base concentrations, bonding occurred at the preferred N7-site leading to stable Ag – ssDNA complexes as were the case with ssDNA2 and 3. There were no bonding at the phosphate sites of these ssDNA2 and 3 molecules as were evident from their ^{31}P spectra.

However, evidence obtained for the individual mononucleotides infer that stable bonds were formed between Ag and the purine nucleobases – adenine and guanine. Although, in the case of the pyrimidine nucleobases – cytosine and thymine, bonding occurred at the N3-site with Ag^+ ions, however, upon reduction, the CH5 and CH6 signals did not only return back to their original (pre- Ag^+ ion addition) chemical shift positions, but also had their signal intensities restored. Thymine nucleobase did not show any change in chemical shift positions of its signals

(especially TH6) unlike cytosine, except for the significant loss of signal intensity after adding Ag^+ ions, but these signal intensities were again restored after reduction.

^{31}P NMR study showed similar peak broadening following the incubation of the ssDNA with Ag^+ ions with Ag-DNA1, consistent with the conformational changes of the DNA backbone, but this was not observed with the four, separate, DNA mononucleotides.

Furthermore, emission studies of the Ag NCs-templated ssDNAs samples, revealed that DNA2 and 3 conjugates were very luminescent. Specifically, two bands were observed at 388 and 581 nm for Ag-ssDNA2, and at 388 and 610 nm for the Ag-DNA3 samples. Only one emission band was seen at 388 nm for the Ag-ssDNA1 sample.

7.4 Future Studies

Going forward, knowledge gained from the study of these metal nanoclusters can be applied in to water research for the novel detection of pathogens and some chemical pollutants associated with water and waste water systems, as well as in the diagnosis of certain diseases.

Of the two metal nanoclusters studied, the Ag NCs showed more remarkable opto-physical properties in aqueous solution, showing more intense emission bands in comparison with the Cu NCs.

Finally, I would consider structural characterisation of the Ag clusters by extended x-ray absorption fine-structure (EXAFS) and radiative lifetime measurements to determine the transition responsible for the fluorescence.

7.5 Reference

- 1 J. Eastoe, *Surfactant Chemistry*, 2003, 1-134.
- 2 M.-P. Pileni, *Nature*, 2003, **2**, 145–150.
- 3 B. Zeiger, *Superatoms, Lect. Seminar*, 2008, 1-3.
- 4 A. Henglein, *J. Phys. Chem.*, 1993, **97**, 5457–5471.
- 5 S. M. Copp, D. Schultz, S. Swasey, J. Pavlovich, M. Debord, A. Chiu, K. Olsson and E. Gwinn, *J. Phys. Chem. Lett.*, 2014, **5**, 959–963.
- 6 Shul'ga Y.M. and Makhaev V.D., *Koord. Khim.*, 1993, **19**, 809.
- 7 J. G. Kester, D. Keller, J. C. Huffman, M. A. Benefiel, W. E. Geiger, C. Atwood, A. R. Siedle, G. A. Korba and L. J. Todd, *Inorg. Chem.*, 1994, **33**, 5438–5442.
- 8 C. Petit, P. Lixonf and M.-P. Pileni, *J. Phys. Chem*, 1993, **97**, 12974–12983.
- 9 K. S. Sarkar, R. and Pal, *Biopolymers*, 2006, **83**, 675–686.
- 10 A. V. Pietrini and P. L. Luisi, *Biochim. Biophys. Acta - Biomembr.*, 2002, **1562**, 57–62.

8 APPENDIX

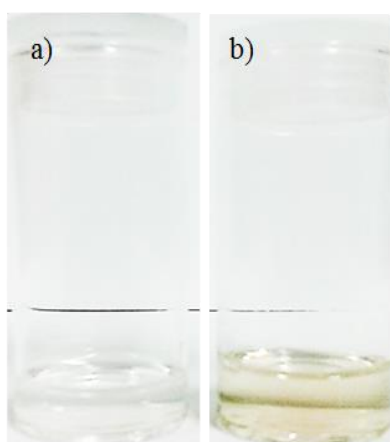


Figure 8.1: Pictures of (a) 90 μM and (b) 1 mM Ag NCs in microemulsion synthesized by photoreduction.



Figure 8.2: 100 mg reverse-phase silica-based Restek cartridge.

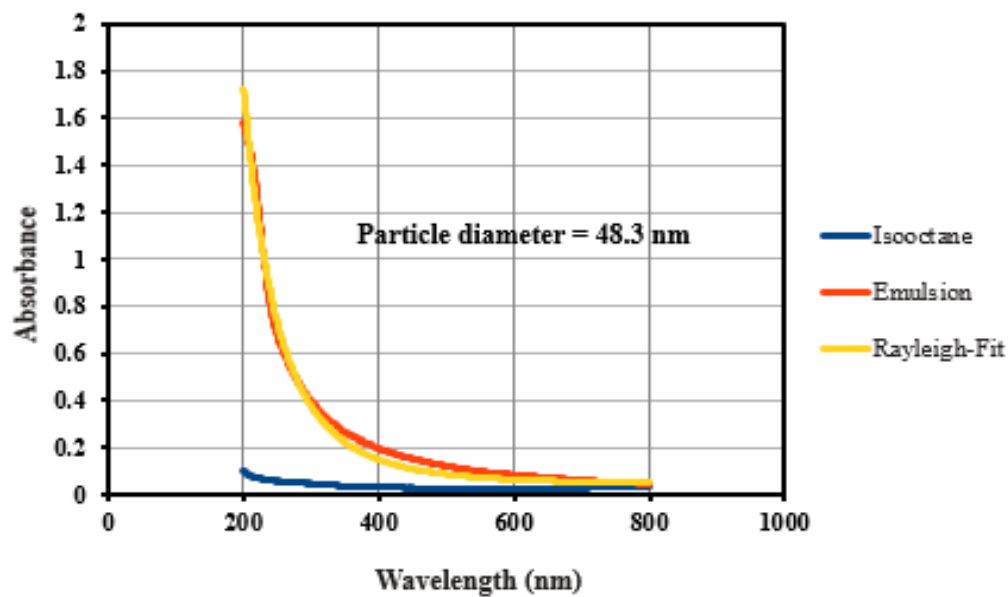


Figure 8.3: Rayleigh curve fitting of Ag NCs in microemulsion.

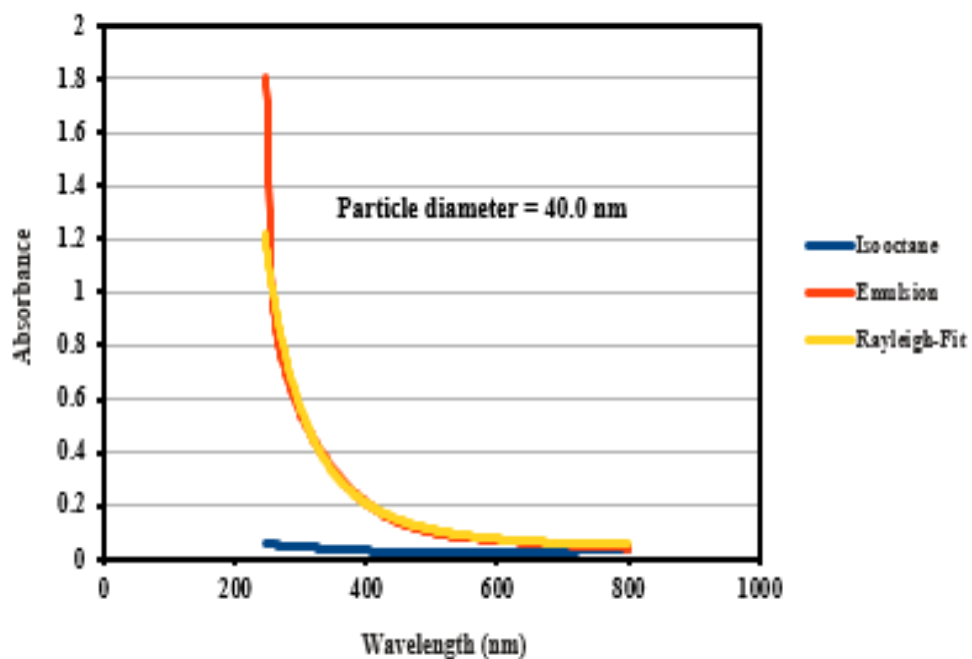


Figure 8.4: Rayleigh fit of the photoreduced Ag NCs UV-Vis data.

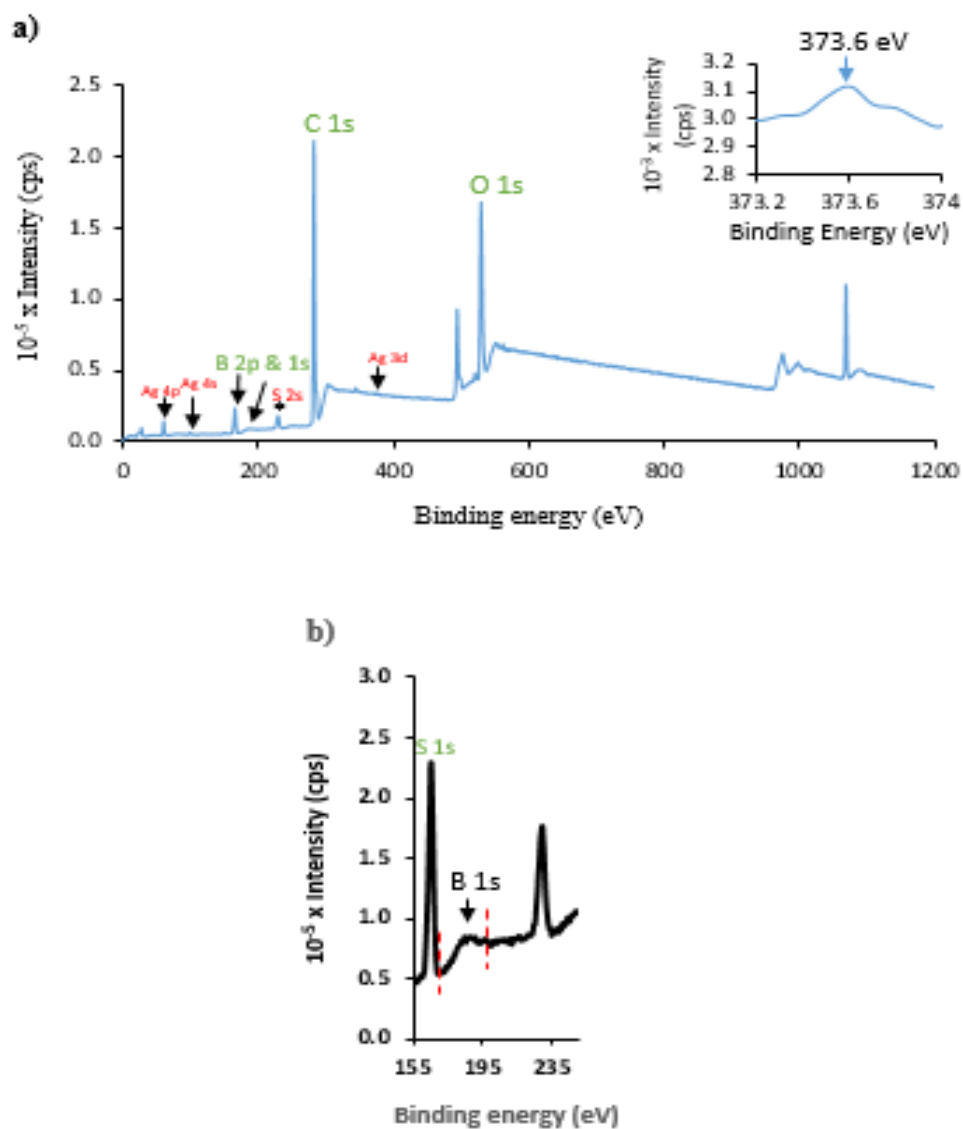


Figure 8.5: XPS spectrum of $[Ag_4B_3O_5.BH_3.2H_2O]^-$ aqueous solution.

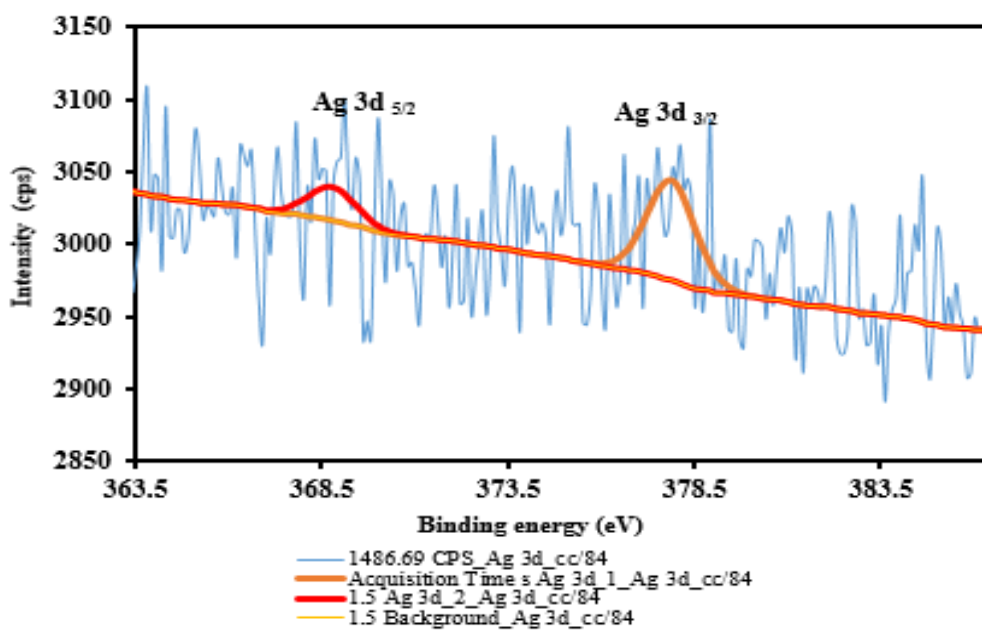


Figure 8.6: XPS spectrum of Ag capped by borate, and borane ligand.

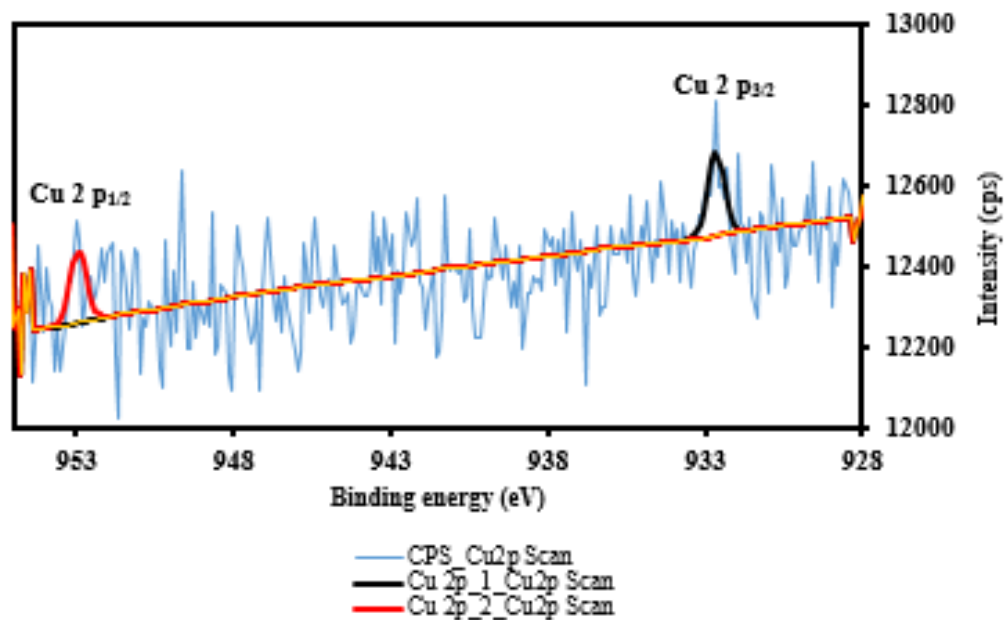


Figure 8.7: XPS spectrum of Cu NCs capped by borate, and borane ligand.

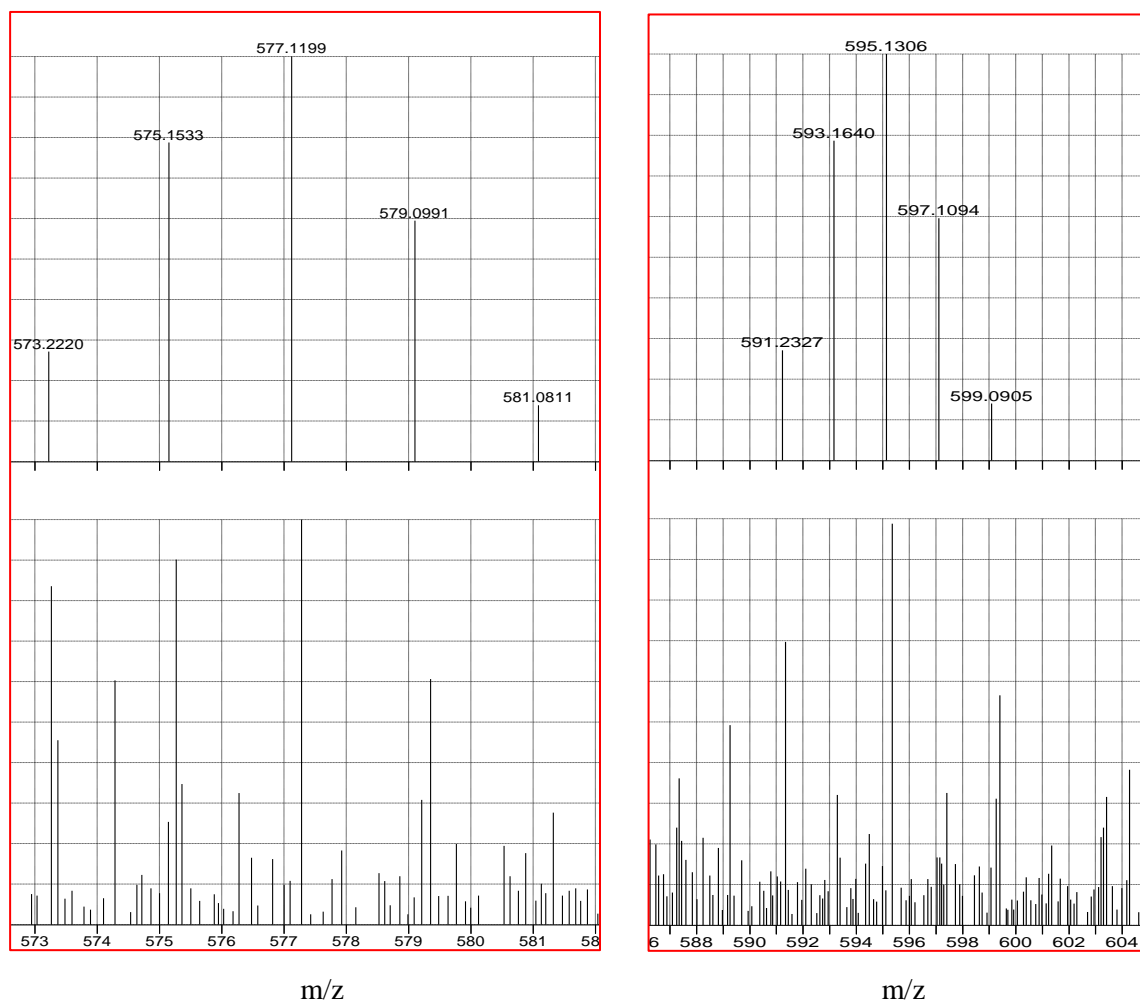


Figure 8.8: ESI-MS of Ag NCs peak at (a) 577 (b) 595. (Top = Simulation, bottom = Experimental).

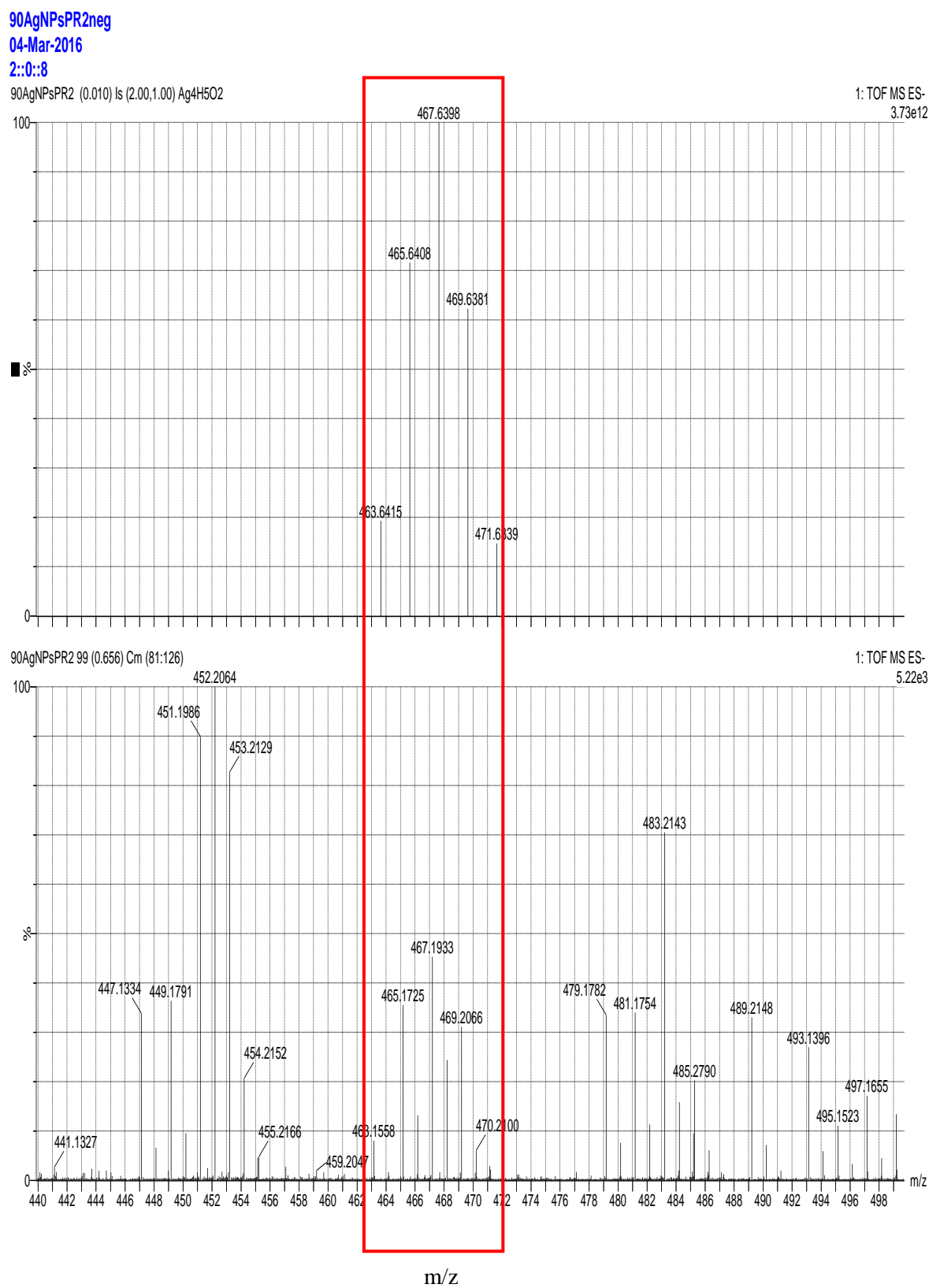


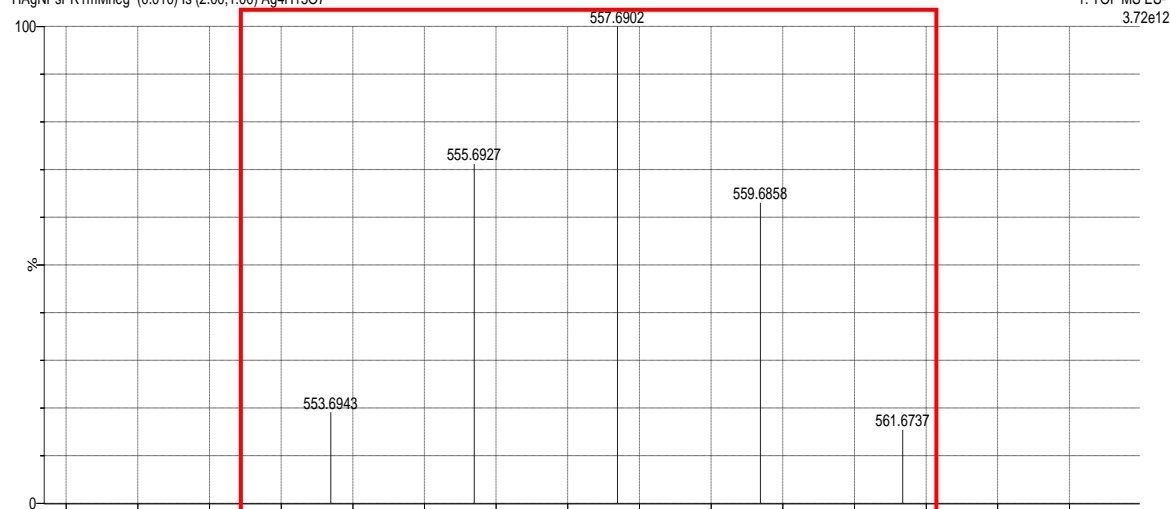
Figure 8.9: ESI-MS spectra of photosynthesized Ag NCs at m/z 467. (Top = Simulation, bottom = Experimental).

1mAgNPsoilsepneg

02-Mar-2016

4::6::0

HAgNPsPR1mMneg (0.010) Is (2.00,1.00) Ag4H15O7

1: TOF MS ES-
3.72e12

HAgNPsPR1mMneg 119 (0.802) Cm (55:132)

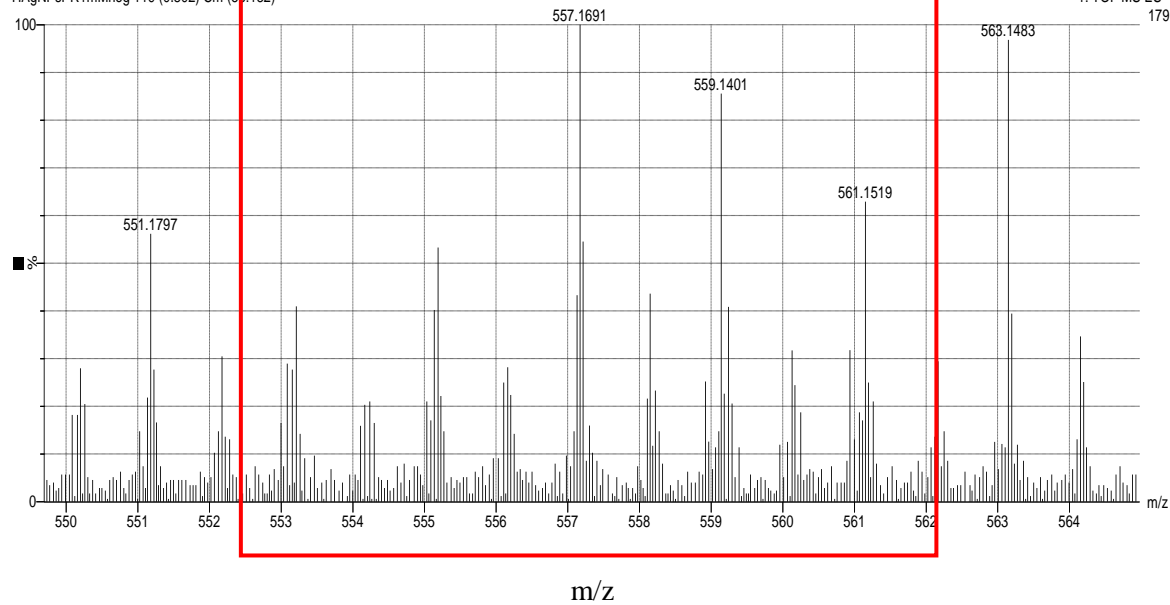
1: TOF MS ES-
179

Figure 8.10: ESI-MS of photoreduced Ag NCs peak at 557. (Top = Simulation, bottom = Experimental).

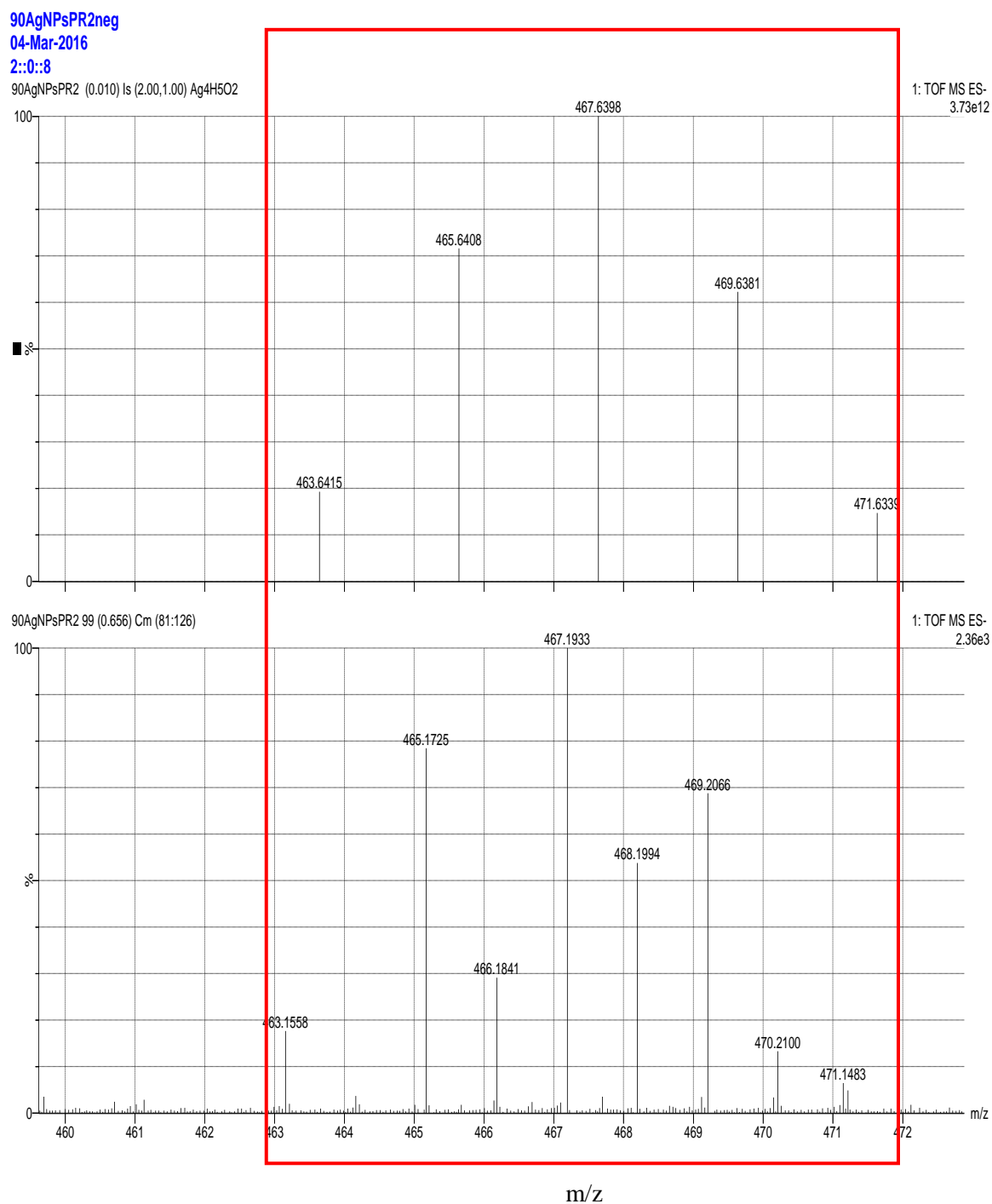


Figure 8.11: ESI-MS spectra of photosynthesized Ag NCs at m/z 467.

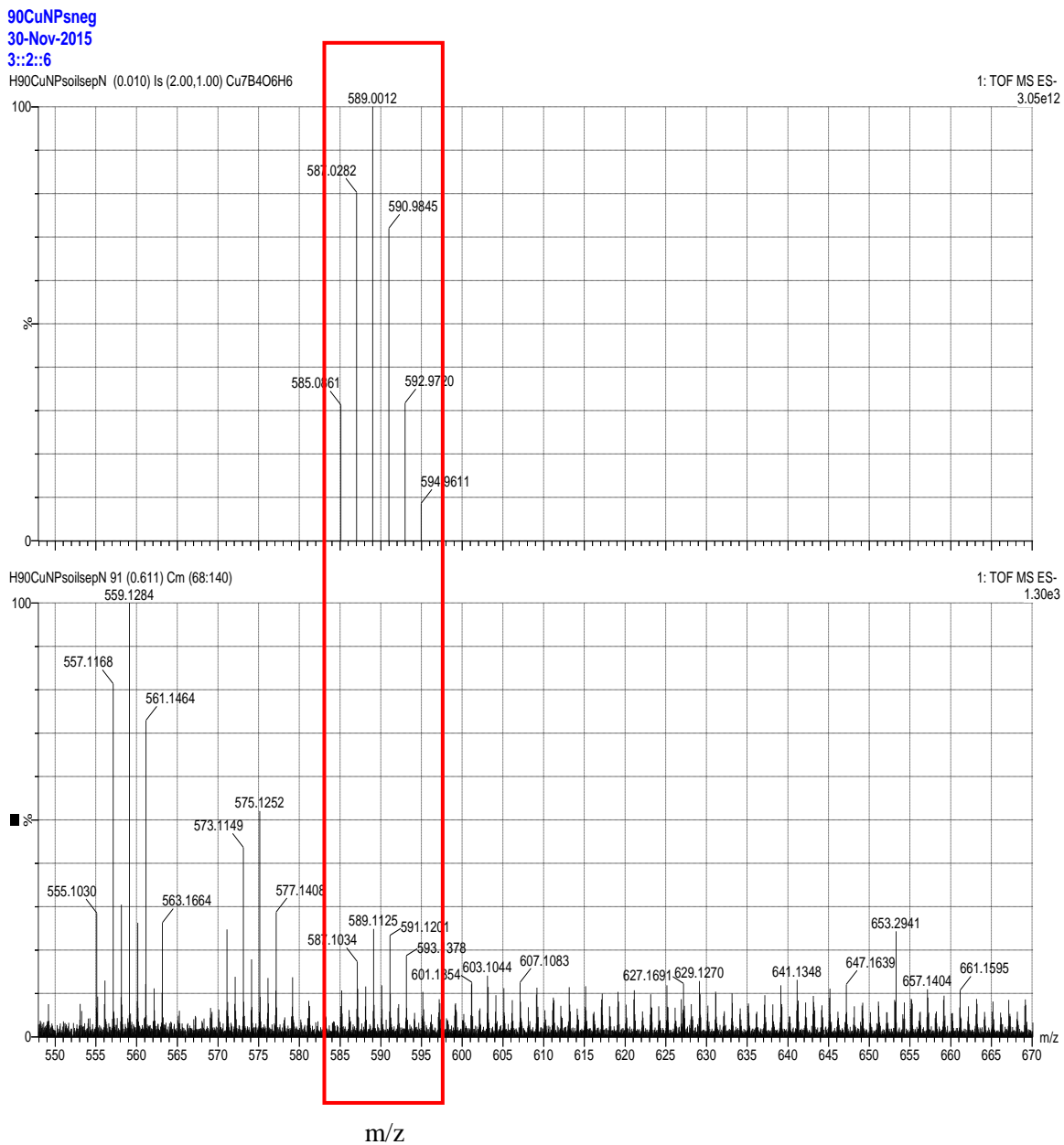


Figure 8.12: ESI-MS spectra of Cu NCs at m/z 589.

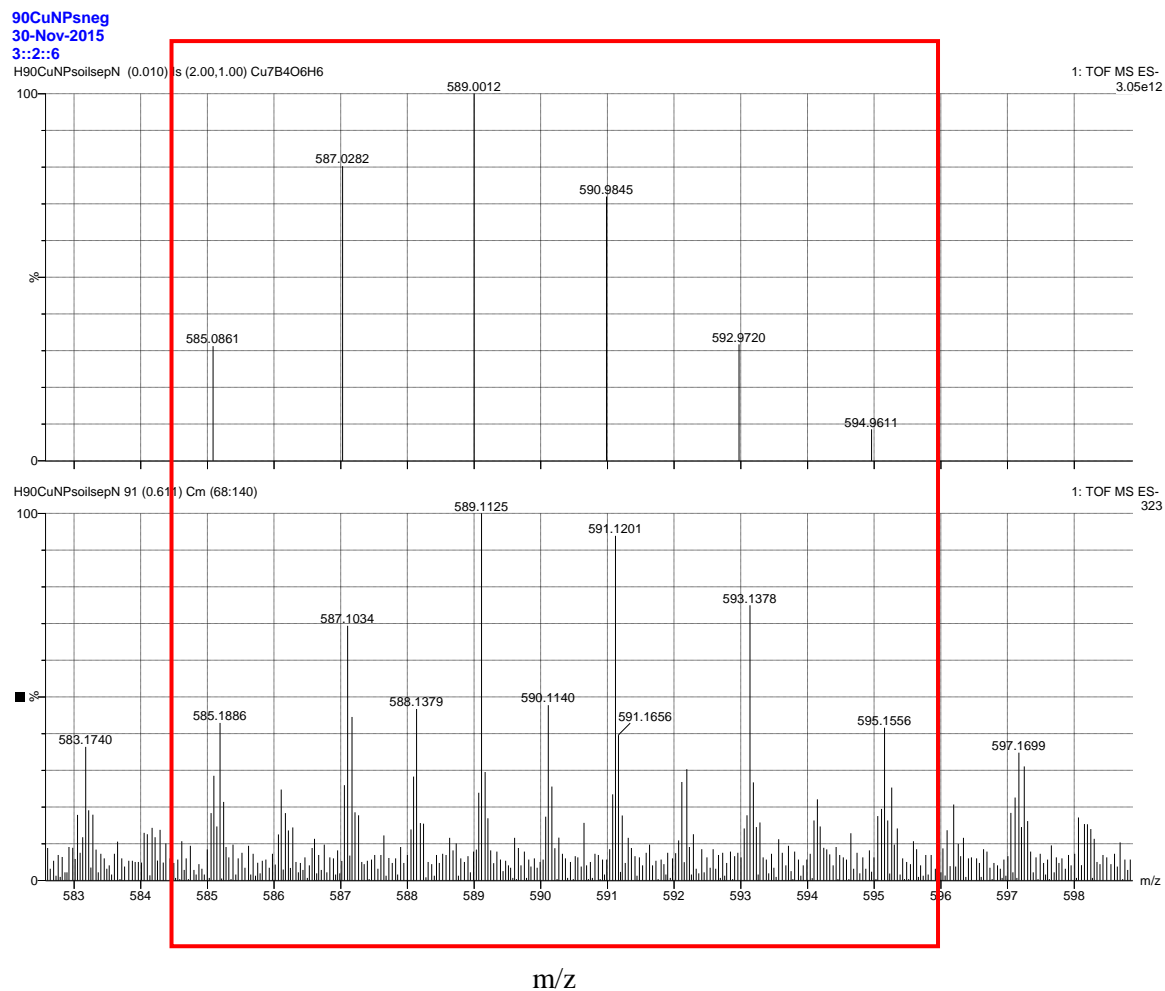


Figure 8.13: Expanded ESI-MS spectra of Cu NCs of the peaks at m/z 589.

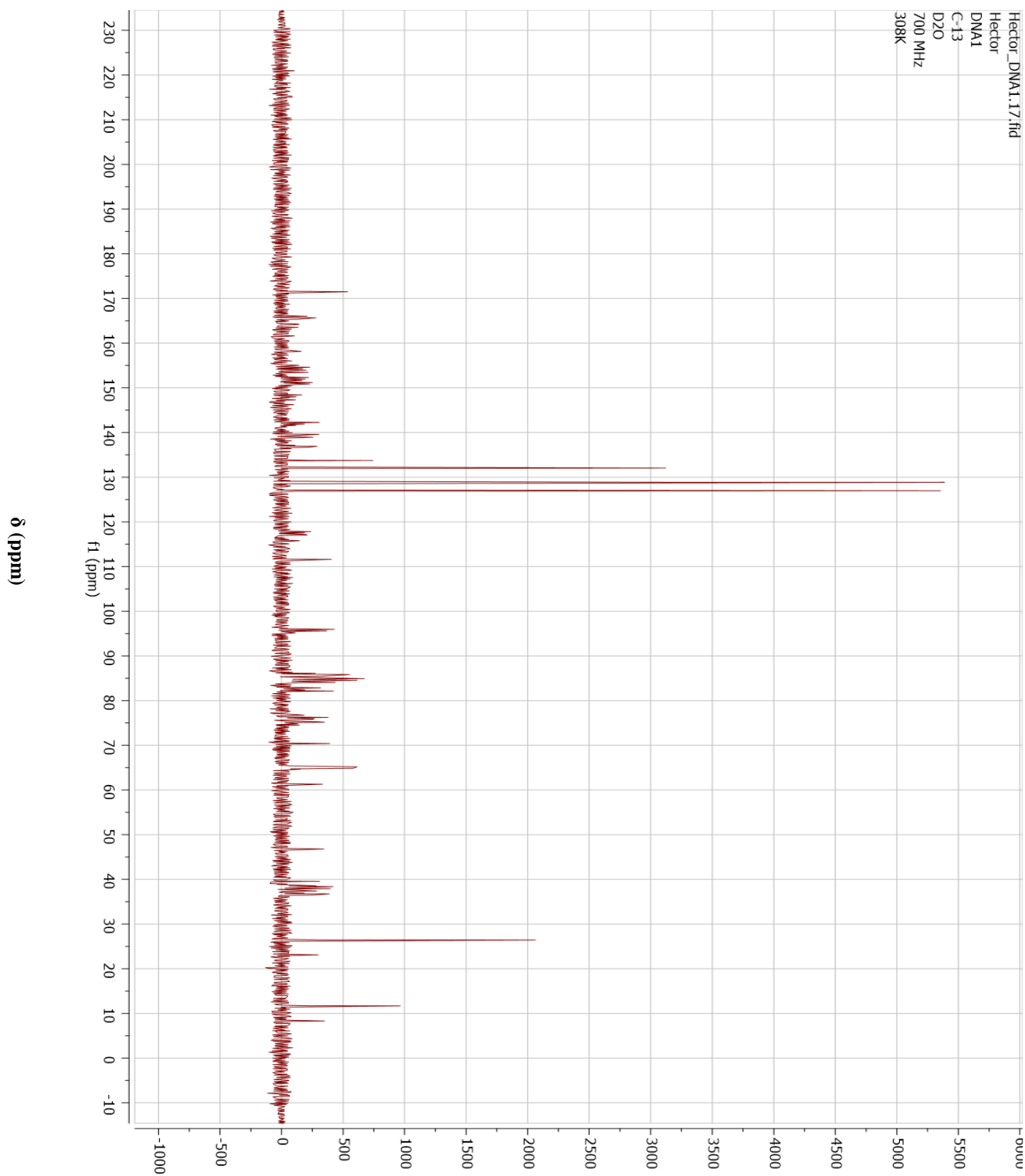


Figure 8.14: ^{13}C NMR spectrum of DNA1 in 99 % D_2O , 308 K.

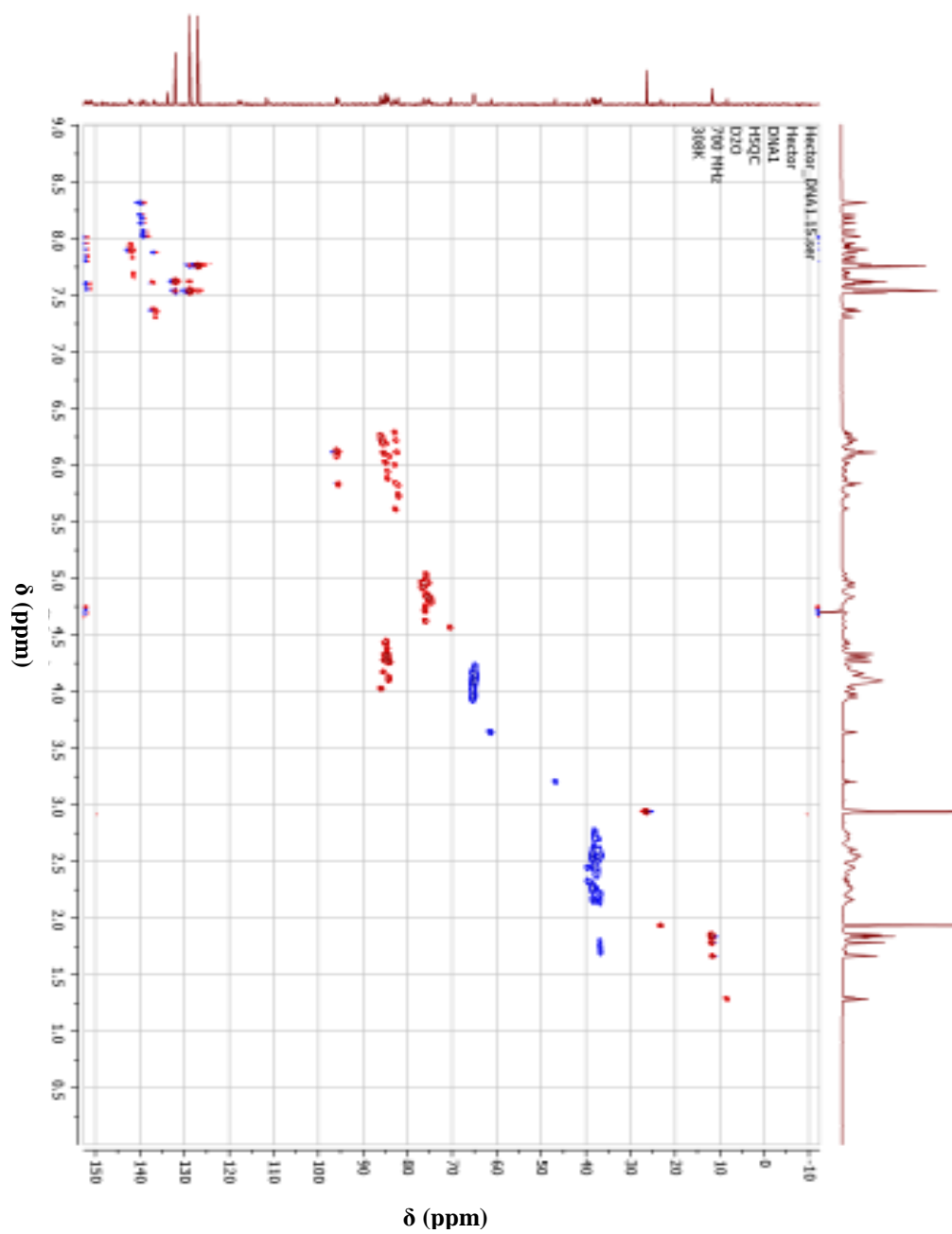


Figure 8.15: HSQC NMR spectrum of DNA1 in 99 % D₂O, 308 K.

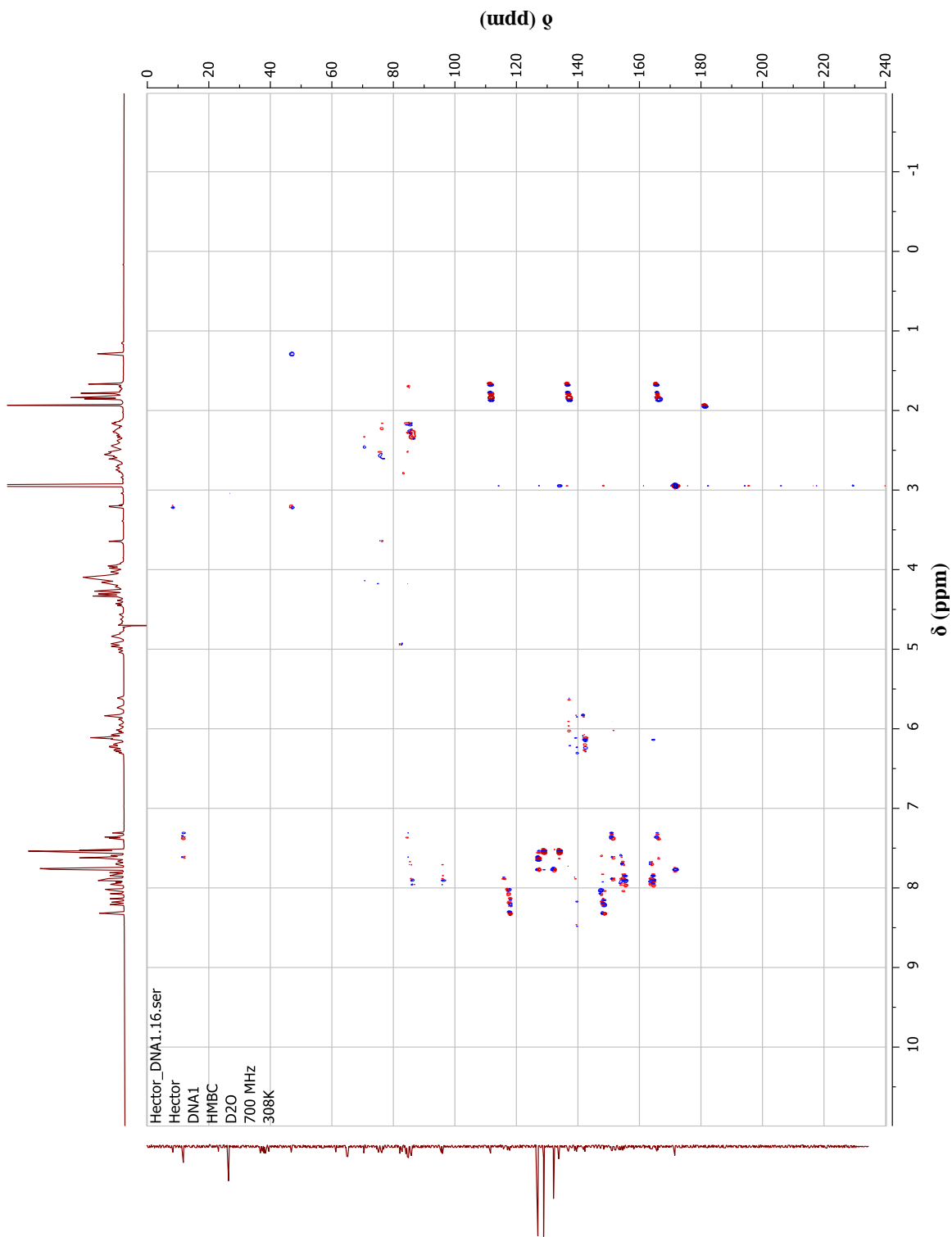


Figure 8.16: HMBC NMR spectrum of DNA1 in 99 % D₂O, 308 K.

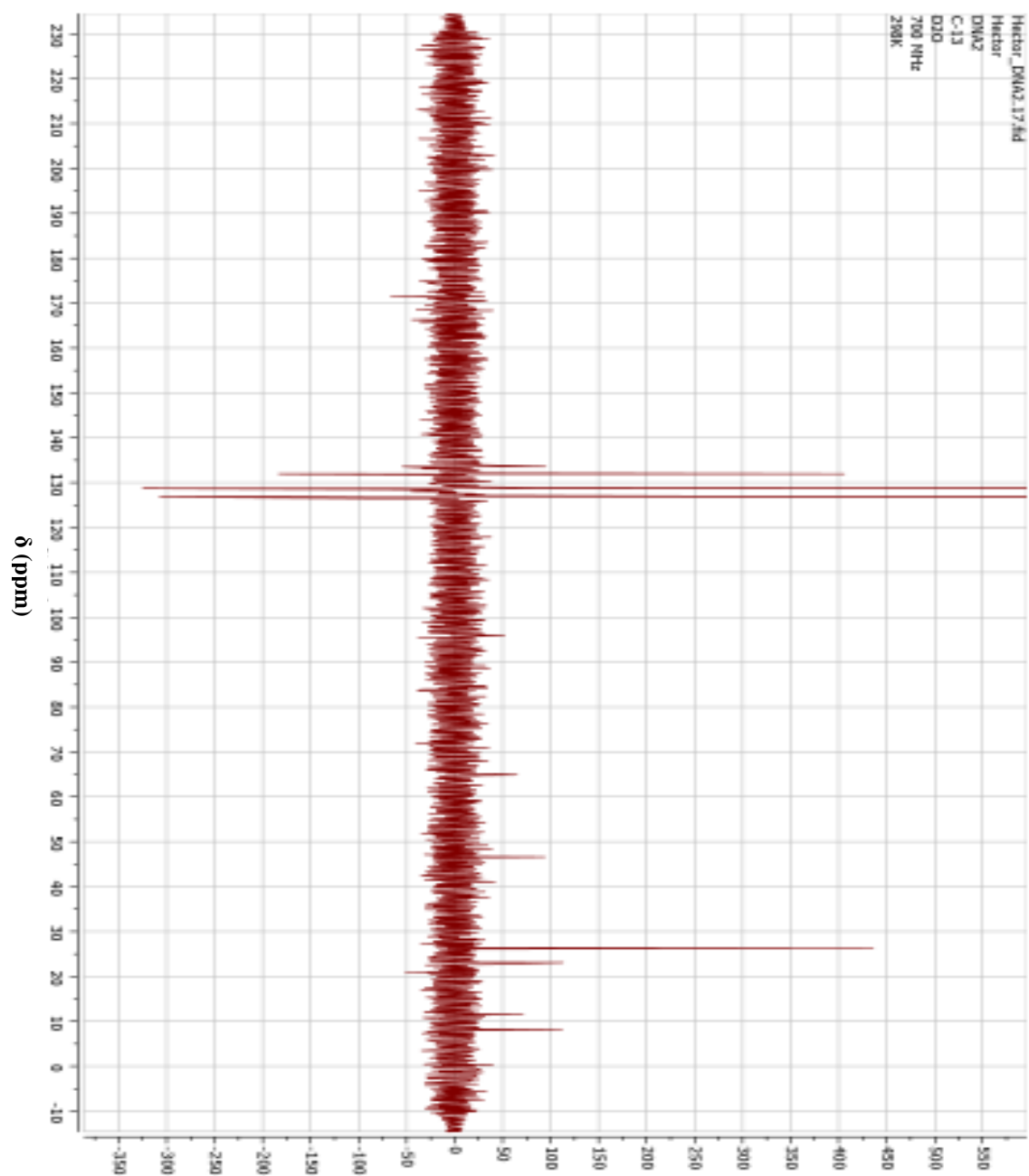


Figure 8.17: ^{13}C NMR spectrum of DNA2 in 99 % D_2O , 298 K.

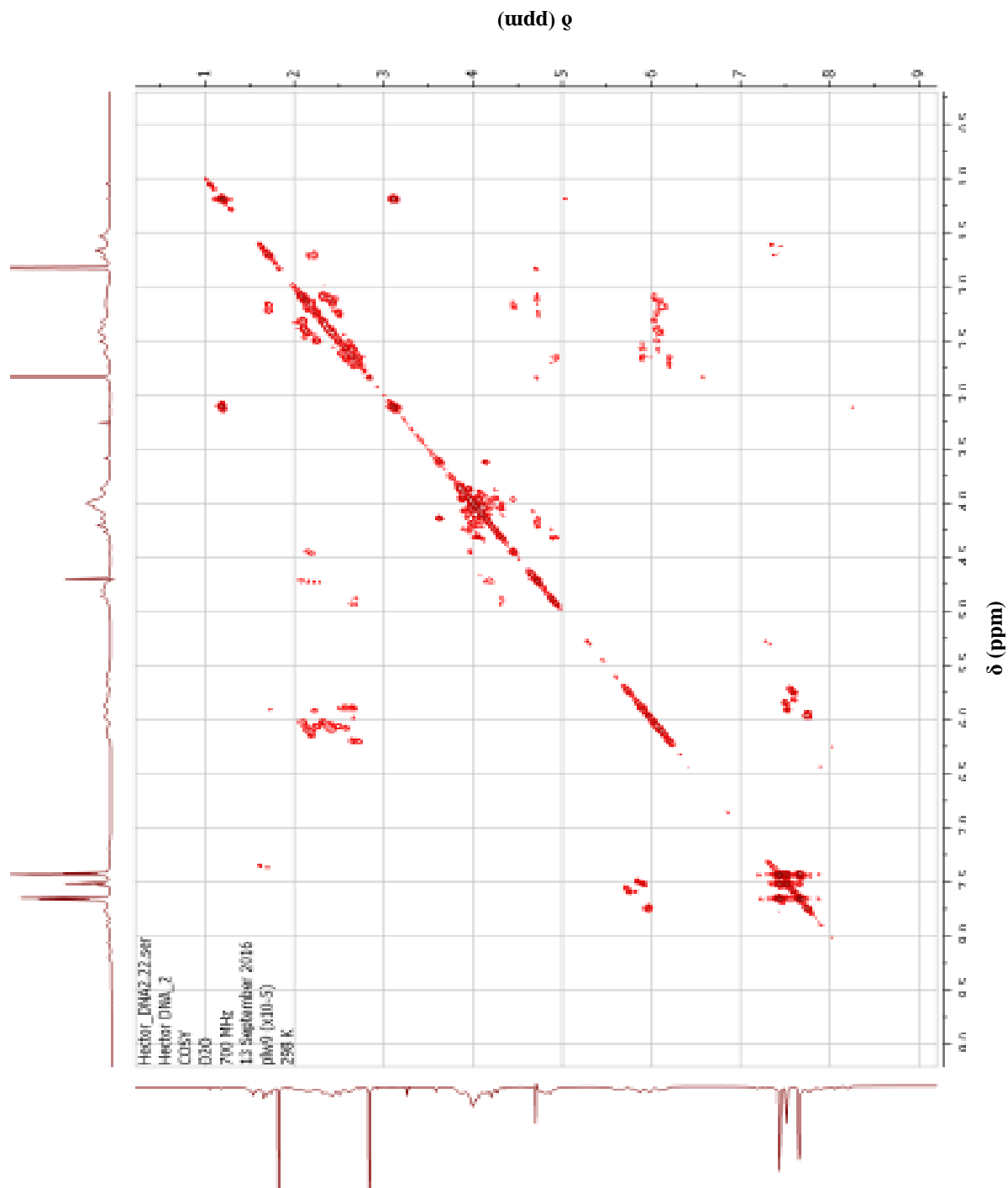


Figure 8.18: COSY NMR spectrum of DNA2 in 99 % D₂O, 298 K.

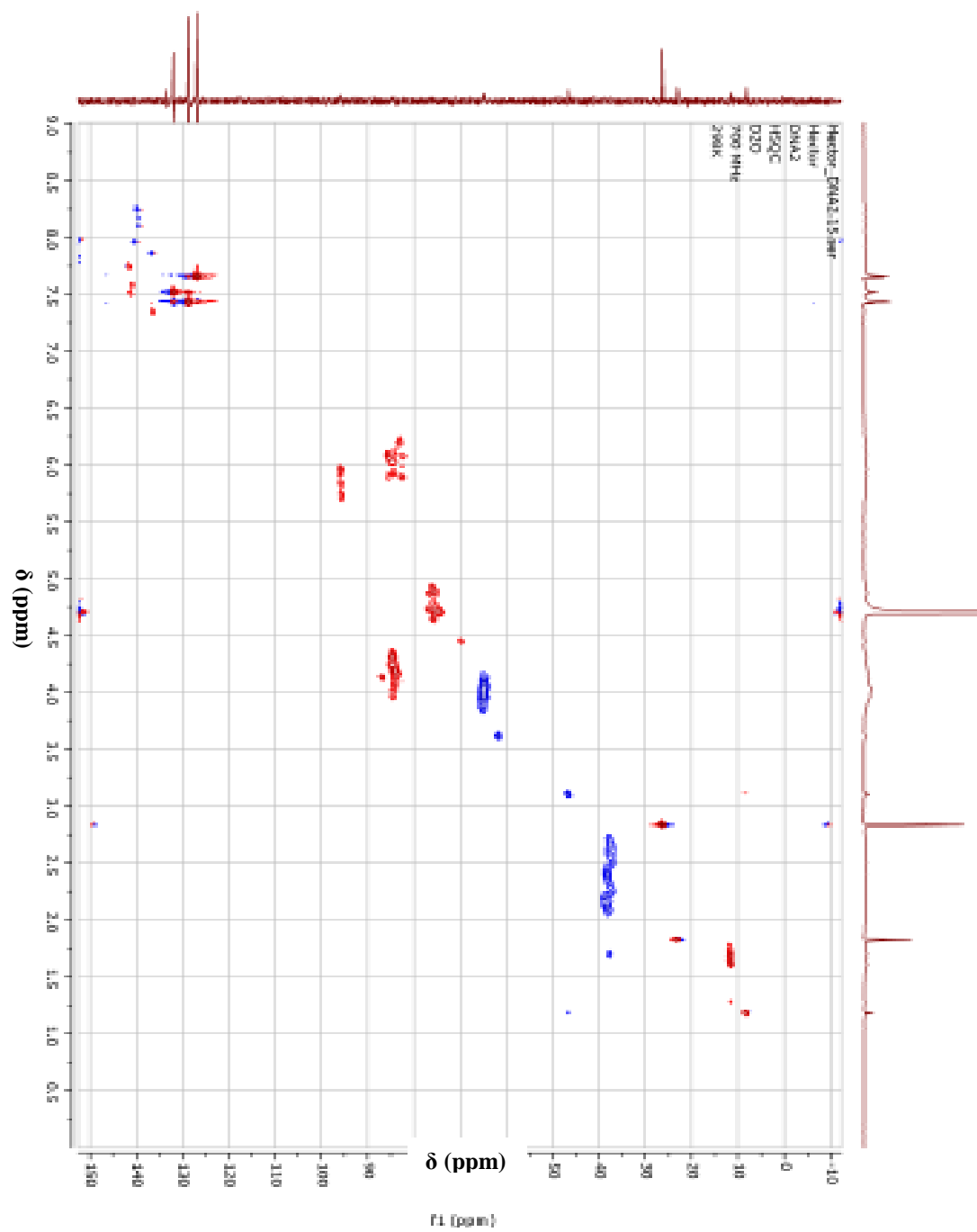


Figure 8.19: HSQC NMR spectrum of DNA2 in 99 % D₂O, 298 K.

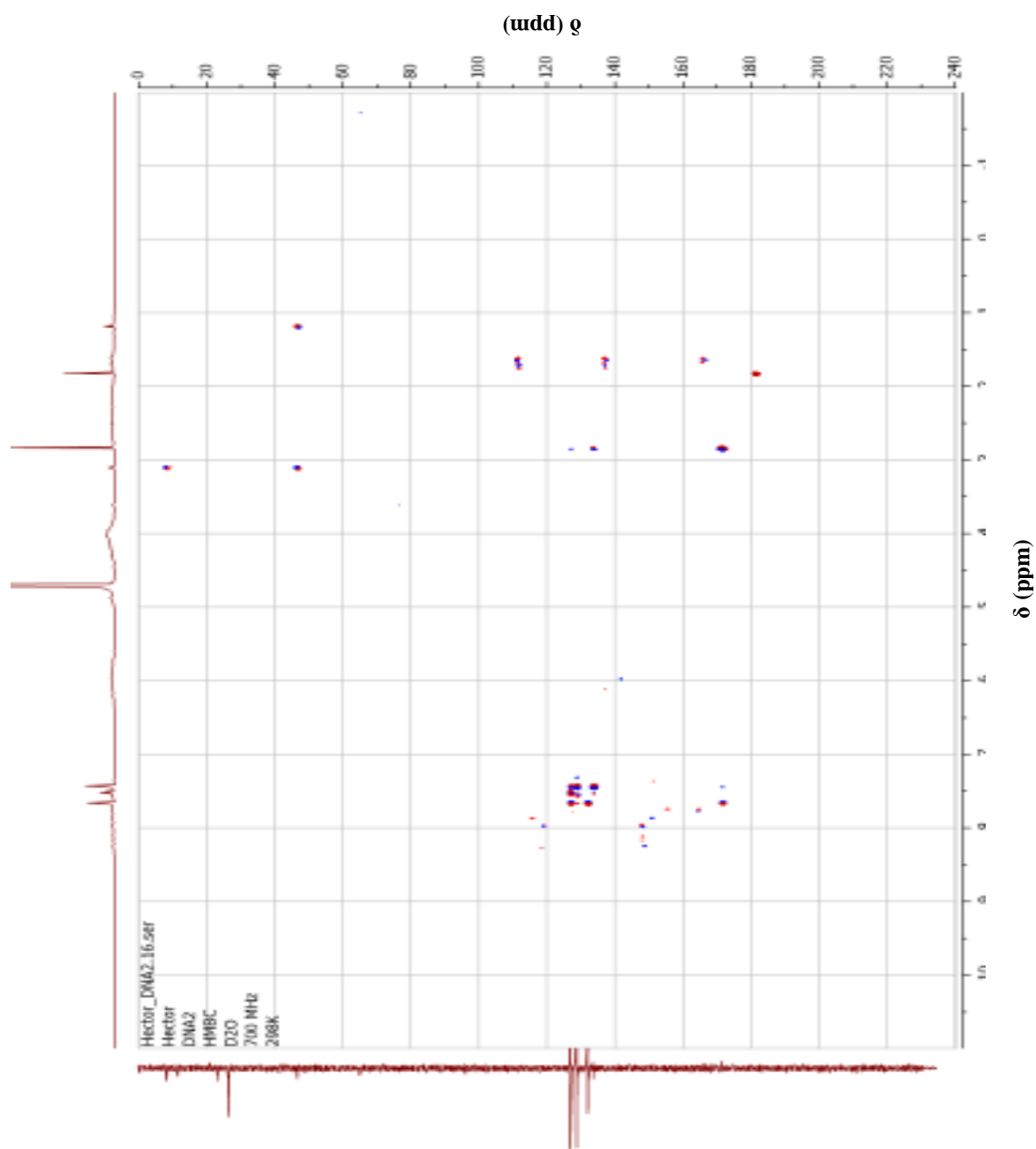


Figure 8.20: HMBC NMR spectrum of DNA2 in 99 % D₂O, 298 K.

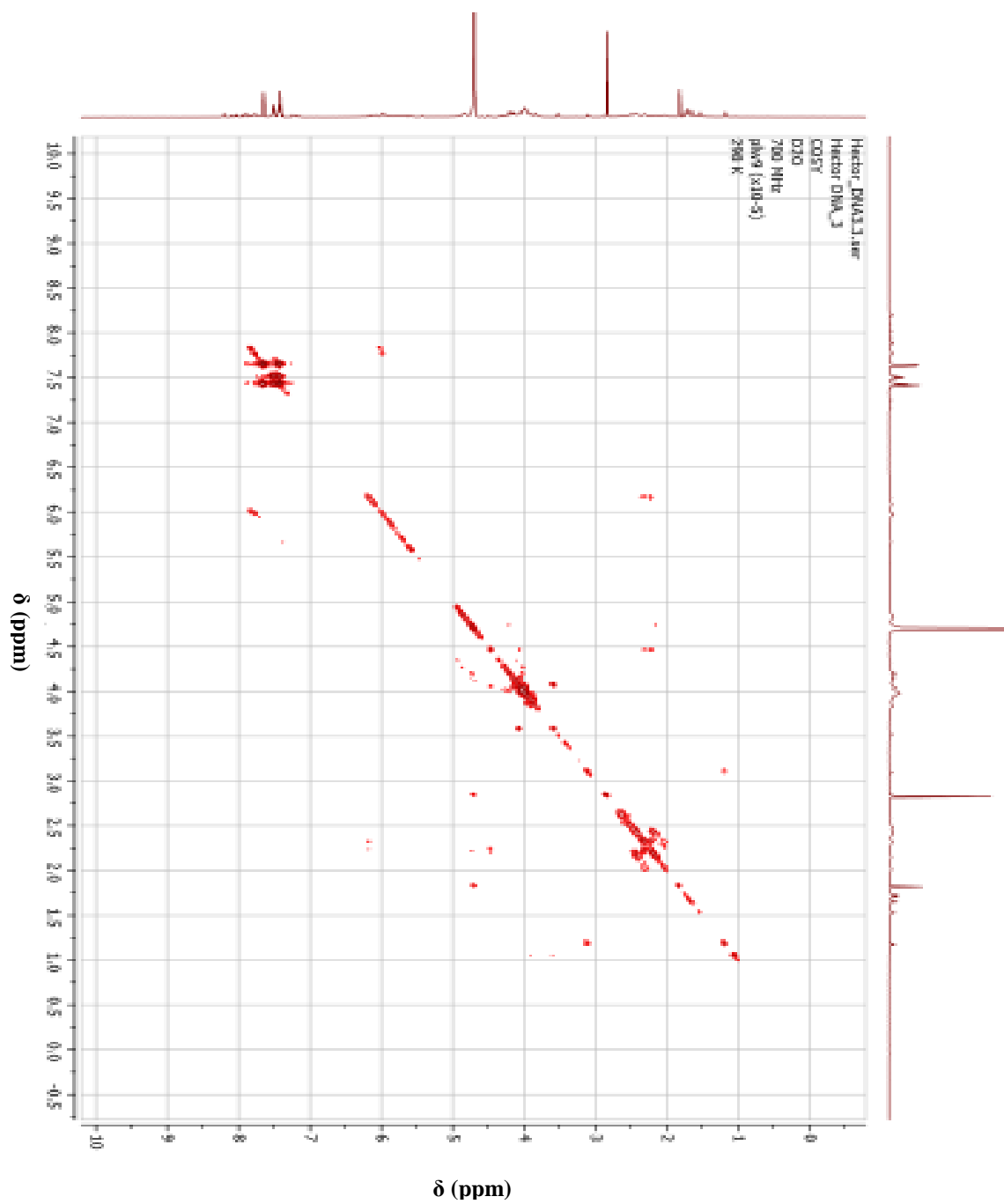


Figure 8.21: COSY NMR spectrum of DNA3 in 99 % D₂O, 298 K.

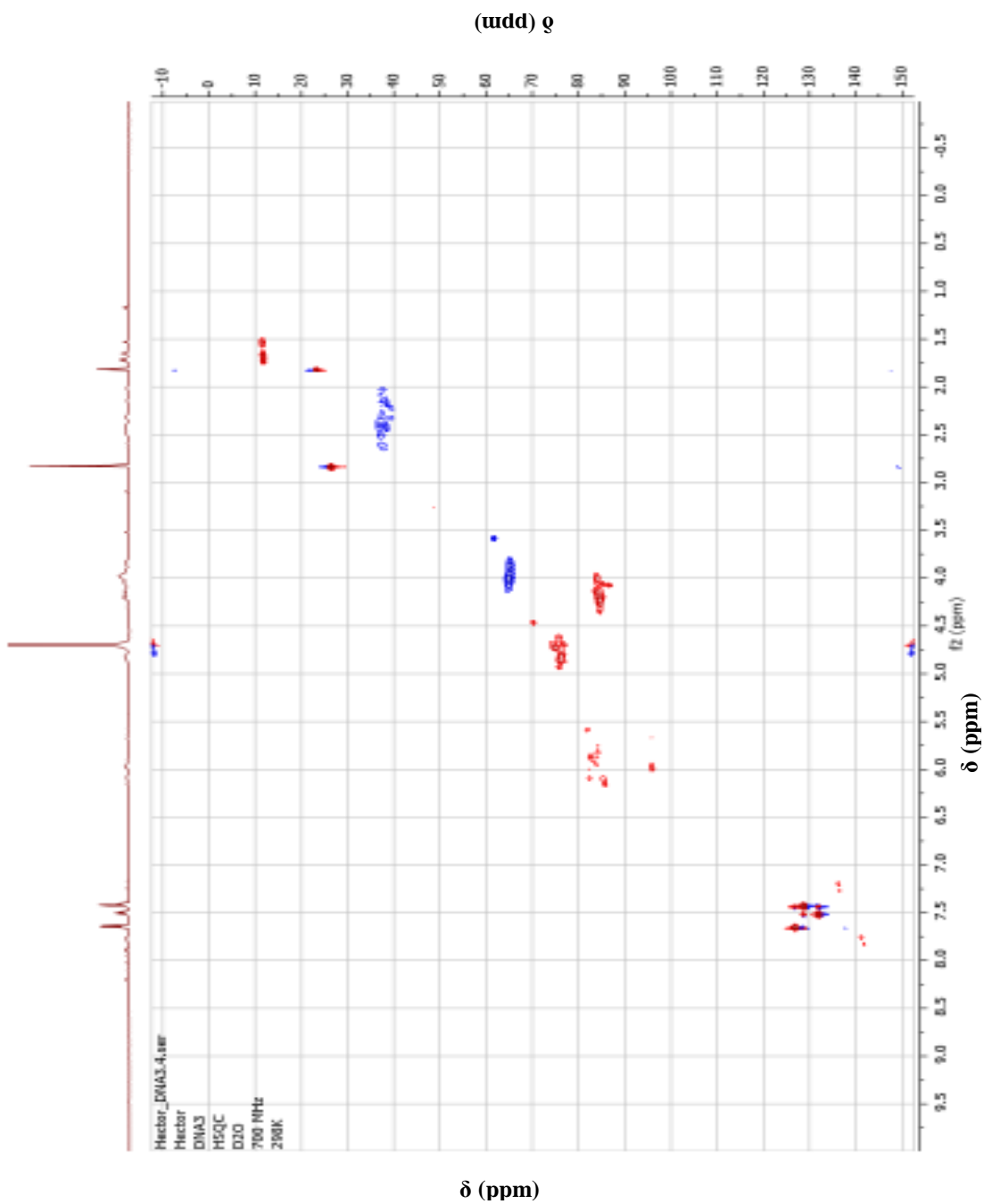


Figure 8.22: HSQC NMR spectrum of DNA3 in 99 % D₂O, 298 K.

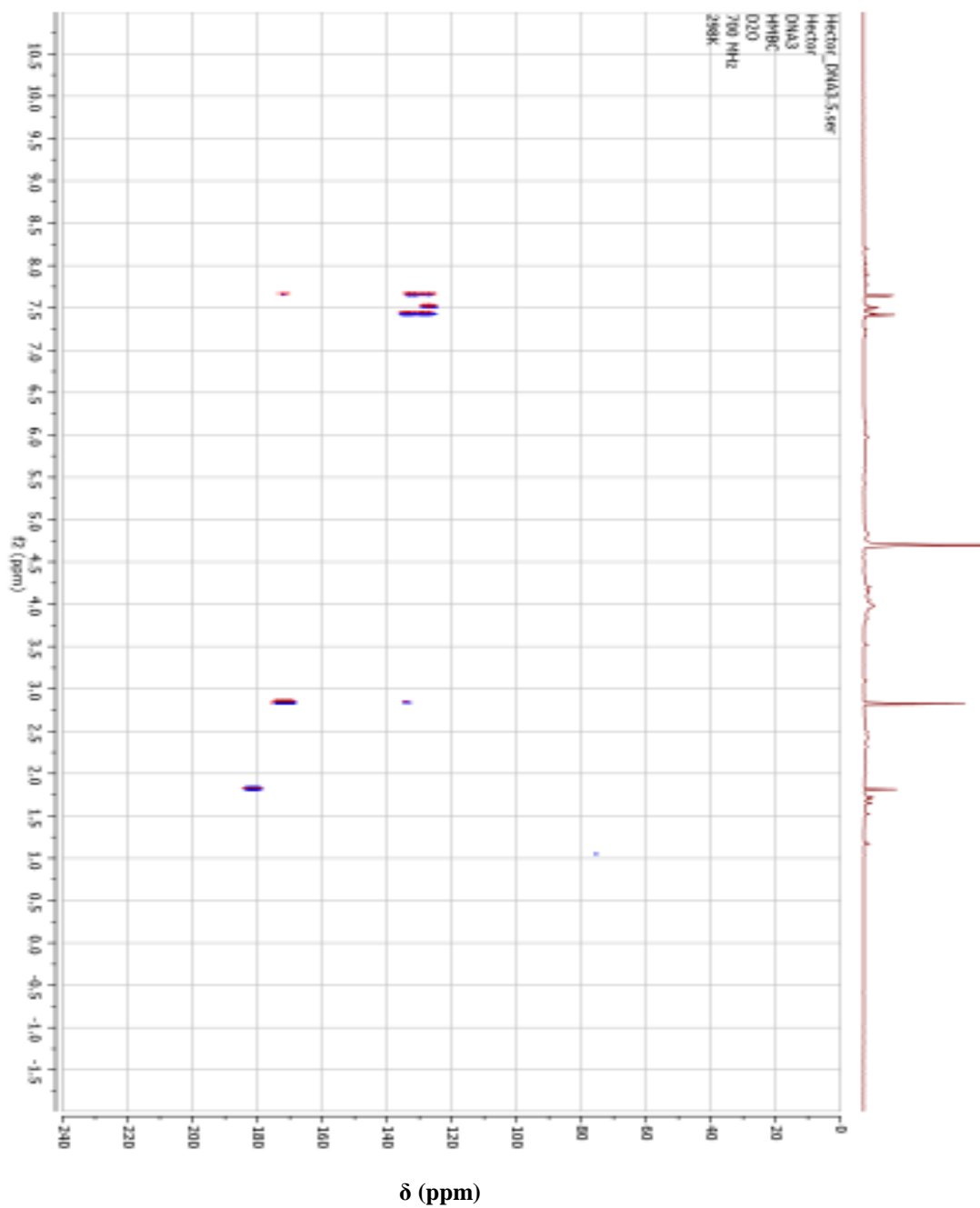


Figure 8.23: HMBC NMR spectrum of DNA3 in 99 % D₂O, 298 K.

